NOTE TO USERS

QUANTUM MOLECULAR DYNAMICS OF LIQUID WATER AND ICE

by

Lisandro Hernández de la Peña

Submitted in partial fulfillment of the requirements
for the degree of Doctor of Philosophy

at

Dalhousie University
Halifax, Nova Scotia
September 2004

Your file Votre référence
ISBN: 0-494-00946-2
Our file Notre référence
ISBN: 0-494-00946-2

DALHOUSIE UNIVERSITY

To comply with the Canadian Privacy Act the National Library of Canada has requested that the following pages be removed from this copy of the thesis:

Preliminary Pages

Examiners Signature Page (pii)

Dalhousie Library Copyright Agreement (piii)

Appendices

Copyright Releases (if applicable)

A mis padres, Isabel y Pedro

TABLE OF CONTENTS

LIST OF TABLES..... viii

LIST OF FIGURES..... ix

ABSTRACT..... xv

LIST OF ABBREVIATIONS AND SYMBOLS USED..... xvi

ACKNOWLEDGMENTS..... xxiv

1. INTRODUCTION..... 1

2. UNDERSTANDING CONDENSED MATTER..... 6

2.1- BASIC CONCEPTS OF STATISTICAL MECHANICS..... 6

2.2- EXPERIMENTAL METHODS..... 12

2.2.1- X-ray scattering..... 13

2.2.2- Neutron scattering..... 14

2.3- COMPUTER SIMULATIONS..... 16

2.3.1- Molecular dynamics..... 17

2.3.2- Calculation of properties..... 23

3. LIQUID WATER AND ICE..... 26

3.1- PHYSICAL PROPERTIES OF LIQUID WATER AND ICE... 26

3.2- MOLECULAR MODELS OF WATER..... 31

3.3- CLASSICAL AND QUANTUM APPROACHES..... 35

4. QUANTUM SIMULATIONS OF LIQUID WATER AND ICE 39

4.1- *AB INITIO* MOLECULAR DYNAMICS..... 40

4.1.1- CP molecular dynamics of liquid water..... 42

4.2- PATH INTEGRAL METHODS..... 46
4.2.1- General background..... 46
4.2.2- PIMD simulations of liquid water with flexible models 55
4.2.3- PI simulations of liquid water and ice with rigid models 57
4.2.4- Feynman-Hibbs effective variational approach ... 62
4.2.5- Centroid molecular dynamics simulation of liquid water 67
4.3- *AB INITIO* PATH INTEGRAL MOLECULAR DYNAMICS.. 71

5. CENTROID DYNAMICS AND THE CMD METHOD..... 75
5.1- EXACT FORMULATION OF CENTROID DYNAMICS..... 75
5.1.1- The centroid density in phase space and centroid variables..... 76
5.1.2- The time evolution of the centroid variables..... 86
5.2- THE CMD METHOD..... 91
5.2.1- CMD approximation..... 92
5.2.2- CMD implementation..... 94

6. THE RIGID BODY-CMD METHOD..... 98
6.1- TORQUES IN QUATERNION FORM..... 98
6.2- THE RIGID BODY-CMD METHOD..... 105
6.2.1- A dynamics with constraints..... 106
6.2.2- The orientational centroid and its conservation... 111
6.3- TESTING THE METHOD WITH A SIMPLE SYSTEM..... 117

7. QUANTUM LIQUID WATER..... 126
7.1- PARAMETERIZATION OF THE METHOD..... 126

7.2- ISOTOPIC EFFECT..... 132
7.2.1- Equilibrium properties..... 132
7.2.2- Dynamical properties..... 138
7.2.3- Model comparison..... 150
7.3- TEMPERATURE DEPENDENCE..... 155
7.4- "EFFECTIVE TUNNELING" IN LIQUID WATER..... 172

8. QUANTUM ICE Ih..... 182
8.1- PARAMETERIZATION OF THE METHOD..... 182
8.2- QUANTUM EFFECTS AND MODEL COMPARISON..... 186
8.3- TEMPERATURE DEPENDENCE..... 201
8.4- CLASSICAL VS. QUANTUM MELTING: PRELIMINARY RESULTS..... 209

9. CONCLUSIONS..... 214

APPENDIX. *QUATERNION PARAMETERS AND ROTATIONS* 220

REFERENCES..... 229

LIST OF TABLES

2.1. Coherent and incoherent scattering cross-section for the atomic components of light and heavy water..... 16

3.1 Parameters of some rigid water models..... 33

7.1. Intermolecular potential energies obtained in the classical and quantum simulations of liquid water at 25°C..... 137

7.2. Translational self-diffusion coefficients, in units of 10^{-5} cm^2/s, for TIP4P liquid water at 25°C..... 140

7.3. Molecular and collective (dielectric) relaxation times (in ps) for TIP4P liquid water at 25°C..... 148

7.4. Energies, relative energy shifts and quantum molecular uncertainties values for the SPC/E and TIP4Pew water models at 25°C..... 152

7.5. Self-diffusion coefficients in 10^{-5} cm^2/s for the SPC/E and TIP4Pew water models..... 153

7.6. Molecular and collective (dielectric) relaxation times (in ps) for the SPC/E and TIP4Pew water models..... 154

7.7. Details of the classical and quantum liquid simulations of TIP4P water 156

8.1. Intermolecular potential energies (in kJ/mol) and quantum molecular uncertainties (in degrees) obtained in the classical and quantum simulations of three water models at 220 K..... 192

7.5. Oxygen-oxygen radial distribution function for the three systems: classical water, quantum H_2O and quantum D_2O, all at ambient conditions..... 133

7.6. Oxygen-hydrogen radial distribution function for the three systems: classical water, quantum H_2O and quantum D_2O, all at ambient conditions..... 134

7.7. Normalized probability distribution of the bead-centroid rotation angle 136

7.8. Linear velocity time correlation functions of classical and quantum H_2O and D_2O..... 139

7.9. Components of the angular velocity time correlation function of liquid H_2O 142

7.10. Power spectra of the *x* and *y* components of the angular velocity time correlation function of liquid H_2O..... 144

7.11. Single molecule orientational correlation functions associated with the Legendre polynomial of order k=1 or k=2..... 146

7.12. Spectral functions I_1 and I_2..... 147

7.13. Oxygen-oxygen radial distribution function of liquid SPC/E water at ambient conditions..... 150

7.14. Oxygen-hydrogen radial distribution function of liquid SPC/E water at ambient conditions..... 151

7.15. Oxygen-oxygen radial distribution function of liquid TIP4P water at –20°C and 50°C..... 157

7.16. Oxygen-oxygen and oxygen-hydrogen radial distribution functions of liquid TIP4P water at 0°C and 50°C..... 158

7.17. Average intermolecular potential energies in kJ/mol as a function of temperature..... 159

7.18. Probability distribution of the bead-centroid angle for ice Ih at –38°C and liquid water at –35°C..... 161

7.19. Estimated molecular uncertainty of the water molecule in quantum liquid water as a function of temperature..... 162

7.20. Dependence of the estimated molecular uncertainty of the water molecule in quantum liquid water as a function of the local structural parameter S_g at –35°C..... 163

7.21. Dependence of the average molecular uncertainty and the average potential energy as a function of the density of liquid H_2O at –35°C..... 165

7.22. Self-diffusion coefficient as a function of temperature..... 166

7.23. Diffusion coefficient ratio (Quantum/Classical) as a function of temperature. 169

7.24. Classical and quantum relaxation times τ_1 and τ_2 as a function temperature 170

7.25. (Classical/Quantum) relaxation time ratio as a function of temperature 171

7.26. Oxygen-oxygen spatial distribution function of classical liquid H_2O at 25°C 173

7.27. Oxygen-oxygen spatial distribution functions of classical and liquid H_2O at 25°C..... 174

7.28. Oxygen-oxygen spatial distribution functions of classical and quantum liquid D_2O at 25°C..... 176

7.29. Oxygen-oxygen spatial distribution functions of classical and liquid H_2O at 50°C represented by the isosurface $g_{OO}(\mathbf{r}_{ij}) = 1.4$..... 177

7.30. Left- Oxygen-oxygen spatial distribution functions of classical and quantum liquid H_2O at 0°C. Right- Oxygen-oxygen spatial distribution functions of classical liquid

H_2O at 50°C and quantum liquid H_2O at 0°C..... 178

7.31. A slice of the superposition of the oxygen-oxygen spatial distribution functions of classical and quantum liquid H_2O at -20°C..... 180

7.32. Free energy barrier associated with molecular displacements across the tunneling region in classical and quantum liquid water as a function of temperature 181

8.1. Convergence of the oxygen-oxygen radial distribution function for quantum H_2O ice Ih (at 160 K) with respect to the value of the discretization parameter *P* 184

8.2. Convergence of the oxygen-hydrogen radial distribution function of quantum H_2O ice Ih (at 160 K) with respect to the value of the discretization parameter *P* 185

8.3. Convergence of the linear velocity time correlation function for quantum of H_2O ice Ih (at 160 K) with respect to the value of the discretization parameter *P* 186

8.4. Oxygen-oxygen and oxygen-hydrogen radial distribution functions of classical and quantum TIP4P ice Ih at 220 K..... 187

8.5. Oxygen-oxygen and oxygen-hydrogen radial distribution functions of classical and quantum SPC/E ice Ih at 220 K..... 189

8.6. Oxygen-oxygen and oxygen-hydrogen radial distribution functions of classical and quantum TIP4Pew ice Ih at 220 K..... 190

8.7. Oxygen-oxygen spatial distribution function of classical and quantum TIP4P ice Ih at 220 K..... 191

8.8. Components of the linear velocity time correlation functions for classical and quantum TIP4P ice Ih at 220 K..... 193

8.9. Fourier transform of the components of the linear velocity time correlation functions for classical and quantum TIP4P ice Ih at 220 K..... 194

8.10. Components of the angular velocity time correlation functions for classical and quantum TIP4P ice Ih at 220 K..... 196

8.11. Fourier transform of the components of the angular velocity time correlation functions for classical and quantum TIP4P ice Ih at 220 K..... 197

8.12. Fourier transform of the components of the linear velocity time correlation functions for classical and quantum SPC/E ice Ih at 220 K..... 199

8.13. Fourier transform of the components of the angular velocity time correlation functions for classical and quantum SPC/E ice Ih at 220 K. 200

8.14. Oxygen-oxygen radial distribution functions of liquid TIP4P water at 160 K and 235 K..... 202

8.15. Oxygen-hydrogen radial distribution functions of liquid TIP4P water at 160 K and 235 K..... 203

8.16. Intermolecular potential energy in kJ/mol as a function of temperature 204

8.17. Quantum-minus-classical intermolecular potential energy difference as a function of temperature..... 205

8.18. Estimated molecular uncertainty of the water molecule in quantum ice Ih as a function of temperature..... 206

8.19. Fourier transform of the linear velocity time correlation function for classical and quantum TIP4P ice Ih at 160 K and 235 K..... 207

8.20. Fourier transform of the angular velocity time correlation function for classical and quantum TIP4P ice Ih at 160 K and 235 K..... 208

8.21. Dependence of the value of the oxygen-oxygen RDF at 3.44 Å as a function of temperature for the classical and quantum melting of ice Ih..... 210

8.22. Average intermolecular potential energies as a function of temperature for the classical and quantum melting of ice Ih. The graph also includes well-converged values of classical and quantum ice at 235 K and classical and quantum liquid water..... 212

8.23. Instantaneous molecular configurations of classical ice Ih at 290 K and the resulting liquid water at 295 K..... 213

8.24. Instantaneous molecular configurations of quantum ice Ih at 255 K and the resulting liquid water at 260 K..... 213

ABSTRACT

Water's unusual properties have continuously fascinated researchers from different areas. Yet, in spite of the vast amount of information collected to date, the fitting together of all the different pieces into a coherent picture has proven to be extremely difficult. A detailed account of isotopic effects, as a specific example of these problems, requires the inclusion of the quantum nature of the protons.

Methods based on Feynman's path integral representation of statistical mechanics have been extensively used to calculate equilibrium properties of quantum systems in condensed phase. They allow standard classical methods, such as molecular dynamics, to be used for the simulation of an otherwise quantum system at finite temperature. Furthermore, approximate quantum dynamical information has also become available through the use of the centroid molecular dynamics (CMD) methodology.

In this thesis, a CMD methodology for systems of rigid bodies is developed by introducing the concept of an *orientational centroid* and by designing an algorithm that samples homogeneously the quantum mechanical orientational uncertainty while ensuring centroid conservation. This *rigid body-CMD* technique, which is significantly more efficient than the standard CMD method, is extensively applied to the study of quantum effects in liquid water and ice Ih.

Quantum effects on the equilibrium and dynamical properties of liquid H_2O and D_2O are studied and are shown to agree with previous results. The present method dramatically improves the agreement with experimental isotopic differences relative to those obtained with classical simulations. Quantization is found to significantly affect the properties of liquid water over a wide range of temperatures, especially in the low temperature region. An unusual behaviour of the quantum mechanical molecular uncertainty is identified and its relationship to the local environment is determined. The "effective tunneling" in liquid water is directly characterized as part of a detailed analysis of the interrelationship between structure and dynamics. Quantum effects in ice Ih are also investigated in detail and are found to be significant.

LIST OF ABBREVIATIONS AND SYMBOLS USED

Abbreviations

AIMD	ab initio MD
CMD	centroid molecular dynamics
CP	Car-Parinello
CPMD	Car-Parrinello molecular dynamics
DSCS	differential scattering cross-section
DFT	density functional theory
NMR	nuclear magnetic resonance
IR	infra-red
PIMC	path integral Monte Carlo
PIMD	path integral molecular dynamics
MD	molecular dynamics
QDO	quasi-density operator
QM	quantum mechanical
RDF	radial distribution function
SDF	spatial distribution function

Roman Symbols

$\langle A \rangle$	average of the quantity A
$C(t)$	classical time correlation function
$C_{AB}(t)$	quantum time correlation function
$C_k^z(t)$	single-molecule orientational autocorrelation function associated to the Legendre polynomial of order k
$\left\langle \hat{B}\hat{A}(t) \right\rangle^{Kubo}$	Kubo transformed quantum time correlation function
D	self-diffusion coefficient

D_α	component of the self-diffusion coefficient $\alpha = x, y, z$
$\int_{x(0)=x(\beta\hbar)} \mathcal{D}x(\tau)[\ldots]$	integration over the path $x(\tau)$ starting and ending at point $x(0) = x(\beta\hbar)$ and include an integration over this point
$\int_{x(0)=x'}^{x(\beta\hbar)=x''} \mathcal{D}x(\tau)[\cdots]$	integration over the path $x(\tau)$ starting at point $x(0) = x'$ and ending at point $x(\beta\hbar) = x''$
E	energy
$\mathbf{e}_\alpha$	unit vectors of the principal frame ($\alpha = x, y, z$)
F	Helmholtz free energy
F_c	centroid force
F_k^{bead}	total force acting on the bead minus centroid force
F_k	total force acting on the bead
$\mathbf{F}_i$	force on particle *i*
$g(\mathbf{r}_1, \mathbf{r}_2)$	two-particles distribution function
$g(\mathbf{r}_{ij})$	spatial distribution function
$g(r)$	radial distribution function
$G(\hat{q}_c)$	real and continuous function that minimizes at the centroid
H	Hamilton's function (except page 29 where is enthalpy)
$\hat{H}$	Hamiltonian operator
$\hbar$	Planck's constant over 2π
H_c	centroid energy variable
$\ddot{\mathbf{I}}$	inertia tensor of a rigid molecule
$I(w)$	Fourier transform of the quantum time correlation function

$I^{Kubo}(w)$	Fourier transform of the Kubo transformed quantum time correlation function
$I^{(c)}(w)$	Fourier transform of the centroid correlation function
I_k^z	spectral function associated to the orientational time $C_k^z(t)$ correlation function
I_x	principal moment of inertia on the x axis
K	kinetic energy
$\mathbf{k}$	wave number
k	bead identifier (except in page 145 where is the order of a polynomial)
k_B	Boltzmann constant
$\mathcal{L}$	Lagrange's function
$\mathbf{L}$	angular momentum vector
L_i	component of the angular momentum vector
M	number of thermostats in a Nose-Hoover thermostat chain
m	particle's mass
M_i	mass of the nucleus i
$\tilde{m}$	reduced mass
$\mathbf{M}(t)$	total dipole moment
N	number of particles (molecules) in the system
$\hat{N}$	quaternion whose components represent the derivatives of the potential with respect to the quaternion parameters
P	total number beads (except in Chapter 3 and where is pressure)
$\hat{p}$	momentum operator

p_c	centroid momentum variable
p_0	mean value of momentum of a imaginary path
$\mathbf{p}^N$	momenta microstate of a N particle system (in a three dimensional space)
$\mathbf{p}_i$	momentum of particle i
$(\mathbf{p}_1,\cdots,\mathbf{p}_N)$	momenta microstate of a N particle system (in a three dimensional space)
$\langle p\|$	bra momentum vector
$\|p\rangle$	ket momentum vector
P_k	Legendre polynomial of order k
$\Pr(\mathbf{r}^N,\mathbf{p}^N)$	probability density of observing a specific configuration
Q	bath inertia parameter of a Nose-Hoover thermostat
$\hat{q}$	quaternion
$\{\hat{q}_k\}$	set of quaternions
q_j	quaternion parameter j=0,1,2,3
$\mathbf{r}^N$	position microstate of a N particle system (in a three dimensional space)
$(\mathbf{r}_1,\cdots,\mathbf{r}_N)$	position microstate of a N particle system (in a three dimensional space)
$(\mathbf{r}^N,\mathbf{p}^N)$	phase space point of a N particle system (in a three-dimensional space)
S	action functional (except page 30 where is entropy)
$S_{FA}(\Omega_k,\Omega_{k+1};\beta/P)$	fixed axis action
S_g	local tetrahedral order parameter
$S(\mathbf{k})$	structure factor

$\langle\ \rangle_{S'}$	path integral average using the action S'
T	temperature
$\hat{T}$	kinetic energy operator
$\widehat{T}$	torques represented as a pure quaternion
$\mathbf{T}_{cl}$	classical torque
$\mathrm{T_m}$	thermodynamic melting temperature
$\mathrm{T_{mph}}$	mechanical phase transition temperature
$\mathbf{T}_q$	quantum torque
$\hat{T}_e$	electronic kinetic energy operator
$\mathbf{T}_k$	total torque acting on the bead k
$\hat{T}_N$	nuclear kinetic energy operator
t_x, t_y, t_z	components of the torque between beads (or quantum torques)
U	potential energy
$\mathbf{u}_1$	unit vector associated to the rotation axis
$\hat{V}$	potential energy operator
$V\left(\mathbf{r}^N\right)$	potential energy
$W(x_0)$	Feynman-Hibbs effective potential
$\widehat{w}$	angular velocity vector represented as a pure quaternion
w_i	component of the angular velocity
$\mathbf{X}$	six-dimensional coordinate that represent the position and orientation of a rigid object
$\hat{x}$	position operator

x	Cartesian axis
x_0	mean value of position of a imaginary path
x_c	centroid position variable
$\langle x \vert$	bra position vector
$\vert x \rangle$	ket position vector
y	Cartesian axis
z	Cartesian axis
Z	partition function
Z_P	P discretized partition function
$Z[\mathbf{r}_N(\tau)]$	electronic partition function

Greek Symbols

β	inverse of temperature in energy units
γ_{lm}	angle subtended at the central atom between the l^{th} and m^{th} bonds
$\Gamma(\Omega_k, \Omega_{k+1})$	arclength of the rotation that transforms the orientation Ω_k into Ω_{k+1}
$\Gamma(k, k+1)$	arclength of the rotation that transforms the orientation k into k+1
$\Delta\Omega_i$	orientational uncertainty associated with the centroid i
$\delta F'$	variation of the Helmholtz Free energy
$\delta(p_0 - p_c)$	Dirac delta function in momentum space
$\delta(x_0 - x_c)$	Dirac delta function in position space
$\delta V(x_0)$	variation of the potential $V(x_0)$

$\hat{\delta}_c(x_c, p_c)$	quasi-density operator
ε	$1/P$ fraction of imaginary time
$\varepsilon_0(\mathbf{r}_N)$	ground state electronic energy
$\varepsilon_n(\mathbf{r}_N)$	electronic energy of level n
θ	twice the quaternion rotation angle (polar representation)
$\{\Lambda_{i,j}\}$	set of Langrangian parameters
$\lambda(t)$	thermostat parameter
μ	fictitious "mass" in Car-Parrinello
$\rho^{(2)}(\mathbf{r}_1, \mathbf{r}_2)$	probability density of simultaneously observing two molecules in configuration $(\mathbf{r}_1, \mathbf{r}_2)$
Ξ	orientation matrix
ρ	density
$\rho_c(x_c)$	centroid density in coordinate space
$\rho_c(x_c, p_c)$	centroid density in phase space
$\rho_0(x_k, x_{k+1}; \beta\hbar / P)$	free translational propagator (one dimensional)
$\rho_0(\mathbf{X}_k, \mathbf{X}_{k+1}; \beta/P)$	generalized free propagator
$\rho_0(\mathbf{r}_k, \mathbf{r}_{k+1}; \beta/P)$	free translational propagator (three dimensional)
$\rho_0(\Omega_k, \Omega_{k+1}; \beta/P)$	free orientational propagator
$\rho_{qm}(x, p)$	quantum mechanical distribution function in phase space
ρ_w	Wigner distribution function
σ	characteristic distance
σ_{inc}	incoherent scattering cross-section

σ_{coh}	coherent scattering cross-section
τ	imaginary or Euclidean time
τ_D	colective (or dielectric) relaxation time
τ_k^z	single molecule relaxation times associated to $C_k^z(t)$
χ_{k+1}	scalar element of the composite quaternion between $\hat{q}_k$ and $\hat{q}_{k+1}$
Ψ	electronic state
$\{\psi_i\}$	Kohn-Sham orbitals
$\hat{\varphi}(x_c, p_c)$	centroid constrained Boltzman operator in phase space
Ω	molecular orientation

ACKNOWLEDGMENTS

I am sincerely grateful to my supervisor Professor Peter G. Kusalik who suggested the original idea of this work and provided an uncountable amount of insights and encouragement. I am also thankful to my colleague Shah, who taught me a great deal about ice simulations and John for carefully reading the manuscript of this thesis.

I express my sincere gratitude to the members of the Chemistry Department who have made my time at Dalhousie fruitful. Dr. A. Rutenberg generously allowed me access to BUG. Dr. F. Cozens for her involvement as a Graduate Student coordinator. Eva, Lauren and Liz have also played a crucial role on my life in Canada.

I am deeply thankful to Angela, Georgina and Glenn for welcoming me into their lives and for sharing with me unforgettable moments.

Finally, I will always be grateful to my parents, Isabel de la Peña Bermúdez and Pedro Félix Hernández Madruga, who have taught me the most important lessons.

1. INTRODUCTION

A microscopic understanding of matter has been the challenge of many scientists for several centuries. With the progress of science and technology the focus has evolved from gases to matter in the condensed state (ie. liquids and solids). The recent development of a variety of experimental techniques and the advancement of the theoretical methods available have permitted a remarkable improvement in the understanding of liquid and solid structures as well as their dynamical properties.

Computer simulations, in particular, have played a major role in the microscopic understanding of matter. Their versatility, adaptability and applicability to different system models have produced many insightful results and have significantly impacted our knowledge of condensed matter. Computer simulations are not aimed to substitute experiments but to complement their findings. The main reason why they are very useful in scientific research is because they provide a level of microscopic detail of a model system that is beyond the scope of today's experimental techniques on real systems. In fact, computer simulations allow us to investigate the influence of a certain property in a system's behaviour by studying the model system in the presence and absence of that specific property. In this way, they create a virtual but fruitful scenario where our very basis of assumed knowledge can be challenged with a careful and consistent plan of "computer experiments" where the main theoretical tool is statistical mechanics.

Classical statistical mechanics [1-3] is often used to probe the relative arrangement of atoms and molecules in condensed phase [4-6]. The Born-Oppenheimer

approximation allows us to decouple the electronic and nuclear motions and, after averaging over the electronic degrees of freedom, to center attention on the remaining problem of sampling the statistical configurations of the nuclei, within the effective interactions induced by the averaged electric potential. In general, the potential surface on which the nuclei move should be found by performing a Boltzmann weighted sum over the electronic states. However, the electronic states of most systems are usually dominated by the lowest energy levels and the result of averaging out the quantum fluctuations of the electrons yields the ground state Born-Oppenheimer energy surface. Classical mechanics then becomes a useful tool to study the spatial configurations of the nuclei, since they are much heavier than the electrons. The relatively high mass of nuclei implies that the quantum uncertainties in their positions are relatively small at ambient temperatures, and as a result can be reasonably considered as classical particles. In this context, additional constraints can be applied, for example the use of rigid models in a molecular liquid result in a distance constraint over pairs of nuclei, etc. [4,6].

There are, however, circumstances where the quantum nature of the nuclei is relevant; such is the case of the protons in water. Methods based on Feynman's path integral representation of statistical mechanics [7,8] can account for the nuclear uncertainty. These methods can utilize standard classical statistical techniques such as Monte Carlo and molecular dynamics for the simulation of a quantum system at finite temperature by providing an isomorphic classical system [9,10]. This isomorphism, which is established through the canonical partition function, has been extensively used to calculate equilibrium properties of systems in condensed phase [9-16], including liquid

water [12-15] and ice [16]. The inclusion of the proton uncertainty in liquid water simulations via path integral simulations and its impact on equilibrium properties have been investigated in rigid [12,14] and flexible molecular models [13,15]. The effect of the proton uncertainty on the structure of liquid water was found to be equivalent to the structural effects associated with raising the temperature about 50 degrees [12], and therefore non-negligible.

In the context of path integral methods, approximate quantum dynamical information has also become available through the use of effective potentials and the centroid molecular dynamics (CMD) methodology [17,18]. This later methodology, while reproducing equilibrium properties, also allows the calculation of (approximate) quantum time-dependent properties and is particularly accurate in systems where the behaviour is close to the classical limit. Using this technique, Lobaugh and Voth [19] determined estimates for the equilibrium and dynamical properties of quantum water. They found that quantum time correlation functions decay faster than the corresponding classical ones [19], consistent with the expected tunneling behaviour in liquid water [12]. The results obtained with an effective potential technique [20] based on the Feynman-Hibbs variational treatment agree reasonably well with the more accurate but computationally more expensive CMD method.

Liquid water and ice, as is well known, have been the focus of much research attention from scientists and engineers over many decades [21-24]. Their importance in living systems and the environment, together with their unique properties, has continued to fascinate researchers from many different fields of study. In spite of the apparent

molecular simplicity of water and the vast amount of experimental information available, which is constantly being increased by the addition of new data from a wide range of techniques, a coherent assembly of the different pieces has proven to be extremely difficult.

Although both rigid and flexible water models have been used to simulate liquid water [25-26], it is well known that most bulk properties are very well reproduced without the inclusion of molecular vibrations. Very recently, first principles simulations of rigid water [27] have been found to reproduce experimental results well, while the inclusion of flexibility in the water model appeared to impact negatively on this agreement. Furthermore, quantum simulations on rigid models [12,14] have confirmed that more than 90% of the bulk effects of quantization appear to be due to the orientational degrees of freedom. This can be understood as a consequence of the fact that the water molecule has small inertia moments but a relatively large total mass.

This thesis is primarily concerned with the development of a method that includes both the quantum mechanical uncertainty of the proton in the context of a rigid molecular model and the calculation of (approximate) real time dynamical information. This technique, called ***rigid body centroid molecular dynamics***, can be thought of as resulting from the removal of vibrations within the context of the original CMD method. The principal advantage of this methodology is that the number of degrees of freedom required in the simulation is decreased significantly; classically by excluding the vibrational motion, and quantum mechanically from the use of a significantly lower value of the discretization parameter, P (due to the rigid rotor treatment of the molecule).

Consequently, the simulation is dramatically less expensive to perform computationally without significant loss of physical insight. This approach also allows the dynamics of the translational degrees of freedom to be treated either classically or quantum mechanically according to the nature of the system under consideration. Additionally, this thesis presents the results of the extensive application of this method to the simulation of quantum effects in liquid water and the most common form of ice, ice Ih.

A description of this thesis is in order. Chapter 2 provides the definitions and some basic concepts used in the microscopic characterization of liquids and solids, as well as describes the method of molecular dynamics as a useful simulation technique. Chapter 3 briefly reviews the physical properties of liquid water and ice, the molecular models that have been used to study them, and ends with a discussion on the limitations of the application of classical statistical mechanical methods. Chapter 4 details the different ways in which quantum mechanics may be included in the investigation of many body problems, and incorporates an extensive discussion of path integral methods and their application to water. Chapter 5 reviews the exact formulation of the centroid theory and discusses the centroid molecular dynamics approximation, as well as its implementation. In Chapter 6 the implementation and testing of the *rigid body-CMD* method is presented. The extensive application of the *rigid body-CMD* method to liquid water is discussed in Chapter 7, which includes analyses of the isotopic effect and the temperature dependence of the quantum effects, as well as a characterization of tunneling in water. The study of quantum effects in ice Ih is presented in Chapter 8. The conclusions and future directions are presented in Chapter 9.

2. UNDERSTANDING CONDENSED MATTER

The study of matter in condensed state has a long and rich history, from both the theoretical and experimental standpoints. From early observations of Brownian motion to recent neutron scattering experiments, experimentalists have worked to improve our understanding of the structure and particle dynamics that characterize liquids, solids and amorphous states. At the same time theoreticians have tried to construct simple models that explain how atoms and molecules behave; whether they are constrained to remain closely packed within the attractive fields of their neighbours or have sufficient thermal energy to escape the lattice confinement of a solid and still remain dominated by the attractive interactions. This chapter will briefly review some basic concepts of statistical mechanics, experimental methods and the technique of molecular simulation that are applicable to both liquid and solids, referring eventually to aspects of water.

2.1. BASIC CONCEPTS OF STATISTICAL MECHANICS

Statistical mechanics is the microscopic theory of many-body systems [1-3]. It provides the means to establish the connection between the microscopic and macroscopic (or thermodynamic) descriptions of a system. Considering an atomic description for notational simplicity the microscopic state of a classical system is specified by the N positions, $\mathbf{r}^N \equiv (\mathbf{r}_1, \cdots, \mathbf{r}_N)$, and N momenta, $\mathbf{p}^N \equiv (\mathbf{p}_1, \cdots, \mathbf{p}_N)$. The values of these variables define a phase space point in a $6N$-dimensional space named *the phase space*.

Equilibrium statistical mechanics prescribes that the properties of the system can be calculated as averages of the appropriate observables over the appropriate phase space probability density. For a closed system at constant temperature and volume, the probability density of observing a specific configuration $\left(\mathbf{r}^N, \mathbf{p}^N\right)$ is given by [2]

$$\Pr\left(\mathbf{r}^N, \mathbf{p}^N\right) = \frac{\exp\left[-\beta H\left(\mathbf{r}^N, \mathbf{p}^N\right)\right]}{\iint \exp\left[-\beta H\left(\mathbf{r}^N, \mathbf{p}^N\right)\right] d\mathbf{r}^N d\mathbf{p}^N}, \tag{2.1}$$

where

$$H\left(\mathbf{r}^N, \mathbf{p}^N\right) = \frac{1}{2m}\sum_{i=1}^{N}\left|\mathbf{p}_i\right|^2 + V\left(\mathbf{r}^N\right), \tag{2.2}$$

is the Hamiltonian of the system and $\beta = 1/k_B T$.

The normalization of the probability density in Equation 2.1 leads us to the concept of the classical canonical partition function [1-3]

$$Z = \frac{1}{N!\left(2\pi\hbar\right)^{3N}} \iint \exp\left[-\beta H\left(\mathbf{r}^N, \mathbf{p}^N\right)\right] d\mathbf{r}^N d\mathbf{p}^N, \tag{2.3}$$

where the factor $1/N!(2\pi\hbar)^{3N}$ is taken into account such that Equation 2.3 is recovered when the quantum canonical partition function is taken to the classical limit. Hence, according to the prescription of statistical mechanics, a particular observable $A\left(r^N, p^N\right)$ can be calculated as

$$\langle A \rangle = \frac{1}{Z} \iint A\left(r^N, p^N\right) e^{-\beta H\left(r^N, p^N\right)} dr^N dp^N . \qquad \textbf{(2.4)}$$

Some thermodynamical properties, however, cannot be expressed as averages of certain functions of the coordinates and momenta of the constituent particles. For example, the Helmholtz free energy is defined in statistical mechanics by [1-3]

$$F = -\frac{1}{\beta} \log Z(T, V, N) . \qquad \textbf{(2.5)}$$

Since F is the thermodynamic potential for a system with T, V and N fixed, and since (as we know from thermodynamics) all remaining thermodynamic functions can be obtained by differentiation of F, Equation 2.5 provides the link between statistical mechanics and thermodynamics. Indeed, thermodynamic properties can be formally expressed in terms of the corresponding differentiation of the canonical partition function. In order words, the canonical partition function, $Z(T,V,N)$, is the essential statistical quantity of a system in equilibrium [1-3].

From Equations 2.1 and 2.2 it is clear that the probability density can be factorized into kinetic and configurational components. Thus, the probability of finding the system in a particular coordinate configuration $\mathbf{r}^N \equiv \{\mathbf{r}_1, \cdots, \mathbf{r}_N\}$, independently of the momenta configuration, is given by [1-3]

$$\Pr^{(N)}(\mathbf{r}_1,\ldots,\mathbf{r}_N) = \frac{\exp\left[-\beta V(\mathbf{r}_1,\ldots,\mathbf{r}_N)\right]}{\int\cdots\int\exp\left[-\beta V(\mathbf{r}_1,\ldots,\mathbf{r}_N)\right]d\mathbf{r}_1\ldots d\mathbf{r}_N}. \tag{2.6}$$

The probability density function, given in Equation 2.6, serves as a source for defining various atomic distribution functions associated with various atomic arrangements. We shall be interested mainly in the pair distribution function, which is the probability density of simultaneously observing two particles in the configuration $(\mathbf{r}_1,\mathbf{r}_2)$. From Equation 2.6 one obtains, by integration over the configurations of the remaining N-2 particles [2],

$$\rho^{(2)}(\mathbf{r}_1,\mathbf{r}_2) = \frac{N!\int\cdots\int\exp\left[-\beta V(\mathbf{r}_1,\ldots,\mathbf{r}_N)\right]d\mathbf{r}_3\ldots d\mathbf{r}_N}{(N-2)!\int\cdots\int\exp\left[-\beta V(\mathbf{r}_1,\ldots,\mathbf{r}_N)\right]d\mathbf{r}_1\ldots d\mathbf{r}_N}. \tag{2.7}$$

The factor $N!/(N\text{-}2)!$ arises since we have exactly $N!/(N\text{-}2)!$ ways of selecting two out of N particles to occupy the configuration $(\mathbf{r}_1,\mathbf{r}_2)$. It is obvious that, if $\rho = N/V$, in absence of interactions $\rho^{(2)}(\mathbf{r}_1,\mathbf{r}_2) \approx \rho^2$, for large N. It is then convenient to introduce the following definition [2],

$$g(\mathbf{r}_1,\mathbf{r}_2) = \frac{\rho^{(2)}(\mathbf{r}_1,\mathbf{r}_2)}{\rho^2}, \tag{2.8}$$

which for a homogeneous system becomes $g(\mathbf{r}_1,\mathbf{r}_2) = g(\mathbf{r}_{12})$. This function, $g(\mathbf{r}_{12})$, is the so-called *spatial distribution function* and describes the average environment that surrounds an atom in the system. Very frequently, however, the structure of a liquid or a

solid is described in terms of the *radial distribution function*, which is the result of an angular average of $g(\mathbf{r}_{12})$ [2,5], i.e.

$$g(r) = \int_0^{2\pi} \int_0^{\pi} g(\mathbf{r}_{12}) d\theta d\phi \,. \tag{2.9}$$

This function describes the structure of the system and it is characteristically different for liquids and solids. Equations 2.8 and 2.9 can be generalized for a molecular system where the dependence of the interaction on the positions and orientations of the molecules needs to be taken into account. This is, in fact, the case for water, due to the relevance of hydrogen bonds in the intermolecular interaction.

The total potential energy of a many-body system, $V(\mathbf{r}^N)$, an essential ingredient of any microscopic theory of matter in condensed phase, may be divided into terms depending on the coordinates of individual particles, pairs, triplets, etc. according to the expansion [1,2]

$$V(\mathbf{r}_1,\ldots,\mathbf{r}_N) = \sum_i V_1(\mathbf{r}_i) + \sum_{1\le i<j\le N} V_2(\mathbf{r}_i,\mathbf{r}_j) + \sum_{1\le i<j<k\le N} V_3(\mathbf{r}_i,\mathbf{r}_j,\mathbf{r}_k) + \cdots . \tag{2.10}$$

The first term in Equation 2.10, $V_1(\mathbf{r}_i)$, represents the effect of an external field on the system, and the remaining terms represents the molecular interactions. However, in practice, the first term can often be neglected and the contributions from three-body, four-body, etc. terms are incorporated into the theory by defining an effective pair potential,

V_{eff}, which fulfills the condition [2,4]:

$$V(\mathbf{r}_1,\ldots,\mathbf{r}_N) \approx \sum_{1\le i<j\le N} V_{eff}(\mathbf{r}_i,\mathbf{r}_j). \tag{2.11}$$

This equation implies that the electronic fluctuations on each atom are relatively small, and therefore pair decomposability is a good approximation. If, on the other hand, the atomic charge fluctuations on the atoms were large, the resulting energy function will effectively couple together more than pairs of particles.

Finally, it is important to note that the properties in any system at equilibrium fluctuate spontaneously with time (unless they are constants of the motion like V and N in this case). It turns out that those fluctuations in time are very closely related to various properties, such as transport coefficients, through the concept *of time correlation functions*. Letting $A(t)$ stand for some dynamical variable, then $A(0)$ denotes the instantaneous value at certain initial time. The time correlation function of variable A at time t is defined by [2,4,5]

$$C(t) = \langle A(0)A(t)\rangle = \frac{1}{Z}\int\int A\left(0;r^N,p^N\right)A\left(t;r^N,p^N\right)e^{-\beta H\left(r^N,p^N\right)}dr^N dp^N. \tag{2.12}$$

As an example of the use in a dynamical property, the diffusion coefficient, D, is given by [4,5]

$$D = \frac{1}{3}\int_0^\infty dt \langle \mathbf{v}_i(t) \cdot \mathbf{v}_i(0) \rangle = \lim_{t\to\infty} \frac{1}{6t} \langle |\mathbf{r}_i(t) - \mathbf{r}_i(0)|^2 \rangle, \qquad (2.13)$$

where $\mathbf{v}_i$(t) and $\mathbf{r}_i$ (t) are the center-of-mass velocity and position of molecule *i*, respectively.

2.2. EXPERIMENTAL METHODS.

The experimental methods most often used in condensed matter can be separated into two broad categories which depend on the scale of measurement: macroscopic or microscopic [5,28]. The macroscopic properties are usually determined experimentally with considerably accuracy, however, the analysis of microscopic properties is, generally, somewhat sensitive to certain assumptions made about the intermolecular potentials, etc. The determination of thermodynamic properties like energies or caloric capacities is an example of macroscopic measurement. Another class of macroscopic measurements is related to transport coefficients. The shear viscosity, bulk viscosity and thermal conductivity are some examples of these quantities where a variety of experimental methods exist [28]. Information at a microscopic level can be obtained with spectroscopic methods like nuclear magnetic resonance (NMR), infra-red spectroscopy (IR), etc. They are examples of microscopic measurements. Naturally, both types of measurements, macroscopic and microscopic, are complementary and are required for the consistent understanding of condensed matter systems [4,5,6].

Among the variety of microscopic measurements radiation-scattering experiments are especially important, at least from the theoretical point of view. Two scattering techniques, in particular, can be distinguished: X-ray diffraction and the scattering of thermal neutrons [2,21,28].

2.2.1. X-ray scattering

X-rays have wavelengths comparable to the spacing of atoms in crystals (about 100 pm) so they are diffracted by crystal lattices. However, the long-range periodicity of a crystal lattice is not a necessary requirement for the production of diffraction effects. The short-range positional and orientational correlation between molecules in a liquid is sufficient to cause interference effects between waves scattered from atoms in different molecules [5,28-32]. Therefore, while the information that comes from X-ray diffraction in solids allows us to specify their internal symmetry, the diffraction pattern of a liquid also contains information about these short-range spatial correlations.

The special feature of X-ray scattering experiments is the fact that the energy of the incident radiation is much greater than the thermal energies of the molecules and the scattering process is effectively elastic. This makes it impossible to study time-dependent phenomena [5,28], but valuable information can be gained about the static structure of the fluid [29-32].

X-ray scattering probes the distribution of electron density in a sample through

the relationship [28-32]

$$DSCS = \left\langle \left| \sum_{i=1}^{N_e} b_e \exp(-i\mathbf{k}\cdot\mathbf{r}_i) \right| \right\rangle, \tag{2.14}$$

where *DSCS* is the differential scattering cross-section, the sum is over the N_e electrons in the sample, b_e is the scattering length for a single electron, the $\{\mathbf{r}_i\}$ are the positions of the electrons, and $\mathbf{k}$ is the momentum transfer for the scattering process. The application of this formula requires that various corrections to the experimental data are made in order to account for effects such as incoherent scattering, beam polarization, multiple scattering, and container absorption [30,32]. With all this considered the cross-section can be written in the form [5,28]

$$DSCS = Nb^2 S(\mathbf{k}), \tag{2.15}$$

where Nb^2 would be the scattering from N independent nuclei and $S(\mathbf{k})$ represents the effect of correlations. $S(\mathbf{k})$ is called the structure factor and is related in a simple way to the Fourier transform of *g(r)* [2,5,28], that is

$$S(\mathbf{k}) = 1 + \rho \int \exp(-i\mathbf{k}\cdot\mathbf{r}) g(\mathbf{r}) d\mathbf{r}, \tag{2.16}$$

where ρ is the density.

2.2.2. *Neutron scattering*

In contrast to x-ray scattering, in the case of thermal neutrons the energy of the

incident particle is comparable with k_BT and the scattering cross section can therefore be measured as a function of energy, as well as momentum transfer. By this means, it is possible to extract information on wave number and frequency-dependent fluctuations in liquids and solids at wavelengths comparable with the spacing between time-dependent processes in liquids [5,33-38]. However, the technical difficulties are formidable and the interpretation of many of these experiments can be difficult [33,34].

One important feature of neutron scattering, which is relevant to liquid water, is related to the phenomena of coherent and incoherent scattering [5,6]. The coherent scattering, which is useful for the analysis of liquid structure, is the result of the interference between the incident and the scattered waves, those scattered waves coming from a isotopically pure collection of nuclei of spin zero. The incoherent scattering can then arise in two ways: first by having isotopes of the same element with different scattering lengths, and second, due to the presence of nuclei with spin different from zero [6].

An important case of spin incoherence is that of hydrogen [6,33,34]. The products of the scattering amplitudes and weighting factors for parallel and anti-parallel spins are almost equal but of opposite phase. Thus, constructive interference cannot occur and the scattered wave escapes from the sample without being modified by interference effects. Table 1 gives the neutron scattering cross section for hydrogen, deuterium and oxygen. We see that the scattering from light water will be mainly by the

hydrogen nuclei and will be almost totally incoherent. The scattering from heavy water will be from both the deuterium and the oxygen and it will show strong interference effects. Thus, most of the information on the structure of water comes from the data on heavy water (in contrast, x-rays will be scattered almost wholly by the oxygen atoms [32]). In the last two decades an important improvement of the use of the isotopic substitution technique has occurred and corrections for inelastic scattering have been developed, producing neutron scattering experiments for light water consistent with other experiments and computer simulations [33-38].

Table 2.1. Coherent and incoherent scattering cross-section for the atomic components of light and heavy water [3].

Isotope	σ_{inc}	σ_{coh}
^{1}H	79.7	1.79
^{2}H	2.2	5.4
^{16}O	0.0	4.24

2.3. COMPUTER SIMULATIONS

The technique of computer simulation has played a major role in the microscopic understanding liquids and solids, including the structure and properties of water in liquid and solid phases. Its usefulness rests ultimately on the fact that it provides a complete and detailed atomistic description of the model system under study, which is otherwise still unattainable through experimental methods on the real system. Further, the results may be regarded as essentially exact for a given intermolecular potential on well-defined models, thereby eliminating the ambiguity that invariably arises in the interpretation of

experimental data on real systems. Still, molecular simulations are distant from traditional "pencil-and-paper" theoretical work and are carried out in a quasi-experimental fashion. In order words, a "computer experiment" is performed on a representative idealized material, where some parameters have been specified in advance, to answer a practical question. The result is naturally subject to scrutiny with a healthy air of skepticism like any experimentally measured data.

Two distinct approaches of molecular simulations are available and have been widely used: the Monte Carlo method of Metropolis et al. [39] and the method of molecular dynamics pioneered by Alder and Wainwright [40]. These two approaches are interrelated by the so-called ergodic hypothesis, which states that an average over an ensemble is equivalent to a time average [1-3], i.e.

$$\frac{1}{Z}\iint A\left(r^N, p^N\right) e^{-\beta H\left(r^N, p^N\right)} dr^N dp^N = \lim_{t\to\infty} \frac{1}{t}\int_0^t A(t)dt. \qquad \textbf{(2.17)}$$

The Monte Carlo method samples the phase space randomly according to the appropriate probability density whereas the molecular dynamics method describes a phase space trajectory.

2.3.1. Molecular dynamics methodology

The relation between molecular dynamics and statistical mechanics is established through the Liouville Theorem, which guarantees that so long as the dynamics is described by Hamilton's Equations the microcanonical phase space density is stationary [41,42].

Therefore, the motion of the phase space point can be considered as being determined by Hamilton's equations [5]

$$\dot{\mathbf{r}}_i = \frac{\partial H}{\partial \mathbf{p}_i} = \frac{\mathbf{p}_i}{m}, \tag{2.18}$$

and

$$\dot{\mathbf{p}}_i = -\frac{\partial H}{\partial \mathbf{r}_i} = \mathbf{F}_i, \tag{2.19}$$

where H is given by Equation 2.2. Thus, given a certain initial phase space point the molecular dynamics method samples in a deterministic fashion the phase space, in contrast to the Monte Carlo method where the phase space points visited have no particular time ordering.

In practice, however, Equations 2.18 and 2.19 are solved approximately with a convenient numerical technique. Within the many approximate techniques, one commonly used is the Gear predictor-corrector method [4]. Briefly, this method proceeds as follows. Starting with an initial set of positions, momenta, accelerations and the time derivative of the acceleration (i.e. $\mathbf{r}(t)$, $\mathbf{p}(t)$, $\mathbf{a}(t)$ and $\mathbf{b}(t)$, respectively) the next configuration is predicted by Taylor expanding in time the known configuration,

$$\mathbf{r}_p(t+\Delta t) = \mathbf{r}(t) + \frac{\mathbf{p}(t)}{m}\Delta t + \frac{\mathbf{a}(t)}{2}\Delta t^2 + \frac{\mathbf{b}(t)}{6}\Delta t^3$$

$$\mathbf{p}_p(t+\Delta t) = \mathbf{p}(t) + m\mathbf{a}(t)\Delta t + m\frac{\mathbf{b}(t)}{2}\Delta t^2$$

$$\mathbf{a}_p(t+\Delta t) = \mathbf{a}(t) + \mathbf{b}(t)\Delta t$$

$$\mathbf{b}_p(t+\Delta t) = \mathbf{b}(t) \qquad \textbf{(2.20)}$$

Here, the vectors $\mathbf{r}(t)$, $\mathbf{p}(t)$, $\mathbf{a}(t)$ and $\mathbf{b}(t)$ can be considered 3-dimensional referring to a particle (or $3N$-dimensional referring to the whole system). The predicted position $\mathbf{r}_p(t+\Delta t)$ is used to calculate the force acting on the particle $\mathbf{F}(t+\Delta t)$. Then, the difference between the predicted and corrected accelerations can be defined by

$$\Delta\mathbf{a}(t+\Delta t) = \mathbf{a}_c(t+\Delta t) - \mathbf{a}_p(t+\Delta t) = \frac{\mathbf{F}(t+\Delta t)}{m} - \mathbf{a}_p(t+\Delta t). \qquad \textbf{(2.21)}$$

This difference is used to correct each predicted variable such that

$$\mathbf{r}_c(t+\Delta t) = \mathbf{r}_p(t+\Delta t) + c_0\Delta\mathbf{a}(t+\Delta t)$$

$$\mathbf{p}_c(t+\Delta t) = \mathbf{p}_p(t+\Delta t) + c_1\Delta\mathbf{a}(t+\Delta t)$$

$$\mathbf{a}_c(t+\Delta t) = \mathbf{a}_p(t+\Delta t) + c_2\Delta\mathbf{a}(t+\Delta t) \qquad \textbf{(2.22)}$$

$$\mathbf{b}_c(t+\Delta t) = \mathbf{b}_p(t+\Delta t) + c_3\Delta\mathbf{a}(t+\Delta t)$$

In this way, the predicted configuration is improved by enforcing Equation 2.19, where clearly, $c_2 = 1$. The values of c_0, c_1 and c_3 can be chosen conveniently to ensure

optimum stability and the accuracy of the trajectories [4]. Additionally, variations on this methodology are easily implemented such as including more (or fewer) positions derivatives, more predictor-corrector iterations, etc. [4]

Hence, the microscopic dynamics of the system can be followed and the phase space sampled in the way described above. However, since Hamilton's equations conserve energy, this method is limited to systems characterized by constant E, V and N (i.e. microcanonical ensemble). In order to carry out constant temperature simulations, for example, a thermostating scheme needs to be included [6,42]. While several different thermostating methods exist in the literature, here two of the most widely used, the Gaussian [43,44]] and Nosé-Hover thermostats [45,46], will be considered.

The Gaussian thermostat [43,44] replaces Equation 2.19 by the following form

$$\dot{\mathbf{p}}_i(t) = \mathbf{F}_i(t) + \lambda(t)\mathbf{p}_i(t), \tag{2.23}$$

where $\lambda(t)$ resembles a viscous damping parameter but here can take both positive and negative values. On the other hand the time derivative of the kinetic energy needs to equal zero,

$$\sum_{i=1}^{N} \frac{\mathbf{p}_i(t)\dot{\mathbf{p}}_i(t)}{m_i} = 0. \tag{2.24}$$

Substituting Equation 2.23 in Equation 2.24 give us an explicit form for the $\lambda(t)$, i.e.

$$\lambda(t) = \frac{\sum_{i=1}^{N} \dot{\mathbf{r}}_i(t)\mathbf{F}_i(t)}{\sum_{i=1}^{N} m_i \dot{\mathbf{r}}_i^2(t)}, \tag{2.25}$$

Therefore, the dynamics is carried out employing Equations 2.23 and 2.25. A new variable, and a new equation, has been added to the system (to one of the equations of motion) such that the conservation of the kinetic energy is enforced. These equations of motion sample the so-called iso-kinetic ensemble (*NVK***P**, where **P** is total momentum) [43,44].

However, in the canonical ensemble the kinetic energy of the system is not constant but instead fluctuates in the appropriate way about its average value. An alternative set of equations has been shown to generate the canonical ensemble distribution of states [45,46]. In this method, known as the Nosé-Hoover thermostat, Equation 2.19 is replaced by

$$\dot{\mathbf{p}}_i(t) = \mathbf{F}_i(t) - \lambda(t)\mathbf{p}_i(t), \tag{2.26}$$

with

$$\dot{\lambda}(t) = \frac{1}{Q}\left(\sum_{i=1}^{N} \frac{p_i^2}{m} - \frac{3N}{\beta}\right), \tag{2.27}$$

where $Q = 3Nt_0^2/\beta$ and t_0 is the bath relaxation time. Here $\lambda(t)$ can be interpreted as a coupling parameter between the dynamical system and a thermal reservoir, the latter

having a conveniently chosen time relaxation parameter. Hence, the molecular trajectories are modified by the inclusion of an extra term in the acceleration equation, like in the Gaussian thermostat, but with a weaker coupling between the system and the thermal reservoir.

The Nosé-Hoover thermostat, as presented above, fails in small or stiff systems [47]. In order to tackle these scenarios, this method is improved by thermostating the thermostat parameter itself, the new thermostat can also be thermostated, etc., leading to a chain of thermostats [47]. For the case of M thermostats in the chain, Equations 2.26 and 2.27 transform into the following series of equations:

$$\begin{aligned}
\dot{\mathbf{p}}_i(t) &= \mathbf{F}_i(t) - \lambda_1(t)\mathbf{p}_i(t) \\
\dot{\lambda}_1(t) &= \frac{1}{Q_1}\left(\sum_{i=1}^{N}\frac{p_i^2}{m} - \frac{3N}{\beta}\right) - \lambda_1(t)\lambda_2(t) \\
\dot{\lambda}_j(t) &= \frac{1}{Q_j}\left(Q_{j-1}\lambda_{j-1}^2 - \frac{1}{\beta}\right) - \lambda_j(t)\lambda_{j+1}(t) \\
\dot{\lambda}_M(t) &= \frac{1}{Q_M}\left(Q_{M-1}\lambda_{M-1}^2 - \frac{1}{\beta}\right),
\end{aligned} \tag{2.28}$$

where $Q_1 = 3Nt_0^2/\beta$ and $Q_j = t_0^2/\beta$ for $2 \le j \le M$. It is important to note that it is only the first thermostat that interacts with all the particles, therefore, in large systems the addition of the extra thermostats is relatively inexpensive since they form a simple one-

dimensional chain.

Similarly, it is possible to carry out simulations at constant pressure by coupling the system to an external reservoir (or barostat) and allowing the volume to fluctuate accordingly. In fact, this barostating method was first published by Anderson [48] and was followed by Nosé's work on thermostats [45]. Clearly, the isothermal-isobaric ensemble can also be simulated with the combined use of a thermostat and a barostat [42].

2.3.2. Calculation of properties

In a MD simulation successive time steps are correlated and do not contain significantly new information. In this case it is sufficient to store and/or analyze information from every 5^{th} or 10^{th} time step. A MD simulation produces a substantial amount of useful information, and it is normal to store vectors of the positions (orientations), velocities (angular velocities), and forces (torques) for each molecule, as well as the instantaneous values of all the calculated properties. The information stored in a MD simulation is time ordered and can be used to calculate the time correlation functions (Equation 2.12) [4,41].

The radial distribution function, *g(r)*, is formally defined by Equation 2.9, but can be simply thought as representing the number of atoms at a distance r from a given atom compared with the number at the same distance in an ideal gas at the same density. *g(r)* can be calculated as follows. For a given configuration the minimum (nearest) image separations, r_{ij}, of all the pairs of atoms are calculated. These separations are sorted into a

histogram where each bin has a width δr and extends from r to $r+\delta r$. The ij and ji separations are sorted simultaneously, and the calculation is limited to a certain maximum distance (say half of the box-length). When all the configurations have been processed, the histogram must be normalized to calculate $g(r)$. An analogous sorting technique can be applied to the spatial pair distribution functions [4].

A wide variety of time correlation functions can also be calculated based on their definition, Equation 2.12. Suppose we are interested in a mechanical property, $A(t)$, which may be expressed as a function of particle positions and velocities. $A(t)$ might be a component of the velocity of a particle, for example. From the simulation data, $A(t)$ will be available at equal intervals of time Δt; typically Δt will be a small multiple of the time step used in the simulation. Using l to label successive steps, i.e. $t=l\Delta t$, the definition of time-average over the period $L\Delta t$, allows us to write the time correlation function of $A(t)$ as [4]

$$C_{AA}(t') = \langle A(t')A(0)\rangle \approx \frac{1}{L}\sum_{l=0}^{L} A(t'+l\Delta t)A(l\Delta t). \qquad \textbf{(2.29)}$$

The calculation may be repeated for different values of t', and the result will be a correlation function evaluated at equally spaced intervals of time Δt apart, from zero to as large a value as is required [4].

The calculations of static and dynamic properties are subject to systematic and statistical errors. Sources of systematic errors include sized-dependence, poor

equilibration, etc. These should, of course, be estimated and eliminated where possible. It is also essential to obtain an estimate of the statistical significance of the results. Simulation averages are taken over runs of finite length, and this is the main source of statistical imprecision in the mean values obtained.

It is often possible to analyze statistical errors in quantities such as $\langle A \rangle$, $\langle \delta A^2 \rangle$, by assuming that $A(t)$ is a Gaussian process [4]. This Gaussian assumption is reasonable if the quantity of interest is essentially the sum of a large number of statistically independent quantities (this is the central limit theorem of probability). For example, the mean value $\langle A \rangle$ can be estimated by

$$\langle A \rangle \approx \langle A \rangle_L = \frac{1}{L} \sum_{l=0}^{L} A_l , \qquad \textbf{(2.30)}$$

where $A_l \approx \frac{1}{t'} \int_0^{t'} A(t_0 l + t) dt$ and $\{A_l\}$ are consecutive short averages (over the period t') of the quantity $A(t)$. The value t' can be chosen such that the quantities $\{A_l\}$ are statistically independent. Consequently, a calculation of the standard deviation of the set $\{A_l\}$ gives an estimate of the statistical error associated with a run of length $t'L$. Naturally, as $L \to \infty$ this statistical uncertainty goes to zero [4].

3. LIQUID WATER AND ICE

Due to the importance of water, there have been numerous books, reviews, etc. discussing and examining its properties, structure, and applications [21-26,49] in both its liquid and solid phases. Consequently, the discussion within the present chapter will focus only on some details pertinent to this thesis.

The chapter is organized as follows. Section 3.1 presents an overview of some of the most important physical properties of liquid water and hexagonal ice. In Section 3.2, water models and their properties are discussed. Finally, Section 3.3 considers the limitations associated with classical simulations of water.

3.1. PHYSICAL PROPERTIES OF LIQUID WATER AND ICE.

Water, which is the only chemical compound that occurs naturally (on earth) in the three principal physical states, solid, liquid and vapour, has been the focus of study of scientists and engineers from many different areas. An enormous amount of work has been published about the structure and properties of liquid water [21-26] and ice [49]. This section, consequently, will simply provide a brief and general overview of some of their most relevant properties.

The origin of the often unusual properties of liquid water and ice begins, of course, with the water molecule, which contains ten electrons, eight from the oxygen atom and one from each hydrogen atom. Due to the presence of the hydrogen nuclei the electronic charge is not distributed symmetrically around the oxygen nucleus. It is drawn

towards the hydrogen nuclei but not sufficiently to neutralize their charge. The peculiar properties of liquid water and ice are very much due to the fact that the molecule is bent [21-24]. (This shape is a consequence of the nature of the electronic ground state wave function.) Then, the molecule has an electric dipole moment oriented along the bisector of the H-O-H angle with the negative side on the oxygen. The center of mass of the molecular electronic distribution is slightly shifted from the oxygen nucleus, and this fact is incorporated in the electrostatic component of some empirical pair potentials to be introduced in the next section.

For free molecules, the dipole moment has been measured to be 1.8546 debyes (=[6.186±0.001]×10^{-30} Cm) [50] and the experimental values of bond length and bond angle are known to be 0.9572±0.0003 Å and 104.52±0.05°, respectively [51]. In the liquid phase at 300 K and 0.1 MPa, the bond length increases to 0.996±0.016 Å and the bond angle changes to 101±5°. The molecular dipole moment in liquid water has also been predicted to be higher than in the vapour phase [52]. The water molecule also changes when going from the liquid to the solid phase but to a lesser extent than from vapour to liquid. The bond length in ice Ih at –20°C, for example, is 0.985 Å [49].

Ice Ih, the most usual form of ice, is obtained by freezing water at atmospheric pressure or by direct condensation of water vapour above about –100°C [49]. There are, nevertheless, at least 13 crystalline phases of ice that have been observed under different conditions of pressure and temperature. The number "I" was assigned by Tammann [53] following his discovery of the first of the high pressure phases of ice, and the "h" is

commonly added to distinguish it from a metastable cubic variant called ice Ic [49].

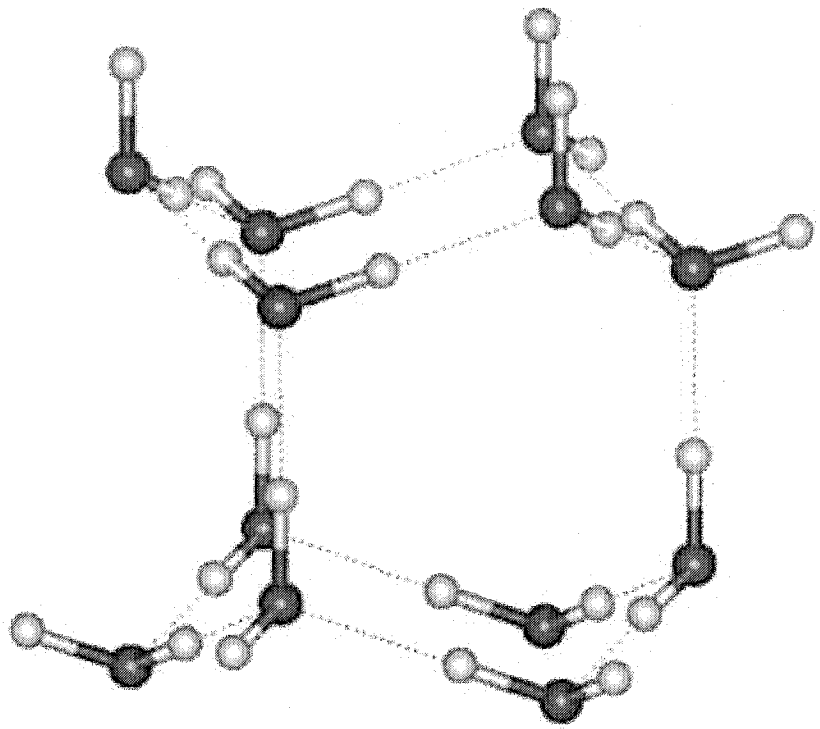

Figure 3.1. Basic structure of ice Ih [54].

The basic structure of ice Ih is shown in Fig. 3.1. It can be understood as being formed by two chair-form hexamers (opposed) on two horizontal planes or by three boat-form hexamers (opposed) on three vertical planes. The vertical direction is distinct from the directions in a perpendicular plane. Although the figure shows well-ordered hydrogen bonds, in reality their distribution is arbitrary and constantly changing [54].

Fig 3.2 shows a phase diagram for the equilibrium between ice Ih and the liquid and vapour phases of water [54]. The cross in the liquid region indicates that water is a liquid at ambient conditions. The triple point, where the three phases are in equilibrium, is at 273.16 K by definition of the Kelvin scale of temperature; the corresponding

pressure is 611.7 Pa [49] (interestingly, ice Ih has two other triple points). The melting curve has a negative slope with the melting point at atmospheric pressure being 273.15 K, and this value is taken as the zero point of Celsius scale of temperature. The negative slope of the melting curve (not well seen in Fig 3.2 due to the logarithm scale in the pressure axis) is a consequence of a peculiarity, the fact that water expands on freezing [since Clapeyron equation states $(dP/dT) = (\Delta\overline{H}/T\Delta\overline{V})$].

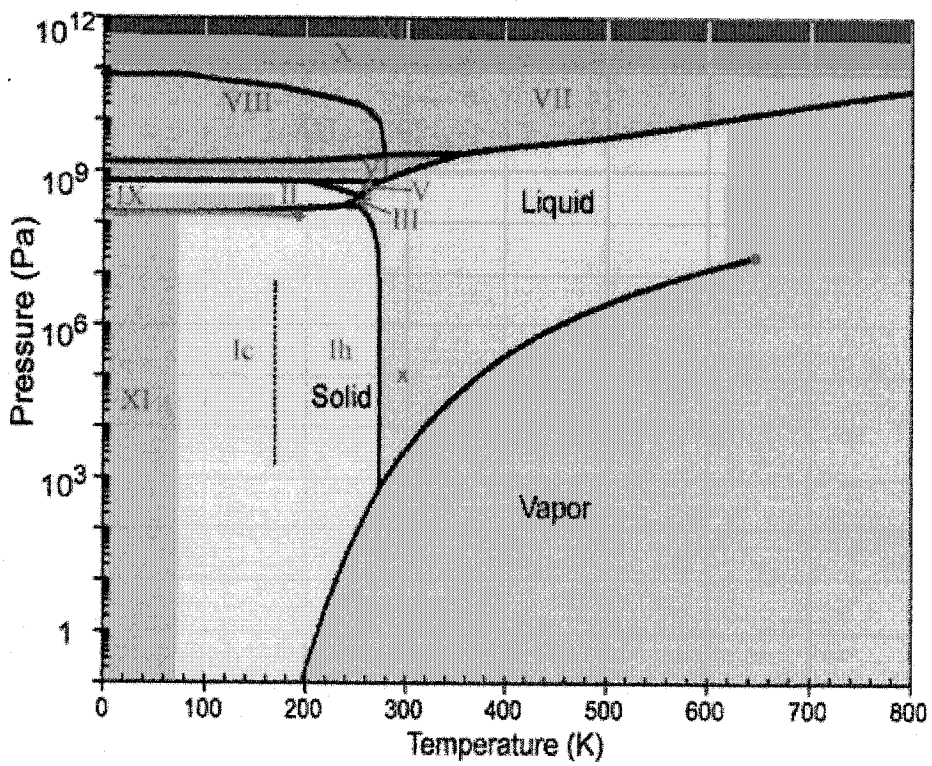

Figure 3.2. Phase diagram of water [54].

The hydrogen bond, being the primary intermolecular force in water, is ultimately a major contributor to the characteristic anomalies of liquid water. Hydrogen bonding represents the interaction between the hydrogen atom of one molecule and the oxygen atom of a neighbouring water molecule, and produces the associated nature of liquid water. Thus, compared with other low molecular weight substances, water has a wide

liquid range of 100 K. Another indication of the existence of strong intermolecular interactions in liquid water is the relatively small value of the latent heat of fusion, which is only 15% of that of vaporization [23].

Water has a 50% larger heat capacity in the liquid (75.2 $Jmol^{-1}K^{-1}$) than in the solid and vapour states [23]. This anomalous behaviour can be shown to be due to a relatively large temperature dependence in liquid water structure, which is a direct manifestation of the inefficient packing of the water molecules. Indeed, its tetrahedral order leaves relatively large spaces unoccupied at the expense of a large hydrogen bond energy; the disruption of this balance by temperature explains the unusually large temperature dependence of the water structure. Furthermore, in non-associated liquids higher pressures lead to more closely packed arrangements and more order. However, in liquid water, its ordering can decrease with increasing pressure due to the rupture of the local structure. The fact that increasing the pressure (or the density) can lead to less order in water is directly related to the density maximum exhibited in the liquid phase at 3.93°C and 1 atm pressure [49]. This connection is most easily established through the well-known Maxwell relationship $(\partial S/\partial P)_T = -(\partial V/\partial T)_P$.

The anomalous behaviour observed for water, like the compressibility minimum and density maximum, is most pronounced in the low pressures range, 1-200 bar. However, water appears perhaps more like other low molecular weight liquids where its transport properties, like thermal conductivity and diffusion, are concerned [23,49].

The replacement of the hydrogen by its heavier isotopes, deuterium and tritium,

has important effects on some water properties. In relation to H_2O, the triple point of D_2O is shifted to 3.82 °C [55] and to 4.49 °C for T_2O [56]. Additionally, the temperature of maximum density is 11.2 °C [55] for D_2O and 13.4 °C for T_2O [57] all of which suggests that T_2O and D_2O appear to have stronger hydrogen bonding than H_2O. Still, perhaps the most compelling evidence of stronger hydrogen bonding in the "heavier" waters is their enthalpies of vaporization; 10.52 kcal/mol for H_2O, 10.87 kcal/mol for D_2O and 10.93 kcal/mol for T_2O [58,59]. In Section 3.3 it will be seen that these changes in the equilibrium properties of water by isotopic substitution cannot be explained within the limits of classical statistical mechanics and are considered a manifestation of quantum effects.

3.2. MOLECULAR MODELS OF WATER.

The starting point in a computer simulation is the specification of the molecular model, which defines the kind and nature of the interactions within the system. This section will provide a general overview of water models and their relationship to the properties of water. Special attention will be given to three rigid water models, since they will be used in the simulations presented in Chapters 6, 7 and 8.

After more than three decades of water simulations, a wide variety of water models has been proposed and used to examine the properties of liquid water [25,26]. A vast majority of the models are empirical and mimic the hydrogen bond interaction with a combination of an attractive (coulombic) interaction and a short-range repulsive term. The attractive interaction, well approximated with classical electrostatics, is usually

modeled with point charges in the nuclei (eg. SPC [60]), or by using one or more additional sites located in the molecular plane (eg. TIP4P [61]) or out of it (eg. ST2 [62,63]). The electronic repulsion between molecules is usually taken into account with the use of a Lennard-Jones potential centered on the oxygen, which also includes the dispersion energy. There are some exceptions, where for example an exponential is preferred to the Lennard-Jones repulsion term (eg. NSPCE [64]). The charges and the repulsion-dispersion parameters are chosen such that some properties of liquid water at ambient conditions (density, heat of vaporization, etc) are recovered with a MD or MC simulation.

Since the earliest calculations it has been consistently found that, in order to reproduce a number of liquid state properties, the dipole moment of the water model had to be higher than the gas phase value. For example, the rigid models mentioned above, SPC, TIP4P, ST2 and NSPCE, have dipole moment values of 2.27, 2.18, 2.36 and 2.18 D, respectively [25,26,60-64]. However, the experimental value of the dipole moment in liquid phase is believed to be in the range 2.6-3.0 D [65,66], although the concept of a molecular dipole moment in liquid water is not well defined formally.

Table 3.1 shows the parameters of two commonly used rigid water models. The SPC/E [67] model only contains 3 charge sites located on the atoms, while the TIP4P [61] contains an additional site and no charge on the oxygen. The TIP4Pew model [68], a recent reparameterization of the TIP4P potential, is also included in Table 3.1. It is worth noting that, in spite of the similarity between the TIP4P and TIP4Pew models, the results obtained can be rather different (for example the latter has a 67 % self diffusion

coefficient) [68]. This example illustrates how sensitive the properties of simulated liquid water are to the potential parameters, and the challenge that a model's construction entails [25,26].

Table 3.1 Parameters of some rigid water models.

Parameter	SPC/E	TIP4P	TIP4Pew
r(OH)/Å	1	0.9572	0.9572
HOH/deg	109.42	104.52	104.52
q(O)/e$^-$	-0.8472	0	0
q(H)/e$^-$	0.4238	0.52	0.52422
Q(M)/Å	-	-1.04	-1.04844
R(OM)/Å	-	0.15	0.125

Another way to describe water interactions is by allowing for molecular vibrations, with the so-called flexible models. Flexibility can be included by adding harmonic or anharmonic potentials for bond length and bond angle in an existing rigid model (eg. SPC/F [23]) or by defining a new set of potentials (eg. CF [70]). The intramolecular potentials are chosen such that the model reproduces the values of the vibrational modes and is able to account for the frequency shift in going from gas to liquid phase. Interestingly, a number of flexible models predict a narrowing of the HOH angle in the liquid phase in relation to the gas phase which seems to be a consequence of the molecular environment in the bulk liquid. However, this fact has not been totally clarified experimentally [71], and it has been argued that a formation of hydrogen bonds tends to rearrange the electrons around the oxygen atom leading to a slight relaxing of the HOH angle [26]. On the other hand, since the dipole moment in a flexible model changes

from gas to liquid phase, a comparison between the results obtained from a flexible and a rigid model is not entirely straightforward.

Another important component of the water-water interaction is believed to be associated with induced moments, which leads us to the class of polarizable models. These models can be constructed by choosing the charges on the sites of a (rigid or flexible) water model to be in agreement with the gas phase dipole moment and assigning a point polarizability to the oxygen atom (e.g. SPCP [72], PTIP4P [73], CKL [74]). Alternatively, polarization effects have also been included in some water models by allowing fluctuations in charges according to the local electric field (e.g. SPC/FQ [75], TIP4P/FQ [75]). However, polarizable models have not proven to be clearly better than the previously described (non-polarizable) models. It is not obvious how to assign a polarizability value, nor how to account for the fact that the electrostatic potential of the water molecule may not be very accurately described with site charges.

Another way to confront the complexity of the interaction in water is by using a potential function that results from an analytical fit to an *ab initio* calculation. The parameterization in these models, known as *ab initio* models, is carried out by calculating the interaction in dimers, trimers or higher order clusters (e.g. MCHO [76], NEMO [77]). Since the interaction energy is a very small fraction of the total energy, a very accurate calculation is required, and still this approach may not capture the collective behaviour of the bulk phase. As a consequence, some authors have preferred to use *ab initio* calculations in order to assign, for example, the polarizability of a model with fluctuating charges (e.g. PPC [78]); such a model is a combination of the empirical and *ab initio*

approaches. The natural next step in this discussion is the so-called *ab initio* molecular dynamics method, however this method as a quantum simulation technique is discussed in Section 4.1.

Generally speaking, it is safe to say that although significant progress has been made in the understanding of the molecular interactions leading to better potential models, a lot more work needs to be done, as no single water model has been demonstrated to reproduce the details of the properties of real water [26].

3.3. CLASSICAL AND QUANTUM APPROACHES.

In spite of the advances achieved in the understanding of liquid water, it is important to recognize that there are limitations associated with the classical approach implied in a standard molecular dynamics simulation. This section will discuss the intrinsic limitations of a classical simulation of liquid water.

Formally, the classical canonical partition function can be written in the following form [1-3]

$$Z = \frac{1}{N!(2\pi\hbar)^{3N}} \int \exp\left[-\beta K\left(\mathbf{p}^N\right)\right] d\mathbf{p}^N \int \exp\left[-\beta V\left(\mathbf{r}^N\right)\right] d\mathbf{r}^N , \qquad \textbf{(3.1)}$$

where the factorization

$$e^{-\beta H\left(\mathbf{r}^N,\mathbf{p}^N\right)} = e^{-\beta K\left(\mathbf{p}^N\right)} e^{-\beta V\left(\mathbf{r}^N\right)} \qquad \textbf{(3.2)}$$

has been used in the definition given by Equation 2.3. In fact, the momentum term in

Equation 3.1 can be further factorized and integrated. The configurational integral in Equation 3.1, however, cannot be easily integrated because the potential $V(\mathbf{r}^N)$ couples all the particle coordinates together.

Now, since the pressure follows the relation $P = -(\partial F/\partial V)_{N,T}$, using Equations 2.5 and 3.1 we can calculate the *equation of state* of the system from [2]

$$\beta P = \left(\frac{\partial \ln Z}{\partial V}\right)_{N,\beta} = \frac{\partial}{\partial V}\left(\ln\left\{\int \exp\left[-\beta V(\mathbf{r}^N)\right] d\mathbf{r}^N\right\}\right). \qquad \textbf{(3.3)}$$

This relationship implies that, within the limits of classical statistical mechanics, the equation of state of a system is independent of the mass of the particles that constitutes it. As a consequence (assuming that the electronic structures of the hydrogen, deuterium and tritium atoms are identical) the equation of state of the liquids H_2O, D_2O and T_2O should be identical. However, the experimental situation reveals that there are noticeable differences between the isotopic waters (see Section 3.1).

In order to understand on physical grounds how quantum mechanics affects liquid water, it is interesting (to try) to imagine why the freezing of D_2O occurs at higher temperatures than H_2O. According to the uncertainty principle, the positions of the hydrogen atoms are blurred over a distance $\sqrt{\beta\hbar^2/m}$, which for a proton at room temperature corresponds to a length of about 0.3Å, whereas for deuterium (and tritium) it is much less. It is then reasonable to believe that the diffusiveness of the location of the protons, in relation to deuterium, introduces additional disorder in the fluid, which

consequently only crystallizes at a lower temperature. Incidentally, the freezing temperature of T_2O is still higher than that of D_2O in agreement with this argument.

From a formal point of view, the failure of classical statistical mechanics is due to the factorization in Equation 3.2. In quantum mechanics, such a factorization does not occur because the relationship [2]

$$e^{\hat{A}} = e^{\hat{A}_1} e^{\hat{A}_2} \tag{3.4}$$

is only valid when the operators $\hat{A}_1$ and $\hat{A}_2$ commute, assuming that $\hat{A} = \hat{A}_1 + \hat{A}_2$. The commutation of the kinetic and potential operators is, in general, prevented by the uncertainty principle, which establishes a relation of non-commutativity between momentum and position. In fact, as will be seen in Section 4.2, the factorization of the Boltzmann operator of quantum statistical mechanics constitutes a route to perform quantum simulations via path integral methods [7-10].

From a practical point of view, water models are constructed by fitting the charges on the nuclei to recover the properties of liquid water. However, the proton charges in real water are slightly diffused and, as a consequence, the interaction is "softer" than for classically localized charges. Therefore, if a model is aimed to reproduce the experimental H_2O properties, the assumption of classical proton localization needs to be compensated with an effective lowering of the charges. As a result, empirical models constructed with classical simulations will underestimate hydrogen bonding. On the other hand, *ab initio* models also assume proton localization

and therefore cannot correct for this problem.

Other equilibrium properties such as the average interacting energy and the radial distribution function (see Equation 2.9) are also independent of the mass according to classical statistical mechanics. In contrast to these equilibrium properties, the dynamical properties calculated in a standard molecular dynamics simulation do change with isotopic substitution due to the fact that the mass appears in the dynamical equations of motion (see Section 2.3.1). However, this change, due to the mass difference, is not enough to account for the experimental difference between the isotopomers H_2O and D_2O [19,20]. This is further evidence of the necessity of the inclusion of quantum effects in liquid water.

4. QUANTUM SIMULATIONS OF LIQUID WATER AND ICE

Classical MD simulations are based on the approximation that all the particles move in time according to the laws of classical mechanics. The great advantage of the application of classical mechanics is that the equations of motion can be solved easily, even for systems containing a large number of atoms. However, the applicability of standard MD simulations is limited to molecular scenarios where quantum effects can be neglected, i.e. when the potential energy can be given as a local function of the particle coordinates. In many circumstances, the quantum nature of electrons and protons has to be considered in order to achieve a realistic description of the dynamics of the system. Since a full quantum treatment of all degrees of freedom is not possible within a reasonable computational effort, the need for approximate techniques becomes evident.

In this sense, it is possible and sensible to take advantage of the mass difference between electrons and nuclei, and uncouple their motions. This schematic picture allows us to organize quantum simulations in two main categories. First, *ab initio* simulations where the electrons are treated quantum mechanically and the nuclei evolve classically. Second, path integral simulations where the nuclei are treated quantum mechanically and the electrons are taken into account through effective interaction potentials. The combination of these two techniques is also possible, leading to the *ab initio* path integral simulation method. This chapter will review the above methods in the same order as mentioned. It is important to note that the organization of the chapter does not follow the historical order in which quantum simulations of liquid water and ice appeared in the

literature; instead I prefer a more pedagogical approach beginning with the simpler techniques and continuing with the more intricate ones.

This chapter does not attempt to review all the methods that have been employed in quantum simulations. The still evolving field of quantum dynamics includes many well-established methodologies (like wave-packet techniques) and many somewhat less well-known or new strategies (like the mixed quantum-classical approach), an evaluation of which is beyond the scope of this thesis. Therefore, the discussion focuses on those methodologies that have been used to examine quantum effects in liquid water and ice, including equilibrium and dynamical properties. At the same time the presentation in Section 4.2, in particular, will provide many relationships and analysis that will be of utility in the upcoming chapters. The centroid molecular dynamics method, which will only be briefly presented here, is the focus of the next chapter.

4.1. *AB INITIO* MOLECULAR DYNAMICS.

In MD simulations, the interaction energies and the forces acting on the atom determine the simulation results. The closer these are to reality, the more reliable (closer to those of the experiment) the simulation results are expected to be. To achieve this, MD simulations can be combined with high level *ab initio* calculations to compute the potential energies and forces needed in MD simulations. This category of simulations is called *ab initio* molecular dynamics simulations (AIMD) [79].

AIMD simulations can be implemented in the following way. At each time step of a MD simulation, an independent *ab initio* program is called to calculate the quantities needed, such as the total interaction energy, forces on the atoms, etc. The quantum calculations could involve Hartree-Fock molecular orbital (HF-MO) [79], full configuration interaction (CI) [80], or density functional theory (DFT) [81] calculations, among others [79]. In principle, any *ab initio* quantum calculation can be incorporated into AIMD, provided that they give the very accurate inter-atomic energies and forces needed in MD. Unfortunately, these calculations are still impractical for use as standard methods for general systems. The principal reason is that *ab initio* QM calculations (of the necessary accuracy) are simply still very time-consuming. In a typical QM calculation corresponding to each MD time step, a large number of integrals, related to the electronic coordinates, must be evaluated and a self-consistent field (SCF) calculation carried out in order to find the "best" electronic state of the system [80]. Since the minimum number of time steps required by a MD simulation is usually a few tens of thousands, this method can be used only for limited systems.

Within each QM calculation, the electronic state Ψ is optimized so as to minimize the energy of the system. It is possible to optimize Ψ using methods other than SCF methods. One of the simplest ways is the steepest descent (SD) approach [82], which changes the approximate wavefunctions according to the direction of the local downhill gradient of energy. An improvement of this method, the conjugate gradient minimization method, has been incorporated into DFT calculations and has been used in AIMD simulation to study some systems (like clusters, etc.)[83].

4.1.1. *Car-Parrinello molecular dynamics of liquid water*

One of the most promising techniques in quantum simulation was published by R. Car and M. Parrinello [84] in 1985. They presented a unified scheme, combining molecular dynamics and density-functional theory, that is able to perform *ab initio* MD simulations where, in principle, the only assumptions are the validity of classical mechanics to describe ionic motion and the Born-Oppenheimer approximation to separate nuclear and electronic coordinates.

In this method the electronic state, Ψ, is considered a classical dynamical variable and a fictitious dynamics is used to optimize the Ψ. In their scheme, DFT [81] is used to calculate the total interaction energy and the forces, and a very efficient way is described to find the Kohn-Sham orbitals $\{\psi_i\}$. The fictitious dynamical optimization of $\{\psi_i\}$ and the real atomic MD are run in parallel with a very short time step, where the nuclei move from one conformation to another and the electronic states $\{\psi_i\}$ automatically "optimize" themselves to the states appropriate to the new conformation.

Formally, the fictitious dynamics of Car-Parrinello (CP) can be derived from the following Lagrangian [84,85]

$$\mathcal{L} = \frac{1}{2}\sum_i f_i \int \mu |\dot{\psi}_i(\mathbf{r})|^2 d\mathbf{r} + \sum_I \frac{1}{2} M_I \dot{\mathbf{R}}_I^2 - E\left[\{\psi_i\},\{\mathbf{R}_I\}\right] + \sum_{i,j} \Lambda_{i,j}\left(\int \mathbf{dr}\psi_i^*(\mathbf{r})\psi_j(\mathbf{r}) - \delta_{ij}\right), \quad \textbf{(4.1)}$$

where μ is a fictitious "mass", related to the fictitious "kinetic energy" (first term) of the electronic variables. In Equation 4.1, f_i is the occupation number of Kohn-Sham orbital i,

M_l the mass of the nucleus l, and in the last term $\{\Lambda_{i,j}\}$ is a set of Langrangian parameters introduced to maintain orthonormality of the Kohn-Sham orbitals.

The dynamical equations from the Lagrangian are [84]

$$M_l \ddot{\mathbf{R}}_l = -\frac{\partial E[\{\psi_i\},\{\mathbf{R}_l\}]}{\partial \mathbf{R}_l} \tag{4.2}$$

and

$$\mu \ddot{\psi}_i = -\frac{\partial E[\{\psi_i\},\{\mathbf{R}_l\}]}{\partial \psi_i^*} + \sum_j \Lambda_{i,j}\psi_j(\mathbf{r}). \tag{4.3}$$

Equation 4.2 describes the classical motion of the nuclei (ions), while Equation 4.3 describes the "classical" motion of the Kohn-Sham orbital $\{\psi_i\}$. It is interesting to note that when $\mu \to 0$, Equation 4.3 reduces to the Kohn-Sham equation and accordingly the energy density functional reduces to the adiabatic energy. In principle, the smaller the μ, the closer $\{\psi_i\}$ approaches the adiabatic states. In fact, in Car-Parrinello molecular dynamics (CPMD), μ cannot be set to zero because there would not be dynamical optimization of $\{\psi_i\}$. Usually, the size of μ is chosen so that the deviation of $\{\psi_i\}$ from the adiabatic states has a negligible effect on the MD simulation, while it still allows as large as possible a time-step [82].

In the CP scheme, the electronic variables are optimized dynamically so that the quantum SCF calculations are avoided. However, similar to conventional AIMD, CPMD

still needs to treat a large number of integrals related to electronic coordinates. For this reason, the current implementation of CPMD use two techniques: plane waves as a basis set and the pseudopotential approximation [79]. It should be pointed out as well that CPMD was originally developed for solid state applications, an area where plane waves are widely used. (In fact, the first application of the CPMD method in water focused on ice Ic and high pressure ice phases [86]).

The initial application of the CPMD scheme to aqueous systems was in a simulation of liquid water [87]. This simulation made use of the supersoft pseudopotentials introduced by Vanderbilt [88] and gradient corrections to the local density approximation. Vanderbilt pseudopotentials allowed them [87] to represent the electron valence orbital in terms of plane waves using a relatively small energy cutoff in the plane wave expansion [87,88]. Furthermore, gradient corrections were shown to improve dramatically the description of hydrogen bonding in DFT. Their results are encouraging insofar as they show that DFT was able to reproduce reasonably well some of the main static and dynamical properties of liquid water. The estimated diffusion coefficient was found to be in the correct range, 10^{-5} cm^2s^{-1}. However, they found some quantitative dependence of the results on the choice of the gradient correction. The results for the pair correlation function were satisfactory overall, although the O-O separation was observed to be too short.

This initial CPMD study was followed by a more extensive study [89], where 64 molecules (rather than the 32 molecules employed in [87]) within (truncated octahedron) periodical boundary conditions were used to calculate bulk properties. Parameters such as

the molecular dipole moment [90] and the oxygen-oxygen pair correlation function, when compared with experimental results showed acceptable agreement. More recently, Grossman and co-workers [91] have assessed the accuracy of several approximations within the CPMD method with a series of simulations of light and heavy water. They found negligible differences in the structural properties of the room temperature liquid obtained using the Perdew-Burke-Ernzerhof (PBE) or the Becke-Lee-Yang-Parr (BLYP) functionals, and relatively small, although not negligible, size effects when using 32 or 54 molecules in the simulation cell. The authors identified a range of values for the fictitious electronic mass (μ) entering the CP Lagrangian for which the electronic ground state is accurately described. They concluded that the use of $\mu \leq 340$ a.u. for H_2O and $\mu \leq 760$ a.u. for D_2O yields trajectories and average properties that are independent of the value chosen. At the same time, structural properties were found to artificially depend on μ if values outside this range are chosen. Finally, they found the oxygen-oxygen radial distribution function to be overstructured compared with the experimental result and the diffusion coefficient to be about 10 times smaller than for real water.

The CPMD method has also been used to simulate liquid water at ambient conditions in the context of a rigid body approximation [27]. Naturally, this approach allows one to access considerably longer time scales by utilizing a larger (about three times) time step than that typical for ordinary CPMD simulations. Interestingly, the authors found that the structural properties and diffusion coefficients obtained with a rigid model are in better agreement with experiment than those determined with fully flexible model simulations.

It is important at this point to stress that there is a clear difference between CP simulations and the purpose of this project. In the CP approach the quantization appears in the description of the interatomic interaction (the ground electronic state) and the behaviour of the atoms (or molecules) follows a classical dynamics (see Equations 4.2 and 4.3). However, our interest is in the quantization of the molecular motion itself, and it is here that the path integral methods play an essential role.

4.2. PATH INTEGRAL METHODS.

This section will review the path integral methods in statistical mechanics [7,8], with particular emphasis on liquid water and ice simulations. Before discussing previous work, the path integral Monte Carlo (PIMC) [9,92,93] and the path integral molecular dynamics (PIMD) methods are introduced [9,94,95]. In order to keep the notation simple, the description below will assume a quantum particle in one dimension, unless indicated otherwise.

4.2.1. General background

The quantum canonical partition function can be written in position coordinates as

$$Z \equiv Tr\left[e^{-\beta\hat{H}}\right] = \int dx \langle x | e^{-\beta\hat{H}} | x \rangle . \qquad \textbf{(4.4)}$$

Assuming that the Hamiltonian operator is simply a sum of the kinetic and potential operators, i.e. $\hat{H} = \hat{T} + \hat{V}$, Trotter's theorem [96] allows the following factorization [95],

$$e^{-\beta\hat{H}} = \lim_{P\to\infty}\left[e^{-\beta\hat{V}/2P}e^{-\beta\hat{T}/P}e^{-\beta\hat{V}/2P}\right]^P. \tag{4.5}$$

(The proof of this theorem is rather involved, for a more comprehensive treatment see reference 97). Using a complete set of momentum and position eigenvectors, each of the elements of this product can be written as

$$\begin{aligned} & e^{-(\beta\hat{V})/2P}e^{-(\beta\hat{T})/P}e^{-(\beta\hat{V})/2P} \\ &= \int dx_1\int dp_1\int dx_2 |x_1\rangle\langle x_1|e^{-\beta\hat{V}/2P}|p_1\rangle\langle p_1|e^{-\beta\hat{T}/P}e^{-\beta\hat{V}/2P}|x_2\rangle\langle x_2| \\ &= \int dx_1\int dp_1\int dx_2 |x_1\rangle e^{-\beta V(x_1)/2P}e^{-\beta p_1^2/2mP}e^{-\beta V(x_2)/2P}\langle x_1|p_1\rangle\langle p_1|x_2\rangle\langle x_2|. \end{aligned} \tag{4.6}$$

Then, the infinite product in Equation 4.5 becomes

$$\begin{aligned} e^{-\beta\hat{H}} = & \lim_{P\to\infty}\int dx_1\cdots\int dx_{P+1}\cdots\int dp_1\cdots\int dp_P|x_1\rangle \\ & \times\prod_{k=1}^{P}\left\{e^{-\varepsilon V(x_k)/2}e^{-\varepsilon p_k^2/2m}e^{-\varepsilon V(x_{k+1})/2}\langle x_k|p_k\rangle\langle p_k|x_{k+1}\rangle\right\}\langle x_{P+1}|, \end{aligned} \tag{4.7}$$

where $\varepsilon = \beta/P$. Using the product of the position and momentum eigenstates, ie. [98]

$$\langle x_k|p_k\rangle\langle p_k|x_{k+1}\rangle = \frac{1}{2\pi\hbar}e^{ip_kx_k/\hbar}e^{-ip_kx_{k+1}/\hbar} = \frac{1}{2\pi\hbar}e^{ip_k(x_k-x_{k+1})/\hbar}, \tag{4.8}$$

the path integral representation of the Boltzmann operator is obtained

$$\begin{aligned} e^{-\beta\hat{H}} = & \lim_{P\to\infty}\left(\frac{1}{2\pi\hbar}\right)^P\int dx_1\cdots\int dx_{P+1}\cdots\int dp_1\cdots\int dp_P|x_1\rangle \\ & \times\prod_{k=1}^{P}\left\{e^{-\varepsilon V(x_k)/2}e^{-\varepsilon p_k^2/2m}e^{-\varepsilon V(x_{k+1})/2}e^{ip_k(x_k-x_{k+1})/\hbar}\right\}\langle x_{P+1}|. \end{aligned} \tag{4.9}$$

This equation can be written in a simpler form by noting that

$$\int dp_1 e^{-\varepsilon p_1^2/2m+i(x_k-x_{k+1})p_1/\hbar} = \left(\frac{2\pi mP}{\beta}\right)^{\frac{1}{2}} e^{-\frac{mP}{2\beta\hbar^2}(x_k-x_{k+1})^2}, \tag{4.10}$$

and

$$\int dp_1 \cdots \int dp_P \prod_{k=1}^{P} \left\{ e^{-\varepsilon p_k^2/2m+i(x_k-x_{k+1})p_k/\hbar} \right\} = \left(\frac{2\pi mP}{\beta}\right)^{\frac{P}{2}} e^{-\frac{mP}{2\beta\hbar^2}\sum_{k=1}^{P}(x_k-x_{k+1})^2}. \tag{4.11}$$

Hence, we finally get

$$\begin{aligned} \langle x'|e^{-\beta\hat{H}}|x''\rangle = \lim_{P\to\infty}\left(\frac{mP}{2\pi\hbar^2\beta}\right)^{\frac{P}{2}} \int dx_2 \cdots \int dx_P \\ \times \exp\left\{-\frac{mP}{2\beta\hbar^2}\left[(x'-x_2)^2 + \cdots + (x_P - x'')^2\right]\right\} \\ \times \exp\left\{-\frac{\beta}{P}\left[\frac{1}{2}V(x') + V(x_2) + \cdots + V(x_P) + \frac{1}{2}V(x'')\right]\right\}, \end{aligned} \tag{4.12}$$

which substituted on Equation 4.4 gives

$$\begin{aligned} Z = \int dx \langle x|e^{-\beta\hat{H}}|x\rangle = \lim_{P\to\infty}\left(\frac{mP}{2\pi\hbar^2\beta}\right)^{\frac{P}{2}} \int dx_1 \cdots \int dx_P \\ \times \exp\left\{-\sum_{k=1}^{P}\left[\frac{mP}{2\beta\hbar^2}(x_k - x_{k+1})^2 + \frac{\beta}{P}V(x_k)\right]\right\}, \end{aligned} \tag{4.13}$$

where $x_{P+1} = x_1$. Equation 4.13 is the *discretized path integral* form of the quantum canonical partition function [9,10,95]. It is clear here that the partition function of a

quantum particle is equivalent to the classical configurational partition function of P classical particles with potential $U(x_1 \ldots x_P;\beta)$, i.e. [9]

$$Z \approx Z_p = \left(\frac{mP}{2\pi\beta\hbar^2}\right)^{P/2} \int\ldots\int dx_1 \ldots dx_P e^{-\beta U(x_1 \ldots x_P;\beta)}, \tag{4.14}$$

where

$$U(x_1 \ldots x_P;\beta) = \frac{mP}{2\beta^2\hbar^2}\sum_{k=1}^{P}(x_k - x_{k+1})^2 + \frac{1}{P}\sum_{k=1}^{P} V(x_k). \tag{4.15}$$

Thus, the quantum system is said to be isomorphic [9,10] to a classical P-particle cyclic chain "polymer" in which each particle k interacts with its neighbours k-1 and k+1 through a harmonic potential with force constant $mP/\hbar^2\beta^2$, and each particle k experiences the potential $V(x_k)/P$. Figure 4.1 shows schematically the case of two quantum particles, i and j, that interact through a classical potential, the straight lines, and between their beads through harmonic potentials, the "wavy" lines [4].

According to Equation 4.15, the root mean square (rms) bond length for a free chain is proportional to $(\beta\hbar^2/mP)^{1/2}$. Hence, classical isomorphism will be a good approximation only if the potential, $V(x)$, does not vary strongly over the rms bond length. If σ is a characteristic distance specifying the length scale on which $V(x)$ changes, then

$$\frac{\beta\hbar^2}{m\sigma^2} << P, \tag{4.16}$$

and we see that the lower the temperature $\left(\beta^{-1}\right)$, the larger P must be. In practice one empirically determines and uses a value of P beyond which the thermodynamic properties do not effectively change [9].

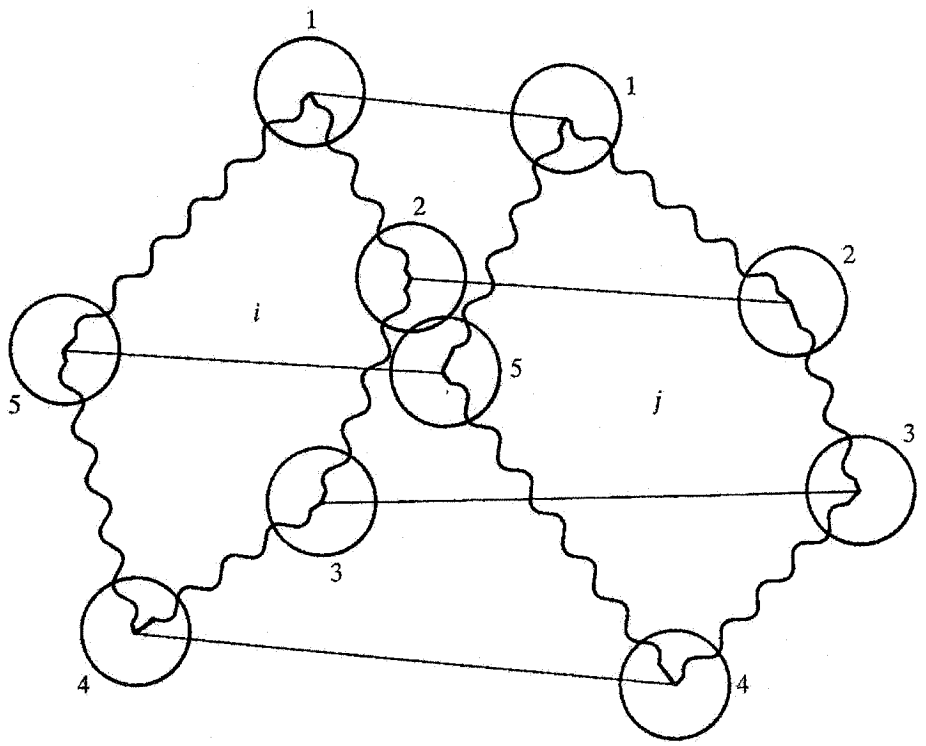

Figure 4.1. Illustration of the interaction between two quantum particles in the path integral isomorphism. The wavy lines represent the harmonic interactions between beads and the straight lines represent the interatomic potential [4].

The calculation of the thermodynamic expectation values in terms of path integrals follows almost automatically. Suppose we wish to compute the expectation value of an operator $\hat{A} = \hat{A}(x)$. By definition, the expectation value of $\hat{A}$ is [1,2]

$$\langle \hat{A} \rangle \equiv \frac{1}{Z(\beta)} \int dx \langle x | \hat{A} e^{-\beta \hat{H}} | x \rangle = \frac{1}{Z(\beta)} \int dx a(x) \langle x | e^{-\beta \hat{H}} | x \rangle, \tag{4.17}$$

where $a(x)$ is the corresponding eigenvalue of the operator $\hat{A}$ acting on the coordinate eigenstate. The corresponding path integral form is [95]

$$\begin{aligned} \langle A \rangle &= \lim_{P \to \infty} \frac{1}{Z_P} \left(\frac{mP}{2\pi\hbar^2 \beta} \right)^{\frac{P}{2}} \int dx_1 \cdots \int dx_P \\ &\qquad \times a(x_1) \exp\left\{ -\sum_{k=1}^{P} \left[\frac{mP}{2\beta\hbar^2} (x_k - x_{k+1})^2 + \frac{\beta}{P} V(x_k) \right] \right\} \\ &= \lim_{P \to \infty} \frac{1}{Z_P} \left(\frac{mP}{2\pi\hbar^2 \beta} \right)^{\frac{P}{2}} \int dx_1 \cdots \int dx_P \\ &\qquad \times \frac{1}{P} \sum_{k=1}^{P} a(x_k) \exp\left\{ -\sum_{k=1}^{P} \left[\frac{mP}{2\beta\hbar^2} (x_k - x_{k+1})^2 + \frac{\beta}{P} V(x_k) \right] \right\}, \end{aligned} \tag{4.18}$$

where is important to remember that $x_{P+1} = x_1$.

The isomorphic classical system can be simulated by either Monte Carlo techniques [92,93] or molecular dynamics [94,95]. In Monte Carlo the configurations can be sampled from the distribution of the classical isomorphism, $\exp\left[-\beta U_P(x_1 \ldots x_P; \beta)\right]$. This is called *path integral Monte Carlo* (PIMC). Estimators of various quantum observables can then be averaged over the configurations sampled. Although this appears to be straightforward, complications can arise, and it is often necessary to make careful choices of estimators. The question of convergence of the properties of the quantum systems as a function of P must be addressed. It is important to realize that, in general, different properties converge differently as P is varied [9].

A different method for simulating quantum systems can be obtained if Equations 4.14 and 4.15 are written in the form [9,95]

$$Z_P = \left(\frac{mP}{2\pi\beta\hbar^2}\right)^{P/2} \prod_{k=1}^{P} \left(\frac{\beta}{2\pi m_k'}\right)^{\frac{1}{2}} \int dp_1 \ldots \int dp_P \int dx_1 \ldots \int dx_P \exp[-\beta H], \qquad \textbf{(4.19)}$$

where

$$H = \sum_{k=1}^{P} \frac{p_k^2}{2m_k'} + U(x_1 \ldots x_P; \beta). \qquad \textbf{(4.20)}$$

It is clear that independent of the choice of $\{m_k'\}$, integration over $(dp_1 \ldots dp_P)$ yields Equation 4.14. In fact, $\{m_k'\}$ can be adjusted for convenience. Since the above Hamiltonian gives rise to the following classical equations of motion for the beads,

$$\left.\begin{aligned} \dot{x}_k &= \partial H / \partial p_k \\ \dot{p}_k &= -\partial H / \partial x_k \end{aligned}\right\} \quad k = 1,\ldots,P, \qquad \textbf{(4.21)}$$

classical MD methods can be used to simulate the equilibrium properties of quantum systems [9,95]. Indeed, starting from a given state $(dx_1 \ldots dx_P, dp_1 \ldots dp_P)$, a fictitious dynamics is generated by numerical integration of the equations of motion. The values of the thermodynamic properties are obtained by averaging the corresponding estimators over this trajectory provided that ergodicity holds. Such molecular dynamics calculations are called *path integral molecular dynamics* (PIMD) [9,95].

Within PIMD, the partition function need not be calculated in Cartesian coordinates. In fact, for large values of P this is expected to be inefficient since the harmonic term becomes dominant while the contribution from the external potential is attenuated (see Equation 4.15). This problem is overcome with a coordinate transformation in the Hamiltonian. Natural and commonly used coordinates are the normal modes, which uncouple the harmonic motion. This transformation is especially useful in the context of the so-called centroid molecular dynamics method [17,18] (discussed below), since the centroid variable becomes uncoupled from the internal motion of the chain. Alternatively, the so-called staging coordinates [99] uncouple the harmonic terms and additionally allow us a convenient way to assign the appropriate masses to each degree of freedom such that the staging modes move on the same time scale, thereby leading to very efficient phase space sampling [99,100].

It is also important to note that whereas standard MD will generate a microcanonical distribution, the form appearing on Equation 4.19 requires a canonical sampling. In order to ensure that a proper canonical distribution is generated, Equations 4.21 (or the equivalent ones obtained through the coordinate transformation mentioned above) must be coupled to a thermostating method. Although several thermostating methods exist in the literature [4,6,42] experience has shown that the Nosé-Hoover chain [47] is a very effective one (see Section 2.3.1).

It is important to recognize, at this point, that the classical trajectories in PIMD (or PIMC) have nothing to do with the real dynamics of the quantum system. The dynamics in this isomorphic system simply provides an algorithm for generating the

partition function and thus allow the calculation of the equilibrium properties of the system [9,95]. The simulation of the real time dynamics of a quantum system is a much more complicated (and still open) problem. Sections 4.2.4 and 4.2.5 below will briefly describe two approximate techniques that have been used to calculate time correlation functions in liquid water. A more rigorous discussion of quantum dynamics via centroid path integrals is postponed until Chapter 5.

Finally, the continuous limit of the path integral representation of the partition function is found by evaluating the limit in Equation 4.13. Introducing $\varepsilon = \beta\hbar/P$, the exponent in that equation becomes [7,95]

$$\begin{aligned}\lim_{P\to\infty}\sum_{k=1}^{P}\left[\frac{mP}{2\beta\hbar^2}(x_k - x_{k+1})^2 + \frac{\beta}{P}V(x_k)\right] &= \lim_{\varepsilon\to 0}\sum_{k=1}^{P}\frac{\varepsilon}{\hbar}\left[\frac{m}{2}\left(\frac{x_k - x_{k+1}}{\varepsilon}\right)^2 + V(x_k)\right] \\ &= \frac{1}{\hbar}\int_0^{\beta\hbar}\left(\frac{m}{2}\dot{x}^2(\tau) + V[x(\tau)]\right)d\tau = \frac{1}{\hbar}\int_0^{\beta\hbar}\mathcal{L}[x(\tau)]d\tau,\end{aligned} \tag{4.22}$$

where the integrand defines the Euclidean Lagragian, $\mathcal{L}(x,\dot{x})$. Therefore, Equation 4.13 transforms into [7,95]

$$Z(\beta,V) = \int_{x(0)=x(\beta\hbar)}\mathcal{D}x(\tau)e^{-\frac{1}{\hbar}S[x(\tau)]}, \tag{4.23}$$

where the notation $\lim_{P\to\infty}\left(\frac{mP}{2\pi\beta\hbar^2}\right)^{\frac{P}{2}} dx_1\cdots dx_P \equiv \mathcal{D}x(\tau)$ has been used. The symbol $\int_{x(0)=x(\beta\hbar)}\mathcal{D}x(\tau)[\ldots]$ represents an integration over all cyclic paths starting and ending at

point x, and includes an integral over this point. The imaginary time or Euclidean action, $S[x(\tau)]$, is defined as [7,95]

$$S[x(\tau)] = \int_0^{\beta\hbar} \mathcal{L}(x(\tau), \dot{x}(\tau)) d\tau \,. \tag{4.24}$$

The equations given to this point can be easily generalized to a many body quantum system where spin statistics can be neglected. This is a very acceptable approximation for liquid water (and ice) over the temperatures of interest in this thesis. A discussion of spin statistics in path integrals can be found in reference [101].

4.2.2. PIMD simulations of liquid water with flexible models.

The first PIMD simulation of liquid water was carried out by Wallqvist and Berne [13]. They used a central force potential with the internal vibrations of the molecule modeled by a set of Morse potentials [102]. In reference [13], each atom was discretized with only 3 beads and 216 molecules were used to simulate liquid properties. The simulations were equilibrated and run for 7.5 ps using a time step of 0.25 fs at 300 K. The problem of ergodicity was handled with a periodic re-sampling of the velocities according to the Maxwell-Boltzmann distribution.

Even though this early attempt underestimated the quantum effects (due to the low value of the discretization parameter) they found the quantum water to be less hydrogen bonded than classical water. This observation was based on a typical definition of the hydrogen bond [13]. They integrated the probability of a pair of molecules with an interaction energy up to –4 kcal/mol and found this number to be higher in the classical

than in the quantum liquid. This result was consistent with the softening observed in the quantum pair distribution functions, i.e. $g_{O\text{-}O}$, $g_{O\text{-}H}$ and $g_{H\text{-}H}$, in comparison with the classical simulations.

More recently, Stern and Berne [15] examined quantum effects in liquid water by performing PIMD simulations on a flexible and polarizable water model that was optimized from *ab initio* calculations. The use of an *ab initio* parameterized potential avoids the implicit inclusion of quantum effects that takes place in the parameterization of empirical water models using classical simulations. In reference [15], the oxygen atoms were treated classically (i.e. P=1) and convergence in the average system energy was observed when the protons were discretized with P=24 beads. In other words, the partition function and the PIMD Hamiltonian transform to

$$Z_P = \left(\frac{mP}{2\pi\beta\hbar^2}\right)^{P/2} \prod_{k=1}^{P} \left\{ \left(\frac{\beta}{2\pi m_k'}\right)^{\frac{1}{2}} \int dp_H^{(k)} \int dx_H^{(k)} \right\} \int dp_O \int dx_O \exp[-\beta H] \qquad \textbf{(4.25)}$$

and

$$H = \frac{p_O^2}{2m_O} + \sum_{k=1}^{P} \left\{ \frac{p_H^{(k)2}}{2m_k} + \frac{m_H P}{2\hbar^2\beta^2} \left(x_H^{(k+1)} - x_H^{(k)}\right)^2 + \frac{1}{P} U\left(x_H^{(1)}, \cdots, x_H^{(P)}; x_O\right) \right\}, \qquad \textbf{(4.26)}$$

instead of Equations 4.19 and 4.20, where the position and momentum coordinates of the oxygen and hydrogen nuclei are denoted here by x_O, $x_H^{(k)}$, p_O and $p_H^{(k)}$, respectively. It is important to note that Equations 4.25 and 4.26 were first published in the work of Lobaugh and Voth [19] in a slightly different context (see Section 4.2.5).

The equations of motion employed in reference [15] were integrated using the staging mode [97] with a Nosé-Hoover chain [47] thermostat in each degree of freedom to ensure convergence. The simulations were performed using 125 water molecules at 298.15 K and showed again that the quantum liquid is less structured and has smaller binding energies than the classical one. Additionally, quantum effects did not appear to significantly modify the average induced dipole moment for a polarizable model, although the distribution was found to be broader.

4.2.3. PI simulations of liquid water and ice with rigid models.

In order to extend the formulas presented above to the case of rigid bodies it is useful to introduce a slightly different notation. If we define a free propagator from point x_k to point x_{k+1} in the time $\beta\hbar/P$ as [7]

$$\rho_0(x_k, x_{k+1}; \beta\hbar/P) = \left(\frac{mP}{2\pi\hbar^2\beta}\right)^{\frac{1}{2}} \exp\left\{-\frac{mP}{2\beta\hbar^2}(x_k - x_{k+1})^2\right\}, \tag{4.27}$$

Equation 4.13 can be rewritten as

$$Z = \lim_{P\to\infty} \int dx_1 \cdots \int dx_P \prod_{k=1}^{P} \left\{\rho_0(x_k, x_{k+1}; \beta\hbar/P) e^{-\frac{\beta}{P}V(x_k)}\right\}. \tag{4.28}$$

Written in this form the generalization is easily done by introducing a six-dimensional coordinate **X** that represent the position and orientation of a rigid object (if the object is linear **X** has 5 dimensions, if additionally the object is constrained to rotate in a plane, **X** has 4 dimensions). Hence, the canonical partition function becomes [12]

$$Z_P(\beta) = \int d\mathbf{X}_1 \cdots \int d\mathbf{X}_P \prod_{k=1}^{P} \left\{ \rho_0(\mathbf{X}_k, \mathbf{X}_{k+1}, \beta/P) \exp\left[-\frac{\beta}{P} U(\mathbf{X}_k) \right] \right\}, \qquad \textbf{(4.29)}$$

where $\mathbf{X}_{P+1} = \mathbf{X}_1$ and $U(\mathbf{X}_k)$ is the potential energy of the rigid object with coordinates $\mathbf{X}_k$. Clearly, this partition function converges to the correct quantum result as P increases.

Since free propagation implies no coupling between translations and rotations, the free propagator $\rho_0(\mathbf{X}_k, \mathbf{X}_{k+1}; \beta / P)$ in this multidimensional space factorizes, i.e. [12]

$$\rho_0(\mathbf{X}_k, \mathbf{X}_{k+1}; \beta/P) = \rho_0(\mathbf{r}_k, \mathbf{r}_{k+1}; \beta/P) \rho_0(\Omega_k, \Omega_{k+1}; \beta/P), \qquad \textbf{(4.30)}$$

where

$$\rho_0(\mathbf{r}_k, \mathbf{r}_{k+1}; \beta/P) = \left(\frac{mP}{2\pi\hbar^2\beta} \right)^{3/2} \exp\left[\frac{-mP}{2\hbar^2\beta} (\mathbf{r}_k - \mathbf{r}_{k+1})^2 \right], \qquad \textbf{(4.31)}$$

is the straightforward extension of Equation 4.27 to three dimensions and $\rho_0(\Omega_k, \Omega_{k+1}; \beta/P)$ is the free orientational propagator, in which Ω_k is the orientational coordinate. Neglecting the possibility of multiple rotations, the free orientational propagator in imaginary time can be approximated by [12]

$$\rho_0(\Omega_k, \Omega_{k+1}; \beta/P) = C \frac{I_x I_y I_z \Gamma(\Omega_k, \Omega_{k+1})}{2\sin\left(\frac{1}{2}\Gamma(\Omega_k, \Omega_{k+1})\right)} \exp\left[(-1/\hbar) S_{FA}(\Omega_k, \Omega_{k+1}; \beta/P) \right], \qquad \textbf{(4.32)}$$

where

$$S_{FA}(\Omega_k,\Omega_{k+1};\beta/P)=\frac{P}{2\beta\hbar}\left(\mathbf{n}\bar{\bar{\mathbf{I}}}\mathbf{n}\right)\Gamma^2(\Omega_k,\Omega_{k+1}), \tag{4.33}$$

is the fixed axis action, C is a constant, $\mathbf{n}$ is the rotation axis that joins Ω_k with Ω_{k+1}, $\Gamma(\Omega_k,\Omega_{k+1})$ is the arclength of this rotation and $\bar{\bar{\mathbf{I}}}$ is the inertia tensor of the rigid molecule.

If we combine Equations 4.29-4.33 we finally obtain the discretized form of the canonical partition function of a rigid quantum object [12]

$$\begin{aligned} Z_P(\beta)=&\left(\frac{mP}{2\pi\hbar^2\beta}\right)^{3P/2}C\left(\frac{I_xI_yI_z}{(\beta\hbar/P)^3}\right)^{P/2}\int d\mathbf{r}_1\cdots\int d\mathbf{r}_P\int d\Omega_1\cdots\int d\Omega_P \\ &\times\prod_{k=1}^{P}\left\{\exp\left[\frac{-mP}{2\hbar^2\beta}(\mathbf{r}_k-\mathbf{r}_{k+1})^2\right]\frac{\Gamma(\Omega_k,\Omega_{k+1})}{2\sin\left[\frac{1}{2}\Gamma(\Omega_k,\Omega_{k+1})\right]}\right. \\ &\left.\times\exp\left[-\frac{P\left(\mathbf{n}\bar{\bar{\mathbf{I}}}\mathbf{n}\right)}{2\beta\hbar^2}\Gamma^2(\Omega_k,\Omega_{k+1})\right]\exp\left[-\frac{\beta}{P}U(\mathbf{r}_k,\Omega_k)\right]\right\}. \end{aligned} \tag{4.34}$$

If we assume that the position of the center of mass of the beads is about the same, ie. $\mathbf{r}_1\approx\mathbf{r}_2\approx\cdots\approx\mathbf{r}_P$, and that the intermolecular potential does not change significantly over the small range of displacements of the center of mass of the molecule i.e. $U(\mathbf{r}_k,\Omega_k)=U(\mathbf{r}_1,\Omega_k)$ for all k, an integration over $d\mathbf{r}_2\cdots d\mathbf{r}_P$ can be carried out in Equation 4.34 to obtain

$$Z_P(\beta) = \left(\frac{m}{2\pi\hbar^2\beta}\right)^{3/2} C\left(\frac{I_x I_y I_z}{(\beta\hbar/P)^3}\right)^{P/2} \int d\mathbf{r} \int d\Omega_1 \cdots \int d\Omega_P$$
$$\times \prod_{k=1}^{P} \left\{ \frac{\Gamma(\Omega_k, \Omega_{k+1})}{2\sin\left[\frac{1}{2}\Gamma(\Omega_k, \Omega_{k+1})\right]} \exp\left[-\frac{P(\mathbf{n}\vec{\mathbf{I}}\mathbf{n})}{2\beta\hbar^2}\Gamma^2(\Omega_k, \Omega_{k+1})\right] \exp\left[-\frac{\beta}{P}U(\mathbf{r}, \Omega_k)\right] \right\}. \quad (4.35)$$

The system described by this equation differs from that of the Equation 4.34 in that all the members of each polymer ring have the same center of mass position **r**, but the orientations remain different, in general. The generalization of Equations 4.34 and 4.35 to multiple particles is straightforward [12].

This was the approach followed in the first quantum simulation of liquid water by Kuharsky and Rossky [12]. They carried out PIMC simulations of liquid H_2O and D_2O at ambient conditions on the ST2 [62,63] water model. Since Equation 4.35 treats the center of mass classically and Equation 4.34 treats the center of mass quantum mechanically, the influence of treating the center of mass motion classically or quantum mechanically was also assessed. This study was later complemented with PIMD simulations of light (H_2O) and heavy (D_2O) liquid water based on the ST2 [62], SPC [60] and TIP4P [61] models.

A discretization parameter as small as P=3 [12], later revised upward to P=5 [14], was judged to be satisfactory for quantizing the rotations for a small test case, an isolated water dimer at room temperature. The simulations were carried out with systems of roughly one hundred water molecules. As expected, the classical liquid was observed to be the most structured, light water the least structured, and heavy water in between. For

example, in the radial distribution functions the maxima decrease and the minima increase in height, and both shift to larger distance as the system becomes more quantum mechanical. These effects are even manifest in the oxygen-oxygen radial distribution function and not just in the partial radial distribution functions for the much lighter H or D atoms. In addition, the heavier the nuclei, the smaller the librational motion. This leads generally to more linear hydrogen bonds ($HO\text{-}H\cdots OH_2$) between the water molecules for classical water compared to light (quantum) water. The structural quantum effects were attributed mainly to the orientational degree of freedom rather than the center-of-mass motion of the rigid bodies. Furthermore, it was found that changes in structural properties in going from classical to quantum water were roughly comparable to the changes which accompany a 50 K temperature increase of the liquid [12]. Viewed in this way, one can conclude that the quantum effects on the structure of liquid water at ambient conditions are not negligible.

Equation 4.34 has also been used to simulate ice Ih near its melting temperature [16]. With the water-water interaction represented by the SPC [60] model, average equilibrium properties such as potential energy, radial distribution functions and structural factors were computed as functions of temperature. The authors found a value of P=5 to be sufficiently large to obtain converged results in comparison to simulations with P=10. The radial distribution functions exhibited a softening when going from classical to quantum systems, closely resembling that observed previously in liquid simulations. Interestingly, the difference between the classical and the quantum intermolecular energy was found to increase as the temperature was lowered. Finally, the

authors roughly estimated the melting temperature for the classical system to be about 280 K while for the quantum system to be about 260 K, implying that quantization decreases the melting temperature of the SPC water model.

4.2.4. *Feynman-Hibbs variational approach.*

It is now useful to review the Feynman-Hibbs variational treatment [7,8], leading to a definition of an effective quasiclassical pair potential, an approach that has been recently applied to liquid water [20]. This treatment begins by writing the path integral form of the partition function (see Equations 4.23 and 4.24) as

$$Z(\beta,V)=\int_{x(0)=x(\beta\hbar)}\mathcal{D}x(\tau)\exp\left\{-\frac{1}{\hbar}\int_0^{\beta\hbar}\left(\frac{m}{2}\dot{x}^2(\tau)+V[x(\tau)]\right)d\tau\right\}. \tag{4.36}$$

Introducing [7,8]

$$Z'(\beta,V)=\int_{x(0)=x(\beta\hbar)}e^{-\frac{1}{\hbar}S'[x(\tau)]}\mathcal{D}x(\tau), \tag{4.37}$$

we have

$$\frac{Z(\beta,V)}{Z'(\beta,V)}=e^{-\beta(F-F')}=\frac{\int_{x(0)=x(\beta\hbar)}e^{-\frac{1}{\hbar}\{S[x(\tau)]-S'[x(\tau)]\}}e^{-\frac{1}{\hbar}S'[x(\tau)]}\mathcal{D}x(\tau)}{\int_{x(0)=x(\beta\hbar)}e^{-\frac{1}{\hbar}S'[x(\tau)]}\mathcal{D}x(\tau)} \tag{4.38}$$
$$=\left\langle e^{-\frac{1}{\hbar}\{S[x(\tau)]-S'[x(\tau)]\}}\right\rangle_{S'},$$

where the notation $\langle\cdots\rangle_{S'}$ indicates a path integral average. However, since for a real function $f(x)$, $\left\langle e^{f(x)}\right\rangle \geq e^{\langle f(x)\rangle}$, we obtain [7,8]

$$F \leq F' + \frac{1}{\beta\hbar}\left\langle S[x(\tau)] - S'[x(\tau)]\right\rangle_{S'}. \tag{4.39}$$

This minimization principle states that if we substitute the exact interacting potential of the system by a family of simpler potentials, we could optimize within this family to get the best one. Feynman suggested the adoption of the potential $V[x_0]$, where [7,8]

$$x_0 = \frac{1}{\hbar\beta}\int_0^{\hbar\beta} x(\tau)d\tau, \tag{4.40}$$

(i.e., the mean value of the Euclidean path) such that the partition function gets a classical form given by

$$Z' = e^{-\beta F'} = \left(\frac{m}{2\pi\beta\hbar^2}\right)\int e^{-\beta V(x_0)}dx_0 . \tag{4.41}$$

Evaluating (with the help of some algebra [7,8]) the second term in the right hand side of Equation 4.39 we have

$$\begin{aligned}\frac{1}{\beta\hbar}\left\langle S[x(\tau)] - S'[x(\tau)]\right\rangle_{S'} &= \frac{1}{\beta\hbar}\left\langle \int_0^{\beta\hbar}\left\{V[x(\tau)] - V[x_0]\right\}d\tau\right\rangle_{S'} \\ &= \frac{\int\left\{W(x_0) - V(x_0)\right\}e^{-\beta V(x_0)}dx_0}{\int e^{-\beta V(x_0)}dx_0},\end{aligned} \tag{4.42}$$

where

$$W(x_0) = \left(\frac{6m}{2\pi\beta}\right)^{\frac{1}{2}} \int V(x) e^{-\frac{6m}{\beta\hbar^2}(x-x_0)^2} dx. \tag{4.43}$$

It is important to note that Equation 4.43 is simply a Gaussian average of the exact interaction potential that includes the mass of the particle and the temperature of the system [7,8].

According to Equation 4.39, the best form of $V(x_0)$ is the one that minimizes its right hand side. Performing a variation on the right hand side of Equation 4.39 (using Equations 4.41 and 4.42) we get

$$\delta F' = \frac{\int \delta V(x_0) e^{-\beta V(x_0)} dx_0}{\int e^{-\beta V(x_0)} dx_0} \tag{4.44}$$

and

$$\begin{aligned} \delta\left\{\frac{1}{\beta\hbar}\left\langle S[x(\tau)] - S'[x(\tau)]\right\rangle_{S'}\right\} = \\ = \frac{\int\left\{-\beta\delta V(x_0)\left[W(x_0) - V(x_0)\right] - \delta V(x_0)\right\} e^{-\beta V(x_0)} dx_0}{\int e^{-\beta V(x_0)} dx_0} \\ + \frac{\int\left[W(x_0) - V(x_0)\right] e^{-\beta V(x_0)} dx_0 \times \int -\beta\delta V(x_0) e^{-\beta V(x_0)} dx_0}{\left[\int e^{-\beta V(x_0)} dx_0\right]^2}. \end{aligned} \tag{4.45}$$

Thus, if the sum of Equations 4.44 and 4.45 is set to zero, we find the solution $V(x_0) = W(x_0)$. This result demonstrates that the best interaction potential associated to the centroid variable is the one obtained by a Gaussian average of the classical potential

as given by Equation 4.43 [7,8]. In practice, the integral in Equation 4.43 may be difficult to solve depending on the shape of the interaction potential (for example, the Lennard-Jones potential is infinity at zero). An approximate solution to this problem is obtained by Taylor expanding the classical potential to second or higher orders. The expansion to second order leads to the so-called quadratic Feynman-Hibbs effective potential [103].

Quantum effects in liquid water have been investigated with MD by implementing the Feynman-Hibbs effective potential as represented by [20,103]

$$V_{FH}(r_{ij}) \approx V_{QFH}(r_{ij}) = V(r_{ij}) + \frac{\beta\hbar^2}{24\tilde{m}}\left(V''(r_{ij}) + 2\frac{V'(r_{ij})}{r}\right), \qquad \textbf{(4.46)}$$

where the prime and double prime are the first and second derivatives with respect to r, respectively, and V_{QFH} is the quadratic Feynman-Hibbs (QFH) potential. Equation 4.46 is written in a three dimensional form and its dependence on mass (the reduced mass $\tilde{m} = m/2$ for identical particles) and temperature, along with the presence of Planck's constant, are the result of the effective average potential accounting for the uncertainty in position between a pair of particles. The thermodynamics, the structure, and the dynamics of light and heavy water were evaluated [20]. Not only was the variation of the heat of vaporization observed between light and heavy water well reproduced, but the drift of the temperature of maximum density in going from classical water to heavy and light water is in agreement with the experimental trends. Quantization appeared to soften significantly the structure of the liquid, especially in the first coordination shell where the tetrahedral arrangement between a central molecule and its nearest neighbours relaxes somewhat.

Quantization also appeared to increase the diffusivity of water molecules by a relatively large factor. In simulations of supercooled water, a strong dependence in the ratio D_{H_2O}/D_{D_2O} was found when decreasing temperature, an observation corroborated by experimental data [102]. Finally, the comparison of these results [20] with other simulation studies based upon the path-integral simulation techniques [12,19] demonstrates that the Feynman-Hibbs approach can be a reasonable and efficient method.

One of the advantages of the Feynman-Hibbs method is that time dependent quantities can be evaluated within a MD run. More precisely, keeping the gross features of quantum effects along the trajectory, the FH effective potential becomes a quantum correction to the classical potential by including the effects of "zero level vibration" and tunneling.

There are, however, a number of limitations associated with this approach. First, the exact interaction potential between atoms is assumed to be known in a sufficiently simple analytical form such that Equation 4.43 can be employed to obtain the effective interaction potential between centroids. Second, the use of the minimum principle (Equation 4.39) guarantees the best approximate result to the thermodynamic properties only, which is useful but approximate nonetheless. Third, the dynamics is assumed to remain completely classical but in an otherwise quantum corrected potential. This last approximation is only reasonable very near the classical limit. In addition, it is important to note that although the effective potential depends on the particle mass and the

temperature of the system, it is independent of the local environment of the particles, something that can play an important role in many condensed matter systems.

An important final point with respect to this effective potential technique is that it suggests that the centroid variable may be an ideal candidate for further development of a quasi-classical description of a quantum mechanical system. An intuitive discussion of such an approach is presented immediately below and will lead to the so-called *centroid molecular dynamics method.*

4.2.5. *Centroid Molecular Dynamics simulation of liquid water*

The variational method presented above could be improved if, instead of using Equation 4.43, we obtain the effective potential in a calculation on the fly and propagate the centroid in a otherwise classical form. Such an approach leads to the centroid molecular dynamics method [17,18,105-111]. Performed in this way, the calculation will be significantly more expensive than the Feynman-Hibbs effective potential technique, however there are several benefits associated with proceeding in this fashion. In fact, all the deficiencies noted in the previous section are improved or eliminated with the CMD method. This section introduces the CMD method as way of improving the Feynman-Hibbs approach. A more detailed discussion of the approximations involved in the CMD approach is postponed until Chapter 5.

Using Equation 4.23 the partition function can be written as

$$Z = \left(\frac{m}{2\pi\beta\hbar^2}\right)^{\frac{1}{2}} \int \rho_c(x_c) dx_c, \tag{4.47}$$

where

$$\rho_c(x_c) = \left(\frac{2\pi\beta\hbar^2}{m}\right)^{\frac{1}{2}} \int_{x(0)=x(\beta)} \mathcal{D}x\,\delta(x_c - x_0)\exp\left\{-S[x(\tau)]/\hbar\right\} \tag{4.48}$$

defines the centroid density, and the variable, x_0, is defined by Equation 4.40.

With the partition function written as in Equation 4.47, the centroid variable becomes the relevant variable from which effective potentials, that take into account the imaginary time path fluctuations of the quantum system at the specified temperature, are derived. Indeed, the centroid is the classical-like coordinate for which the perturbation theory has no first-order correction [7] and where a variational approach can be used to improve on the perturbation expansion [7,8]. More recently, Cao and Voth [106] have introduced a diagrammatic representation for the perturbation expansion of Equation 4.48 and have used standard renormalization techniques to improve on the perturbative method.

By introducing the definition

$$V_{eff}(x_c) = -\frac{1}{\beta}\ln\left[\rho_c(x_c)\right], \tag{4.49}$$

where $V_{eff}(x_c)$ is the exact centroid effective potential, the partition function in Equation 4.47 can be rewritten as

$$Z = \left(\frac{m}{2\pi\beta\hbar^2}\right)^{\frac{1}{2}} \int dx_c \exp\left\{-\beta V_{eff}(x_c)\right\}. \tag{4.50}$$

It is important to note that the effective potential as described by Equation 4.49 is completely general. CMD uses this potential as the surface on which to propagate the centroid classically. In other words, the centroid trajectories are generated by the effective classical-like equations of motion [17,18,105-111]

$$m\ddot{x}_c(t) = -\frac{dV_{eff}(x_c)}{dx_c}, \tag{4.51}$$

where the centroid force, $-dV_{eff}(x_c)/dx_c$, is a quantum mechanical mean force for the centroid given by [109]

$$-\frac{dV_{eff}(x_c)}{dx_c} = -\frac{\int_{x(0)=x(\beta\hbar)} \mathcal{D}x(\tau)\delta(x_c - x_0)\left\{dV[x(0)]/dx_c\right\} e^{-\frac{1}{\hbar}S[x(\tau)]}}{\int_{x(0)=x(\beta\hbar)} \mathcal{D}x(\tau)\delta(x_c - x_0) e^{-\frac{1}{\hbar}S[x(\tau)]}}. \tag{4.52}$$

In practice, the centroid force needs to be evaluated at each simulation step by performing a separate path integral calculation, either via PIMC or PIMD. If the PIMD method is chosen, the combination of Equations 4.51 and 4.52 indicates the coupled use of real and imaginary (or Euclidean) time, respectively. It can be shown (see Chapter 5)

that the real time evolution of the centroid according to this prescription leads to an accurate representation of the exact quantum time correlation functions [105,110].

In this manner, Lobaugh and Voth [19] have evaluated dynamical quantities such as the mean-square displacement or the time correlation function of atomic velocities, in addition to the equilibrium properties for liquid water using a flexible potential model. In their work, the calculations were carried out using path integral molecular dynamics (PIMD) and the Hamiltonian

$$H = \frac{\mathbf{p}_O^2}{2m_O} + \sum_{k=1}^{P}\left\{\frac{\mathbf{p}_H^{(k)2}}{2m_k'} + \frac{m_H P}{2\hbar^2\beta^2}\left(\mathbf{r}_H^{(k+1)} - \mathbf{r}_H^{(k)}\right)^2 + \frac{1}{P}U\left(\mathbf{r}_H^{(1)},\cdots,\mathbf{r}_H^{(P)};\mathbf{r}_O\right)\right\}, \quad \textbf{(4.53)}$$

where the proton and oxygen coordinates and momenta of the water are $\mathbf{r}_H$, $\mathbf{r}_O$, $\mathbf{p}_H$ and $\mathbf{p}_O$, respectively. This Hamiltonian is the three-dimensional version of Equation 4.26, which implies that the oxygen was treated classically and the hydrogen quantum mechanically. A substantial difference between the work of Lobaugh and Voth [19] and that of by Stern and Berne [15] (in Section 4.2.2) is that the former utilizes two interconnected MD algorithms. The approach taken by Lobaugh and Voth [19] was to divide the real (or centroid) time into many small centroid moves. At each of these small time steps, a separate PIMD calculation is then run to obtain the average centroid force. The latter PIMD calculation is run with constraints on the Cartesian positions of the centroids and without moving the classical degrees of freedom. Typically, a small number of PIMD time steps was necessary to average the centroid forces for each small centroid time step.

A modified flexible version of SPC/F2 [19] was used for the intermolecular interaction between the water molecules. In agreement with other work the quantization of this flexible model led to a liquid system that was somewhat less structured and exhibited less hydrogen bonding than its classical counterpart. Additionally, the calculated quantum time correlation functions were shown to decay faster than the classical ones. For example, the single molecule rotational relaxation times, as well as the collective dielectric relaxation time constant, were smaller for the quantized system, indicating faster dynamics due to nuclear tunneling [19].

4.3. *AB INITIO* PATH INTEGRAL MOLECULAR DYNAMICS

The ideas of Sections 4.1 and 4.2 can be unified. In the context of the Born-Oppenheimer approximation it is possible to treat both the nuclear and electronic degrees of freedom quantum mechanically [95,112,113]. By including the electrons and nuclei explicitly, the partition function for a system can be written as [95]

$$Z = \int_{\mathbf{r}_N(0)=\mathbf{r}_N(\beta\hbar)} \mathcal{D}\mathbf{r}_N(\tau) \int_{\mathbf{r}_e(0)=\mathbf{r}_e(\beta\hbar)} \mathcal{D}\mathbf{r}_e(\tau) \times \exp\left\{-\frac{1}{\hbar}\int_0^{\beta\hbar} d\tau \left[K_N(\dot{\mathbf{r}}_N(\tau)) + K_e(\dot{\mathbf{r}}_e(\tau)) + V_{NN}(\mathbf{r}_N(\tau)) + V_{ee}(\mathbf{r}_e(\tau)) + V_{eN}(\mathbf{r}_e(\tau),\mathbf{r}_N(\tau))\right]\right\}, \quad \textbf{(4.54)}$$

where $\mathbf{r}_N$ and $\mathbf{r}_e$ are multidimensional vectors representing the nuclear and electronic configurations. The symbols K_N , K_e, V_{NN} , V_{ee} and V_{eN} represent the nuclear kinetic energy, the electronic kinetic energy, the nuclear interaction, the electronic interaction and the nuclear-electronic interaction functions, respectively.

It is convenient, however, to define the functional $Z[\mathbf{r}_N(\tau)]$ as

$$Z[\mathbf{r}_N(\tau)] = \int_{\mathbf{r}_e(0)=\mathbf{r}_e(\beta\hbar)} \mathcal{D}\mathbf{r}_e(\tau) \exp\left\{-\frac{1}{\hbar}\int_0^{\beta\hbar} d\tau \left[K_e(\mathbf{r}_e(\tau)) + V_{ee}(\mathbf{r}_e(\tau)) + V_{eN}(\mathbf{r}_e(\tau),\mathbf{r}_N(\tau))\right]\right\}, \tag{4.55}$$

such that the partition function is recast in the form

$$Z = \int_{\mathbf{r}_N(0)=\mathbf{r}_N(\beta\hbar)} \mathcal{D}\mathbf{r}_N(\tau) \exp\left\{-\frac{1}{\hbar}\int_0^{\beta\hbar} d\tau \left[K_N(\mathbf{r}_N(\tau)) + V_{NN}(\mathbf{r}_N(\tau))\right]\right\} Z[\mathbf{r}_N(\tau)]. \tag{4.56}$$

It is interesting to note that $Z[\mathbf{r}_N(\tau)]$ is the so-called influence functional [7], and is identical to the electronic partition function of the system. Assuming that only the electronic ground state, with energy $\varepsilon_0(\mathbf{r}_N)$, is relevant [2,95]

$$Z[\mathbf{r}_N] = \sum_n e^{-\beta\varepsilon_n(\mathbf{r}_N)} \approx e^{-\beta\varepsilon_0(\mathbf{r}_N)}. \tag{4.57}$$

Substitution of Equation 4.57 into Equation 4.56 leads to

$$Z = \int_{\mathbf{r}_N(0)=\mathbf{r}_N(\beta\hbar)} \mathcal{D}\mathbf{r}_N(\tau) \exp\left\{-\frac{1}{\hbar}\int_0^{\beta\hbar} d\tau \left[K_N(\mathbf{r}_N(\tau)) + V_{NN}(\mathbf{r}_N(\tau)) + \varepsilon_0[\mathbf{r}_N(\tau)]\right]\right\}. \tag{4.58}$$

It is easily seen that Equation 4.58 is the generalization of Equation 4.23 for more than one nucleus (where the electronic energy is shown explicitly). Therefore, the partition function above can be written in a discretized form and the path integral can be carried out via molecular dynamics. However, the external potential in Equation 4.58 includes the calculation of the electronic ground state surface energy $\varepsilon_0(\mathbf{r}_N)$. In the discretized

picture this implies that the electronic ground state eigenvalue $\varepsilon_0(\mathbf{r}_N)$ needs to be evaluated at each imaginary time slice i.e. at P different nuclear configurations. Unfortunately, electronic structure calculations are already expensive for a single nuclear configuration (especially when dealing with a system of sufficient size that mimics a liquid or a solid). One positive aspect of this problem is that the P electronic calculations are independent, and as a consequence, can be performed in a parallel fashion [95,112,113].

This ambitious approach was used by Chen and co-workers [114] to study hydrogen bonding in liquid water under ambient conditions. The authors used 64 water molecules in a cubic box and a DFT approach for the *ab initio* calculations of the interatomic interactions. A fictitious electronic mass of 500 a.u. was employed and the path integral was discretized with P=16 beads on the hydrogen atoms. Interestingly, the results from this work indicate that the previously reported (in path integral simulations [12-14]) "softening" of the interaction potential may be at least partially overcome by an increase in the molecular dipole moment that arises, reportedly, when both nuclei and electrons are treated quantum mechanically. However, since no energies were reported, the extent of the suggested cancellation of these effects is unknown, as well as its relationship with the well-known experimental fact that the enthalpy of vaporization of D_2O is about 1.4kJ/mol [115] higher than H_2O.

Finally, it should be clear that, in principle, the centroid molecular dynamics methodology could also be implemented in conjunction with an *ab initio* evaluation of

the electronic structure. The interest in such a method (again) arises because it allows one to extract dynamical information. However, such a calculation has not been carried out due to the tremendous computational effort that a full quantum mechanical treatment entails. This is clearly another reason to develop efficient alternatives to the usual CMD method, one of the principal aims of this thesis.

5. CENTROID DYNAMICS AND THE CMD METHOD

Path integral methods have been a valuable tool for the study of quantum effects in many-body systems. The isomorphism between the canonical distribution of a quantum system in equilibrium and a classical ring of quasi-particles allows the use of the Monte Carlo or molecular dynamics methods, standard tools of classical statistical mechanics, to solve the quantum mechanical problem. This relationship between classical statistical mechanics and quantum mechanics is particularly powerful if one is interested in a quasi-classical description of a quantum system. In such a case, the notion of a path centroid variable [17,18] is an important concept due to both its intuitive physical meaning and the convenience of the mathematical structure of the theory that amounts. This chapter will review the so-called *path centroid perspective* and will establish the applicability and limitations of the CMD method. Section 5.1 presents a careful discussion of the exact formulation of centroid dynamics while Section 5.2 is devoted to the approximations implied by the centroid molecular dynamics method as well as a description of its implementation. For notational simplicity the description in this Chapter refers to a particle in a two-dimensional phase space x-p.

5.1. EXACT FORMULATION OF CENTROID DYNAMICS

From the discussion in Sections 4.2.4 and 4.2.5, it is understood that the centroid variable allows a classical-like calculation of equilibrium quantities in statistical systems. Additionally, it may seem intuitively reasonable that it should also be possible to extract dynamical information from the centroid dynamics as long as the system remains close to

the classical limit. In order to clarify the accuracy of the CMD method for the calculation of equilibrium and dynamical properties, the phase space formulation of the Feynman path centroid density [108] is utilized. The presentation below is based essentially on the work of Jang and Voth [18,110,111]; for an alternaltive approach on centroid dynamics see reference [116].

5.1.1. The centroid density in phase space and the centroid variables

The uncertainty principle makes the concept of phase space somewhat problematic since particles cannot simultaneously have a well-defined position and momentum. However, functions that bear some resemblance to phase space distribution functions have been extensively used in the study of quantum mechanical systems. The most popular of these distribution still seems to be the Wigner distribution function [117], however some other representations exist since convenience is the basic criterion for the choice of a distribution function for a particular problem [118]. Thus, it seems reasonable to start with the quantum-mechanical distribution function represented as [110]

$$\rho_{qm}(x,p) = Tr\left[\frac{\hbar}{2\pi}\int_{-\infty}^{\infty} d\eta \int_{-\infty}^{\infty} d\xi e^{i\xi(\hat{x}-x)+i\eta(\hat{p}-p)-\beta\hat{H}}\right], \tag{5.1}$$

where ξ, η, x and p are scalars and $\hat{x}$, $\hat{p}$ and $\hat{H}$ are the position, momentum and Hamiltonian operators, respectively. Two arguments can be given to rationalize this choice. First, integration over the scalars x and p gives the quantum partition function, i.e.

$$\int dx \int dp \rho_{qm}(x,p) = 2\pi\hbar Tr\left[e^{-\beta\hat{H}}\right] = 2\pi\hbar Z. \tag{5.2}$$

Second, Equation 5.1 is closely related to the Wigner distribution function [110]

$$\rho_w = Tr\left[\frac{\hbar}{2\pi}\int_{-\infty}^{\infty} d\eta \int_{-\infty}^{\infty} d\xi e^{i\xi(\hat{x}-x)+i\eta(\hat{p}-p)} e^{-\beta\hat{H}}\right], \tag{5.3}$$

which has been used quite extensively to study the properties of quantum systems [118]. The initial strategy is then to show that $\rho_{qm}(x,p)$, given in Equation 5.1, is just the centroid density in phase space i.e. $\rho_{qm}(x,p) = \rho_c(x_c,p_c)$. In order to write $\rho_{qm}(x,p)$ in path integral form it is possible to follow the relations 4.5-4.12 analogously.

Assuming that the Hamiltonian operator is simply a sum of the kinetic and potential operators, i.e. $\hat{H} = \hat{T} + \hat{V}$, by application of Trotter's formula [96] we know that

$$e^{i\xi\hat{x}+i\eta\hat{p}-\beta\hat{H}} = \lim_{P\to\infty}\left[e^{-\left(\beta\hat{V}-i\xi\hat{x}\right)/2P} e^{-\left(\beta\hat{T}-i\eta\hat{p}\right)/P} e^{-\left(\beta\hat{V}-i\xi\hat{x}\right)/2P}\right]^P. \tag{5.4}$$

One of the elements in this product can be written as

$$\begin{aligned} & e^{-\left(\beta\hat{V}-i\xi\hat{x}\right)/2P} e^{-\left(\beta\hat{T}-i\eta\hat{p}\right)/P} e^{-\left(\beta\hat{V}-i\xi\hat{x}\right)/2P} \\ &= \int dx_1 \int dp_1 \int dx_2 |x_1\rangle\langle x_1| e^{-\left(\beta\hat{V}-i\xi\hat{x}\right)/2P} |p_1\rangle\langle p_1| e^{-\left(\beta\hat{T}-i\eta\hat{p}\right)/P} e^{-\left(\beta\hat{V}-i\xi\hat{x}\right)/2P} |x_2\rangle\langle x_2| \\ &= \int dx_1 \int dp_1 \int dx_2 |x_1\rangle e^{-\left(\beta V(x_1)-i\xi x_1\right)/2P} e^{-\left(\beta\frac{p_1^2}{2m}-i\eta p_1\right)/P} e^{-\left(\beta V(x_2)-i\xi x_2\right)/2P} \langle x_1|p_1\rangle\langle p_1|x_2\rangle\langle x_2|. \end{aligned} \tag{5.5}$$

Thus, the product in Equation 5.4 becomes

$$e^{i\xi\hat{x}+i\eta\hat{p}-\beta\hat{H}} = \lim_{P\to\infty}\int dx_1\cdots\int dx_{P+1}\cdots\int dp_1\cdots\int dp_P|x_1\rangle$$
$$\times\prod_{k=1}^{P}\left\{e^{-\varepsilon V(x_k)/2+i\xi x_k/2P}e^{-\varepsilon p_k^2/2m+i\eta p_k/P}\right.$$
$$\left.e^{-\varepsilon V(x_{k+1})/2+i\xi x_{k+1}/2P}\langle x_k|p_k\rangle\langle p_k|x_{k+1}\rangle\right\}\langle x_{P+1}|, \tag{5.6}$$

where $\varepsilon = \beta/P$. Introducing the scalars x_c and p_c (as x and p in Equation 5.1) and integrating over ξ and η we have

$$\int d\xi\int d\eta e^{i\xi(\hat{x}-x_c)+i\eta(\hat{p}-p_c)-\beta\hat{H}} = \lim_{P\to\infty}\int dx_1\cdots\int dx_{P+1}\cdots\int dp_1\cdots\int dp_P|x_1\rangle$$
$$\times\int d\xi\int d\eta e^{-i\xi x_c-i\eta p_c}\prod_{k=1}^{P}\left\{e^{-\varepsilon V(x_k)/2+i\xi x_k/2P}e^{-\varepsilon p_k^2/2m+i\eta p_k/P}\right.$$
$$\left.\times e^{-\varepsilon V(x_{k+1})/2+i\xi x_{k+1}/2P}\langle x_k|p_k\rangle\langle p_k|x_{k+1}\rangle\right\}\langle x_{P+1}|$$
$$= \lim_{P\to\infty}\int dx_1\cdots\int dx_{P+1}\cdots\int dp_1\cdots\int dp_P|x_1\rangle$$
$$\times\int d\xi\int d\eta e^{-i\xi x_c-i\eta p_c}e^{i\xi\sum_{k=1}^{P}(x_k+x_{k+1})/2P}e^{i\eta\sum_{k=1}^{P}p_k/P} \tag{5.7}$$
$$\times\prod_{k=1}^{P}\left\{e^{-\varepsilon V(x_k)/2}e^{-\varepsilon p_k^2/2m}e^{-\varepsilon V(x_{k+1})/2}\langle x_k|p_k\rangle\langle p_k|x_{k+1}\rangle\right\}\langle x_{P+1}|$$
$$= 4\pi^2\lim_{P\to\infty}\int dx_1\cdots\int dx_{P+1}\cdots\int dp_1\cdots\int dp_P|x_1\rangle\delta(x_0-x_c)\delta(p_0-p_c)$$
$$\times\prod_{k=1}^{P}\left\{e^{-\varepsilon V(x_k)/2}e^{-\varepsilon p_k^2/2m}e^{-\varepsilon V(x_{k+1})/2}\langle x_k|p_k\rangle\langle p_k|x_{k+1}\rangle\right\}\langle x_{P+1}|,$$

where the relationships

$$\int d\eta\exp\left\{i\eta\left\{\left(\sum_{k=1}^{P}p_k/P\right)-p_c\right\}\right\} = 2\pi\delta(p_0-p_c) \tag{5.8}$$

and

$$\int d\xi \exp\left\{ i\xi \left[\sum_{k=1}^{P} \left(x_k + x_{k+1} \right)/2P - x_c \right] \right\} = 2\pi\delta\left(x_0 - x_c \right), \tag{5.9}$$

have been used together with

$$p_0 = \frac{1}{P}\left(p_1 + p_2 + \cdots + p_P \right) \tag{5.10}$$

and

$$x_0 = \frac{1}{P}\left(\frac{1}{2}x_1 + x_2 + \cdots + x_P + \frac{1}{2}x_{P+1} \right). \tag{5.11}$$

Introducing the product of momentum and position eigenstates (Equation 4.8) we obtain the path integral representation of the quantum distribution function given in Equation 5.1, namely [110]

$$\rho_c\left(x_c, p_c \right) = Tr\left\{ \hat{\varphi}\left(x_c, p_c \right) \right\}, \tag{5.12}$$

where

$$\begin{aligned} \hat{\varphi}\left(x_c, p_c \right) &= \frac{\hbar}{2\pi} \int d\xi \int d\eta e^{i\xi\left(\hat{x} - x_c \right) + i\eta\left(\hat{p} - p_c \right) - \beta\hat{H}} \\ &= \lim_{P\to\infty} \left(\frac{1}{2\pi\hbar} \right)^{P-1} \int dx_1 \cdots \int dx_{P+1} \cdots \int dp_1 \cdots \int dp_P \left| x_1 \right\rangle \delta\left(x_0 - x_c \right) \delta\left(p_0 - p_c \right) \\ &\quad \times \prod_{k=1}^{P} \left\{ e^{-\varepsilon V\left(x_k \right)/2} e^{-\varepsilon p_k^2/2m} e^{-\varepsilon V\left(x_{k+1} \right)/2} e^{ip_k\left(x_k - x_{k+1} \right)/\hbar} \right\} \left\langle x_{P+1} \right| \end{aligned} \tag{5.13}$$

The similarity between Equations 5.13 and 4.9 indicates that the operator $\hat{\varphi}\left(x_c, p_c \right)$ is the centroid constrained Boltzmann operator in phase space.

From Equations 5.2 and 5.12, it immediately follows that the partition function can be written as

$$Z = \iint \frac{dx_c dp_c}{2\pi\hbar} \rho_c\left(x_c, p_c\right). \tag{5.14}$$

Equations 5.12 and 5.13 are, clearly, the phase space equivalent of Equation 4.48. However, the centroid constraints given by equations 5.10 and 5.11 have appeared this time as a natural consequence of the mathematical manipulations rather than by the intuitive arguments given in Section 4.2.5.

Equation 5.13 can be written in a way that is simpler, and more closely related to the discussion in the Sections 4.2.1 and 4.2.5. To achieve this, we need to perform an explicit integration over the momenta. The integration in Equation 5.13 over p_1 is

$$\begin{aligned}\int dp_1 e^{-\varepsilon p_1^2/2m + i\eta p_1/P + i\left(x_k - x_{k+1}\right)p_1/\hbar} &= \left(\frac{2\pi mP}{\beta}\right)^{\frac{1}{2}} e^{-\frac{mP}{2\beta}\left(\frac{\eta}{P} + \frac{x_k - x_{k+1}}{\hbar}\right)^2} \\ &= \left(\frac{2\pi mP}{\beta}\right)^{\frac{1}{2}} e^{-\frac{mP}{2\beta}\left(\frac{\eta^2}{P^2} + \frac{2\eta}{P\hbar}\left(x_k - x_{k+1}\right)\right)} e^{-\frac{mP}{2\beta\hbar^2}\left(x_k - x_{k+1}\right)^2},\end{aligned} \tag{5.15}$$

where Equation 5.8 has been employed to replace the delta function in the momentum. The P integrations over momenta yield

$$\begin{aligned}&\int dp_1 \cdots \int dp_P \prod_{k=1}^{P} \left\{ e^{-\varepsilon p_k^2/2m + i\eta p_k/P + i\left(x_k - x_{k+1}\right)p_k/\hbar} \right\} \\ &\quad = \left(\frac{2\pi mP}{\beta}\right)^{\frac{P}{2}} e^{-\frac{m}{2\beta}\left(\eta^2 + \frac{2\eta}{\hbar}\left(x_1 - x_{P+1}\right)\right)} e^{-\frac{mP}{2\beta\hbar^2}\sum_{k=1}^{P}\left(x_k - x_{k+1}\right)^2}.\end{aligned} \tag{5.16}$$

Integrating Equation 5.16 over η yields

$$\int d\eta e^{-\frac{m}{2\beta}\left(\eta^2+\frac{2\eta}{\hbar}(x_1-x_{P+1})\right)+i\eta p_c}=\left(\frac{2\pi\beta}{m}\right)^{\frac{1}{2}}e^{-\frac{\beta}{2m}\left[p_c-\frac{im}{\beta\hbar}(x_1-x_{P+1})\right]^2}. \tag{5.17}$$

Combining Equations 5.13, 5.16 and 5.17 we finally obtain [110]

$$\langle x'|\hat{\varphi}(x_c,p_c)|x''\rangle=e^{-\frac{\beta}{2m}\left[p_c-\frac{im}{\beta\hbar}(x'-x'')\right]^2}\langle x'|\hat{\varphi}(x_c)|x''\rangle, \tag{5.18}$$

where

$$\begin{aligned}\langle x'|\hat{\varphi}(x_c)|x''\rangle=&\left(\frac{2\pi\hbar^2\beta}{m}\right)^{\frac{1}{2}}\lim_{P\to\infty}\left(\frac{mP}{2\pi\hbar^2\beta}\right)^{\frac{P}{2}}\int dx_2\cdots\int dx_P\delta(x_0-x_c)\\&\times\exp\left\{-\frac{mP}{2\beta\hbar^2}\left[(x'-x_2)^2+\cdots+(x_P-x'')^2\right]\right\}\\&\times\exp\left\{-\frac{\beta}{P}\left[\frac{1}{2}V(x')+V(x_2)+\cdots+V(x_P)+\frac{1}{2}V(x'')\right]\right\}\\=&\left(\frac{2\pi\hbar^2\beta}{m}\right)^{\frac{1}{2}}\int_{x(0)=x'}^{x(\beta\hbar)=x''}\mathcal{D}x(\tau)\delta(x_c-x_0)\exp\left\{-S[x(\tau)]/\hbar\right\},\end{aligned} \tag{5.19}$$

in which the limit $P\to\infty$ has been taken in the last equality. In view of Equation 5.12, we actually have

$$\rho_c(x_c,p_c)=e^{-\frac{\beta}{2m}p_c^2}\rho_c(x_c), \tag{5.20}$$

where

$$\rho_c(x_c) = \left(\frac{2\pi\hbar^2\beta}{m}\right)^{\frac{1}{2}} \int_{x(0)=x(\beta\hbar)} \mathcal{D}x(\tau)\delta(x_c - x_0)\exp\left\{-S[x(\tau)]/\hbar\right\}. \qquad \textbf{(5.21)}$$

The result in Equations 5.20 and 5.21 exhibits the desired classical form, and coincides with the analysis provided by Feynman and discussed in Section 4.2.5. In fact, Equation 5.21 is identical to Equation 4.48. Hence, it becomes clear that the quantum mechanical distribution in Equation 5.1 is the centroid density; in other words, the Boltzmann operator can be *expressed in centroid form* through Equations 5.1 or Equations 5.20 and 5.21.

How are other operators represented *in centroid form*? Interestingly, other operators are expressed in centroid form through a different procedure than the one that has been used for the Boltzmann operator. This is in contrast to the case of the Wigner prescription where all the operators are manipulated in the same fashion. However, some differences are expected since the Wigner transform of the Boltzmann operator involves a product with the Boltzmann operator itself (see Equation 5.3) whereas this is not the case within the centroid approach (see Equation 5.1). On the other hand, the Wigner transform of the Boltzmann operator is not always positive definite (which has led to the use of the Husimi functions [118,119]), but the centroid density is, and in that sense is very much classical-like. It has been argued [110] that, the property of positivity of the centroid distribution (in contrast with the Wigner distribution) suggests that some of the quantum mechanical information has been lost, and that is why auxiliary quantities are needed to recover full information.

It seems reasonable at this point to define the operator $\hat{\delta}_c(x_c,p_c)$ in the following way [110]

$$\hat{\delta}_c(x_c,p_c) \equiv \hat{\varphi}(x_c,p_c)/\rho_c(x_c,p_c), \tag{5.22}$$

since this definition allows us to write

$$\frac{1}{Z}e^{-\beta\hat{H}} = \iint \frac{dx_c dp_c}{2\pi\hbar}\frac{\rho_c(x_c,p_c)}{Z}\hat{\delta}_c(x_c,p_c). \tag{5.23}$$

This relationship means that the canonical ensemble can be considered to be an incoherent mixture of the operator $\hat{\delta}_c(x_c,p_c)$ with different position and momentum centroids, having a probability density given by $\rho_c(x_c,p_c)/Z$. Examining Equations 5.18, 5.19 and 5.22 we note that $\hat{\delta}_c(x_c,p_c)$ is hermitian, and that its diagonal elements in the coordinate representation are positive. However, positive definiteness is not guaranteed in general [110], which is why this operator is known in the literature as a "quasi-density operator" (QDO) [110].

With the interpretation given above for the canonical ensemble, it becomes possible to establish a correspondence between the operator $\hat{A}$ and the centroid variable A_c,

$$A_c = Tr\left\{\hat{\delta}_c(x_c,p_c)\hat{A}\right\}, \tag{5.24}$$

utilizing the identities

$$\langle A_c \rangle_c = \frac{1}{Z}\iint \frac{dx_c dp_c}{2\pi\hbar}\rho_c(x_c,p_c)A_c = \frac{1}{Z}Tr\left\{\iint \frac{dx_c dp_c}{2\pi\hbar}\rho_c(x_c,p_c)\hat{\delta}_c(x_c,p_c)\hat{A}\right\} = \frac{1}{Z}Tr\left\{e^{-\beta\hat{H}}\hat{A}\right\} = \langle A \rangle. \tag{5.25}$$

Thus, the centroid average of A_c is identical to the canonical average of A. These definitions allow us to establish a strategy to calculate equilibrium averages in the context of the centroid constrained representation of quantum statistical mechanics. Hence, the position and momentum operators yield the corresponding variables [110]

$$x_c = Tr\left\{\hat{\delta}_c(x_c,p_c)\hat{x}\right\} \tag{5.26}$$

and

$$p_c = Tr\left\{\hat{\delta}_c(x_c,p_c)\hat{p}\right\}, \tag{5.27}$$

where it is clear that the position and momentum centroids are the average position and momentum of the state represented by $\hat{\delta}_c(x_c,p_c)$.

The centroid force is also of crucial importance. In order to define the centroid force, it is first noted that if one changes the path variable in Equation 5.19 to $y(\tau) = x(\tau) - x_c$, it becomes

$$\rho_c(x_c) = C\int_{y(0)=y(\beta\hbar)} \mathcal{D}y(\tau)\delta\left(\frac{1}{\beta\hbar}\int_0^{\beta\hbar} y(\tau)d\tau\right)e^{-S[y(\tau)+x_c]/\hbar}, \tag{5.28}$$

where $x_0 - x_c = \frac{1}{\beta\hbar}\int_0^{\beta\hbar} y(\tau)d\tau$, $\mathcal{D}x(\tau) = \mathcal{D}y(\tau)$ and C is a short notation for the constant.

Further,

$$\begin{aligned}\frac{d}{dx_c}S[y(\tau)+x_c] &= \frac{d}{dx_c}\left\{\int_0^{\beta\hbar}\frac{m}{2}\dot{y}(\tau)d\tau + \int_0^{\beta\hbar}V[y(\tau)+x_c]d\tau\right\} \\ &= \int_0^{\beta\hbar}\frac{d}{dx_c}V[y(\tau)+x_c]d\tau = -\int_0^{\beta\hbar}F[y(\tau)+x_c]d\tau,\end{aligned} \tag{5.29}$$

where Equation 4.24 has been used. The derivative for the centroid density is then

$$\begin{aligned}\frac{d}{dx_c}\rho_c(x_c) &= C\int_{y(0)=y(\beta\hbar)}\mathcal{D}y(\tau)\delta\left(\frac{1}{\beta\hbar}\int_{0-}^{\beta\hbar}y(\tau)d\tau\right) \\ &\qquad \times\frac{d}{dx_c}\left(-\frac{S[y(\tau)+x_c]}{\hbar}\right)\exp\left\{-S[y(\tau)+x_c]/\hbar\right\} \\ &= C\int_{y(0)=y(\beta\hbar)}\mathcal{D}y(\tau)\delta\left(\frac{1}{\beta\hbar}\int_{0-}^{\beta\hbar}y(\tau)d\tau\right) \\ &\qquad \times\left(\frac{1}{\hbar}\int_0^{\beta\hbar}F[y(\tau)+x_c]d\tau\right)\exp\left\{-S[y(\tau)+x_c]/\hbar\right\},\end{aligned} \tag{5.30}$$

which is equivalent to

$$\frac{d}{dx_c}\rho_c(x_c) = C\int_{x(0)=x(\beta\hbar)}\mathcal{D}x(\tau)\delta(x_0-x_c)\left(\frac{1}{\hbar}\int_0^{\beta\hbar}F[x(\tau)]d\tau\right)e^{-S[x(\tau)]/\hbar}. \tag{5.31}$$

Accordingly, using Equations 5.19, 5.22 and 5.31 it is possible to obtain an expression for the centroid force

$$F_c = Tr\left\{\hat{\delta}_c(x_c,p_c)F(\hat{x})\right\} = \frac{1}{\rho_c(x_c)}Tr\left\{\hat{\varphi}(x_c)F(\hat{x})\right\}$$
$$= \frac{1}{\rho_c(x_c)}C\int_{x(0)=x(\beta\hbar)}\mathcal{D}x(\tau)\delta(x_0-x_c)\left(\frac{1}{\beta\hbar}\int_0^{\beta\hbar}F[x(\tau)]d\tau\right)\exp\left\{-S[x(\tau)]/\hbar\right\} \quad \textbf{(5.32)}$$
$$= \frac{1}{\beta}\frac{\frac{d}{dx_c}\rho_c(x_c)}{\rho_c(x_c)} = \frac{1}{\beta}\frac{d}{dx_c}\ln\left\{\rho_c(x_c)\right\}.$$

Defining a centroid potential of mean force as

$$V_{cm}(x_c) = -\frac{1}{\beta}\ln\left\{\rho_c(x_c)\right\}, \quad \textbf{(5.33)}$$

the centroid force of Equation 5.32 can be written as

$$F_c(x_c) = -\frac{d}{dx_c}V_{cm}(x_c). \quad \textbf{(5.34)}$$

Clearly, $V_{cm}(x_c)$ is the centroid effective potential defined in the Section 4.2.5 (of Equation 4.49). Similarly, it is possible to define the centroid Hamiltonian as the sum of the centroid kinetic energy and the centroid potential energy [110], ie.

$$H_c = T_c + V_c. \quad \textbf{(5.35)}$$

It is interesting to note that $V_{cm}(x_c)$ is in general different from V_c.

5.1.2. The time evolution of the centroid variables

The next step in the present discussion is the time evolution of the centroid variables introduced in the previous section. Using the Heisenberg representation of the

position operator, i.e. $\hat{x}(t) = e^{i\hat{H}t/\hbar}\hat{x}e^{-i\hat{H}t/\hbar}$, and taking into account Equation 5.24 we can write that the average centroid position is given by [110]

$$\langle x_c(t)\rangle = \langle \hat{x}\rangle = \iint \frac{dx_c dp_c}{2\pi\hbar}\frac{\rho_c(x_c,p_c)}{Z} Tr\left\{\hat{\delta}(x_c,p_c)e^{i\hat{H}t/\hbar}\hat{x}e^{-i\hat{H}t/\hbar}\right\} \tag{5.36}$$

or

$$\langle x_c(t)\rangle = \langle \hat{x}\rangle = \iint \frac{dx_c dp_c}{2\pi\hbar}\frac{\rho_c(x_c,p_c)}{Z} Tr\left\{\hat{\delta}(t;x_c,p_c)\hat{x}\right\}, \tag{5.37}$$

where

$$\hat{\delta}(t;x_c,p_c) = e^{-i\hat{H}t/\hbar}\hat{\delta}(x_c,p_c)e^{i\hat{H}t/\hbar}. \tag{5.38}$$

Therefore, the time evolution of the centroid variable can be expressed as

$$x_c(t) = Tr\left\{\hat{\delta}(t;x_c,p_c)\hat{x}\right\}, \tag{5.39}$$

which transforms Equation 5.37 into [110]

$$\langle x_c(t)\rangle = \langle \hat{x}\rangle = \iint \frac{dx_c dp_c}{2\pi\hbar}\frac{\rho_c(x_c,p_c)}{Z} x_c(t). \tag{5.40}$$

This result means that although the centroid variables evolve in time (see Equation 5.39), when this trajectory is averaged according to the centroid distribution the stationary canonical average is recovered. It will be seen later that these centroid trajectories contain information on the dynamical spontaneous fluctuations of the

ensemble, but before we get into the calculation of quantum time correlation functions, it is interesting to look at the time evolution of some other centroid variables.

From Equation 5.38, one knows that the time dependence of the QDO is governed by the quantum Liouville equation [110]

$$\frac{d}{dt}\hat{\delta}_c(t;x_c,p_c) = -\frac{i}{\hbar}\left[\hat{H}',\hat{\delta}_c(t;x_c,p_c)\right], \tag{5.41}$$

where the time evolution is governed by a time independent Hamiltonian $\hat{H}'$, which in general may be different from $\hat{H}$. Thus, for a general centroid variable without explicit time dependence we have

$$\frac{d}{dt}A_c(t) = Tr\left\{\frac{d}{dt}\hat{\delta}_c(t;x_c,p_c)\hat{A}\right\} = \frac{i}{\hbar}Tr\left\{\hat{\delta}_c(t;x_c,p_c)\left[\hat{H}',\hat{A}\right]\right\}. \tag{5.42}$$

Two special cases of Equation 5.42 are of interest [110], ie.

$$\frac{dx_c(t)}{dt} = \frac{p_c(t)}{m} \tag{5.43}$$

and

$$\frac{dp_c(t)}{dt} = F_c(t) = Tr\left\{\hat{\delta}(t;x_c,p_c)F(\hat{x})\right\}. \tag{5.44}$$

This result is remarkable. A comparison with Equations 2.18 and 2.19 reveals the classical-like appearance of these formulas, which can be interpreted as the centroid version of Ehrenfest's theorem [120]. It is important to note, however, that the centroid

force is not a function of the position centroid at time t only (as can be see from the second equality of Equation 5.44).

An additional significant result is obtained by applying Equation 5.42 to the time dependent centroid Hamiltonian $H_c(t) = Tr\left[\hat{\delta}_c(t;x_c,p_c)\hat{H}'\right]$

$$H_c(0) = H_c(t). \tag{5.45}$$

In the classical limit, the centroid position and momentum becomes the classical position and momentum of the particle and the centroid Hamiltonian goes to the the classical Hamiltonian [110].

As the last step, it is important to show that the centroid time correlation functions can be related analytically to the Kubo transformed quantum time correlation functions [121]. This connection is relevant because the usual quantum time correlation function, $C_{AB}(t) = \left\langle \hat{A}(t)\hat{B}(0)\right\rangle$, is related to the Kubo transformed quantum time correlation function, $\left\langle \hat{B}\hat{A}(t)\right\rangle^{Kubo}$, in frequency space by [105,107,121],

$$I(w) = (\hbar w/2)\left[\coth(\hbar w/2) + 1\right] I^{Kubo}(w), \tag{5.46}$$

where $I(w)$ and $I^{Kubo}(w)$ are the Fourier transforms of the quantum and Kubo transformed correlation functions, respectively.

Let's see then, how the centroid time correlation function is related to the Kubo transform quantum time correlation function. (The proof presented below was given by

N. Blinov and P. N. Roy [122]). It is convenient to begin with the definition of the Kubo transformed quantum time correlation function [121],

$$\left\langle \hat{B}\hat{A}(t)\right\rangle^{Kubo} \equiv \frac{1}{Z}\frac{1}{\beta\hbar}\int_0^{\beta\hbar} Tr\left\{e^{-(\beta-u)\hat{H}}\hat{B}e^{-u\hat{H}}e^{i\hat{H}t}\hat{A}e^{-i\hat{H}t}\right\}du. \tag{5.47}$$

Using [123,124]

$$\frac{\partial}{\partial\lambda}e^{-\beta\hat{H}'} = -\int_0^{\beta} e^{-(\beta-u)\hat{H}'}\frac{\partial\hat{H}'}{\partial\lambda}e^{-u\hat{H}'}du \tag{5.48}$$

for the derivative of the exponential of an arbitrary operator with respect to a parameter and applying it to the operator $\hat{H}' = \hat{H} - i(\lambda/\beta)\hat{B}$, we obtain

$$\left(\frac{1}{i}\frac{\partial}{\partial\lambda}e^{-\beta\hat{H}+i\lambda\hat{B}}\right)\Bigg|_{\lambda=0} = \frac{1}{\beta\hbar}\int_0^{\beta\hbar} e^{-(\beta-u)\hat{H}}\hat{B}e^{-u\hat{H}}du. \tag{5.49}$$

Taking into account that (according to Equations 5.1 and 5.2) [122]

$$e^{-\beta\hat{H}'} = \iint\frac{dx_c dp_c}{2\pi\hbar}\iint d\xi d\eta e^{i\xi(\hat{x}-x_c)+i\eta(\hat{p}-p_c)-\beta\hat{H}'}, \tag{5.50}$$

Equation 5.47 can be written as

$$\left\langle \hat{B}\hat{A}(t)\right\rangle^{Kubo} = \frac{1}{Z}\iint\frac{dx_c dp_c}{2\pi\hbar}Tr\left\{\left(\frac{1}{i}\frac{\partial}{\partial\lambda}\iint d\xi d\eta e^{i\xi(\hat{x}-x_c)+i\eta(\hat{p}-p_c)-\beta\hat{H}+i\lambda\hat{B}}\right)\Bigg|_{\lambda=0} e^{i\hat{H}t}\hat{A}e^{-i\hat{H}t}\right\}. \tag{5.51}$$

For the particular case of a linear operator $\hat{B} = a_1\hat{x} + a_2\hat{p}$, where a_1 and a_2 are scalars, we obtain [122]

$$\begin{aligned}\left\langle \hat{B}\hat{A}(t)\right\rangle^{Kubo} &= \frac{1}{Z}\int\int\frac{dx_c dp_c}{2\pi\hbar}\left(\frac{1}{i}\frac{\partial}{\partial\lambda}e^{i\lambda B_c}\right)\Bigg|_{\lambda=0} \\ &\quad\times Tr\left\{\int\int d\xi d\eta e^{i\xi(\hat{x}-x_c)+i\eta(\hat{p}-p_c)-\beta\hat{H}}e^{i\hat{H}t}\hat{A}e^{-i\hat{H}t}\right\} \\ &= \frac{1}{Z}\int\int\frac{dx_c dp_c}{2\pi\hbar}\rho_c(x_c,p_c)B_c Tr\left\{\hat{\delta}(t;x_c,p_c)e^{i\hat{H}t}\hat{A}e^{-i\hat{H}t}\right\} \\ &= \frac{1}{Z}\int\int\frac{dx_c dp_c}{2\pi\hbar}\rho_c(x_c,p_c)B_c A_c(t).\end{aligned} \tag{5.52}$$

This result proves that the quantum time correlation function can be obtained in a classical-like fashion by following the time evolution of the centroid variables. The extension of Equation 5.52 to non-linear operators $\hat{B}$ has also been accomplished in reference [125], however, it should be noted that in the case of diffusion coefficients, relaxation times and certain other observables this result is sufficient.

5.2. THE CENTROID MOLECULAR DYNAMICS METHOD (CMD)

It is important to recognize that the relationships presented thus far, in Sections 5.1.1 and 5.1.2, are the exact result of analytical manipulation. In Section 5.1 it has been shown that the canonical ensemble can be expressed by a set of initial positions and momenta centroids sampled according to the equilibrium phase space centroid distribution function. The determination of this equilibrium centroid distribution function is not difficult, however, the exact quantum dynamics of the centroid variables requires the solution of the quantum Liouville equation (Equation 5.41). Therefore, in the case of many-body systems approximate methods are necessary. In this section, the CMD approximation is presented. The discussion focuses first on the motivation and

justification of the CMD method and it is followed by an analysis of the CMD implementation.

5.2.1. The CMD approximation

It is clear from Section 5.1 that the essential element in the centroid formalism, including the dynamical evolution of the centroid variables, is the QDO. Thus, the CMD method relies on the following approximation to the time evolution of the QDO [111],

$$\hat{\delta}_c(t;x_c,p_c) \approx \hat{\delta}_c(x_c(t),p_c(t)), \tag{5.53}$$

where the calculation of the phase space trajectories, $x_c(t)$ and $p_c(t)$, is carried out according to Equations 5.43 and 5.44. Utilizing Equations 5.20 and 5.32, this approximation implies that $F_c(t)$ is only a function of the centroid position, $x_c(t)$. Equations 5.43 and 5.44 then take a closed form [111], ie.

$$m\dot{x}_c = p_c(t) \approx Tr\left\{\hat{\delta}(x_c(t),p_c(t))\hat{p}\right\} \tag{5.54}$$

and

$$\dot{p}_c \approx F_{CMD}(t) \equiv Tr\left\{\hat{\delta}(x_c(t),p_c(t))\hat{F}\right\} = F_c(x_c(t)). \tag{5.55}$$

This last equation indicates that the approximate centroid force is determined by the instantaneous centroid position with a functional form identical to the one at zero time. Since the zero-time centroid force is the negative gradient of the centroid potential of mean force (see Equation 5.32), the CMD potential can be defined to be [111]

$$V_{CMD} = V_{cm}(x_c) = -\frac{1}{\beta}\ln\{\rho_c(x_c)\}. \tag{5.56}$$

Thus, the CMD approximation indicates a classical time evolution of the phase space centroids on the quantum centroid potential of mean force, V_{CMD}. This approximation, originally proposed on an quasi-intuitive level (see reference [18,105]), is exact in the harmonic, classical and free particle limits (ie. Equation 5.53 becomes an identity) [110,111].

There are two general and notable cases where the CMD approximation is reasonable. First, when the fluctuations about the centroid are independent of the centroid location (like in the harmonic oscillator where the CMD approximation is known to be exact [110]). In fact, in any system in condensed phase where linear response theory is a good approximation CMD would be applicable (since only when the quantum fluctuations about the centroid are independent of its motion the response is linear) [110]. The second case is when the system exhibits strong regression behaviour because the form of the QDO remains close to its form at t=0 as the particles (centroids) move [111]. For example, when the system approaches the classical limit the QDO "shrinks" to zero and it cannot deviate from its t=0 value. Therefore, systems where the CMD method is a good approximation are those reasonably close to the classical limit and where linear response theory is a valid approximation.

An important property of CMD is that, if the system is ergodic, the method will generate exact equilibrium averages [111], i.e.,

$$\lim_{\tau\to\infty}\frac{1}{\tau}\int_0^{\tau}dtA_c(t)=\langle A\rangle, \tag{5.57}$$

where

$$A_c(t)=Tr\left\{\hat{\delta}_c(x_c(t),x_c(t))\hat{A}\right\}. \tag{5.58}$$

This property can be easily verifed from Equations 2.17 and 5.25 and the fact that $\hat{\delta}_c(x_c(0),p_c(0))=\hat{\delta}_c(x_c,p_c)$.

It is interesting to note that, although the exact time dependent centroid Hamiltonian is a constant of motion according to Equation 5.45, the CMD method, in general, does not conserve this quantity. This has been shown in reference [111] and it is a point of departure for improvement of the CMD method, or the design of alternative approaches within the centroid framework.

5.2.2. The CMD implementation

CMD resembles classical MD in many aspects, and this similarity (which is particularly useful for present purposes) is better seen in the discretized picture. In the discretized picture the continuous path is approximated by P beads, and this discretization parameter is chosen such that the calculation is sufficiently well-converged to the $P\to\infty$ limiting result. The Hamiltonian for a discretized quantum particle can be written as (see Equations 4.15 and 4.20) [9]

$$H = \sum_{k=1}^{P}\left(\frac{p_k^2}{2m_k'} + \frac{mP}{2\hbar^2\beta^2}(x_k - x_{k+1})^2 + \frac{1}{P}V(x_k)\right), \tag{5.59}$$

where p_k and x_k are the momenta and positions of the beads. The kinetic term in Equation 5.59 is completely arbitrary (arbitrary moments and masses) and allows one to define a Hamiltonian with which to carry out the path integral evaluation via a molecular dynamics simulation. The second term in the Hamiltonian is the potential due to nearest-neighbor harmonic coupling between beads that arises from the free particle part of the density matrix (see Section 4.2). The last term is the interaction felt by each bead due to the external potential, where in condensed phase simulations this contribution is usually the intermolecular interaction. In writing Equation 5.58 we have assumed we have only positional coordinates and translational motion.

In the discretized path integral picture (i.e. for finite P), the path centroid variable is identical to the center of mass of the isomorphic polymer of classical quasiparticles (or beads) such that (see Equation 5.11) [17]

$$x_0 = \frac{1}{P}\sum_{k=1}^{P} x_k . \tag{5.60}$$

Thus, a constraint is a necessary ingredient of the dynamics defined by the Hamiltonian in Equation 5.59. A molecular dynamics algorithm designed to carry out this centroid-constrained path integral calculation can be described as follows. The total force acting on the bead k, F_k, can be expressed as $F_k = F_q + F_{cl}$, where F_q and F_{cl} are the forces

associated with the quantum and intermolecular potentials identified in Equation 5.59, respectively. Furthermore, CMD defines the force acting on the centroid as

$$F_c = \frac{1}{P}\sum_{k=1}^{P} F_k . \tag{5.61}$$

It is then this force that must be averaged over the path fluctuations (i.e. in imaginary time). To obtain the force acting on the beads (this is the force that will govern the motion of the beads relative to the centroid) it is necessary to subtract the centroid force from the total force acting on each bead:

$$F_k^{bead} = F_k - F_c . \tag{5.62}$$

Thus, it becomes clear that this formulation of CMD is equivalent to requiring

$$\sum_{k=1}^{P} F_k^{bead} = 0 . \tag{5.63}$$

Obviously this condition will conserve the total linear momentum of the P beads, and if this sum is set to zero as an initial condition, i.e.

$$\sum_{k=1}^{P} p_k = 0 , \tag{5.64}$$

the centroid or "beads' center of mass" will be a conserved quantity in the dynamics. The use of thermostats on the beads, however, leads to a slightly different form of Equation 5.64. It turns out that this interpretation of the implementation of the CMD method will

be very helpful in applying this method in the context of rotational motion, which is the main goal of the next chapter.

6. THE RIGID BODY-CMD METHOD

Path integral methods have been successfully used in the simulation of water, as has been pointed out in Section 4.2. A variety of techniques in this context have been applied to calculate equilibrium and dynamical properties of liquid water and of ice, including the rigid body approximation (see Section 4.2.3) and the centroid molecular dynamics method for flexible molecular models (see Section 4.2.5).

This chapter develops and discusses an approach that allows the implementation of the CMD method for treating explicitly the rotational uncertainty in the motion of a rigid body. This methodology, called *rigid body-centroid molecular dynamics*, is applicable to the 3-dimensional rotation of any arbitrary rigid object and, consequently, can be used to simulate condensed phase systems close to the classical limit (i.e at relatively high temperature). Section 6.1 provides the torques acting between the molecular beads according to the discretized picture of the path integral formalism of quantum statistical mechanics. In Section 6.2 the implementation of *the rigid body-CMD* method is described in detail; in addition, the definition of the orientational centroid and some subtle issues associated to its conservation are also addressed. Finally, in Section 6.3, the successful application of this technique in the simulation of a simple molecular (water) system is demonstrated.

6.1. TORQUES IN QUATERNION FORM

This section starts with a simple and straightforward derivation of the classical rotational equations of motion in quaternion form [126]. The development below

stresses the simplicity of the quaternion approach to rotational motion, and in particular, allows us to specify the structure of the torques in quaternion form. The Appendix reviews some of the most important mathematical properties of quaternions and their relation to rotation operators, as well as the notation. Once a general equation for the torques is obtained a specific expression for the torque acting on the beads is determined.

Let us consider the rotational motion of a rigid body. In this case, the Lagrangian becomes [128]

$$\mathcal{L} = K - V = \frac{1}{2}\sum_{i=1}^{3} I_i w_i^2 - V(\Omega), \tag{6.1}$$

where K is the rotational kinetic energy and $V(\Omega)$ is the component of the interaction potential, which depends only on the orientation of the rigid body, Ω. If we choose the quaternion parameters as the generalized coordinates, the Lagrange equation for the quaternion coordinate q_j is

$$\frac{\partial \mathcal{L}}{\partial q_j} - \frac{d}{dt}\frac{\partial \mathcal{L}}{\partial \dot{q}_j} = 0, \tag{6.2}$$

which can be expressed as

$$\sum_{i=1}^{3} \frac{\partial K}{\partial w_i}\cdot\frac{\partial w_i}{\partial q_j} - \frac{\partial V}{\partial q_j} - \frac{d}{dt}\left(\sum_{i=1}^{3} \frac{\partial K}{\partial w_i}\cdot\frac{\partial w_i}{\partial \dot{q}_j} - \frac{\partial V}{\partial \dot{q}_j}\right) = 0, \tag{6.3}$$

where w_i is a component of angular velocity and the sum is over the components x, y, z and j=0,1,2,3 (see Appendix). Since the potential energy $V(\Omega)$ only depends on the

object's orientation and not on any "velocity", i.e. $\left(\partial V / \partial \dot{q}_j\right) = 0$, Equation 6.3 reduces to

$$\sum_{i=1}^{3} \frac{\partial K}{\partial w_i} \cdot \frac{\partial w_i}{\partial q_j} - \frac{d}{dt}\left(\sum_{i=1}^{3} \frac{\partial K}{\partial w_i} \cdot \frac{\partial w_i}{\partial \dot{q}_j}\right) = \frac{\partial V}{\partial q_j}. \tag{6.4}$$

Now, the principal angular velocities are related to the time derivatives of the quaternions by [129] (see Appendix for details of its derivation)

$$\begin{bmatrix} w_1 \\ w_2 \\ w_3 \\ 0 \end{bmatrix} = 2 \cdot \begin{bmatrix} -q_3 & q_0 & q_2 & -q_1 \\ -q_0 & -q_3 & q_1 & q_2 \\ q_1 & -q_2 & q_0 & -q_3 \\ q_2 & q_1 & q_3 & q_0 \end{bmatrix} \cdot \begin{bmatrix} \dot{q}_2 \\ \dot{q}_1 \\ \dot{q}_3 \\ \dot{q}_0 \end{bmatrix} = 2 \cdot \Xi \cdot \dot{\bar{q}} = \hat{w}. \tag{6.5}$$

If we differentiate the components of $\hat{w} = 0 + \mathbf{w}$ in Equation 6.5 with respect to q_j and $\dot{q}_j$ we have

$$\left\{ \begin{array}{l} \frac{\partial w_1}{\partial q_0} = 2\dot{q}_1 \\ \frac{\partial w_2}{\partial q_0} = -2\dot{q}_2 \\ \frac{\partial w_3}{\partial q_0} = 2\dot{q}_3 \end{array} \right\} \quad \left\{ \begin{array}{l} \frac{\partial w_1}{\partial q_1} = -2\dot{q}_0 \\ \frac{\partial w_2}{\partial q_1} = 2\dot{q}_3 \\ \frac{\partial w_3}{\partial q_1} = 2\dot{q}_2 \end{array} \right\} \quad \left\{ \begin{array}{l} \frac{\partial w_1}{\partial q_2} = 2\dot{q}_3 \\ \frac{\partial w_2}{\partial q_2} = 2\dot{q}_0 \\ \frac{\partial w_3}{\partial q_2} = -2\dot{q}_1 \end{array} \right\} \quad \left\{ \begin{array}{l} \frac{\partial w_1}{\partial q_3} = -2\dot{q}_2 \\ \frac{\partial w_2}{\partial q_3} = -2\dot{q}_1 \\ \frac{\partial w_3}{\partial q_3} = -2\dot{q}_0 \end{array} \right\} \tag{6.6}$$

and

$$\left\{ \begin{array}{l} \frac{\partial w_1}{\partial \dot{q}_0} = -2q_1 \\ \frac{\partial w_2}{\partial \dot{q}_0} = 2q_2 \\ \frac{\partial w_3}{\partial \dot{q}_0} = -2q_3 \end{array} \right\} \quad \left\{ \begin{array}{l} \frac{\partial w_1}{\partial \dot{q}_1} = 2q_0 \\ \frac{\partial w_2}{\partial \dot{q}_1} = -2q_3 \\ \frac{\partial w_3}{\partial \dot{q}_1} = -2q_2 \end{array} \right\} \quad \left\{ \begin{array}{l} \frac{\partial w_1}{\partial \dot{q}_2} = -2q_3 \\ \frac{\partial w_2}{\partial \dot{q}_2} = -2q_0 \\ \frac{\partial w_3}{\partial \dot{q}_2} = 2q_1 \end{array} \right\} \quad \left\{ \begin{array}{l} \frac{\partial w_1}{\partial \dot{q}_3} = 2q_2 \\ \frac{\partial w_2}{\partial \dot{q}_3} = 2q_1 \\ \frac{\partial w_3}{\partial \dot{q}_3} = 2q_0 \end{array} \right\}. \tag{6.7}$$

Then by substituting Equations 6.6 and 6.7 into Equation 6.4 and using $\frac{\partial K}{\partial w_i} = I_i w_i = L_i$ for each quaternion parameter q_j, we can write the compact form

$$4 \cdot \begin{bmatrix} \dot{q}_1 & -\dot{q}_2 & \dot{q}_3 & \pm\dot{q}_0 \\ -\dot{q}_0 & \dot{q}_3 & \dot{q}_2 & \pm\dot{q}_1 \\ \dot{q}_3 & \dot{q}_0 & -\dot{q}_1 & \pm\dot{q}_2 \\ -\dot{q}_2 & -\dot{q}_1 & -\dot{q}_0 & \pm\dot{q}_3 \end{bmatrix} \cdot \begin{bmatrix} L_1 \\ L_2 \\ L_3 \\ 0 \end{bmatrix} + 2 \cdot \begin{bmatrix} q_1 & -q_2 & q_3 & \pm q_0 \\ -q_0 & q_3 & q_2 & \pm q_1 \\ q_3 & q_0 & -q_1 & \pm q_2 \\ -q_2 & -q_1 & -q_0 & \pm q_3 \end{bmatrix} \cdot \begin{bmatrix} \dot{L}_1 \\ \dot{L}_2 \\ \dot{L}_3 \\ 0 \end{bmatrix} = \begin{bmatrix} \frac{\partial V}{\partial q_0} \\ \frac{\partial V}{\partial q_1} \\ \frac{\partial V}{\partial q_2} \\ \frac{\partial V}{\partial q_3} \end{bmatrix}, \quad \textbf{(6.8)}$$

where L_i is clearly a component of the angular momentum vector, **L**. From Equation 6.8 it is easy to obtain the equations of motion, which can be expressed in quaternion form as

$$\dot{\hat{L}} = \frac{1}{2} \cdot \Xi \cdot \hat{N} - 2 \cdot \Xi \cdot \dot{\Xi}^T \cdot \hat{L}, \quad \textbf{(6.9)}$$

where

$$\dot{\hat{L}} = \begin{bmatrix} \dot{L}_1 \\ \dot{L}_2 \\ \dot{L}_3 \\ 0 \end{bmatrix}, \quad \hat{N} = \begin{bmatrix} -\frac{\partial V}{\partial q_2} \\ -\frac{\partial V}{\partial q_1} \\ -\frac{\partial V}{\partial q_3} \\ -\frac{\partial V}{\partial q_0} \end{bmatrix}, \quad \hat{L} = \begin{bmatrix} L_1 \\ L_2 \\ L_3 \\ 0 \end{bmatrix}, \quad \textbf{(6.10)}$$

and $\dot{\Xi}^T$ is the transpose of the time derivative of the matrix Ξ defined by Equation 6.5.

It is important to recognize the quaternion character of Equation 6.9. However

because of Equations 6.10 it is obvious that $\dot{\hat{L}} = 0 + \dot{\mathbf{L}}$ and $\hat{L} = 0 + \mathbf{L}$ whereas $\hat{N}$ is not a pure quaternion in general. Equation 6.9 was first published and used by Evans [126,131]. He observed that the evolution of the angular momentum can be determined knowing the initial angular momentum, the particular orientation of the rigid body and having evaluated the derivatives in $\hat{N}$. It is clear then (by comparison with Equation A-25) that the principal torques in quaternion form, $\hat{T}$, are defined by [126]

$$\hat{T} = \frac{1}{2} \cdot \Xi \cdot \hat{N}. \tag{6.11}$$

As previously noted by Evans [129,130], the quaternion parameters, in contrast to Euler angles, give equations of motion without singularities. This is simply due to the fact that Ξ only becomes singular when $q_0^2 + q_1^2 + q_2^2 + q_3^2 = 0$, but this never occurs because of the quaternion unitary constraint $q_0^2 + q_1^2 + q_2^2 + q_3^2 = 1$ (see Appendix).

Now we proceed to the derivation of the torque acting on the beads of a free rigid quantum object, which requires the evaluation of $\hat{N}$ from the interaction potential. According to the discretized path integral formalism, in addition to the intermolecular interaction, there is an interaction between beads that arises from the discretization of the kinetic part of the Euclidean Lagrangian (see Section 4.2). One way of obtaining the form of this bead's interaction (maybe the simplest) is by using the free real time orientational propagator [97,132] in imaginary time. This is achieved by employing the identity $t = -i\beta\hbar$ in the real time orientational propagator, which has been derived by L. Schulman [97,132]. In fact, this identity allows one to switch from quantum mechanics

(real time) to statistical mechanics (imaginary time) and was used by Feynman [7] to find Equation 4.27 from the real time translational propagator already derived by him [7]. (It is also possible to switch back to quantum mechanics from statistical mechanics by using the identity $\beta = it/\hbar$. [7,97])

By transforming the free orientational matrix of a spherical top [97,132] to imaginary time in discretized form employing the identity $t = -i\beta\hbar/P$ we have

$$\rho_0(\Omega_k,\Omega_{k+1};\beta/P) = \left[\frac{IP}{2\pi\beta\hbar^2}\right]^{3/2} \frac{\Gamma(k,k+1)}{2\sin\left[\frac{1}{2}\Gamma(k,k+1)\right]} \times \exp\left[\frac{\beta\hbar^2}{8IP}\right]\exp\left[-\frac{IP\Gamma^2(k,k+1)}{2\hbar^2\beta}\right], \tag{6.12}$$

where I can be approximated by $\sqrt[3]{I_x I_y I_z}$ and $\Gamma(k,k+1)$ is the arclength between beads k and k+1 [ie. $\Gamma(k,k+1) \equiv \Gamma(\Omega_k,\Omega_{k+1})$, see equations 4.32 and 4.33]. From Equation 6.12 the interaction between beads can be found to be

$$V(k,k+1) = \frac{IP\Gamma^2(k,k+1)}{2\hbar^2\beta^2} - \frac{1}{\beta}\ln\left(\frac{\Gamma(k,k+1)}{2\sin\left[\frac{1}{2}\Gamma(k,k+1)\right]}\right) \approx \frac{IP\Gamma^2(k,k+1)}{2\hbar^2\beta^2}, \tag{6.13}$$

where the second term in Equation 6.13 has been neglected since at the temperatures of interest it is much smaller than the first term. It is important to note that the approximation in Equation 6.13 is not a requirement of the present method.

The arclength (in Equation 6.13) can be related to the quaternion parameters [127] by $\Gamma(k,k+1) = 2\arccos(\chi_{k+1})$, where $\chi_{k+1} = q_0^{k+1}q_0^k + q_1^{k+1}q_1^k + q_2^{k+1}q_2^k + q_3^{k+1}q_3^k$ is the

scalar element of the composite quaternion between $\hat{q}_k$ and $\hat{q}_{k+1}$, and $\hat{q}_k \equiv \left(q_0^k, q_1^k, q_2^k, q_3^k\right)$, $\hat{q}_{k+1} \equiv \left(q_0^{k+1}, q_1^{k+1}, q_2^{k+1}, q_3^{k+1}\right)$ are the quaternion parameters that specify the orientations of the beads k and k+1, respectively.

Using Equations 6.10 and 6.13 it is then possible to show that

$$\hat{N} = \frac{2IP}{\hbar^2\beta^2}\frac{\Gamma(k,k+1)}{\sqrt{1-\chi_{k+1}{}^2}} \times \begin{bmatrix} \frac{1}{q_1q_3q_0}\left[-q_1^{k+1}(q_2q_3q_0) + q_2^{k+1}(q_1q_3q_0) - q_3^{k+1}(q_1q_2q_0) - q_0^{k+1}(q_1q_2q_3)\right] \\ \frac{1}{q_0q_2q_3}\left[q_1^{k+1}(q_2q_3q_0) - q_2^{k+1}(q_1q_3q_0) - q_3^{k+1}(q_1q_2q_0) - q_0^{k+1}(q_1q_2q_3)\right] \\ \frac{1}{q_1q_2q_0}\left[-q_1^{k+1}(q_2q_3q_0) - q_2^{k+1}(q_1q_3q_0) + q_3^{k+1}(q_1q_2q_0) - q_0^{k+1}(q_1q_2q_3)\right] \\ \frac{1}{q_1q_2q_3}\left[-q_1^{k+1}(q_2q_3q_0) - q_2^{k+1}(q_1q_3q_0) - q_3^{k+1}(q_1q_2q_0) + q_0^{k+1}(q_1q_2q_3)\right] \end{bmatrix} \quad \textbf{(6.14)}$$

where the unitary constraint on the quaternion parameters (see Appendix) has been used and the label k has been dropped since there is no chance for confusion. From Equations 6.11 and 6.14 we finally find the expression for the torque acting on the bead k about its x, y and z axes due to the bead k+1, specifically

$$\begin{aligned} t_x &= \frac{2IP}{\hbar^2\beta^2}\frac{\Gamma(k,k+1)}{\sqrt{1-\chi_{k+1}{}^2}}\left(-q_3q_2^{k+1} + q_0q_1^{k+1} + q_2q_3^{k+1} - q_1q_0^{k+1}\right) \\ t_y &= \frac{2IP}{\hbar^2\beta^2}\frac{\Gamma(k,k+1)}{\sqrt{1-\chi_{k+1}{}^2}}\left(-q_0q_2^{k+1} - q_3q_1^{k+1} + q_1q_3^{k+1} + q_2q_0^{k+1}\right) \\ t_z &= \frac{2IP}{\hbar^2\beta^2}\frac{\Gamma(k,k+1)}{\sqrt{1-\chi_{k+1}{}^2}}\left(q_1q_2^{k+1} - q_2q_1^{k+1} + q_0q_3^{k+1} - q_3q_0^{k+1}\right). \end{aligned} \quad \textbf{(6.15)}$$

Obviously, analogous terms arise due to the bead k-1, which is also coupled to the bead k through the potential of Equation 6.13 [133].

It is worth noting that the final form for the torques depends on the particular convention chosen for the description of the rotational motion. This dependence is taken into account through the matrix Ξ in Equation 6.5 (see Appendix A for details on the derivation of this equation) since $\hat{N}$ only depends on the relative orientation between two beads (k and k+1) and is independent of the convention chosen.

6.2. THE RIGID BODY-CMD METHOD

The discussion presented in Section 5.2.2 can be extended to the treatment of a collection of rigid objects [133]. For present purposes it is sufficient (although not necessary) to assume that these bodies possess a classical-like mass but a relatively small (quantum-like) inertia moment at a certain finite temperature. It is clear that the coordinates of any of these rigid objects can be specified by a (unique) center of mass position and a quantum (uncertain within a certain neighborhood) orientation. As a consequence, an effective potential can be defined by introducing the concept of an orientational centroid and by taking into account the (molecular) orientational uncertainty by analogy to the Cartesian development [133]. Thus, in view of the similarity in the physical meaning of the translational and rotational centroids, the calculation of equilibrium and dynamical properties can be carried out by evaluating the centroid forces and centroid torques according to the CMD approximation. However, the extension of the centroid methodology to rotations [133], while initially appearing straightforward, also has several subtleties, not the least of which is the well known non-commutativity property of finite rotations. Additionally, in resolving the problem, three frames will be required to describe rotations, the laboratory frame with respect to which the centroid

moves, the centroid frame with respect to which the beads move, and the local frames of the beads.

6.2.1. A dynamics with constraints

Analogous to the translational case, a rotational Hamiltonian can be defined for a single quantum rotor in a classical potential as [133]

$$H = \sum_{k=1}^{P}\left[\left\{\frac{L_{x,k}^2}{2I_x'} + \frac{L_{y,k}^2}{2I_y'} + \frac{L_{z,k}^2}{2I_z'}\right\} + \left\{\frac{IP\Gamma^2(k,k+1)}{2\hbar^2\beta^2}\right\} + \frac{1}{P}V(\mathbf{r},\hat{q}_k)\right], \tag{6.16}$$

where the first (kinetic) term is, as before, arbitrary, the second term is of a quantum nature (discussed in Section 6.1), and the third term is due to the external classical potential which depends on the center of mass position (**r**) and the beads' orientational coordinates (the quaternions, $\{\hat{q}_k\}$). It is worth noting the similarity between Equation 6.16 and its translational analog Equation 5. 59.

The torque due to the harmonic orientational coupling between beads, $\mathbf{T}_q = (t_x, t_y, t_z)$, acting on a particular bead k, was derived in Section 6.1 (see Equation 6.15). Clearly, the total torque, $\mathbf{T}_k$, acting on the bead k of a particular molecule also includes a torque, $\mathbf{T}_{cl}$, due to the intermolecular orientational interaction, i.e. $\mathbf{T}_k = \mathbf{T}_q + \mathbf{T}_{cl}$. Analogous to the translational case, we can define $\mathbf{T}_k^{bead} = \mathbf{T}_k - \mathbf{T}_c$, where the centroid torque is [133]

$$\mathbf{T}_c = \frac{1}{P}\sum_{k=1}^{P}\mathbf{T}_k \,. \tag{6.17}$$

Therefore, the orientational centroid can be conserved dynamically by requiring the sum of the torques acting on the beads to be zero in the centroid frame [133]

$$\sum_{k=1}^{P}\mathbf{T}_k^{bead} = 0, \tag{6.18}$$

and by imposing the initial constraint on the angular momentum sum in the centroid frame

$$\sum_{k=1}^{P}\mathbf{L}_k = 0, \tag{6.19}$$

where $\mathbf{L}_k$ is a vector with components $L_{x,k}$, $L_{y,k}$ and $L_{z,k}$ (see Equation 6.16).

One of the differences between these equations and the ones (written in Section 5.2.2) for translations is related to the frame of reference. The torque $\mathbf{T}_q$, as given by Equation 6.15, is in bead k principal frame whereas the calculation of $\mathbf{T}_{cl}$ is carried out in the laboratory frame. Moreover, the constraint on $\mathbf{T}_k^{bead}$ given by Equation 6.18 is in the centroid frame while the bead's equations of motion are integrated in the principal frame. Therefore, the knowledge of the relative orientation between the different frames is crucial and quaternions are also particularly useful in this context. In order to illustrate this one may ask "what is the orientation, $\hat{q}_{k'}$, of the bead k in the laboratory frame if the centroid orientation in the laboratory frame is known to be $\hat{q}_{c'}$, and the orientations of the

bead k and the centroid with respect to an arbitrary frame are known to be $\hat{q}_k$ and $\hat{q}_c$, respectively?" The relative orientation of the bead with respect to the centroid is given by $\hat{q}_{comp} = \hat{q}_k[\hat{q}_c]^{-1}$ where $\hat{q}_{comp}$ is known as the composite quaternion [129]. Thus, the answer is $\hat{q}_{k'} = \hat{q}_{comp}\hat{q}_{c'} = \hat{q}_k[\hat{q}_c]^{-1}\hat{q}_{c'}$. If the arbitrary reference frame is conveniently chosen to be the centroid frame, that is $\hat{q}_c \equiv (1,0,0,0)$, we obtain $\hat{q}_{k'} = \hat{q}_k\hat{q}_{c'}$. Proceeding in this manner the bead's dynamics can be carried out by evolving the orientations $\hat{q}_k$ with centroid frame $\hat{q}_c \equiv (1,0,0,0)$. The bead's orientation in the laboratory frame is given by $\hat{q}_{k'}$ which is easily calculated once the centroid orientation in laboratory frame, $\hat{q}_{c'}$, is known. As will be seen later, there are some other benefits associated with the choice $\hat{q}_c \equiv (1,0,0,0)$.

The rotational equations of motion for bead k in the principal frame (that is in bead k frame) can now be written as [4]

$$\dot{\hat{q}}_k = \frac{1}{2}\Xi_k \cdot \hat{w}_k \tag{6.20}$$

and

$$\dot{\mathbf{L}}_k = \mathbf{T}_k^{bead} - \mathbf{w}_k \times \mathbf{L}_k \tag{6.21}$$

where Equation 6.20 have been derived in the Appendix (see Equation A-20 or Equation 6.5) and Equation 6.21 is the usual rotational equation of motion [4,128] (equivalent to Equation 6.9). Clearly, these equations of motion can be integrated with a convenient

numerical technique such as the Gear predictor-corrector algorithm [4] (see Section 2.3).

It is instructive to analyze the dynamics generated by Equations 6.18, 6.20 and 6.21 in the absence of external torques, i.e. $\mathbf{T}_{cl} = 0$, for particular numbers of beads, where it is assumed as an initial condition that the beads are all aligned (and Equation 6.19 is satisfied).

i) P=1. As expected the classical limit is reached and the centroid describes the motion of the particles in a classical sense. There is no bead dynamics.

ii) P=2. In this case, it is easily shown that $\mathbf{T}_1^{bead} = -\mathbf{T}_2^{bead}$ or that the torques acting on the beads exactly cancel. In fact, Equation 6.15 implies that this cancellation occurs naturally. Thus, the dynamics conserves the centroid.

iii) P>2. In this case the interpretation of the constraint can no longer be easily pictured physically, due to the non-commutativity property of orientations. All that can be said is that the P orientations will disperse with (imaginary) time while still satisfying the constraints.

It is important to note that, in general, the force between molecules depends on their relative orientation (as is the case for water). As a consequence a centroid force will also need to be calculated. The calculation of the centroid force is carried out with the three-dimensional version of Equation 4.66 in a straightforward manner.

According to the discussion in Section 4.2.1, the efficiency of the path integral evaluation is significantly improved with the use of a thermostating scheme. By using a

Nose-Hoover thermostat chain [47] on each bead, Equation 6.21 transform into the following set of equations (see Equations 2.28)

$$\dot{\mathbf{L}}_k(t) = \mathbf{T}_k^{bead}(t) - \mathbf{w}_k(t) \times \mathbf{L}_k(t) - \lambda_{k,1}(t)\mathbf{L}_k(t) + \mathbf{S}(t)$$

$$\dot{\lambda}_{k,1}(t) = \frac{1}{Q_1}\left(\sum_{k=1}^{P}\left\{\frac{L_{x,k}^2(t)}{I_x'} + \frac{L_{y,k}^2(t)}{I_y'} + \frac{L_{z,k}^2(t)}{I_z'}\right\} - \frac{3(P-1)}{\beta}\right) - \lambda_{k,1}(t)\lambda_{k,2}(t)$$

$$\dot{\lambda}_{k,j}(t) = \frac{1}{Q_j}\left(Q_{j-1}\lambda_{k,j-1}^2(t) - \frac{1}{\beta}\right) - \lambda_{k,j}(t)\lambda_{k,j+1}(t) \qquad \textbf{(6.22)}$$

$$\dot{\lambda}_{k,M}(t) = \frac{1}{Q_M}\left(Q_{M-1}\lambda_{k,M-1}^2(t) - \frac{1}{\beta}\right),$$

where $\lambda_{k,1}$, $\lambda_{k,j}$ and $\lambda_{k,M}$ are the parameters of the thermostat chain for bead k. Due to the centroid constraint the total number of degrees of freedom is $3(P-1)$ and consequently, $Q_1 = 3(P-1)t_0^2/\beta$ and $Q_j = t_0^2/\beta$ for $2 \le j \le M$. The vector $\mathbf{S}$ (in principal frame) in the first equality of Equations 6.22 is calculated with the following centroid frame equation

$$\mathbf{S}(t) = \frac{1}{P}\sum_{k=1}^{P}\lambda_{k,1}(t)\mathbf{L}_k(t). \qquad \textbf{(6.23)}$$

Equation 6.23 ensures the preservation of Equation 6.19 in the thermostated dynamics.

6.2.2. *The orientational centroid and its conservation*

Using the torques derived in Section 6.1 and those due to the external potential, in conjunction with the centroid constraints, a dynamics (thermostated or otherwise) can be generated such that the "orientational neighborhood" is sampled and the average centroid torque (and the centroid force) estimated. Further, according to the discussion presented above, since all the beads can be started with the same orientation, the initial common bead orientation is actually the initial centroid orientation. It is then relevant to ask "what is the centroid orientation at a time τ later?" An answer to this question requires a definition of the orientational centroid.

The orientational centroid can be defined as that orientation, $\hat{q}_c$, that minimizes the function $G(\hat{q}_c)$, where [133]

$$G(\hat{q}_c) = \sum_{k=1}^{P} \Gamma^2(\hat{q}_c, \hat{q}_k), \tag{6.24}$$

and $\Gamma(\hat{q}_c, \hat{q}_k)$ is the rotation angle (or arclength) between the centroid orientation and the orientation of bead k, $\hat{q}_k$. With this definition one can obviously find the centroid of a set of orientations through a Monte Carlo search that exploits this minimization condition as a criterion for rejection/acceptance of trial centroid moves. Convergence is then achieved by finding that trial centroid that can no longer be improved. Such a search procedure also allows one to confirm centroid conservation at any stage of a CMD simulation. Other minimization algorithms designed to average quaternions have also been published recently [134]. It is interesting to note that a similar minimization algorithm could be

implemented for the determination of the translational centroid; however, it is much easier to find it analytically by using Equation 5.60. Unfortunately, an analytical definition for the orientational centroid is not known. Moreover, the definition of an orientational centroid given above may have numerous other applications that have explicit orientational dependence.

Clearly, Equation 6.24 is just the application of least squares on spherical distances, Γ, and can also be used to argue for the existence of the centroid (or minimum). According to a usual real analysis theorem [135], since the function $G(\hat{q}_c)$ is real and continuous, and by the compactness of its domain (the 4-dimensional sphere), it has a minimum value. The uniqueness of this minimum, however, is not guaranteed in general. In fact, there are obvious situations where more than one minimum may exist; for example, if the P (4-dimensional) points are homogeneously distributed around the "equator" then the function $G(\hat{q}_c)$ minimizes at both the "north" and "south" poles. However, if all the points lie in a common hemisphere one may expect intuitively to find a unique minimum. Indeed, this result has been recently proven [134] for an arbitrary but finite number of dimensions although this proof will not be presented here (since it involves the use of exponential mapping and other elements from Lie theory).

Interestingly, as an important difference in relation to translational motion, the use of Equation 6.24 allows one to find that the constraints given by Equations 6.18 and 6.19 (and 6.23 in the thermostated dynamics) are not sufficient to ensure the exact conservation of the centroid (in a MD simulation using finite size time steps as will be seen explicitly below). Indeed, as the bead dynamics proceed one observes that the

real centroid drifts slightly from the original or ideal orientational centroid [133]. This small drift occurs as a consequence of small errors arising from the lack of commutativity of finite rotations [128] and can be eliminated by exploiting the geometric properties of the quaternion parameters. On the other hand, finite rotations can not be avoided in molecular dynamics simulations since the integration of the equations of motion must be carried out numerically. The question of how to conserve an orientational centroid is then posed, without loss of generality, in the following form: if we let the centroid be the quaternion $\hat{q}_c \equiv (1,0,0,0)$, can we find a set of bead orientations that satisfies this centroid ?

This problem is solved by representing the orientation of one bead in terms of the orientations of the remaining beads [133]. The two-bead case is straightforward; the beads are inverse quaternions of each other, $\hat{q}_2 = \hat{q}_1^{-1}$ (this case becomes obvious because it reduces to a one-dimensional problem, involving a single rotation angle). A simple proof can be given as follows: let us define a transition quaternion, $\hat{q}_t$, that transforms $\hat{q}_1$ into $\hat{q}_2$, as $\hat{q}_2 = \hat{q}_t \hat{q}_1$. Then, since $\hat{q}_2 = \hat{q}_1^{-1}$, we have $\hat{q}_t = \hat{q}_2 (\hat{q}_1)^{-1} = \hat{q}_2 \hat{q}_2$, which means that in order to transform $\hat{q}_1$ into $\hat{q}_2$, two identical transformations need to occur. It should be intuitively (or according to Equation 6.19) clear that the centroid defined by two orientations is some orientation located symmetrically between them. Thus, we find that $\hat{q}_c = \sqrt{\hat{q}_t}\hat{q}_1 = \hat{q}_2 \hat{q}_1 = \hat{1}$ where $\hat{1}$ is the unit quaternion (1,0,0,0). In other words, if two beads are inverse quaternions of each other their centroid is the quaternion $(1,0,0,0) \equiv \hat{1}$.

A solution for the three-bead case begins by defining (see Appendix) [133]

$$\hat{q}_1 = \cos(\theta_1/2) + \mathbf{u}_1 \sin(\theta_1/2) \tag{6.25}$$

and

$$\hat{q}_2 = \cos(\theta_2/2) + \mathbf{u}_2 \sin(\theta_2/2), \tag{6.26}$$

where θ_1 and θ_2 are the rotation angles, and $\mathbf{u}_1$ and $\mathbf{u}_2$ are the rotation axes of the quaternions $\hat{q}_1$ and $\hat{q}_2$, respectively. It is interesting to examine first their relationships for two simple cases:

1) If $\mathbf{u}_1 = \mathbf{u}_2 = \mathbf{u}$, then the rotation axis of the third bead $\mathbf{u}_3 = -\mathbf{u}$, and its rotational angle $\theta_3 = \theta_1 + \theta_2$. Furthermore, if additionally $\theta_1 = -\theta_2$, the quaternion $\hat{q}_3$ becomes the unit quaternion, i.e. the centroid itself.

2) If the angle between $\mathbf{u}_1$ and $\mathbf{u}_2$ is $2\pi/3$ and $\theta_1 = \theta_2 = \theta$, then $\theta_3 = \theta$ and $\mathbf{u}_3 = -\mathbf{u}_1 - \mathbf{u}_2$.

In general, the third quaternion (that satisfies the centroid $\hat{1}$) is given by [133]

$$\hat{q}_3 = \cos(\theta_3/2) + \mathbf{u}_3 \sin(\theta_3/2), \tag{6.27}$$

where

$$\theta_3 = \sqrt{\theta_1^2 + \theta_2^2 + 2\theta_1\theta_2(\mathbf{u}_1 \cdot \mathbf{u}_2)} \tag{6.28}$$

and

$$\mathbf{u}_3 = -\left(\frac{\theta_1}{\sin(\theta_1/2)}\mathbf{u}_1 + \frac{\theta_2}{\sin(\theta_2/2)}\mathbf{u}_2\right) \Bigg/ \left|\frac{\theta_1}{\sin(\theta_1/2)}\mathbf{u}_1 + \frac{\theta_2}{\sin(\theta_2/2)}\mathbf{u}_2\right|. \qquad (6.29)$$

Due to the cyclic nature of the rotations, Equations 6.27-6.29 can become ill-conditioned if all the orientations are not confined to one hemisphere [133]. This limitation however is not a problem in simulations closed to the classical limit where the quantum rotational uncertainty is small.

In principle, relationships similar to Equations 6.27-6.29 could be found for more than three beads, however iterative procedures based on the two-bead and three-bead expressions are easily implemented for an arbitrary number of beads [133]. For example, let $\{\hat{q}_k\}$ be a set of P orientations. From $\hat{q}_1$ and $\hat{q}_2$ and using the three-bead formula (Equations 6.27-6.29) we find a third (temporary) quaternion, denoted here by $\hat{q}_{temp}$. It is then clear for the case P=3 that $\hat{q}_3 = \hat{q}_{temp}$. From the discussion of the two-bead case this result implies that the influence on the centroid of the quaternions $\hat{q}_1$ and $\hat{q}_2$ is equivalent to (or can be substituted by) a single bead, specifically $(\hat{q}_{temp})^{-1}$, which obviously together with $\hat{q}_3 = \hat{q}_{temp}$ conserve the centroid $\hat{1}$. For the case of four beads, we proceed in a similar fashion. First we calculate $\hat{q}_{temp}$ from the bead quaternions $\hat{q}_1$ and $\hat{q}_2$, then using $(\hat{q}_{temp})^{-1}$ and $\hat{q}_3$ (and Equations 6.27-6.29) we calculate a new $\hat{q}_{temp}$ which in this case equals $\hat{q}_4$. In general, for P beads it is necessary to calculate $\hat{q}_{temp}$ $P-2$ times. The first $\hat{q}_{temp}$ is calculated from $\hat{q}_1$ and $\hat{q}_2$ as before. Subsequent $\hat{q}_{temp}$ are calculated by using $(\hat{q}_{temp})^{-1}$ from the previous step and the next bead, and finally at the last step

$\hat{q}_P = \hat{q}_{temp}$. This procedure can then be used in addition to the dynamical constraint on the torques described above (see Equations 6.18 and 6.19) to guarantee conservation of the centroid during the integration of the beads' equations of motion. It is important also to remark that the above procedure could be utilized in a Monte Carlo algorithm to determine sets of bead quaternions that satisfy the centroid, thereby providing an alternate means for the evaluation of the constrained path integral.

Finally, before moving into its applications, it is interesting to reflect on a more formal justification of the rigid body CMD-method. In relation to the centroid theory discussed in Chapter 5, it would be nice to be able to provide a similar analytical justification of this rotational version (based, for example, on a quasi-density operator). However, the conceptual problems associated with path integrals in curved spaces are formidable [97]. The multiple connectivity of the orientational space (which is directly related to its curvature) demands the use of topological techniques, which were in fact used by Schulman [97,132] in the derivation of the real time propagator of a spherical top (real time version of Equation 6.12). Schulman wrote in his book (page 214 on reference [97]), "If you like excitement, conflict and controversy, especially when nothing very serious is at stake, then you will love the history of quantization of curved spaces". It is then understandable why one needs to invoke topological arguments [like the compactness of the domain of $G(\hat{q}_c)$] to argue about the existence of the centroid (and with some restrictions, its uniqueness). Topological methods, however, cannot provide the means to calculate the orientational centroid. Thus, the very existence of an *analytical* solution for the beads' orientations such that they conserve the centroid

$(1,0,0,0) \equiv \hat{1}$ (given in equations 6.27-6.29) and the property of associativity of these equations seems almost like a mathematical curiosity. It is worth mentioning that Schulman's work was certainly inspired by Feynman who wrote in his delightful book on path integrals (page 355 on ref [7]), "...path integrals suffer most grievously from a serious defect. They do not permit a discussion of spin operators or other such operators in a simple and lucid manner. ... It can be handled if the amplitudes and quantities are considered as quaternions instead of ordinary complex numbers, but the lack of commutativity of such numbers is a serious complication."

6.3. TESTING THE METHOD WITH A SIMPLE SYSTEM

We turn now to explicit results of calculations designed to demonstrate the success of the methodology described in the previous section. An isolated TIP4P [61] water molecule coupled to a thermal bath at 298 K is examined in the absence and presence of an external homogeneous electric field. The electric field is defined to be in the *z* direction and is approximately equal in magnitude to the average local field present in liquid water (~2 V/Å) [136]. The required path integral evaluation was carried out for different numbers of beads (between 3 and 6) and in every case each bead was coupled to a Nosé-Hoover chain thermostat [47] of length 4 (see Equations 6.22). The simulation utilizes 256 otherwise independent water molecules being controlled with a single thermostat [46] to allow for appropriate fluctuations in the single-molecule kinetic energies in field-on conditions. The equations of motion were integrated using a 4^{th}-order Gear predictor-corrector algorithm [4] and real time step sizes of 1 fs and 0.125 fs for the

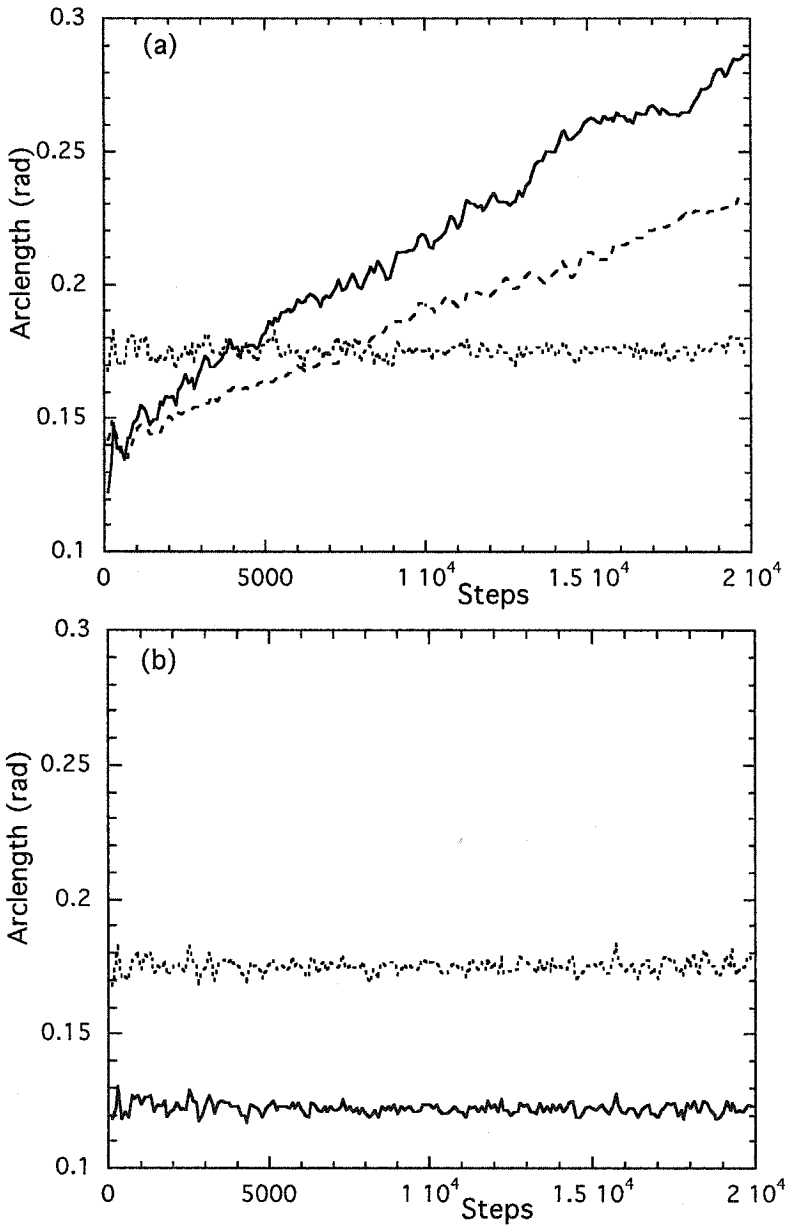

Figure 6.1. Time dependence of the average rotation angle between the beads and between the beads and the centroid. The solid lines correspond to the bead-centroid angle and the dotted lines correspond to the bead–bead angle, both in radians. The dashed line in (a) corresponds to the bead-centroid angle in a system with a smaller imaginary time step. (a) Results from dynamics utilizing only Equations 6.18-6.20, 6.22 and 6.23. (b) Results obtained utilizing Equations 6.18-6.20, 6.22, 6.23 and 6.27-6.29.

classical and the quantum simulations, respectively. Further computational details are given in the next chapter.

Fig. 6.1 shows the time behavior of the instantaneous rotation angle (averaged over the 5 beads of all 256 independent molecules) between the beads and the centroid orientation for field-free isolated molecules as a function of centroid steps. The drift in the centroid orientation (manifested as a consistently increasing value for the bead-centroid arclength) is clearly observed in Fig. 1(a), where only the conditions required by Equations 6.18-6.20, 6.22 and 6.23 have been utilized, is due to the non-commutativity of finite rotations. The smaller drift obtained by using a smaller imaginary time step (see Fig. 6.1(a)) confirms this explanation. It is important to recall that, although finite rotations do not commute, infinitesimal rotations do commute [128], and as the time step is decreased the drift decreases as well. In Fig. 6.1(b), which only shows the results from the simulation with a normal bead time step, this drift has been eliminated by the further application (to each set of 5 beads) of the iterative procedure discussed in the context of Equations 6.27-6.29. In this study this procedure has been implemented by correcting a randomly selected bead orientation at every step of the constrained dynamics. It should be noted that the correction required at each step is always very small (as is implied by Fig. 6.1 (a)); consequently its impact on the equations of motion is small and any heating effects are easily controlled by the thermostat [133]. We have chosen to correct for the centroid at every imaginary time step to minimize such effects.

A requirement of CMD is a homogeneous sampling of the imaginary time phase space. Fig. 6.2 shows probability distributions representing the quantum mechanical

rotational uncertainty of a water molecule as mapped by the algorithm in the absence and presence of the electric field. The discrete values from the simulation appear to follow exactly the continuous lines that represent the expected normalized Gaussian form (including its angular differential element). In Fig. 6.2 we also see that the influence of the field is to slightly contract the quantum mechanical angular distribution (i.e. as expected the external potential slightly contracts the quantum uncertainty).

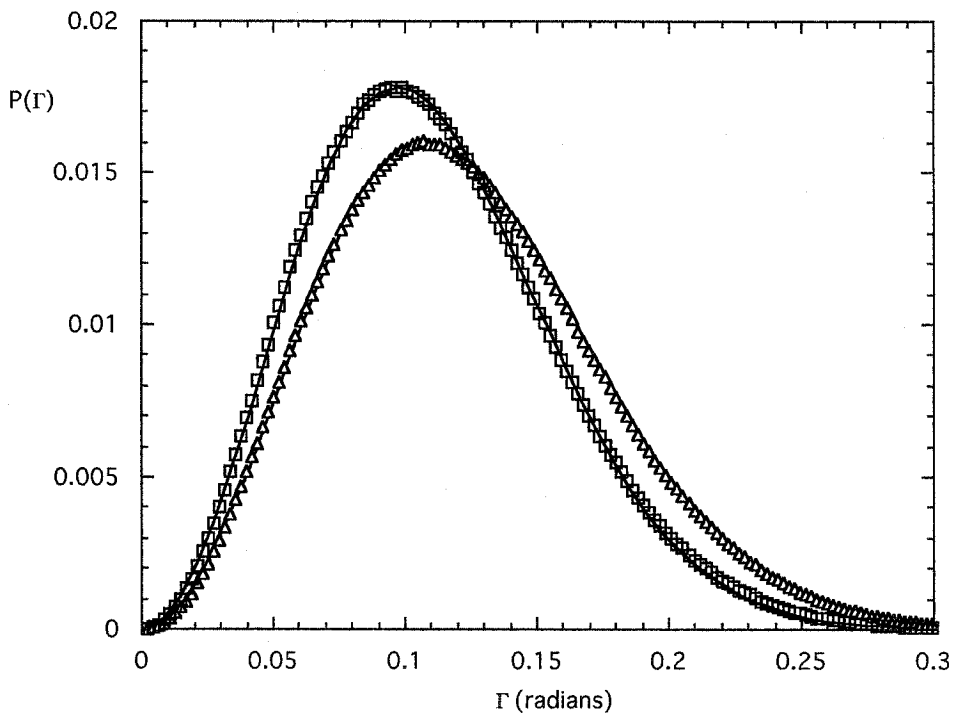

Figure 6.2. Probability distribution of the bead-centroid angle of a water molecule. The triangles represent results from a simulation carried out in the absence of a field, and the squares are results obtained in the presence of a field. The lines are the ideal distributions fitted to the data.

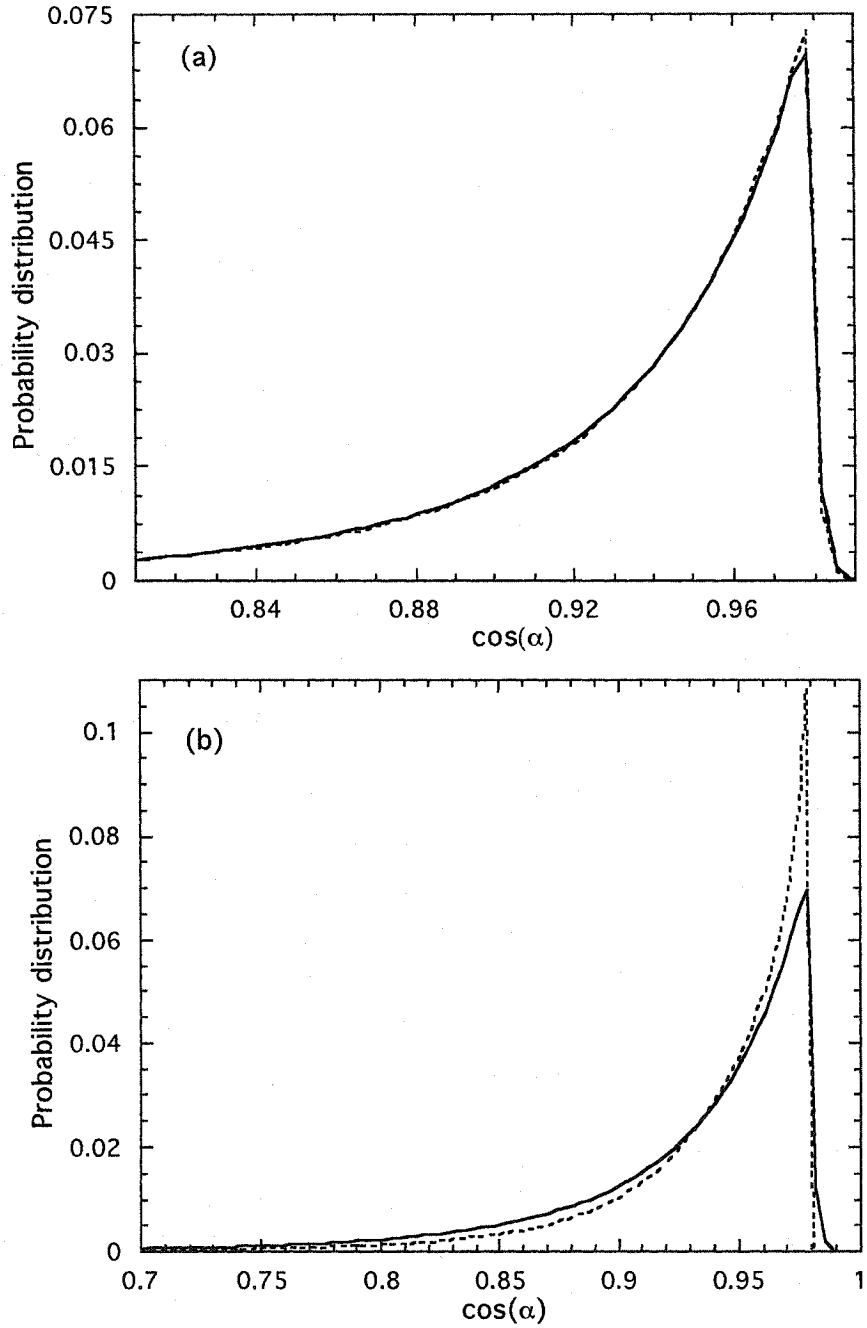

Figure 6.3. Dipole moment orientational distributions of the water molecule as a function of cos(α), where α is the angle between the dipole and the field vector. (a) Results for quantum mechanical calculations at different *P*. The solid, dot-dashed and dashed lines represent *P*=6, *P*=5 (which overlaps with *P*=6 line) and *P*=3, respectively. (b) Classical (dotted line) and quantum (solid line) distributions.

The probability distribution for the orientation of the molecular dipole moment in the presence of the external field and its dependence on P, the discretization parameter, are shown in Fig. 6.3. As can be seen in Fig. 6.3(a), results from quantum calculations with different values of P demonstrate that convergence is achieved at rather low values of the discretization parameter; in particular, the results at P=5 become indistinguishable from those at P=6. Fig. 6.3(b) compares the probability distributions for the orientation of the dipole moment obtained from classical and quantum simulations. The broadening observed in the distribution from the quantum system is clearly a manifestation of quantum dispersion.

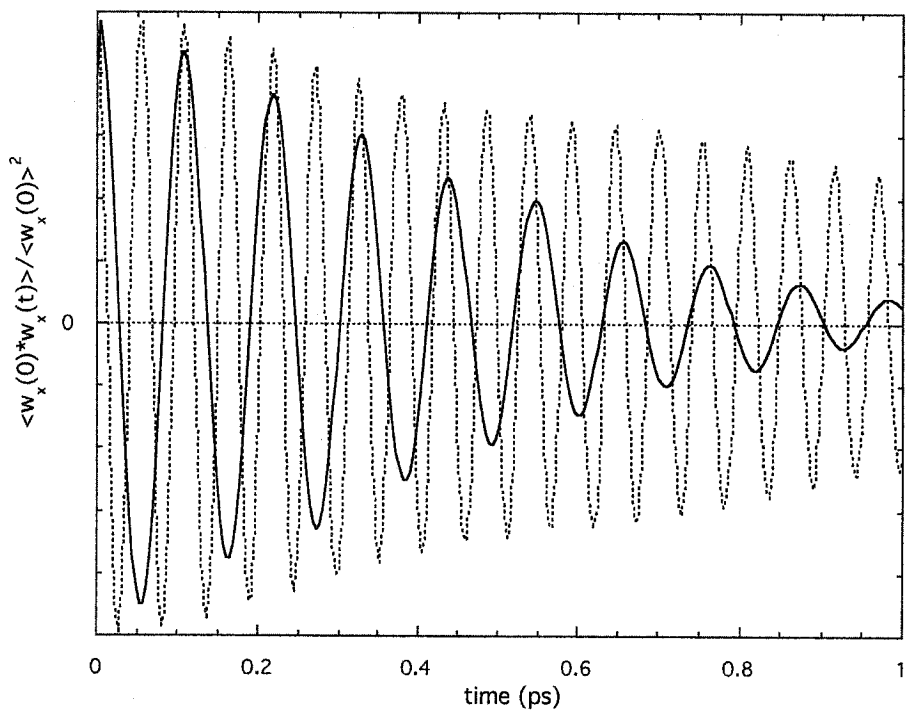

Figure 6.4. Classical (dashed line) and quantum (solid line) normalized time correlation functions for the x component of the angular velocity.

One of the principal benefits of the CMD approach is in its ability to characterize the quantum dynamics. The application of CMD to translational degrees of freedom has

established a strategy for the calculation of (approximate) quantum time correlation functions [105-111]. This strategy (see Equation 7.3) can be applied in the context of the rotational centroid provided that the system is close to the classical limit and the interactions are not strongly anharmonic [105,110,111]. The classical and quantum time correlation functions for the x component of the angular velocity for water molecules in field-on conditions are shown in Fig. 6.4. As expected we see that the effect of quantization is to reduce the structure in this function.

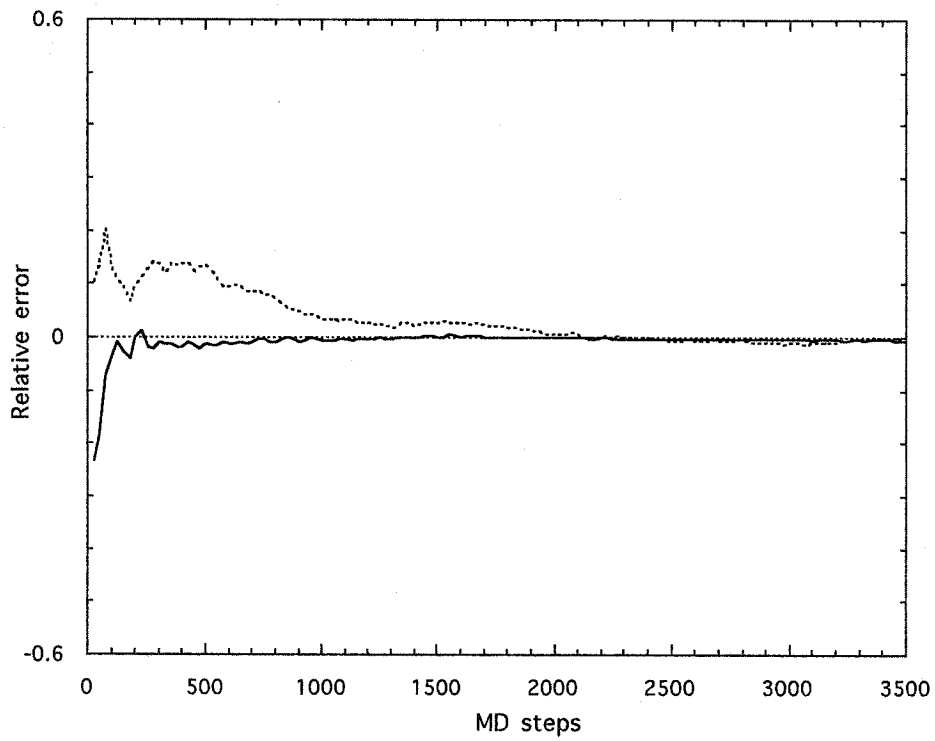

Figure 6.5. Convergence of the centroid force and the centroid torque on a molecule in liquid water as a function of the MD imaginary sampling. The dashed line represents a randomly selected component of the force and the solid line represents a randomly selected component of the torque.

In order to consider a more realistic application for the present methodology, a preliminary liquid water simulation at 298 K has been performed. The TIP4P water model with a discretization parameter, P=5 was used. (A complete description of these calculations and their results will be given in the next chapter). Fig. 6.5 illustrates the convergence of the forces and torques within a CMD simulation where the axes and the molecules have been selected at random. The relative errors shown in Fig. 6.5 are the relative differences between the current running average and the "exact" (long-time) average, where the "exact" values were determined from a simulation consisting of 10^5 imaginary steps. We see that to obtain reasonably converged forces and torques a few thousand steps are required in the imaginary time sampling. This makes the application of the so-called "primitive" CMD approach (where well-averaged forces and torques are required for each centroid step [137]) computationally very demanding; however utilization of the "adiabatic" CMD approach [137] requires considerably less computational effort to produce a smooth dynamical trajectory. It is also evident from Fig. 5 that the centroid torques converge more rapidly than the centroid forces.

In summary, the CMD method has been extended to the rotations of rigid bodies by designing an algorithm that in a context of a molecular dynamics simulation samples homogeneously the orientational neighborhood associated with their quantum degrees of freedom. This algorithm ensures that the rotational centroid (or the average orientation of the set of beads) remains constant at each step. To help achieve this, a general definition for the average orientation (rotational centroid), as well as a straightforward procedure for determining it numerically, have been provided. The methodology that has been

presented here will be particularly advantageous for the quantum simulation of the dynamical properties of (simple) molecular systems in condensed phases and near their classical limit (such as liquid water or ice), within the rigid body approximation, as will be demonstrated in the next two chapters.

7. QUANTUM LIQUID WATER

Our understanding of liquid water has benefited from the progress made in the area of computer simulation, including the advent of quantum simulations. A number of path integral simulations studies of the equilibrium and/or dynamical properties of liquid water has been reported to date (see Section 4.2) employing both rigid and flexible water models. The purpose of this chapter is to present the results of quantum simulations of liquid water obtained using the *rigid body centroid molecular dynamics* methodology described in Chapter 6. This chapter is organized as follows. Section 7.1 presents the details of the simulation methodology and a number of parameterization tests carried out in the implementation of the *rigid body-CMD* method. In Section 7.2, the results obtained for equilibrium and dynamical properties of light and heavy water are presented, including an analysis on model dependence. In Section 7.3, the results of equilibrium and dynamical properties of simulated liquid H_2O over a temperature range from –35 to 100°C are examined to assess the temperature dependence of the quantum effects. Finally, in Section 7.4, tunneling behaviour in water is examined through the use of oxygen-oxygen spatial distribution functions.

7.1. SIMULATION DETAILS AND PARAMETERIZATION OF THE METHOD

Classical molecular dynamics simulations were performed for liquid water at 25°C. A Gaussian thermostat [43] was used to control the temperature of 256 molecules that interact through the TIP4P [61] pair potential at a constant density of 0.997 g/cm. The Ewald summation technique [4] with conducting boundary conditions was employed

together with a truncated octahedrom simulation cell in combination with periodic boundary conditions. The equations of motion were integrated using a 4^{th}-order Gear predictor-corrector algorithm [4], in which the rotational degrees of freedom were represented with quaternions [129,130]. Quantum simulations were performed under the same conditions with the additional bead dynamics controlled with a separate Nosé-Hoover chain thermostat [47] for each bead and the appropriate bead constraints (see Section 6.2). The time steps used in the classical and quantum simulations were 1 fs and 0.125 fs, respectively. The imaginary time dynamics was carried out with a time step of 0.5 fs with inertia moments (for each axis) on each bead twice that of the real molecule. The classical and quantum simulations were equilibrated for 0.1 ns and averaged for 0.5 ns. All quantum simulations started from well-equilibrated classical configurations.

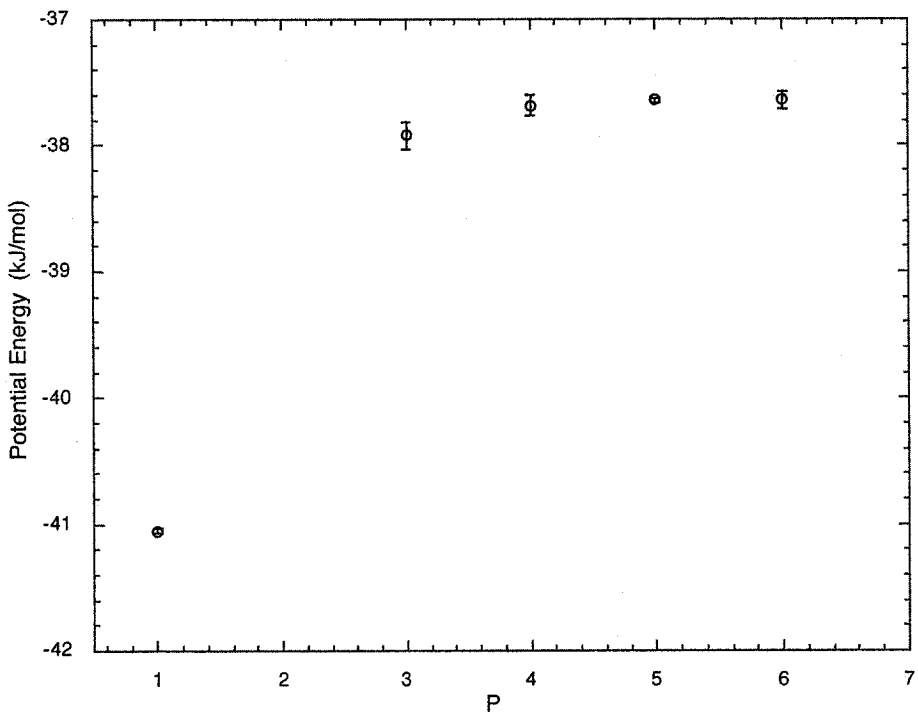

Figure 7.1. Convergence of the intermolecular potential energy of the liquid H_2O system as a function of the path integral discretization parameter, *P*.

The convergence, with respect to P, of the quantum simulations of liquid water is very clearly seen in the average interaction energies presented in Fig. 7.1 (where the value of P=1 is the classical result). It is important to have demonstrated convergence, particularly when examining isotopic effects in quantum simulations. In Fig. 7.1, we have included an error bar estimate for each value. Although the values for P=3 and 4 account for a significant part of the quantum effect, convergence is only attained for P=5 and 6 where the average potential energies are the same within the statistical error.

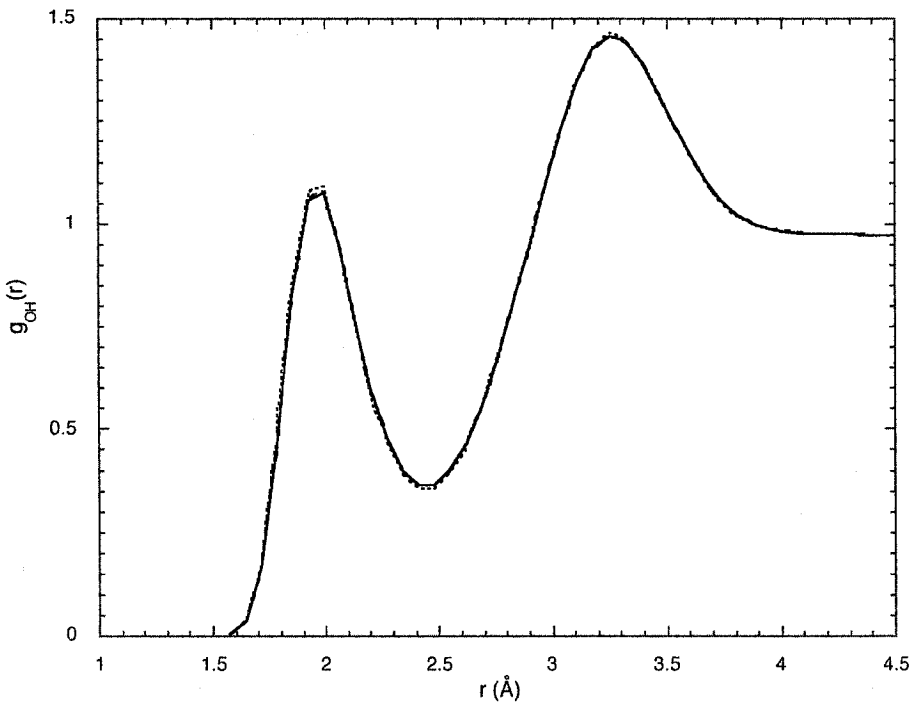

Figure 7.2. Convergence of the oxygen-hydrogen radial distribution function of liquid H_2O with respect to the value of the discretization parameter, P. The results represented by a dotted line, a dashed line, dotted-dashed line and solid line correspond to the values P=3,4,5 and 6, respectively.

Further evidence of the convergence of the results with respect to P is obtained by checking other equilibrium and dynamical properties of the liquid. Fig. 7.2 shows the convergence of the oxygen-hydrogen radial distribution function for simulations

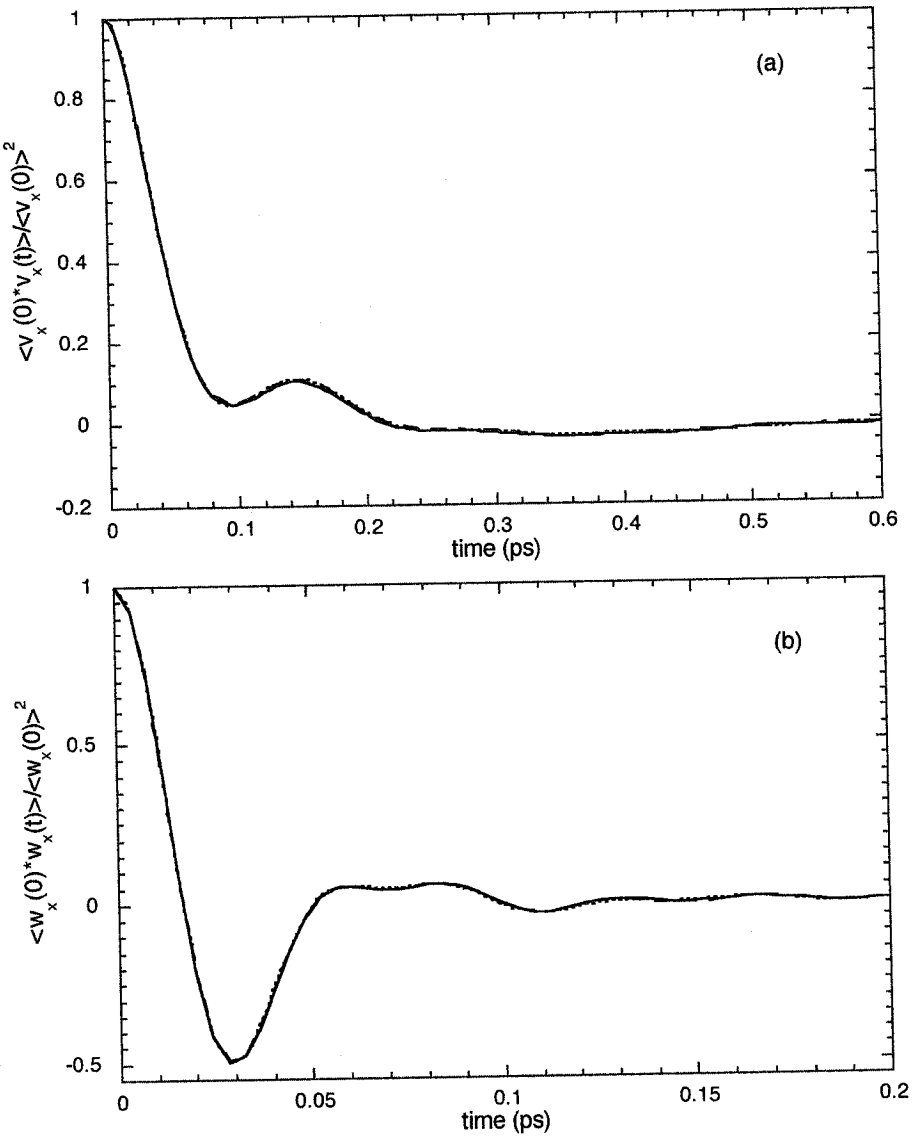

Figure 7.3. Behaviour of (a) the linear and (b) the angular velocity time correlation functions for different values of the discretization parameter P. The dotted line, the dashed line and the solid line correspond to the values P=4,5 and 6, respectively.

carried out with values of P=3,4,5 and 6. The simulation with P=3 differs only slightly (shifted towards more classical behaviour) from the results for P=4, 5 or 6, which are otherwise indistinguishable. Fig. 7.3 demonstrates the similarity in the translational and rotational velocity time correlation functions for P=4,5 and 6, where again the curves for P=3 (not shown in this figure) demonstrate slightly shifted behaviour. From this analysis

we can conclude that the use of a value of P=5 for the discretization parameter provides converged results in the present quantum simulations of both liquid H_2O and D_2O. It is important to note that in previous equilibrium PIMD calculations of Rossky and co-workers [14] with rigid water models, convergence was also observed with P=5. We also remark that this relatively low value of P required for convergence is one of the assets of the present rigid-body approach; the value of P for the quantum description of the hydrogen in water is typically more than 20 [15,19] (Ref. [114] is an exception to this since P was set to 16, however convergence was not demonstrated).

There are essentially two ways to evaluate path integrals via molecular dynamics coupled with the centroid evolution [137]. In the primitive algorithm the centroids have a classical-like time step, and are only propagated further once sufficiently well converged average (centroid) forces and torques have been accumulated; in the adiabatic approach a very small centroid (real) time step is used together with very small bead masses (relative to the real centroid mass) such that the beads move much faster than the centroid. The adiabatic approach is significantly more efficient and is usually implemented [137] on suitable coordinates that uncouple the centroid motion and the bead motion (normal coordinates). In the present study a "quasi-adiabatic" approach has been chosen. In this approach a small number (i.e. 1-5) of steps in imaginary time are performed for every small centroid time step [19]. A number of tests to address its reliability were carried out. A centroid time step (0.125 fs) significantly smaller than the usual classical time step was chosen and several values for the number of imaginary time steps were tested. It is clear

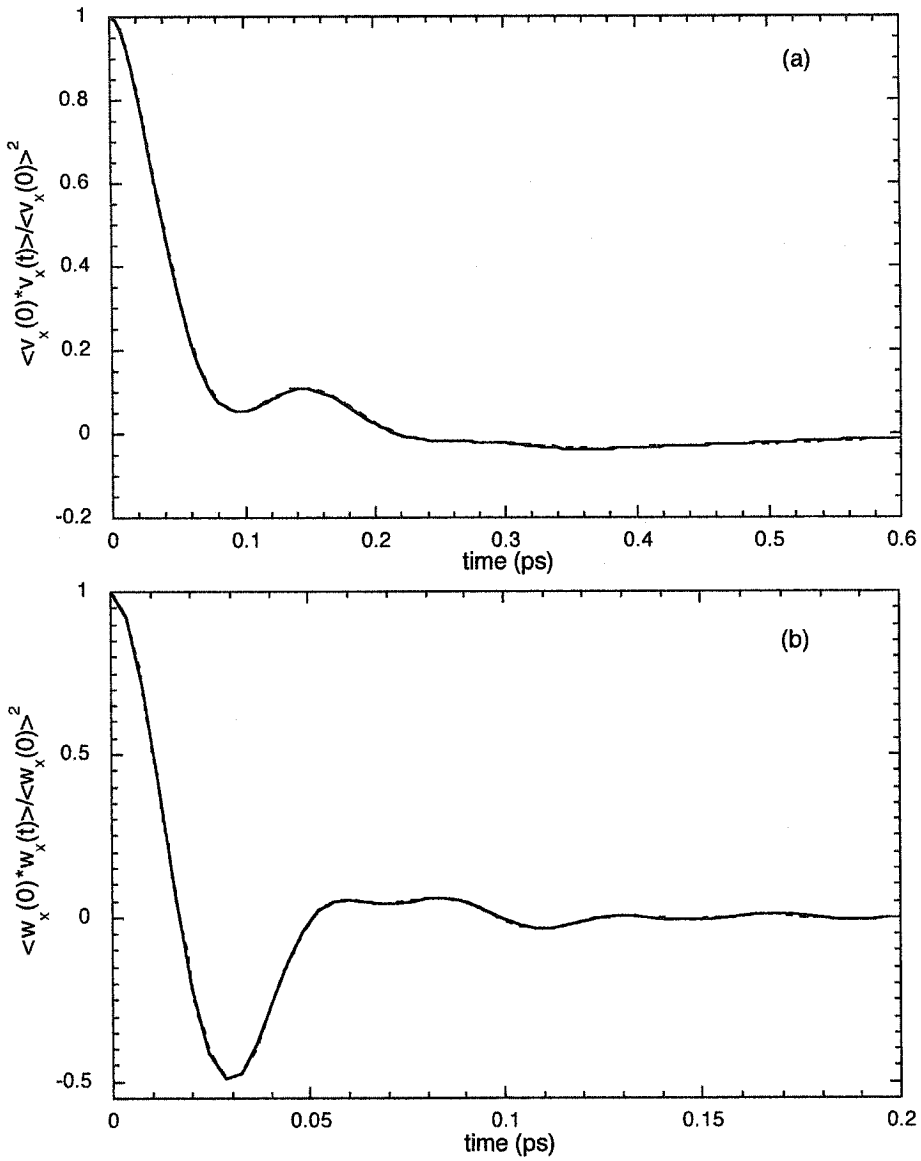

Figure 7.4. Convergence of (a) the linear and (b) the angular velocity time correlation function for different quantum steps per centroid step. In both graphs, the solid line and the dashed line correspond to 3 and 5 quantum steps, respectively.

that the results should be independent of the number of imaginary time steps performed at each real time step provided that a small enough real time step has been chosen and that convergence (in the adiabatic sense) of the centroid forces and centroid torques has been achieved. It was found that structural functions such as $g_{OH}(r)$, or the average energies, are unchanged with the use of 3 or 5 imaginary steps (this explicit comparison is not

shown). A more challenging test is perhaps in the dynamical properties; results for the linear velocity and angular velocity auto-correlation functions are shown in Fig. 7.4. The results obtained with 3 or 5 imaginary steps are identical within the estimated errors. As a consequence, 3 imaginary time steps were used for each real time step in all remaining simulations. We remark that testing utilizing the primitive algorithm (with 300 imaginary steps per regular centroid step) confirmed the validity of our quasi-adiabatic implementations of CMD [138].

7.2. ISOTOPIC EFFECT

In this section, the results of classical and quantum simulations of liquid H_2O and D_2O at 25°C are presented [138]. The discussion begins with an examination of the equilibrium properties of TIP4P water and is followed by an analysis of the dynamical properties of this same water model. Finally, the results presented are compared with those obtained for two other rigid water models.

7.2.1. Equilibrium properties

The oxygen-oxygen and oxygen-hydrogen radial distribution functions were calculated for H_2O and D_2O via the classical MD and rigid-body CMD techniques; they are presented in Figs. 7.5 and 7.6. These structural functions, as determined from classical molecular dynamics, are essentially identical for H_2O and D_2O (see Section 3.3), and thus it is not necessary to include the classical D_2O radial distribution results in all further analysis.

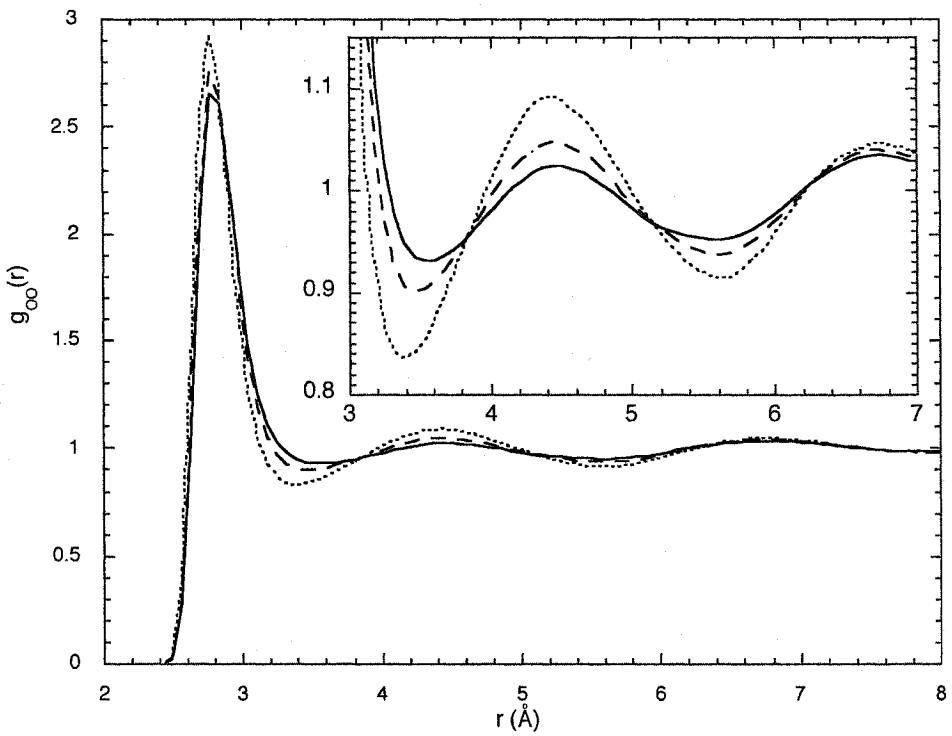

Figure 7.5. Oxygen-oxygen radial distribution function for the three systems: classical water (dotted line), quantum H_2O (solid line) and quantum D_2O (dashed line), all at ambient conditions.

Fig. 7.5 compares the oxygen-oxygen radial distribution functions for classical H_2O and quantum H_2O and D_2O. As expected, the quantum H_2O is the least structured and the classical H_2O (D_2O) is the most structured, while the quantum D_2O result lies in between. Hence, it is clear that as the system becomes more quantum mechanical there is effectively a softening of the structure with diminished peaks and raised valleys. This trend agrees with previous quantum simulation results performed on either flexible [13,15,19] or rigid water models [12,14], although the present results exhibit much better convergence (as can be seen in the insert of Fig. 7.5), presumably due to the longer length of real time simulation. The oxygen-hydrogen radial distribution functions, shown in Fig. 7.6, confirm the behaviour observed in $g_{OO}(r)$. The peak at 1.9 Å, associated with the hydrogen bond, clearly shows that classical H_2O water exhibits the strongest

hydrogen bonding, followed by the quantum D_2O and quantum H_2O liquids, respectively. The agreement between these results and previous simulations using flexible models confirms the previous observation [12] that most of the quantum effect in water comes from rotational uncertainty. Furthermore, the agreement between the present results and previously reported PI simulations with rigid water models reaffirms a very important property of CMD, that of generating equilibrium averages if the system is ergodic [111]. It is noteworthy that the simulations presented here are carried out with an orientational centroid constraint, while those of Rossky and co-workers [12,14] utilized rigid body quantum simulations where non-constrained path integrals were evaluated.

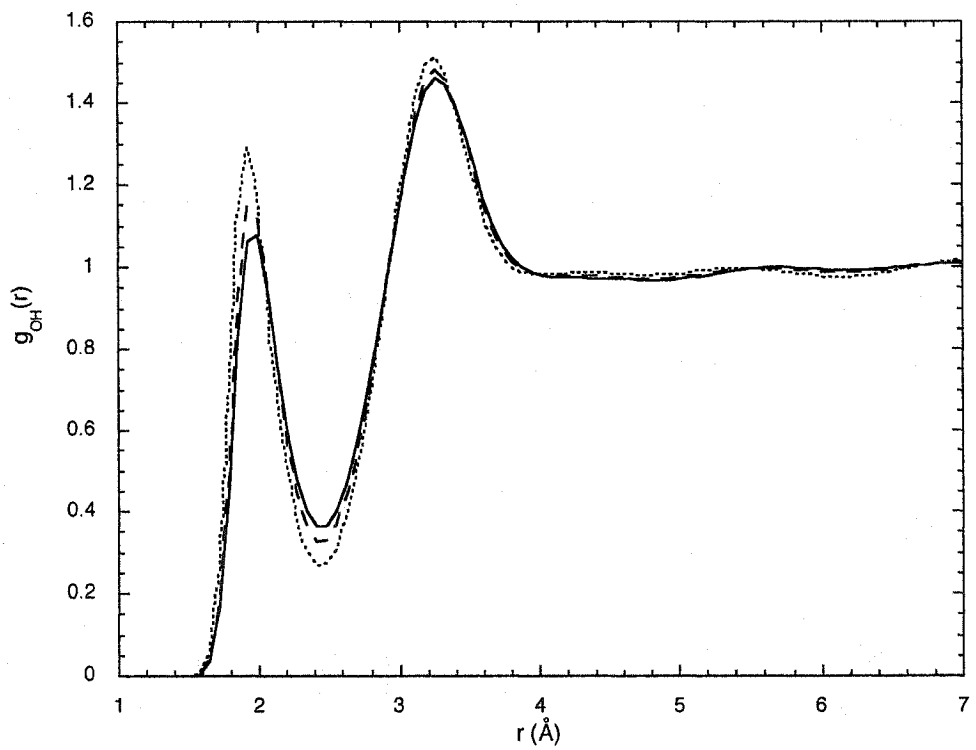

Figure 7.6. Oxygen-hydrogen radial distribution function for the three systems: classical water (dotted line), quantum H_2O (solid line) and quantum D_2O (dashed line), all at ambient conditions.

The apparent softening of the intermolecular interactions found in the quantum simulation results presented above (using a rigid model approximation) appear as a consequence, exclusively, of the effect of quantum mechanics upon molecular orientations. In liquid water, due to the low inertia moments of the molecule, there is a quantum mechanical uncertainty associated with the orientation of the molecule (which is directly related to the quantum uncertainty of the proton positions). Since in the context of the rigid body-CMD method each quantum molecule is represented by a set of coupled beads (which have the same center of mass but different orientations), the relative orientation of the beads is a measure of the molecular orientational uncertainty itself. Additionally, at high temperatures the molecular uncertainty becomes zero (i.e. the system becomes classical) and therefore it is convenient to define the average bead orientation (or centroid) as a reference orientation from which the beads expand to a certain angle, Γ.

In Fig. 7.7 the probability distributions of the bead-centroid angle Γ, as mapped by the rigid body-CMD methodology, are shown. These probability distributions are calculated by averaging over the angle (or curved distance) between each bead and the respective orientational centroid for all beads and all molecules. Clearly, they represent the quantum mechanical rotational uncertainty of the light and heavy water molecules in their liquids. (It is noted that although this probability distribution is expected to have a Gaussian shape if plotted versus the bead-centroid rotation angle through a particular axis, when plotted versus the bead-centroid rotation angle on an arbitrary axis it

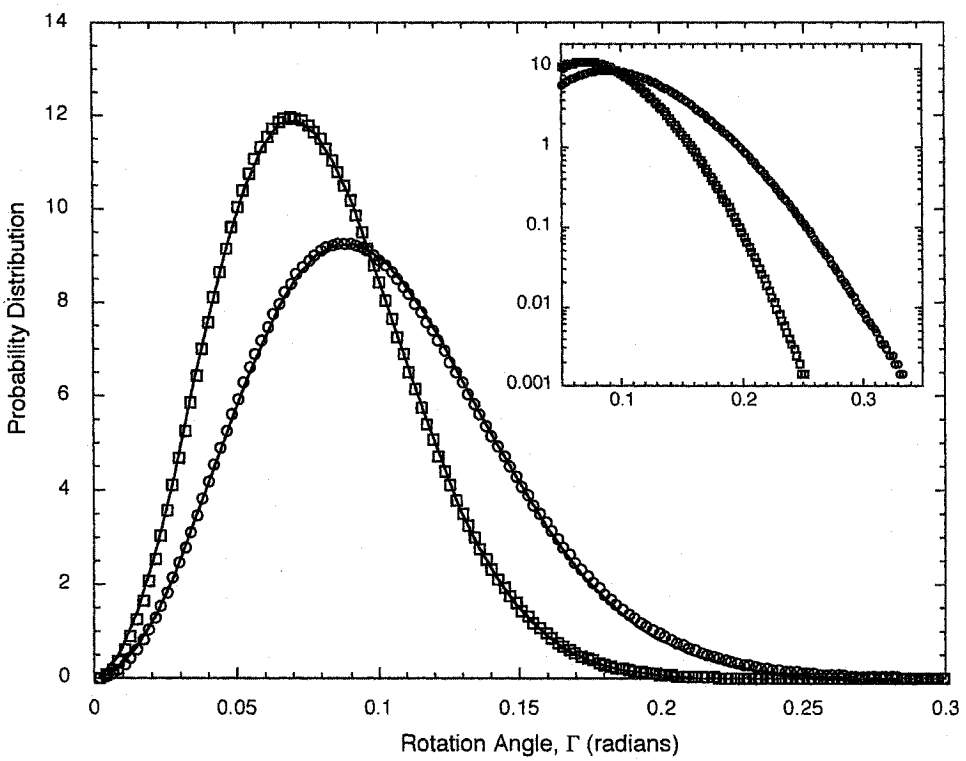

Figure 7.7. Normalized probability distribution of the bead-centroid. rotation angle. The circles and squares correspond to liquid H_2O and liquid D_2O, respectively.

approaches zero for small angles as the differential element of the rotation angle goes to zero). In this figure the symbols represent explicit data points, while the continuous lines represent fits of these points to the expected Gaussian behaviour. The tails of the probability distributions are expanded in the insert with a logarithm scale. As expected, the H_2O molecule has a significantly larger orientational uncertainty than the D_2O molecule, and this leads to an increased softening of the effective intermolecular potential for H_2O in relation to D_2O. The average orientational uncertainties (calculated as twice the average rotation angle between the beads and the centroid) of the H_2O and D_2O molecules are 11.3° and 8.9°, respectively, which is somewhat smaller than the value derived from the estimated de Broglie wavelength (~0.3 Å) of a free proton at room

temperature. It is also apparent from Fig. 7.7 that the probability of finding an angle between any bead and the centroid larger than $\pi/2$ (90°) is effectively zero, which is a requirement for the existence of a unique rotational centroid in the present approach [133] (see Section 6.2.2).

Table 7.1. Intermolecular potential energies (in kJ/mol) obtained in the classical and quantum simulations of liquid water at 25°C.

	Classical	Quantum		Relative shift (in %)	
		H_2O	D_2O	Class/H_2O	Class/D_2O
This work	-41.05±0.02	-37.43±0.02	-38.63±0.02	8.8	5.9
TIP4P[(a)]	-41.9	-39.1	-39.9	6.7	4.8
SPC[(a)]	-42.7	-39.7	-40.5	7.0	5.2
SPC/F[(b)]	-47.51±0.04	-43.69±0.06	-	8.0	-
SPC/F_2[(b)]	-49.44±0.04	-45.36±0.05	-	8.2	-
MCDHO[(c)]	-47.40±0.08	-41.0±0.4	-	13.5	

(a) Ref. [14], (b) Ref. [19], (c) Ref. [15].

In Table 7.1, the values of the average potential energies obtained in the present classical and quantum simulations are compared with previous calculations. The relative change in the potential energy due to the rotational quantization for the present H_2O and D_2O systems is 8.8% and 5.9%, respectively. It can be clearly seen that the classical-to-quantum shift in energy for light water is essentially identical to the relative changes found by Lobaugh and Voth [19] using the CMD methodology in an atomic approach on a flexible model. Our relative changes for H_2O and D_2O are, however, somewhat larger than those reported by Rossky and co-workers [12]. It is worth mentioning that the energy difference between the quantum D_2O and quantum H_2O simulations is 1.2 kJ/mol, and this result is very close to the difference in the experimental heats of vaporization of

D_2O and H_2O (1.4 kJ/mol [115]). Finally, is worth noting that although a very recent first principles study has reported that the "softening" observed above is apparently compensated by an increase in the molecular dipole moment [114], the quantitative extent of this compensation is unknown, as is the relationship between their energies and the experimental heats of vaporization.

7.2.2. Dynamical properties

Since the translational degrees of freedom have not been quantized, the translational dynamical information of the present quantum simulations is immediately available from the centroid time correlation function. The velocity autocorrelation function for classical and quantum H_2O and D_2O systems is presented in Fig. 7.8. It is apparent that there is a significant difference between the classical and the quantum results of liquid H_2O (see Fig. 7.8a). The principal changes seen in this function are the loss of structure (i.e. a dampening of the oscillatory behaviour) and a shift of the maxima and minima to longer times for the quantized system with respect to the classical simulation result.

These differences are consistently smaller in the D_2O system, although still noticeable (see Fig. 7.8b). In order to interpret this effect, we remark that the principal intermolecular forces in water (hydrogen bond interactions) are very directional, but in the quantum system the forces are averaged over the molecular rotational uncertainty. These averaged (or centroid) forces are smaller than the classical ones, and consequently they generate a more strongly dampened velocity time correlation function with

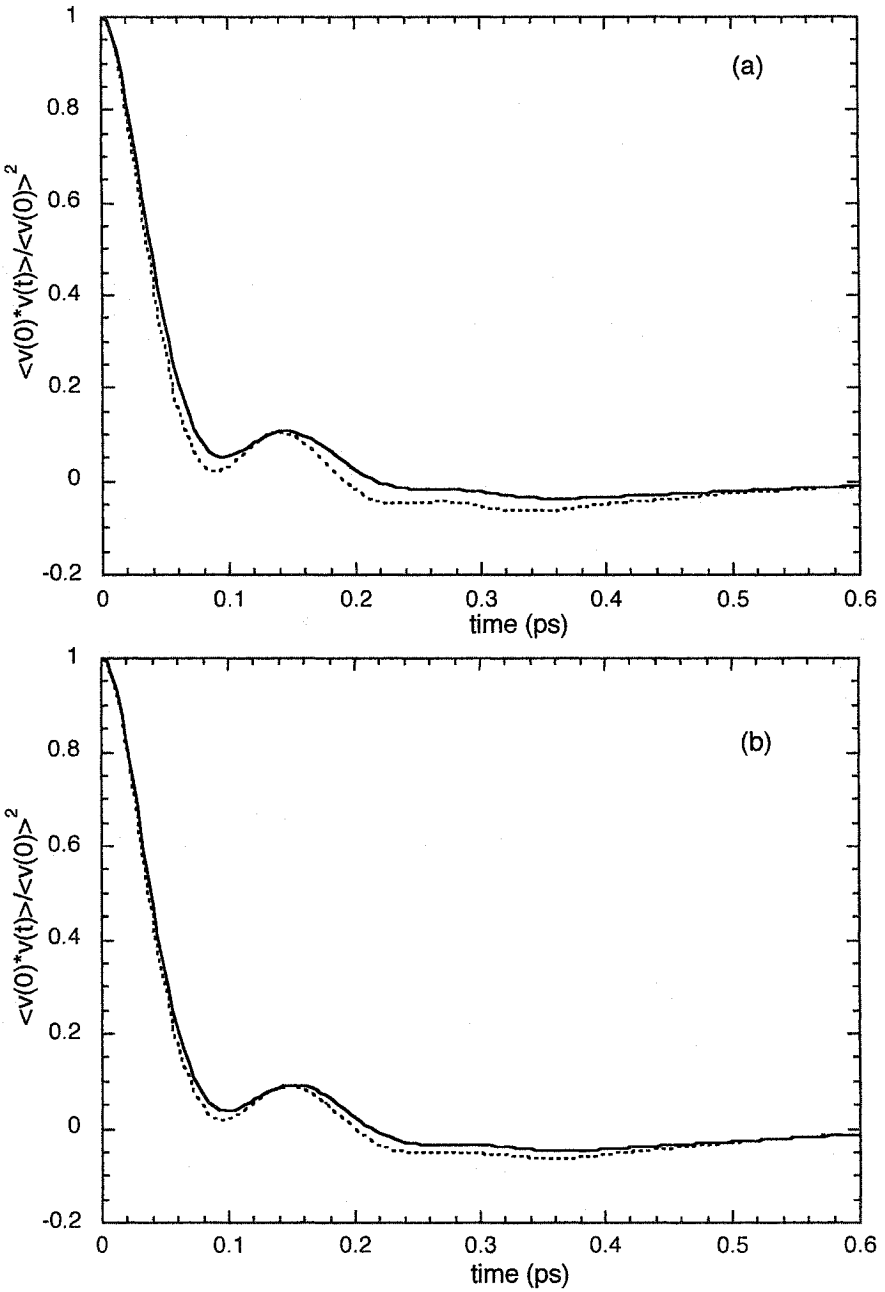

Figure 7.8. Linear velocity time correlation functions of classical and quantum (a) H_2O and (b) D_2O. The dashed lines correspond to classical results and the solid lines correspond to quantum results.

maxima and minima shifted towards longer times. Hence, the quantum system is not only less structured in space (as discussed above) but is also less correlated in time in comparison with the classical system. We have also observed that for the Cartesian

components of the velocity time correlation function (not shown), each of the individual x, y or z components of the velocity time correlation function experience such "softening"; however, there is no evidence of this shift being particularly larger in any specific direction.

Table 7.2. Translational self-diffusion coefficients, in units of 10^{-5} cm^2/s, for TIP4P liquid water at 25°C. The errors of the calculated values are about 1%. The experimental values are from Ref. [139].

System		D	D_x	D_y	D_z	Exp
H_2O	Class	3.58	3.36	4.25	3.14	2.3
	Quant	5.48	5.18	6.51	4.74	
D_2O	Class	3.45	3.22	4.14	2.98	1.9
	Quant	4.57	4.35	5.39	3.97	
H_2O/D_2O	Class	1.04	1.04	1.03	1.05	1.21
	Quant	1.20	1.20	1.21	1.19	

Table 7.2 presents the translational self-diffusion coefficients and their local frame components obtained for the classical and quantum simulations of light and heavy liquid water through the well known relationships [4,139],

$$D_\alpha = \int_0^\infty \langle [\mathbf{v}_\alpha(0)\cdot\mathbf{e}_\alpha(0)]\cdot[\mathbf{v}_\alpha(t)\cdot\mathbf{e}_\alpha(0)]\rangle dt \qquad (7.1)$$

and

$$D = \frac{1}{3}\sum_\alpha D_\alpha , \qquad (7.2)$$

where $\mathbf{e}_\alpha$ are the unit vectors of the principal frame ($\alpha = x,y,z$) and $\mathbf{v}_\alpha(t)\cdot\mathbf{e}_\alpha(0)$ is the

α component of the linear velocity of the center of mass defined in the local frame at $t = 0$. The local frame is defined such that the z axis lies along the axis of symmetry and the x axis is in the plane of the molecule. As can be seen from Table 7.2 the quantum self-diffusion coefficients are, as expected, larger than the classical values, the effect being most pronounced for light water. The discrepancy between the absolute values and the experimental results are due to the TIP4P parametrization of the water-water interaction which, even classically, overestimates the self-diffusion coefficient. We note, however, that the isotopic ratio of the self-diffusion coefficient from the quantum calculations is significantly closer than the corresponding classical value to the experimental isotopic ratio, which implies that the quantum simulations much more accurately capture the differences between the dynamics of H_2O and D_2O. The isotopic ratio obtained from our classical simulations with the TIP4P potential are in excellent agreement with that previously obtained for the SPC/E model [139], confirming the inability of classical dynamics to capture isotopic effects in liquid water.

The effect of quantization given as the ratio $D_{H_2O}^{quan}/D_{H_2O}^{class}$ is in very good agreement with previously reported results from CMD simulations. The ratio $D_{H_2O}^{quan}/D_{H_2O}^{class}$ of 1.7±0.8 reported by Lobaugh and Voth [19] is statistically indistinguishable from the present value of 1.53±0.09. Again, the significantly smaller error bar arises from our significantly longer real time trajectories. We note that Guillot

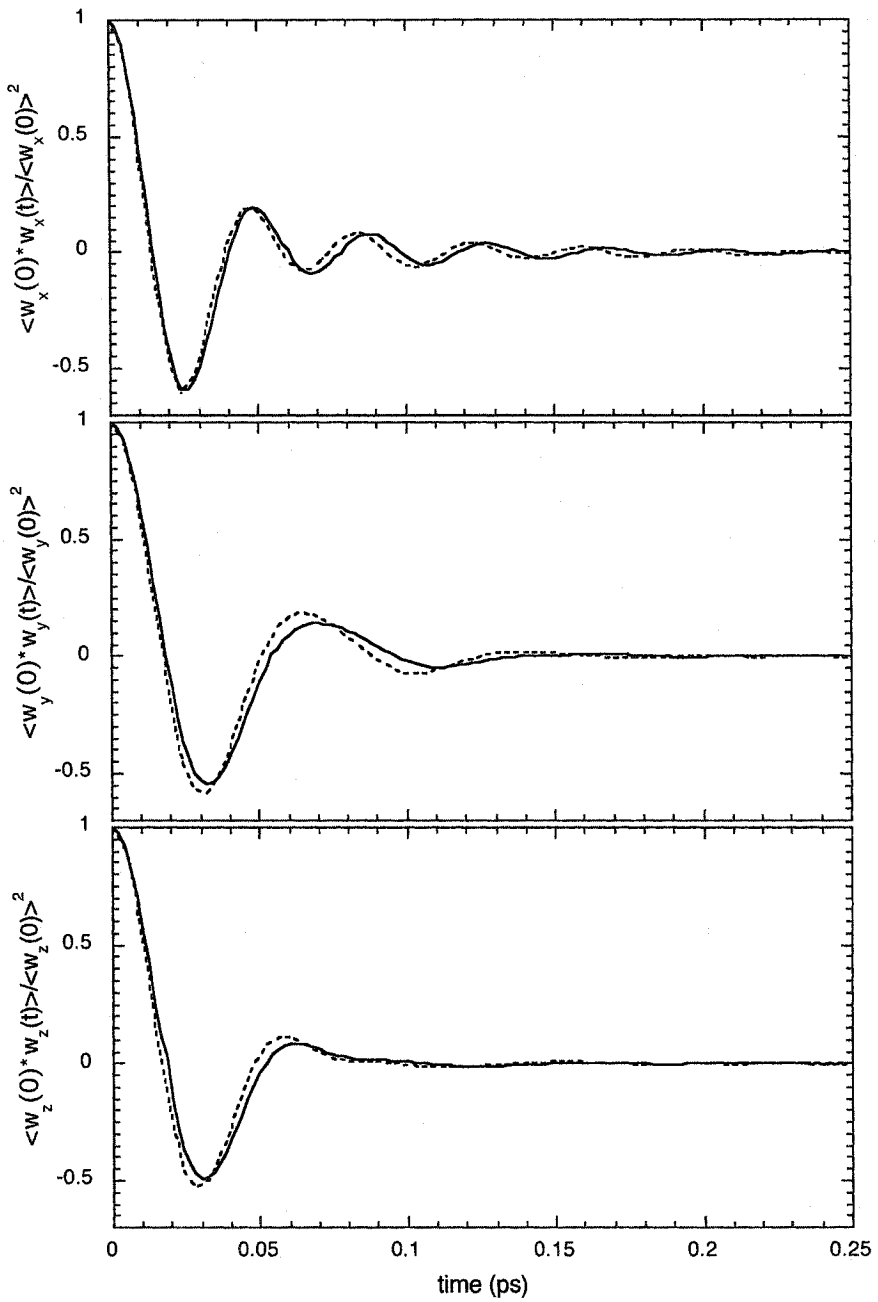

Figure 7.9. Components of the angular velocity time correlation function of liquid H_2O. The dashed lines correspond to the classical functions and the solid lines correspond to the quantum results.

and Guissani [20] in their effective quantum potential simulations also found a ratio of 1.7, but have not reported error bars. It is important to emphasize that the roughly 50% increase in the translational diffusion constant, in going from classical to quantum

dynamics for liquid H_2O, is even more dramatic taking into account that this effect is an indirect consequence of the quantization (in the sense that is the rotational and not the translational motion that has been treated quantum mechanically). The fact that the orientational quantization is found to have a significant impact on the translational dynamics is clearly a consequence of the strong coupling between the rotational and translational motions of water molecules in the liquid.

In order to determine angular velocity quantum time correlation functions, we recall that the CMD approach offers the possibility of extracting approximated quantum correlation functions, $\langle A(t)A(0)\rangle$, from the centroid correlation function, $\langle A^{(c)}(t)A^{(c)}(0)\rangle$, which can be accumulated during the simulation. These two correlation functions are related in frequency space by (see Equation 5.46) [19,105-111]

$$I(w) = (\hbar w/2)\left[\coth(\hbar w/2) + 1\right] I^{(c)}(w), \tag{7.3}$$

where $I(w)$ and $I^{(c)}(w)$ are the Fourier transforms of the quantum and centroid correlation functions, respectively. In Fig. 7.9 the components of the angular velocity time correlation function of liquid H_2O as obtained from classical and quantum simulations are shown. In the *x* component, we see a shift of the maxima and minima in the quantum correlation function towards longer times with respect to the classical result. In the *y* and *z* components, we additionally observe a very significant dampening of the oscillations in the quantum functions relative to the classical ones.

These observations are further clarified in Fig. 7.10 where the power spectra of two components of the angular velocity time correlation function are shown. Since the z and y components (which are oriented along the dipole moment and perpendicular to the molecular plane, respectively) have similar time dependence (see Fig. 7.9) their power spectra have a similar shape and we have chosen to include only one of them. The power spectrum of the x-component, which is associated with the smallest inertial moment, appears skewed towards higher frequencies while the y and z components have a more symmetric shape. The observed bands at about 700 and 500 cm^{-1}, which are due to the librational oscillations of the molecule in the liquid, are clearly shifted to lower frequencies in the quantum simulation. This shift to lower frequencies observed in the

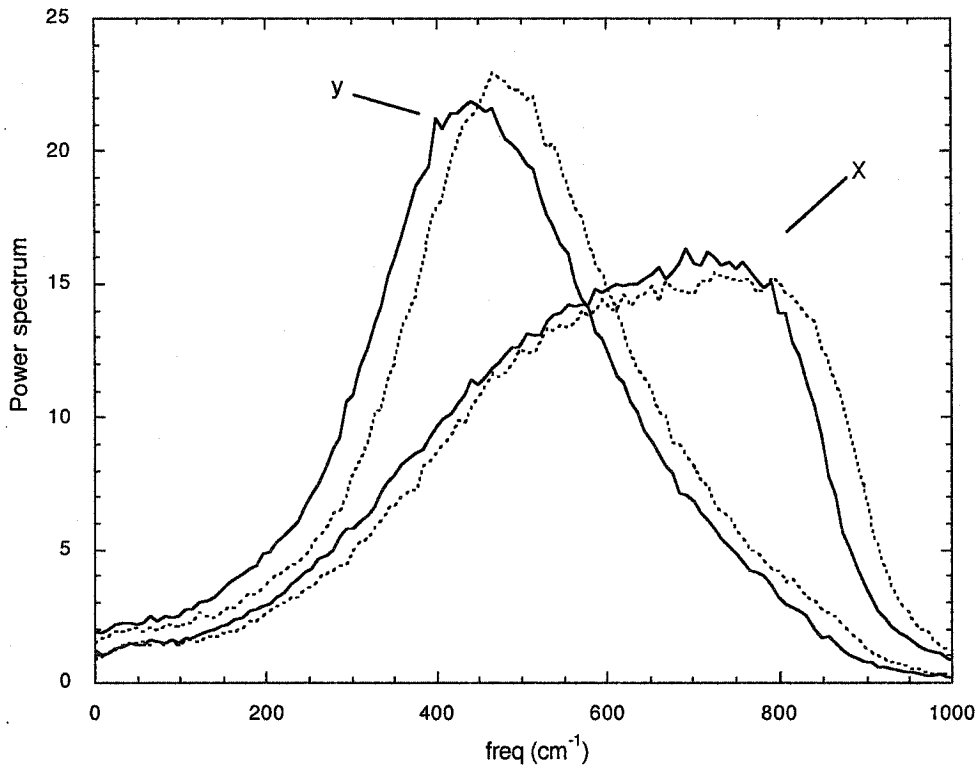

Figure 7.10. Power spectra of the x and y components of the angular velocity time correlation function of liquid H_2O. The dotted lines correspond to the classical simulation and the solid lines correspond to the quantum simulation.

quantum simulation results is, obviously, a reflection of the slower oscillatory behaviour in the quantum time correlation functions in relation to the classical behaviour, as seen in Fig. 7.9. The dampening of the oscillations of the y-component of the quantum time correlation function (see Fig. 7.9) appears in Fig. 7.10 as a decrease in the intensity of the principal band in its power spectrum. These effects can again be associated with the apparent softening of the interaction potential as a consequence of the CMD averaging of the centroid torques, and as expected they were found to be smaller for D_2O than for H_2O. The differences observed between the effects of quantization on the x, y and z components of the angular velocity appear to be a consequence of the uneven impact of the softening within the (heterogeneous) local molecular environment (which will be examined in detail below). It is interesting to point out that direct use of the centroid angular velocity time correlation function instead of the approximate quantum time correlation function (obtained from Equation 7.3) does not change the above observations. This indicates that most of the effects of quantization are already captured directly with the classical-like evolution of the centroid (due to the effective centroid potential).

The single-molecule orientational autocorrelation functions, $C_1^z(t)$ and $C_2^z(t)$, defined as

$$C_k^z = \left\langle P_k\left[\mathbf{e}_z(t)\cdot\mathbf{e}_z(0)\right]\right\rangle, \tag{7.4}$$

where $\mathbf{e}_z$ is the z-axis of the molecule (aligned with molecular dipolar vector) and P_k denotes the Legendre polynomial of order k, were obtained from the present simulations

of the liquid H_2O and D_2O systems. Spectral functions were then calculated as [140]

$$I_k^z = w^2 \,\mathrm{Re}\int_0^\infty C_k^z(t)\exp(iwt)dt. \tag{7.5}$$

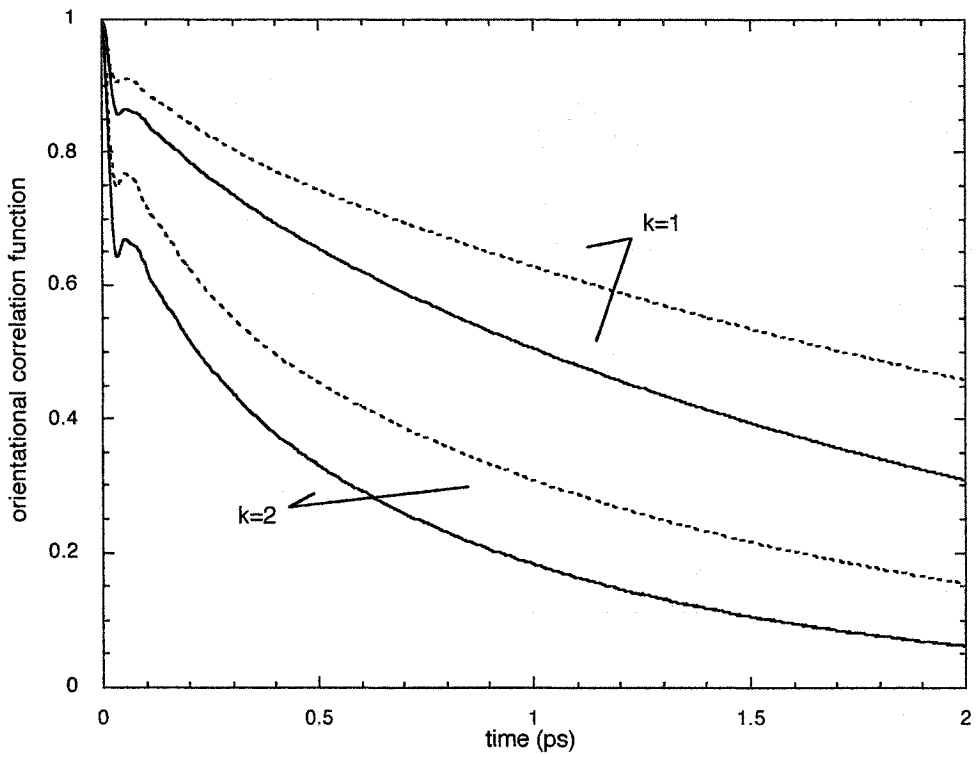

Figure 7.11. Single molecule orientational correlation functions associated with the Legendre polynomial of order k=1 or k=2. The dashed lines correspond to the classical results and the solid lines correspond to the quantum functions.

The functions $C_1^z(t)$, $C_2^z(t)$, $I_1^z(w)$ and $I_2^z(w)$ determined for the liquid H_2O system are presented in Fig. 7.11 and Fig. 7.12. A significant increase of the rate of decay is observed in Fig. 7.11 in the time domain behaviour of $C_1^z(t)$ and $C_2^z(t)$ from the quantum simulations. A slight shift to longer times of the peak at about 0.1 ps is better resolved in the frequency domain spectrum of Fig. 7.12 as a shift to lower frequencies of

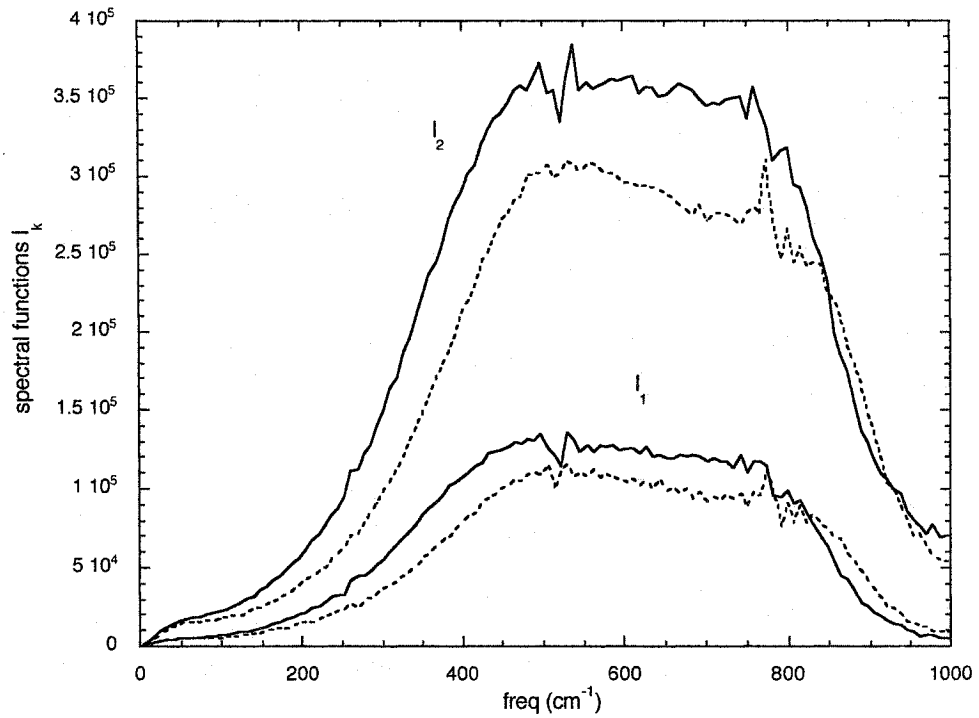

Figure 7.12. Spectral functions I_1 and I_2. The dashed lines represent the classical results and the solid lines represent the quantum curves.

the quantum result. The wide band located from 300 to 700 cm^{-1} in Fig. 7.12 is characteristic of the molecular librational motion of the molecular dipole in the liquid and has been previously reported in Raman experiments [141] and in classical simulation studies of light and heavy liquid water [140]. It is interesting to note that the shift observed here is somewhat similar to the one reported previously in classical simulations [140] and associated with an increase in the temperature of the liquid. The analogy between quantum effects and the effects of raising the temperature, made in the early simulation studies of the structure of quantum water [12], is discussed in Sections 7.3 and 7.4. As expected, it was also found that the shift associated with the softening of the

potential is stronger within liquid H_2O than in D_2O in comparison to their classical counterparts.

From the quantum and classical orientational auto-correlation functions, $C_1^z(t)$ and $C_2^z(t)$, relaxation times can be calculated and compared. The single molecule orientational correlation times, or self-times, have been obtained by integrating the appropriate autocorrelation functions, i. e. $\tau_k^z = \int_0^\infty C_k^z(t)dt$. In this study the orientational autocorrelation functions have been determined to sufficiently long times (2 ps) to allow the dominant contributions to τ_k^z to be obtained by direct numerical integration. The appropriate tail corrections to the self-times were evaluated by assuming a simple exponential decay in $C_k^z(t)$ at long times.

Table 7.3. Molecular and collective (dielectric) relaxation times (in ps) for TIP4P liquid water at 25°C. Experimental values are from Ref. [139].

System		τ_1^z	τ_2^z	τ_D
H_2O	Class	2.79±0.03	0.952±0.005	7±1
	Quant	1.71±0.03	0.578±0.005	4±1
	Exp	-	-	8.3
D_2O	Class	3.16±0.03	1.073±0.005	7±1
	Quant	2.33±0.03	0.781±0.005	5±1
	Exp	-	-	10.4
D_2O/H_2O	Class	1.13	1.13	1.0
	Quant	1.36	1.35	1.2
	Exp	-	-	1.26

The self-times values obtained, listed in Table 7.3, are similar to those reported previously by other authors [19,139] and represent a further confirmation that the diffusive motion in a quantum liquid is faster than in a classical one. For example, the ratio ($\tau_1^{z\,class} / \tau_1^{z\,quant}$) was reported by Lobaugh and Voth [19] as 1.5±0.5 while in this study we have obtained essentially the same value, 1.6±0.07, where the considerably smaller errors bars arise from the much longer real time trajectories of the present work. It is clearly seen from Table 7.3 that quantization sharply decreases the relaxation times for liquid H_2O, although it has a lesser impact in D_2O, as expected and in agreement with the results presented above.

The collective (or dielectric) relaxation times obtained from

$$\tau_D = \int_0^\infty \frac{\langle \mathbf{M}(t) \cdot \mathbf{M}(0) \rangle}{M^2} \qquad \textbf{(7.6)}$$

for classical and quantum simulations of D_2O and H_2O are also presented in Table 7.3. It can be again seen that the impact of rotational quantization is quite significant, especially in H_2O. While the absolute values obtained from the quantum simulations shift farther from the experimental results, the isotopic ratios calculated from the quantum simulations appear to approximate more closely the experimental isotopic ratio. However, the relatively large errors associated with these collective relaxation times make it difficult to draw any specific conclusions about the values of the ratios given in Table 7.3. Nevertheless, the errors associated with the present results are considerably smaller than those of other quantum simulation studies [19].

7.2.3. Model comparison

It is important to demonstrate that the results presented in Sections 7.2.1 and 7.2.2 are sufficiently general, and consistent for several different water models. In order to examine the dependence of the isotopic effects on the choice of water model, quantum simulations were carried out on two other rigid water models, the SPC/E [67] and TIP4Pew [68] potentials. The conditions under which these simulations were carried out were identical to those used for the TIP4P model [61], results for which have already been presented.

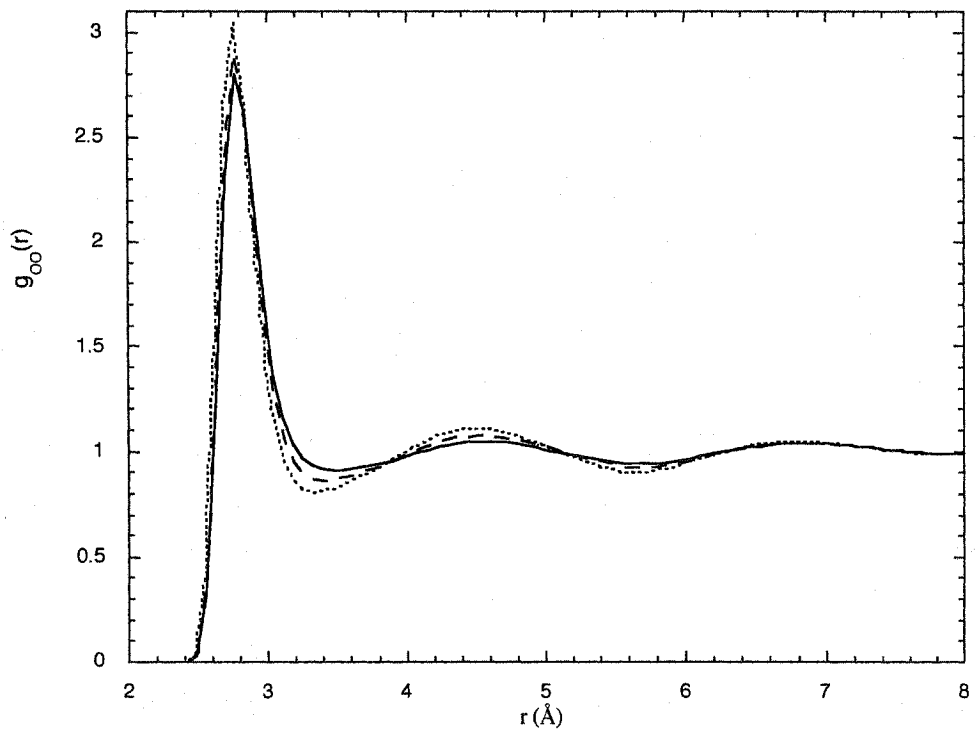

Figure 7.13. Oxygen-oxygen radial distribution function of liquid SPC/E water at ambient conditions. The dotted, solid and dashed lines correspond to the classical, quantum H_2O, quantum D_2O results, respectively.

Fig. 7.13 shows the oxygen-oxygen radial distribution function obtained in classical and quantum simulations of light and heavy SPC/E water. The result for

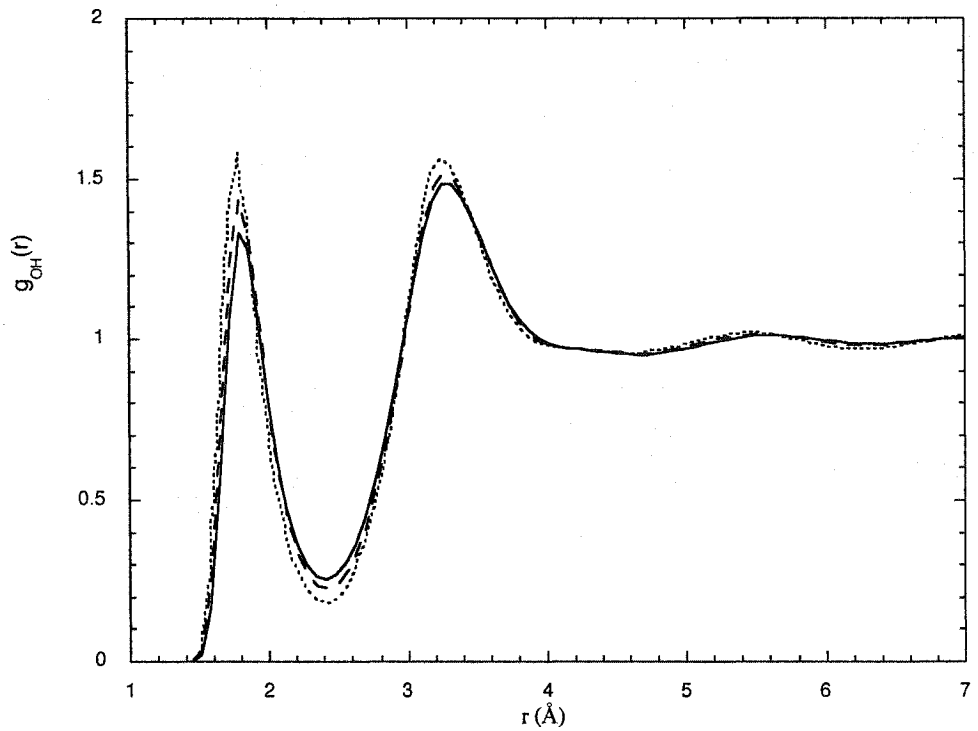

Figure 7.14. Oxygen-hydrogen radial distribution function of liquid SPC/E water at ambient conditions. The dotted, solid and dashed lines correspond to the classical, quantum H_2O, quantum D_2O results, respectively.

classical D_2O coincides with classical H_2O and is not shown. Once again, one observes that the classical system is more structured, followed by quantum D_2O and the least structured quantum H_2O systems. A comparison with Fig. 7.5 indicates that the effect of quantization is qualitatively extremely similar. This observation is further confirmed with the oxygen-hydrogen radial distribution function for SPC/E presented in Fig. 7.14. The oxygen-oxygen and oxygen-hydrogen radial distribution functions for TIP4Pew also qualitatively confirm these results (and are not shown).

A quantitative analysis of the model dependence can be carried out on values of intermolecular potential energies, relative energy shifts and average molecular uncertainties (calculated as in Section 7.2.1). Table 7.4 reports values obtained for these

quantities for the SPC/E and TIP4Pew water models. The results indicate that the TIP4Pew and SPC/E models show a slightly smaller quantum shift in the energy than was found for TIP4P. The values calculated for the TIP4Pew water model are generally closer to the values of the TIP4P potential. This result is reasonable considering that the TIP4Pew [68] model is much similar to TIP4P [61] than is the SPC/E [67] model (see Section 3.2). It is also interesting to note that the estimated values of the molecular uncertainty are also slightly smaller than the ones presented previously for TIP4P. Furthermore, it is reasonable to expect that the smaller the molecular uncertainty, the smaller the quantum effects in the energy should be. This hypothesis is confirmed by comparing the values of molecular uncertainty for light water presented in Table 7.4 with the corresponding value of TIP4P. The energy shifts in quantum D_2O, on the other hand, are less dependent on the estimated molecular uncertainty.

Table 7.4. Energies, relative energy shifts and quantum molecular uncertainties (see text) values for the SPC/E and TIP4Pew water models at 25°C.

Model	System		Energy (kJ/mol)	Relative shift (%)	Quantum uncertainty (°)
SPC/E	Class		-45.93	-	0
	Quant	H_2O	-42.33	7.8	10.7
		D_2O	-43.48	5.3	8.5
TIP4Pew	Class		-45.99	-	0
	Quant	H_2O	-42.11	8.4	11.0
		D_2O	-43.58	5.2	8.9

Table 7.5. Self-diffusion coefficients in 10^{-5} cm^2/s for the SPC/E and TIP4Pew water models. The errors are about 1% of the reported values.

Model	System	D	D_x	D_y	D_z
SPC/E	Class H_2O	2.49	2.30	3.25	1.93
	Quant H_2O	3.90	3.66	4.90	3.15
	Class D_2O	2.48	2.26	3.21	1.97
	Quant D_2O	3.34	3.09	4.29	2.64
	Cl (H_2O/D_2O)	1.00	1.02	1.01	0.98
	Qu (H_2O/D_2O)	1.17	1.18	1.14	1.19
TIP4Pew	Class H_2O	2.41	2.20	2.97	2.06
	Quant H_2O	4.07	3.90	4.93	3.39
	Class D_2O	2.37	2.18	2.94	1.98
	Quant D_2O	3.42	3.23	4.10	2.91
	Cl (H_2O/D_2O)	1.02	1.01	1.01	1.04
	Qu (H_2O/D_2O)	1.19	1.21	1.20	1.16

Table 7.5 reports the values of the self-diffusion coefficient obtained in the classical and quantum simulations of liquid samples with the SPC/E and TIP4Pew potentials. For the SPC/E model, the *y* component appears to have the smallest quantum H_2O/D_2O ratio, whereas in the TIP4Pew model it is the *z* component that is smallest. However, since these differences are just at the limit of the estimated errors they may well represent numerical noise. This is consistent with the fact that in the TIP4P results all the components had essentially the same quantum H_2O/D_2O ratio (see Table 7.2). Importantly, the results show that, independent of the model chosen, the H_2O/D_2O ratios of the self-diffusion coefficients calculated through quantum simulations are in much better agreement with experiment than the values determined classically. This indicates

that the present quantum simulations, in comparison with the classical calculations, make a significant improvement in relation to the description of the microscopic dynamics of the system.

Table 7.6. Molecular and collective (dielectric) relaxation times (in ps) for the SPC/E and TIP4Pew water models.

System		τ_1^z	τ_2^z	τ_D
SPC/E	Class H_2O	4.14±0.03	1.405±0.005	10±1
	Quant H_2O	2.63±0.03	0.871±0.005	6±1
	Class D_2O	4.80±0.03	1.620±0.005	12±1
	Quant D_2O	3.53±0.03	1.172±0.005	10±1
	Cl (D_2O/H_2O)	1.16	1.15	1.2
	Qu (D_2O/H_2O)	1.34	1.34	1.7
TIP4Pew	Class H_2O	4.28±0.03	1.462±0.005	11±1
	Quant H_2O	2.42±0.03	0.811±0.005	6±1
	Class D_2O	4.80±0.03	1.631±0.005	10±1
	Quant D_2O	3.44±0.03	1.160±0.005	9±1
	Cl (D_2O/H_2O)	1.12	1.12	0.9
	Qu (D_2O/H_2O)	1.42	1.43	1.5

The effect of quantization in the dynamics can be estimated with the $D_{H_2O}^{quan}/D_{H_2O}^{class}$ ratio. The results obtained for SPC/E and TIP4Pew water are 1.56 and 1.69, respectively. These values are in very good agreement with previously reported results [19] and with the TIP4P ratio of 1.53 (see Table 7.2). This agreement is further confirmation of the relevance of the quantum mechanical effects in the microscopic dynamics of liquid water.

Table 7.6 contains the calculated values of several relaxation times for the SPC/E and TIP4Pew molecular models. The classical and quantum molecular relaxation time ratios obtained for these two models are comparable with the ones obtained for the TIP4P water potential (see Table 7.3). For the three models, the quantum ratios are significanlty larger than the classical ones, in agreement with the expected faster dynamics in the quantum system. Once again, quantization significantly increases the relaxation dynamics of the system, in agreement with the results reported above for TIP4P water (see Section 7.2).

7.3. TEMPERATURE DEPENDENCE

Changes in temperature can be expected to modify the influence of quantization. In the path integral picture this is clearly seen by noting that in the limit $\beta \rightarrow 0$ (high temperatures) the imaginary time "trip" collapses to zero (since $\tau = -i\beta\hbar$) and the quantum mechanical partition function approaches the classical one (see, for example, Equation 4.36). Alternatively, since quantization introduces a softening of the intermolecular interaction (see Sections 7.2.1 and 7.2.3), it has been asserted [12] that the effects of quantization in the structural properties of a system are somewhat analogous to raising the classical system's temperature. In liquid water, in particular, Kuharsky and Rossky [12] found the structural properties of quantum liquid water at room temperature to be similar to the structural properties of classical water 50 degrees hotter. This analogy turns out to be a useful way to illustrate the importance of quantization in liquid water. In this section, the discussion focuses on two issues. The increasing importance of quantum

effects with the decrease of the temperature, and the analogy between quantum effects and temperature changes.

Table 7.7. Details of the classical and quantum liquid simulations of TIP4P water.

TEMP (°C)	SYSTEM	RUN LENGTH (ns)	DENSITY (g/cm^3)
-35	Class	2	0.973250[a]
	Quant	1	
-20	Class	1.6	0.993490[b]
	Quant	1	
0	Class	1	0.999868[b]
	Quant	1	
25	Class	0.4	0.997075[b]
	Quant	0.5	
50	Class	0.4	0.988066[b]
	Quant	0.25	
100	Class	0.4	0.958384[b]
	Quant	0.25	

(a) from references [143,144],(b) from reference [145]

Quantum and classical simulations were carried out on the TIP4P water model over a range of temperatures, from 100 °C to –35 °C. The classical simulations were realized with a standard molecular dynamics code and the quantum simulations were performed via rigid body-CMD. The run length and the (experimental) densities used in the simulations are given in Table 7.7. The values at 25 °C (results presented in Sections 7.2.1 and 7.2.2) have also been included for completeness. It is important to note that the length in real time and of the quantum simulations at 0, -20 and -35 °C was 1 ns. To help achieve these long runs, the evaluation of the forces and torques for each bead was

performed in parallel in the simulation code by using the Open-MP protocol (Open-Multi Processing protocol [142]).

The oxygen-oxygen radial distribution functions at –20°C and 50°C for classical and quantum liquid water are presented in Fig. 7.15. The classical results reveal that there is a very strong temperature dependence of the maximum of this function at 2.8-2.9Å (see also Fig. 7.5). Although both maxima in the classical results decrease with quantization, the effect of the softening of the structure is more pronounced at the lower temperature. At 50°C, while the classical $g_{OO}(r)$ retains some structure, the quantum radial distribution function exhibits only a "nearest neighbor" first peak, which indicates that structural quantum effects are still significant at this temperature. The oxygen-hydrogen RDFs (not shown) confirmed the observations made in Fig. 7.15.

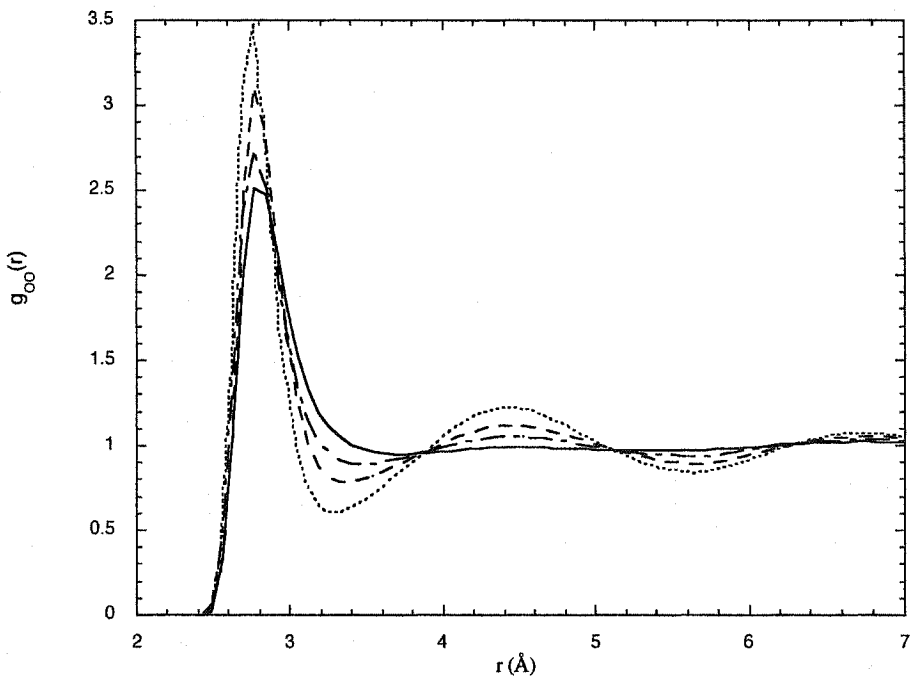

Figure 7.15. Oxygen-oxygen radial distribution function of liquid TIP4P water at –20°C and 50°C. The dotted, dashed, dashed-solid and solid lines correspond to the –20°C-classical, –20°C-quantum, the 50°C-classical and 50°C-quantum simulation results, respectively.

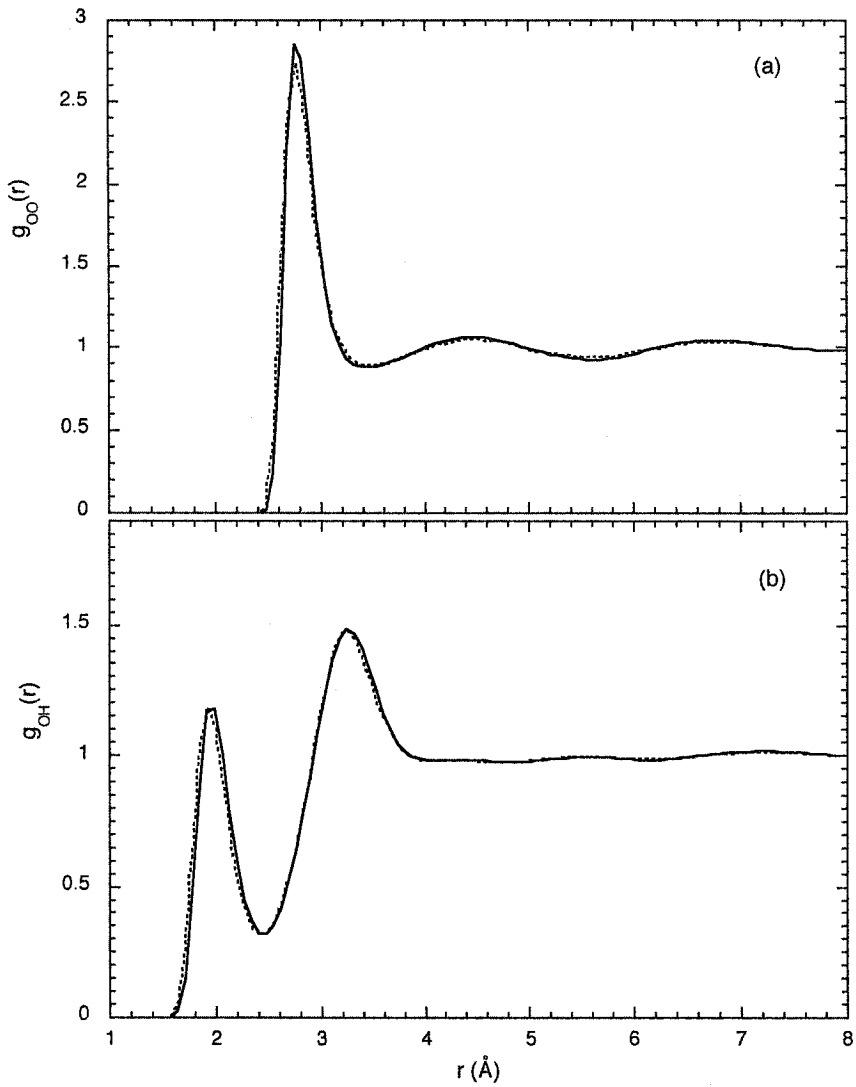

Figure 7.16. Oxygen-oxygen (a) and oxygen-hydrogen (b) radial distribution functions of liquid TIP4P water at 0°C and 50°C. The solid lines correspond to the quantum simulation results at 0°C while the dotted lines correspond to classical results at 50°C.

A direct examination of the analogy between quantum and temperature effects is made in Fig. 7.16. In this figure, the RDFs from quantum simulations at 0°C are compared with the RDFs of classical liquid water at 50°C. The functions exhibit very similar behaviour, in agreement with Kuharsky and Rossky's observations [12]. It constitutes clear evidence that quantum effects in liquid water are significant. The quantum oxygen-oxygen RDF at 0°C has a slightly higher maximum at ~2.8 Å in

comparison with the classical oxygen-oxygen RDF at 50°C. The first peak in the quantum oxygen-hydrogen RDF at 0°C, however, appears shifted slightly towards larger radii in relation to the classical RDF at 50°C. These differences suggest that, although the analogy is qualitatively valuable, its quantitative implications may change with the property under examination.

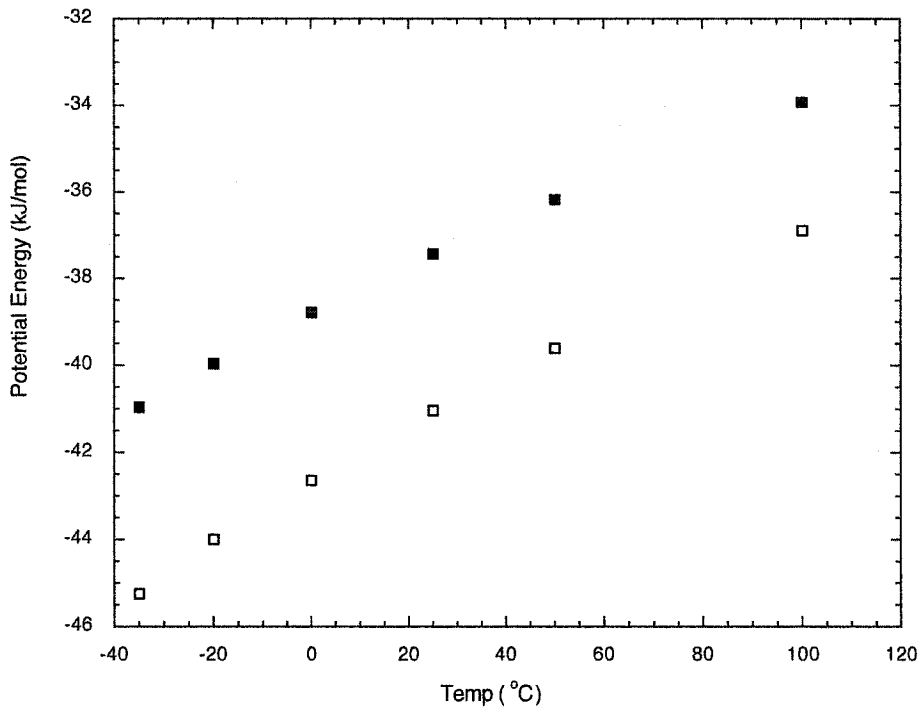

Figure 7.17. Average intermolecular potential energies in kJ/mol as a function of temperature. The solid squares are values from the quantum simulations and the open squares are the classical results.

The values obtained for the average potential energy in the classical and quantum simulations are plotted in Fig. 7.17 as a function of temperature. At all temperatures, the quantum energy is higher than the classical one, and the difference between them increases when moving towards lower temperatures. Interestingly, the energy difference, quantum-minus-classical, grows almost linearly in this temperature range indicating a consistently smaller heat capacity for the quantum system in agreement with Kuharsky

and Rossky results [12]. It is easily observed from Fig. 7.17 that the average energy from the quantum simulation at –35 °C is very similar to the classical result at 25 °C, suggesting a temperature "shift" due to quantization of 60 °C for this property. This observation agrees with the analogy between the impact of quantum effects on the equilibrium or structural properties and an apparent temperature increase [12], although the shift is somewhat larger than the ones found in the RDF comparisons (Fig. 7.16).

The differences between the classical and quantum systems arise as a consequence of the quantum mechanical molecular (orientational) uncertainty of the quantum water molecule. Therefore, it is interesting to pose the question "how does the quantum mechanical uncertainty in liquid water change with temperature?" It can be read in virtually any textbook on the subject (see, for example, [1-3]) that the quantum mechanical uncertainty of a particle's coordinates (for example, in an atomic system) is expected to grow when temperature is lowered. A simple and general rationale for this behaviour is that a lower average kinetic energy means a lower uncertainty in momentum and, as a consequence, a higher uncertainty in the particle's position. This analysis is strictly valid only for systems composed of weakly interacting particles. However, a decrease in temperature will lead to an increased order and, in a system with relatively strong interactions, this effect may be quite substantial. In such circumstances, the potential energy may become sufficiently influential such that the quantum mechanical uncertainty does not increase with the lowering of the temperature, but in fact remains constant or even decreases.

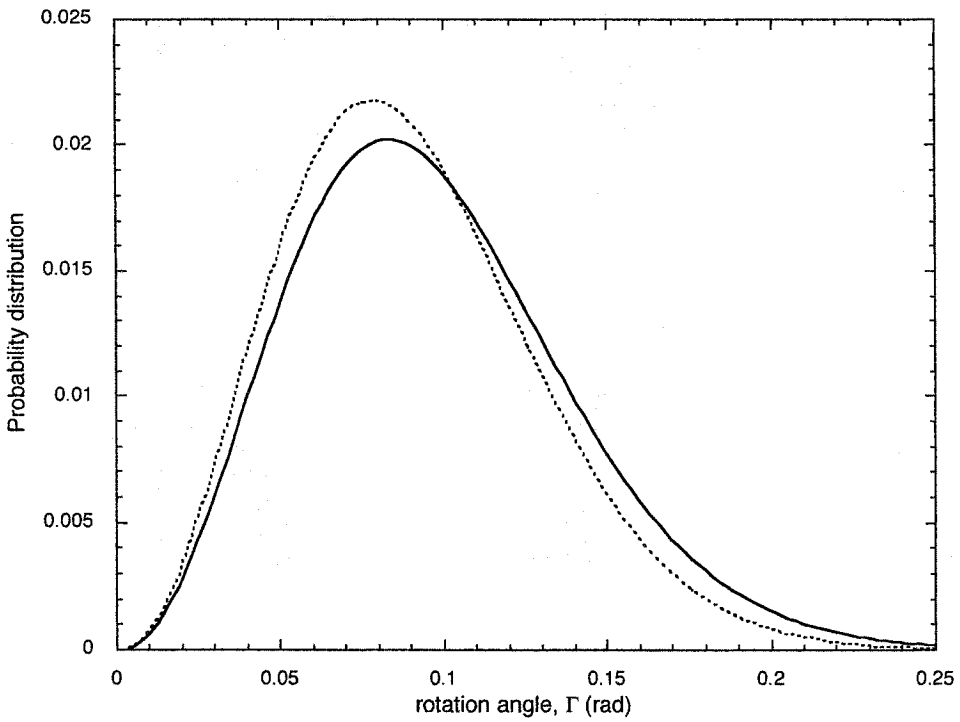

Figure 7.18. Probability distribution of the bead-centroid angle for ice Ih at –38°C (dotted line) and liquid water at –35°C (solid line).

Let's begin an exploration of the above mentioned question for water. Fig 7.18 displays the probability distribution of the bead-centroid average angle for ice-Ih and liquid water at –38°C and –35°C, respectively. The details of the application of the rigid body-CMD methodology to ice Ih are discussed in the next chapter (although they are very similar to those presented in section 7.1); the ice Ih results are included in Fig. 7.18 as they are of particular relevance to the current discussion. Specifically, it is apparent from those distributions that the molecular uncertainty is smaller for ice Ih than it is for water at essentially the same temperature, indicating a significant influence of the local molecular environment on the magnitude of the quantum mechanical orientational uncertainty.

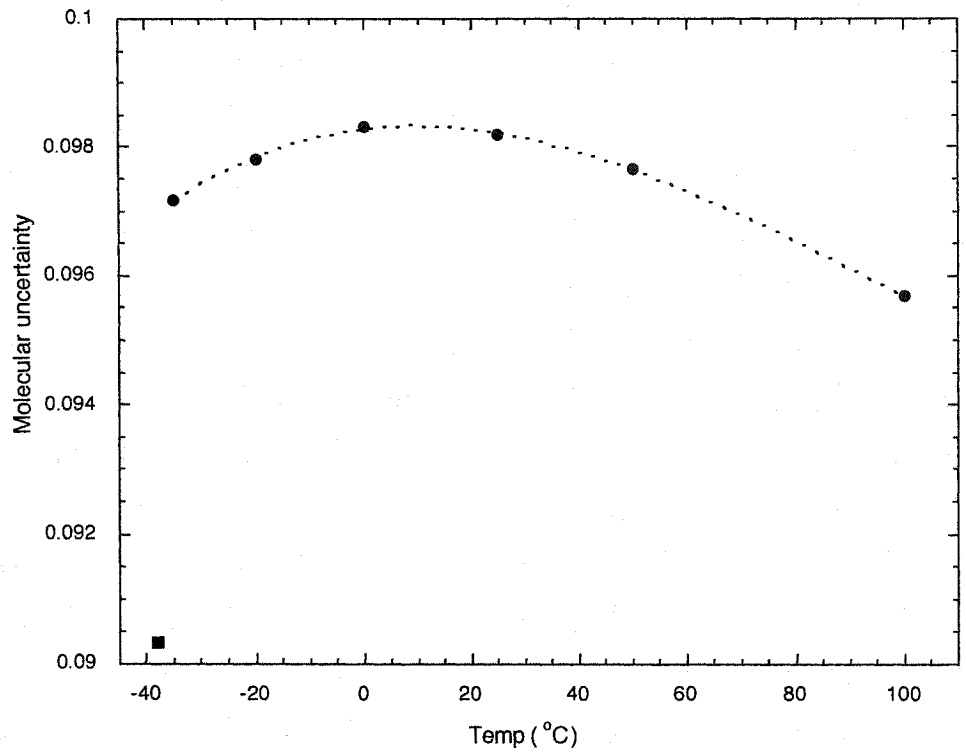

Figure 7.19. Estimated molecular uncertainty of the water molecule in quantum liquid water as a function of temperature (circles). The graph includes the estimated value for ice Ih at –38°C (square).

The basic shape of the probability distributions of the bead-centroid angle in liquid water at other temperatures is essentially identical to those shown in Fig. 7.18 and as circles in Fig. 7.7. Thus, it is more convenient simply to use mean values of these distributions as a comparative measure of the molecular uncertainty. Fig. 7.19 reports the behaviour of the quantum mechanical uncertainty of the water molecule (using the average values of the corresponding distributions) as a function of temperature. Also included in Fig. 7.19 is the value of molecular uncertainty for H_2O ice-Ih at –38°C. In this figure, we observe the expected increase in the quantum mechanical uncertainty when going from 100 °C to about 0 °C; it is followed by a decrease of the quantum mechanical uncertainty on further lowering of the temperature from about 0 °C to –35 °C.

This behaviour may be described as a previously uncharacterized anomalous property of water. The effect of diminishing the quantum mechanical uncertainty at lower temperatures is hypothesized to be due to the increasing influence of the local molecular structure, that more than offsets the direct influence of lower temperature. It is remarked that a similar explanation is used to account for the density maximum exhibited by water [146].

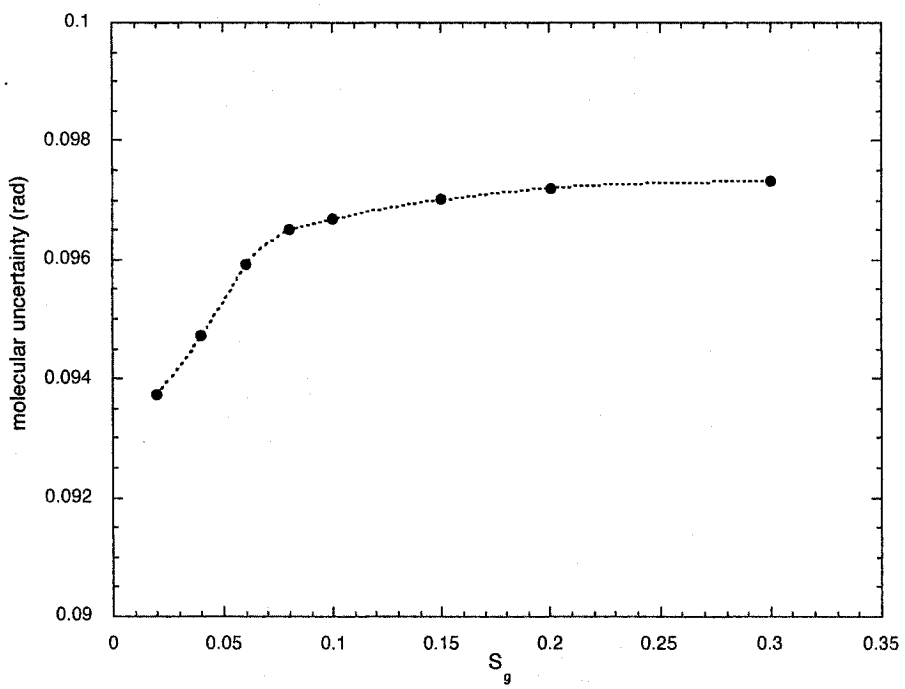

Figure 7.20. Dependence of the estimated molecular uncertainty of the water molecule in quantum liquid water as a function of the local structural parameter S_g at –35°C.

In order to test this hypothesis, the impact of the local molecular environment on the quantum mechanical uncertainty can be directly examined. For this purpose a local tetrahedral order parameter, denoted S_g, is introduced. It is given by [147]

$$S_g = \frac{3}{32}\sum_{l=1}^{3}\sum_{m=1}^{4}\left[\cos(\gamma_{lm}) + \frac{1}{3}\right]^2, \tag{7.7}$$

where γ_{lm} is the angle subtended at the central atom between the l^{th} and m^{th} bonds and the factor 3/32 normalizes S_g to the range $0 \leq S_g \leq 1$. This order parameter is small for molecules with a very tetrahedral (or ice-like) environment and grows for less tetrahedral molecular environments [147]; in fact, an ice Ih crystal at –38°C returns an S_g value lower than 0.01. Thus, within quantum simulation the molecular uncertainty can be calculated for molecules with similar local environments (as measure by S_g) at a particular temperature. Fig. 7.20 shows the dependence of the molecular uncertainty as a function of the tetrahedral order in liquid water at –35°C. In this graph, the first point represents the molecular uncertainty (in radians) for molecules with an S_g value between 0 and 0.02, while the second point is the uncertainty for molecules with an S_g value between 0.02 and 0.04, etc. It is clear that, although the quantum mechanical uncertainty does not have a simple dependence on the tetrahedral order, it does change monotonically with it. Moreover, molecules in a more ice-like environment have, at the same temperature, a smaller quantum mechanical uncertainty than molecules in more disordered (or less tetrahedral) environments. This clearly explains why the molecular uncertainty in H_2O ice-Ih is smaller than in H_2O liquid water (see Figs. 7.18 and 7.19). These results are further evidence of the notable strength of the water-water interaction in liquid phase, and the importance of the water structure in the properties of liquid water.

Since the behaviour observed in Fig. 7.19 resembles the dependence of liquid water density with temperature, and since the calculations have been carried out at the experimental densities, one might suspect that the density is somehow responsible for the

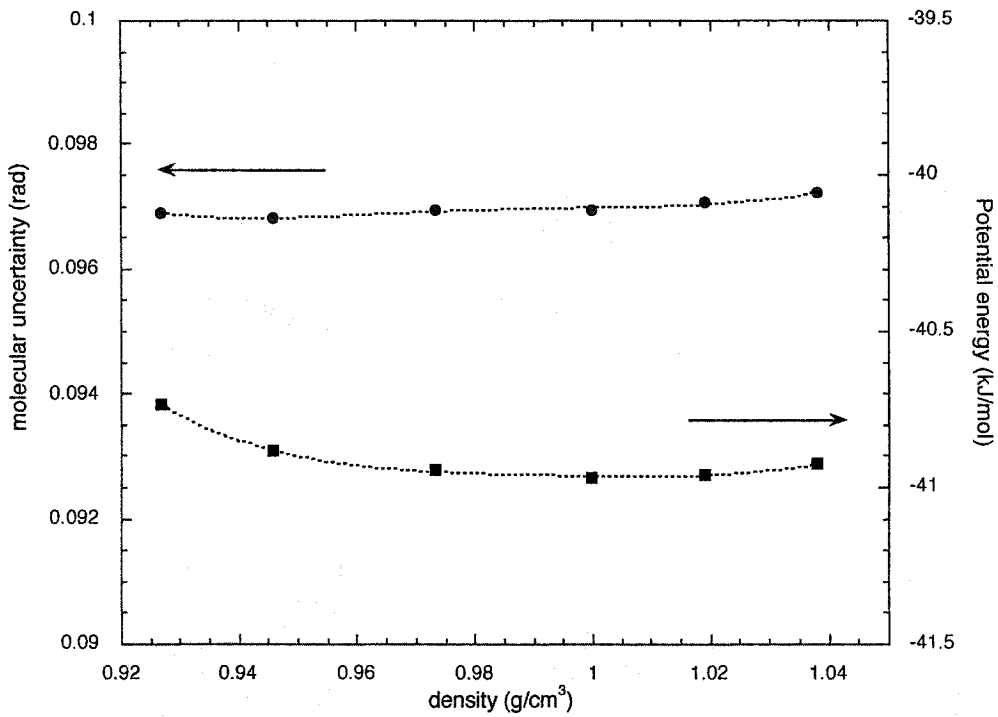

Figure 7.21. Dependence of the average molecular uncertainty (circles) and the average potential energy (squares) as a function of the density of liquid H_2O at –35°C.

curvature of the molecular uncertainty for TIP4P water. The results shown in Fig. 7.21, however, demonstrate that, at least at –35°C, the molecular uncertainty is not significantly affected by changes in density (within the density range of interest). The potential energy, on the other hand, seems to approach a shallow minimum at about 1.0 g/cm^3, consistent with behaviour previously observed in classical simulations of liquid water [148]. In the quantum simulations presented here, the TIP4P water potential is effectively modified by the inclusion of the orientational uncertainty, and hence this extremum is shifted somewhat relative to that of previously reported classical simulations [148].

According to the results presented in Sections 7.2.2 and 7.2.3 (as well as previously reported quantum simulations [19,20]) quantization has a significant impact on the dynamical properties of simulated water at 25°C. It is important then to analyze the temperature dependence of quantum effects in the dynamical properties of liquid water.

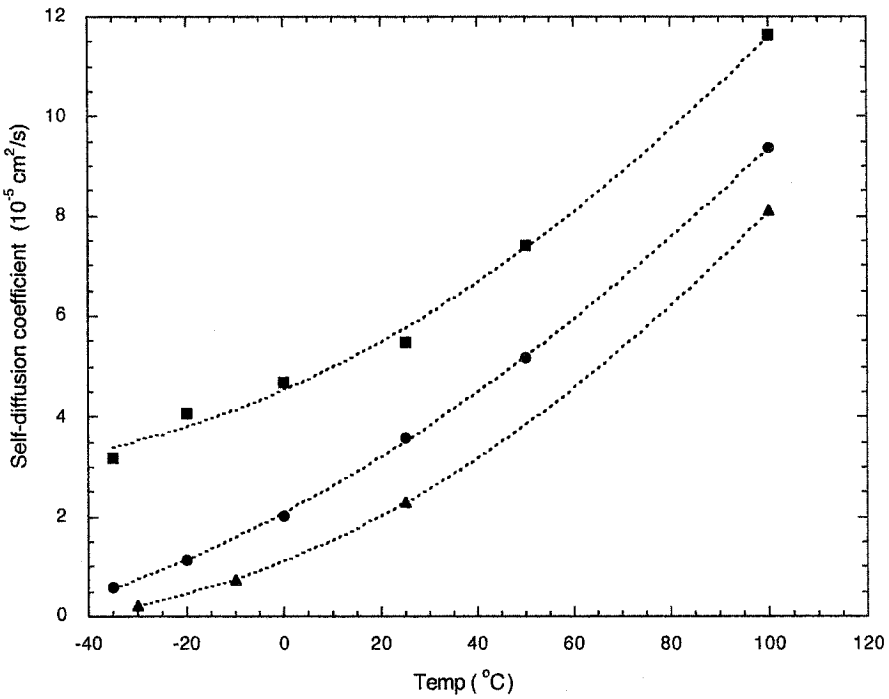

Figure 7.22. Self-diffusion coefficient as a function of temperature. The circles, squares, and triangles, represent the classical, quantum and experimental values, respectively. Experimental values taken from ref [104]. (The dotted lines are a convenient polynomial fit to aid the eye).

Fig. 7.22 shows the values of the self-diffusion coefficients as a function of temperature obtained from the classical and quantum simulations and compares them with experimental results [104]. It is clear that classical simulations with the TIP4P model overestimate the experimental values at all temperatures. The results from the quantum simulations appear still further above the classical values. It is apparent from Fig. 7.22 that the classical values decay slightly faster than the experimental ones,

whereas the dependence of the quantum results with temperature exhibit a curvature and resemble the experimental data.

An interpretation of a systematically higher diffusion coefficient in the quantum simulation in relation to the classical liquid deserves careful examination. In a classical MD simulation the forces and torques acting on a molecule are just the appropriate derivative of the classical potential evaluated at the position and orientation of the molecule (i.e. $\mathbf{F}_i = \left(\partial V(\mathbf{r})/\partial \mathbf{r}\right)_{\mathbf{r}_i}$ and $\mathbf{T}_i = \left(\partial V(\Omega)/\partial \Omega\right)_{\Omega_i}$). Within the rigid body-CMD method, the forces and torques acting on the centroid are an average of the local (or classical) forces and torques over the appropriate uncertainty and can be written as

$$\mathbf{F}_{c,i} = \left\langle \left(\partial V(\mathbf{r})/\partial \mathbf{r}\right)_{\mathbf{r}_i} \right\rangle_{\Delta\Omega_i} = \left\langle \mathbf{F}_i \right\rangle_{\Delta\Omega_i} \tag{7.8}$$

and

$$\mathbf{T}_{c,i} = \left\langle \left(\partial V(\Omega)/\partial \Omega\right)_{\Omega_i} \right\rangle_{\Delta\Omega_i} = \left\langle \mathbf{T}_c \right\rangle_{\Delta\Omega_i}, \tag{7.9}$$

where $\Delta\Omega_i$ denotes the orientational uncertainty associated with the centroid i (Equations 7.8 and 7.9 are written in discretized form in Equations 5.61 and 6.17, respectively). This averaging process leads to the relationships $\left|\mathbf{F}_{c,i}\right| \le \left|\mathbf{F}_i\right|$ and $\left|\mathbf{T}_{c,i}\right| \le \left|\mathbf{T}_i\right|$. In other words, the centroid must experience smaller forces and torques (in magnitude) than a classical particle would, assuming the same configuration and potential for each. This result implies that as the interaction becomes non-local it undergoes an effective "smoothing" (the effective centroid interaction potential could in fact be calculated by the appropriate

integration of Equations of 7.8 and 7.9 according to, for example, Equations 5.56 and 5.34). Therefore, the centroid dynamics evolve on a surface with higher minima and lower maxima, in comparison with the classical potential surface. Since this "smoothing" only occurs at the scale of the molecular uncertainty, the higher minima can be interpreted as a zero-point vibration effect and the lower maxima as an "effective tunneling". The latter is certainly very much connected to the enhanced dynamical behaviour of quantum water in comparison with the classical liquid.

The impact of quantization can be judged by using the (Quantum/Classical) diffusion coefficient ratios. Fig. 7.23 shows the behaviour of the calculated ratios as a function of temperature, as well as the ratios obtained by Guillot and Guissani [20]. The results obtained via *rigid-body-CMD* agree remarkable well with the ones published by Guillot and Guissani [20], especially considering that this previous work used a different model potential and simulation method (see Section 4.2.4). It is clear from Fig. 7.23 that the effect of quantization grows quite significantly as the temperature of the system decreases. These results suggest that while the diffusive motion in classical dynamics is very significantly impeded by lowering the temperature, the dynamics in the quantum system is less affected. In other words, while a quantum molecule with a certain kinetic energy is able to escape from the local environment of its neighbours, the classical molecule with that same kinetic energy would remain trapped.

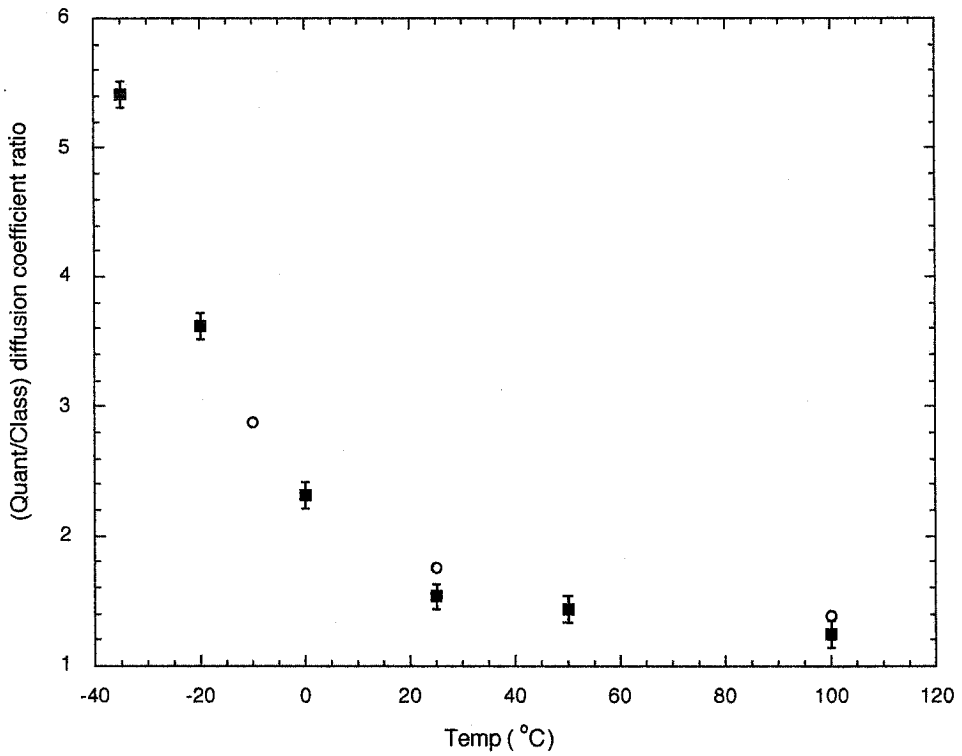

Figure 7.23. Diffusion coefficient ratio (Quantum/Classical) as a function of temperature. The solid squares are the calculated results whereas the circles are from reference [20].

Further confirmation of the increasing importance of quantum effects at lower temperatures can be found by calculating the appropriate orientational relaxation times. Fig. 7.24 shows the classical and quantum relaxation times as a function of temperature. The values of τ_1 and τ_2 were calculated from the corresponding dipole time correlation functions as described in Section 7.2.2. Clearly, the relaxation times are significantly diminished in the quantum liquid in agreement with the observed faster dynamics. In addition, the quantum effect becomes more important at lower temperatures. Fig. 7.25 shows the (Classical/Quantum) relaxation time ratios for τ_1 and τ_2. In spite of the difference in the absolute values of τ_1 and τ_2 (observed in Fig. 7.24), these ratios for τ_1 and τ_2 exhibit a very similar behaviour. Fig. 7.25 indicates that, although the relaxation

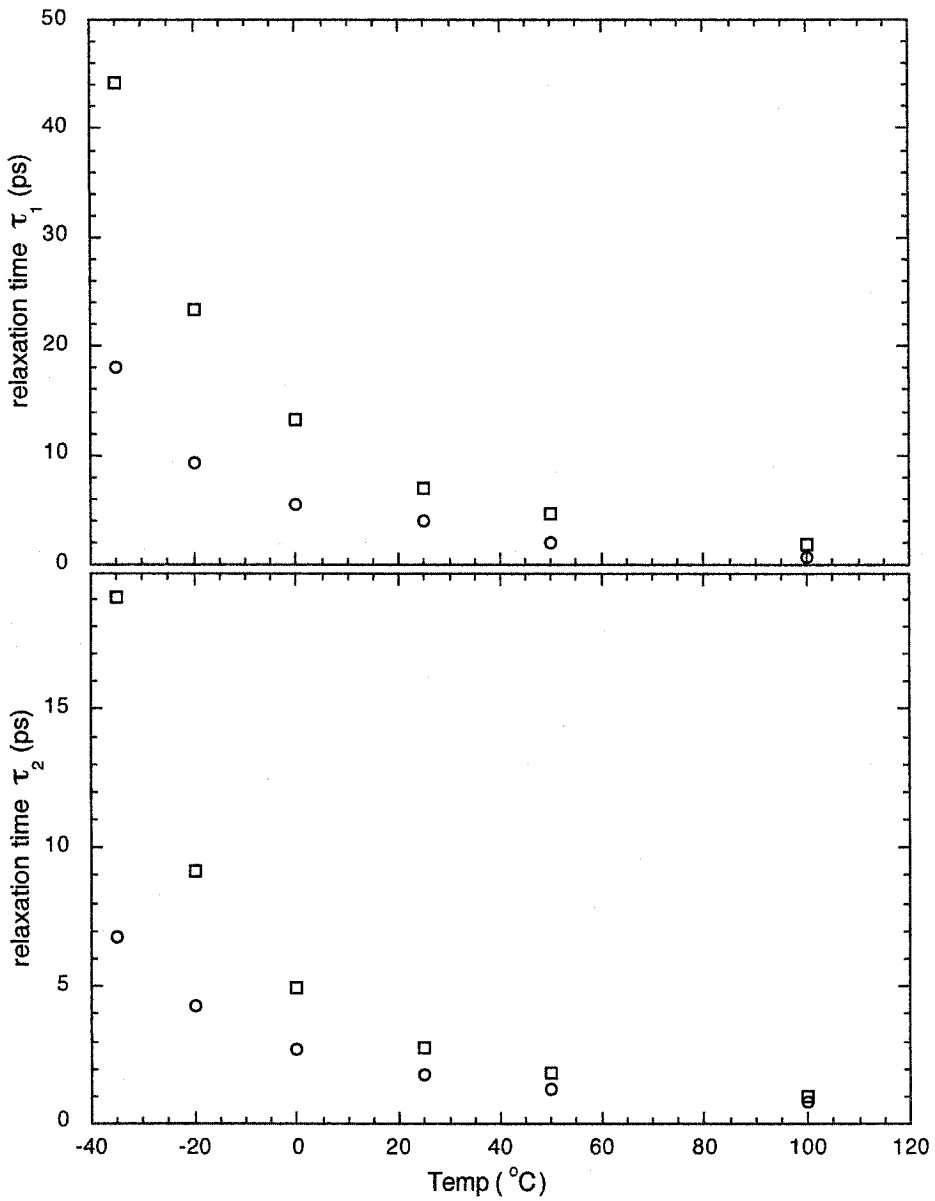

Figure 7.24. Classical and quantum relaxation times τ_1 and τ_2 as a function of temperature. The squares and circles correspond to the classical and quantum results, respectively.

times grow for both the classical and quantum systems, their growth is much more pronounced in the classical system than in the quantum liquid. This result is in agreement with the observations made previously about "effective tunneling" behaviour.

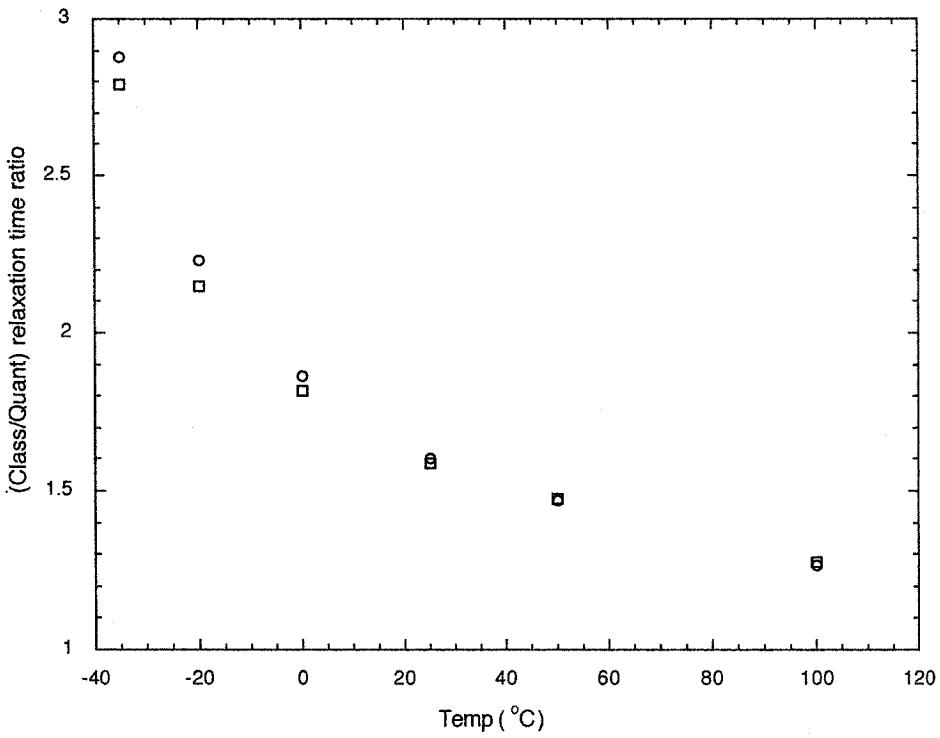

Figure 7.25. (Classical/Quantum) relaxation time ratio as a function of temperature. The square and the circles correspond to τ_1 and τ_2 ratios, respectively.

It is clear at this point that, in general, a classical simulation is able to capture the qualitative behaviour of liquid water over a range of temperatures. Nonetheless, quantum mechanical uncertainty is an inherent property of real water systems. The quantum simulations presented in this work account for it by including an orientational molecular uncertainty. The consistent increase of the relative effects of quantization in the dynamical properties of liquid water upon supercooling indicates that while quantum effects are important at 25°C, their relevance grows dramatically as temperature is decreased. The orientational uncertainty of the molecule allows for "effective tunneling" which enhances the water molecule's ability to make and break hydrogen bonds as well as to respond faster to an evolving local molecular environment.

7.4. "EFFECTIVE TUNNELING" IN LIQUID WATER

One of the major difference between classical and quantum simulations of water is that the latter allows for "tunneling behaviour". As has been discussed in Sections 7.2 and 7.3, its impact on the dynamical properties of water is significant. It is then relevant to ask –what is the nature of this "effective tunneling" in water? In this section, an unambiguous identification of the changes that take place in the local structure of liquid water due to quantization is carried out with the use of oxygen-oxygen spatial distribution functions (SDFs), $g_{OO}(\mathbf{r}_{ij})$. This identification will then afford us a more complete characterization of tunneling behaviour in quantum liquid water.

In contrast to the "one-dimensionality" of the radial distribution functions, the SDFs expand the radial and angular coordinates of the interatomic separation vector, $\mathbf{r}_{ij}$, and essentially become spatial maps that directly characterize the local three-dimensional structure surrounding molecules in the liquid [149]. The analysis of SDFs has been used previously in liquid water [149] and its solutions [150] and has lead to a better understanding of the local structure. Kusalik and co-workers [149, 150] have clarified a number of structural questions in liquid water by examining in detail the oxygen-oxygen and oxygen-hydrogen SDFs at several temperatures. They have verified the strong tendency for tetrahedral coordination of the nearest neighbours and compared it with the approximate reconstruction of the pair distribution function from scattering experiments carried out by Soper [36,151]. Kusalik and co-workers [149-150] have also identified an interstitial feature responsible for the additional coordination in liquid water. Since this

interstitial feature joins (bridges) the second and first coordination shells, it can be considered to be the result of the continually forming and collapsing of the local hydrogen bond network and therefore coupled to the mobility in the liquid [149,150].

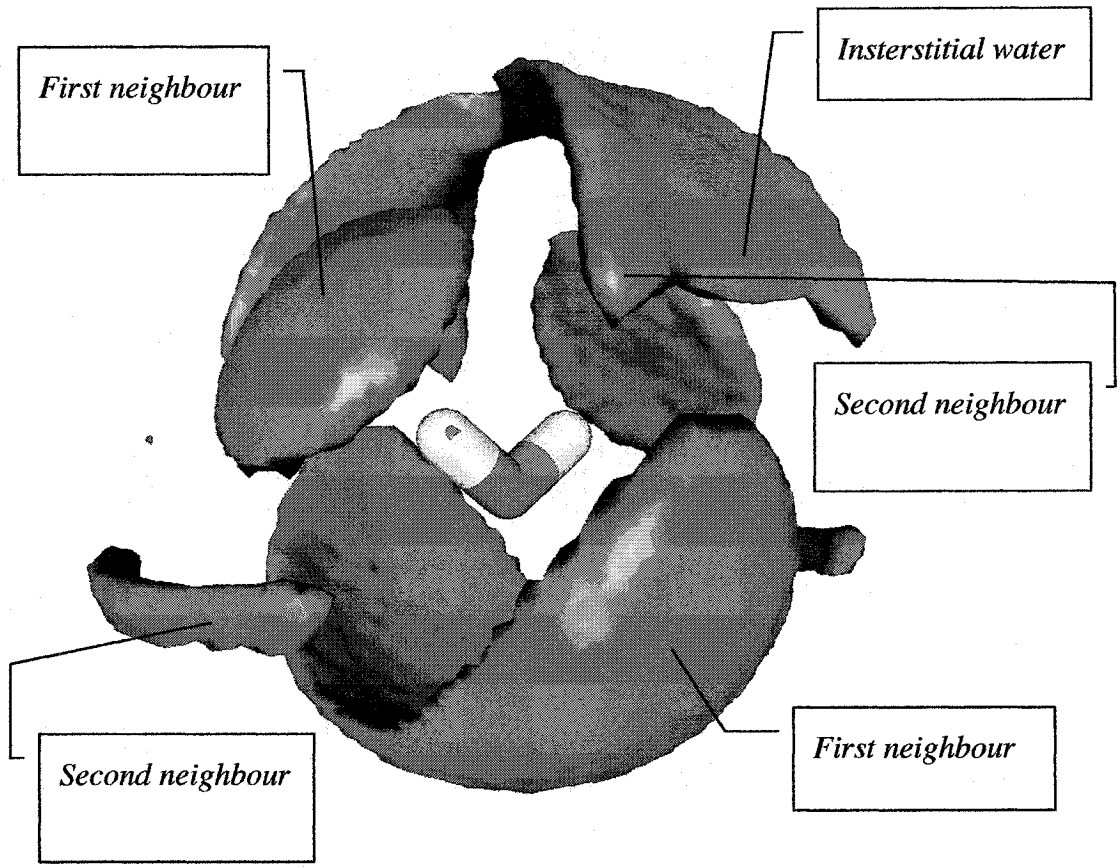

Figure 7.26. Oxygen-oxygen spatial distribution function of classical liquid H_2O at 25°C. The isosurface corresponds to $g_{OO}(\mathbf{r}_{ij}) = 1.4$.

Fig. 7.26 shows the oxygen-oxygen spatial distribution function of liquid water at 25 °C represented at the isosurface $g_{OO}(\mathbf{r}_{ij}) = 1.4$. The figure indicates the first and second neighbours features, as well as the region associated with interstitial water. It is important to note that due to the existence of two symmetry planes (the molecular plane and a plane perpendicular to the molecule that contains the C_2 molecular axis) each

feature is only labeled once in Fig. 7.26. A central water molecule has been included to help in the visualization of the local frame. The relationship between the interstitial coordination and the dynamics in liquid water has been directly tested within the context of classical MD simulations [150]. By artificially restricting the movement from a hydrogen donor to an interstitial position the self-diffusion coefficient was reduced roughly by a factor of 2, providing further evidence of the important role of interstitial water in water dynamics.

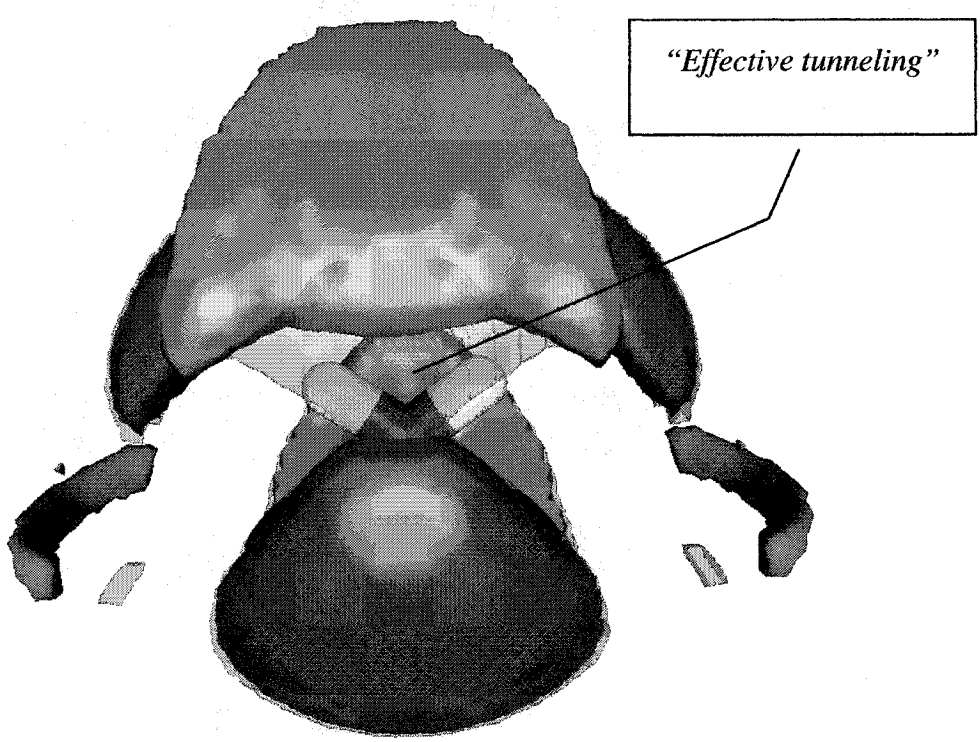

Figure 7.27. Oxygen-oxygen spatial distribution functions of classical (red) and quantum (semi-transparent blue) liquid H_2O at 25°C represented by the isosurface $g_{OO}(\mathbf{r}_{ij}) = 1.4$.

Fig. 7.27 shows a comparison (by superposition) of the quantum oxygen-oxygen (semi-transparent blue) SDF and the classical oxygen-oxygen (red) SDF of liquid

H_2O obtained from quantum and classical simulations at 25°C with $g_{OO}(\mathbf{r}_{ij}) = 1.4$. We first observe that within the first neigbours features the blue colour dominates the outside surface while the red colour dominates inside (only the red colour inside the H-donating feature is visible in the perspective visualized). Therefore in quantum water the first neighbours are slightly shifted towards larger radii than in the classical liquid. The region of "effective tunneling" is also identified in Fig. 7.27. In this region the probability density of the quantum system has attained a value of at least 1.4, whereas for the classical SDF is below this threshold (see also Fig. 7.26). It is important to note that this region is associated with interstitial water and therefore to the mechanisms of diffusion. The existence of this region of higher probability density in the quantum liquid is a direct result of an *effective barrier lowering*. It takes place in the quantum simulation as a result of the inclusion of the quantum mechanical orientational uncertainty in the water interaction and is responsible for the enhanced dynamical behaviour of the quantum molecules (see Section 7.3).

It can be clearly seen in Fig. 7.27 that the "effective tunneling" in liquid water is mainly localized to a specific region in front of and behind the plane of the molecule. More precisely, although quantization has little effect on the appearance of the well-known tetrahedral coordination of water, it does lower the barrier between a H-bond-donating neighbour (single cupped feature below the central molecule) and the "interstitial" water (cf. Fig. 7.26). Consequently, water molecules in the quantum liquid have a greater tendency to "jump" from a first-neighbour position to a second-neighbour location. These result underlines the importance of interstitial coordination in the

structure of liquid water and confirms further the connection between interstitial water and the mechanism for molecular diffusion [149,150].

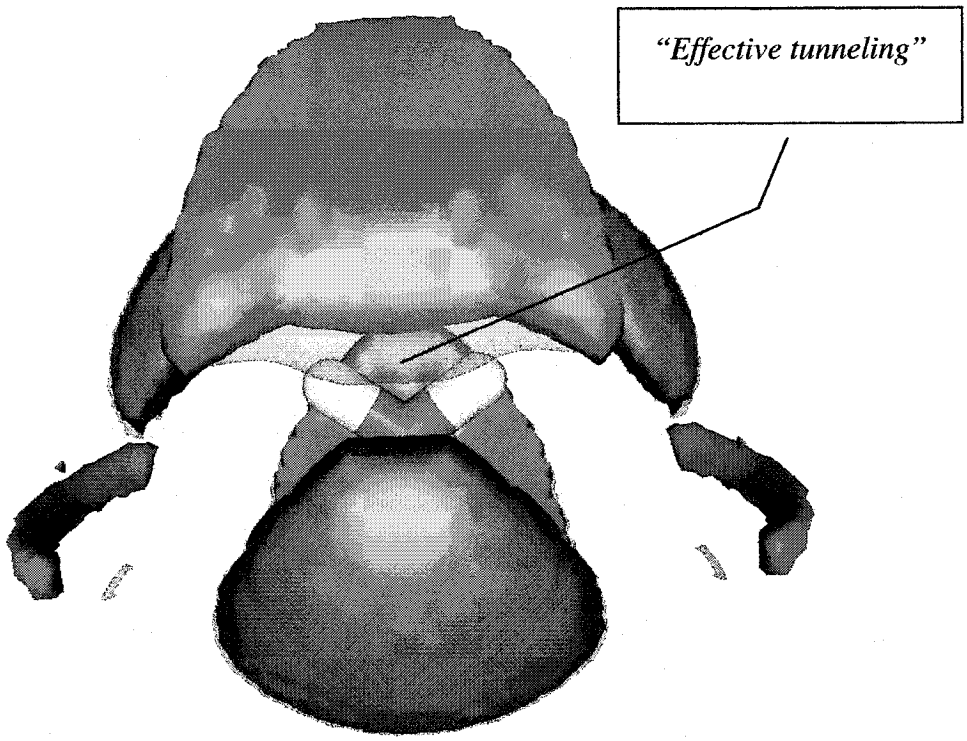

Figure 7.28. Oxygen-oxygen spatial distribution functions of classical (red) and quantum (semi-transparent green) liquid D_2O at 25°C represented by the isosurface $g_{OO}(\mathbf{r}_{ij}) = 1.4$.

In Fig. 7.28, the superposition of the quantum SDF and the classical SDF of liquid D_2O at 25 °C is shown. The isosurfaces in this figure also correspond to $g_{OO}(\mathbf{r}_{ij}) = 1.4$, allowing a direct comparison with Fig. 7.27. As expected, the "penetration" of the quantum spatial distribution function into the low-probability classical region is more pronounced in quantum H_2O (Fig. 7.27) than in quantum D_2O, leading to a smaller region of "effective tunneling" in the latter. This result is naturally in agreement with the lower

molecular uncertainty of D_2O in comparison with H_2O (see Sections 7.2.1 and 7.2.2).

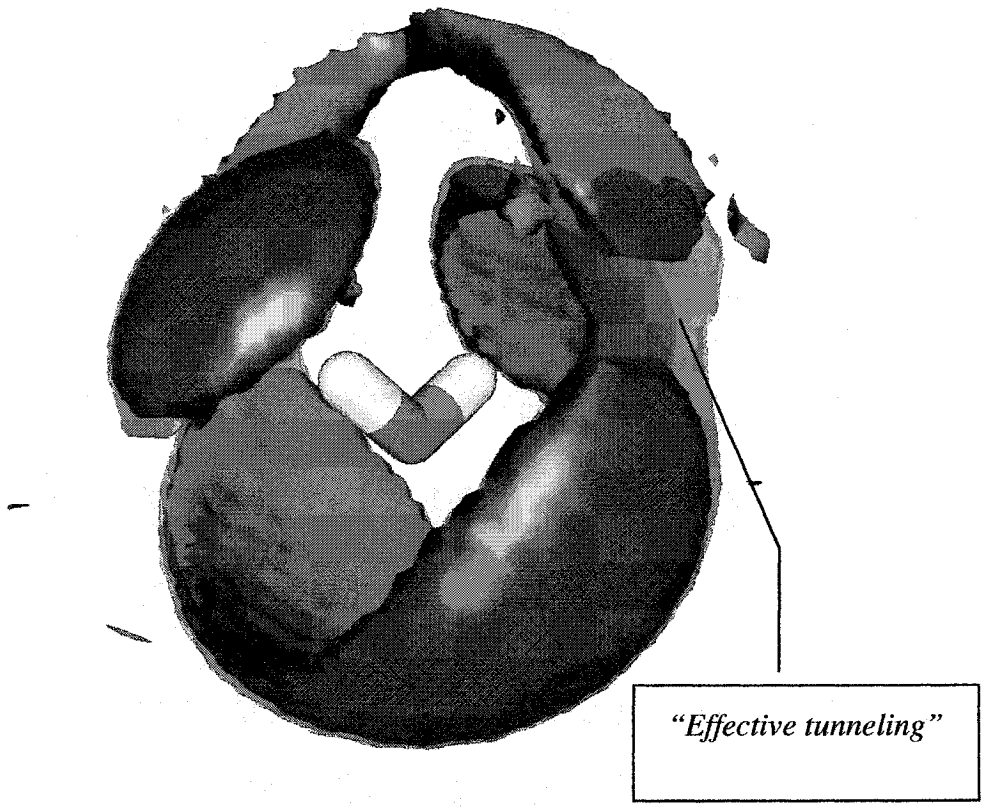

Figure 7.29. Oxygen-oxygen spatial distribution functions of classical (red) and quantum (semi-transparent blue) liquid H_2O at 50°C represented by the isosurface $g_{OO}(\mathbf{r}_{ij}) = 1.4$.

Since the structure of liquid water changes with temperature, it is interesting to look at "effective tunneling" at other temperatures. Fig. 7.29 shows the oxygen-oxygen SDFs of classical and quantum of liquid H_2O at 50 °C with the isosurface $g_{OO}(\mathbf{r}_{ij}) = 1.4$. The spatial structure of classical water is different from the classical structure at 25 °C. The second neighbour features have almost disappeared in comparison with classical water at 25 °C at the same threshold value (Fig. 7.27). It can be clearly seen (especially due to the perspective of the Fig. 7.29) that the first neighbours features are shifted

slightly outward in the quantum liquid. This observation is also valid for figures 7.27 and 7.28, and is a manifestation of the weakening in the attractive interaction that occurs when going from the classical to the quantum system. The region of "effective tunneling" is very clearly seen in this figure, and appears narrower than the one evident in Fig. 7.26.

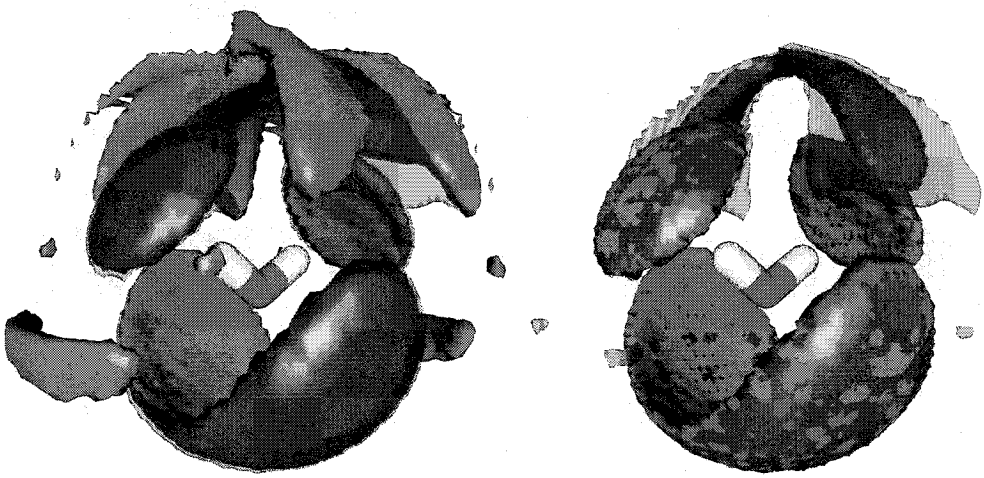

Figure 7.30. Left- Oxygen-oxygen spatial distribution functions of classical (red) and quantum (semi-transparent blue) liquid H_2O at 0°C. Right- Oxygen-oxygen spatial distribution functions of classical (red) liquid H_2O at 50°C and quantum (semi-transparent blue) liquid H_2O at 0°C. All isosurfaces are represented by $g_{OO}(\mathbf{r}_{ij}) = 1.43$.

As was discussed in Section 7.3, the effects of quantization have been compared to the effects associated with raising the temperature [12], however some differences are naturally expected (see Fig. 7.16). Fig 7.30 shows the oxygen-oxygen SDFs of quantum liquid water at 0°C (left and right), as well as the oxygen-oxygen SDFs of classical liquid at 0°C (left) and 50°C (right). All the isosurfaces in this figure are plotted at a threshold of 1.43. The image on the left depicts the effect of quantization on the local structure of water at 0°C, which is analogous to the effects described in Figs. 7.27 and 7.29 at higher temperatures. The picture on the right compares the effect of quantization and the effect

of temperature in the structure of liquid water (and so is analogous to Fig. 7.16). It can be seen that the increase in temperature (going from the red-left to the red-right isosurfaces) shifts the first neighbour features to larger separations very similar to the shift produced by quantization. The gap between the interstitial and the H-donor first-neighbour features also decreases when the temperature is raised although not to the same extent as demonstrated by "effective tunneling". The second neighbor features, on the other hand, disappear on increasing the temperature of the system in qualitative agreement with the diminished structure in the corresponding SDFs. However, the quantum SDF (on the left of Fig. 7.30) exhibits some second neighbor features not apparent in the 50 °C classical system.

Fig. 7.31 shows a slice of the classical and quantum oxygen-oxygen SDFs of liquid H_2O at –20 °C. Once again, the first neighbour regions are slightly displaced towards larger separations in the quantum system with respect to the classical result. In addition, one can see that the quantum mechanical tunneling analogous to that observed at higher temperatures.

The spatial distribution function is related to a free energy by the well-known relationship [2]; $\Delta F = -(1/\beta)\ln g(\mathbf{r})$, where ΔF is the change in free energy associated with the displacement of a molecule initially at infinity to the position $\mathbf{r}$. Therefore, by knowing the SDF values across the tunneling region, the free energy barrier can be easily estimated. The values of free energy barrier in the classical and quantum systems are plotted as a function of temperature in Fig. 7.32. It is clearly seen that the quantum

Figure 7.31. A slice of the superposition of the oxygen-oxygen spatial distribution functions of classical (red) and quantum (semi-transparent blue) liquid H_2O at -20°C with a threshold of 1.13.

system has, at all temperatures, an effective barrier lower than the classical one, in complete agreement to the concept of tunneling. Additionally, it is observed that the values of the classical system grow more rapidly with decreasing temperature than the quantum results, again confirming that tunneling is more significant at lower temperatures.

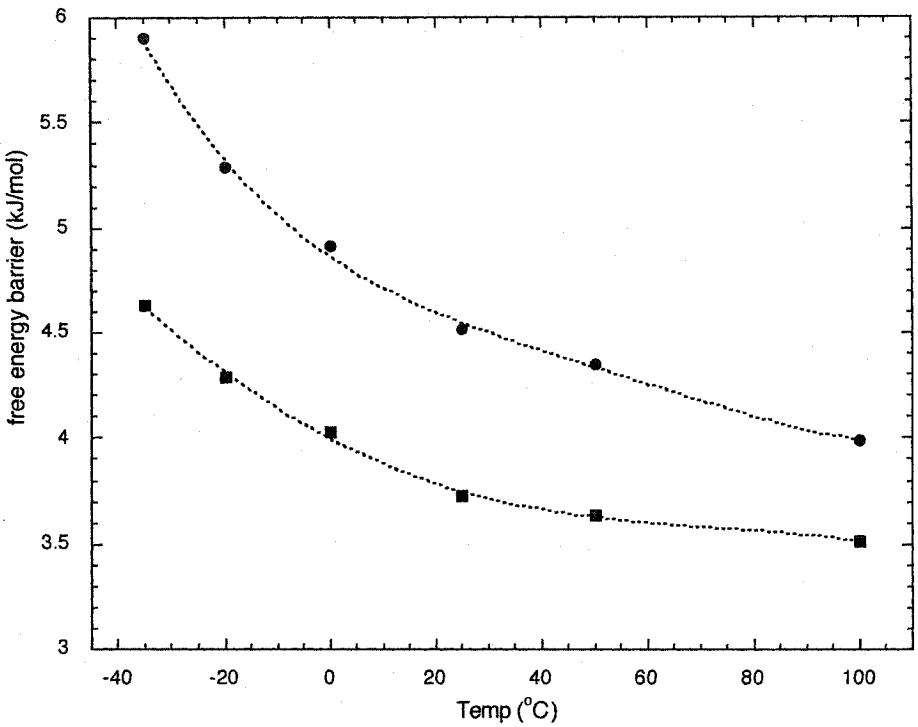

Figure 7.32. Free energy barrier associated with molecular displacements across the tunneling region in classical (circles) and quantum (squares) liquid water as a function of temperature.

Finally, it is important to point out that, since rotational and translational motions are very strongly coupled in liquid water, the orientational uncertainty associated with the molecule has a strong influence on its translational behaviour. Therefore, the low inertia moments of the water molecule cause the molecule to diffuse in a way that is (qualitatively similar but) quantitatively different from its otherwise classical behaviour.

8. QUANTUM ICE Ih

In the previous chapter the *rigid body-CMD* method was applied to the study of a variety of properties of liquid water. In this chapter, this method is used to study the most common (terrestrial) form of ice, ice Ih. The purpose is to demonstrate further the utility and versatility of the rigid body-CMD methodology, as well as to investigate quantum effects in high temperature ice. The chapter is organized as follows. In Section 8.1, the results from parameterization tests are presented. Section 8.2 investigates the differences between classical and quantum simulations of ice Ih at 220 K for three different rigid water models. Section 8.3 analyses the influence of temperature on quantum and classical simulation results in the range from 160 K to 235 K. Finally, a preliminary study of classical and quantum melting of ice Ih is presented in Section 8.4.

8.1. SIMULATION DETAILS AND PARAMETERIZATION

The classical simulations were carried out using a standard MD code, starting from an initial ice Ih crystal containing 360 water molecules (45 hexagonal unit cells) at the appropriate density. The disordered proton arrangement of the initial configurations was assigned using BF rules [152] such that the total dipole moment of the sample was less than 5% of its maximum possible value. The Ewald method [4] was used with conducting boundary conditions to handle the electrostatic interactions, with periodic boundary conditions to simulate an infinite system. The quantum simulations were carried out according to the rigid body-CMD methodology where the final classical ice configuration was the starting point of the quantum calculations (as in Chapter 7). The

bead dynamics were again controlled with a Nose-Hoover chain [47] thermostat of length 4. The imaginary time sampling was carried out with a time step of 0.5 fs with inertia moments (for each axis) on each bead twice that of the real molecule. The quasi-adiabatic implementation employed 3 imaginary steps on each classical step. In all cases, the starting lattice was allowed to relax at constant temperature and pressure for 10 ps. Zero pressure was applied using an Andersen barostat [48] in x, y and z directions to try to avoid any stress in the lattice structure. After the equilibration period, the barostat was turn off for the constant temperature and density production runs. The time steps used in the classical and quantum simulations were 1 fs and 0.125 fs, respectively.

Since an extensive analysis of the parameters required for quantum simulations was carried out for the liquid calculations (some of which are presented in Section 7.1), it is possible to take advantage of this work by exploring the parameter space in the vicinity of these previous values. The set of parameters includes the relaxation time of the Nose-Hoover chain [47] thermostat, the bead inertia moments and imaginary time step size, the number of quantum steps per real time step, the real time step size, and the number of beads. Considering that classical simulations of liquid water and ice are technically very similar, it is reasonable to expect that, in general, the parameters used in the quantum liquid simulations will be very similar to the ones required for the simulation of quantum ice. This hypothesis was verified by a number of tests which demonstrated that the results were independent of the parameter value chosen within a reasonable range of the parameter space. Some of the results obtained in those tests are presented below.

Due to the differences in temperature between the liquid simulations of Chapter 7 and the ice simulations of this chapter, as well as the distinctive structure and dynamics in the liquid and solid phases, runs with 5, 6 and 7 beads were carried out at 160 K (the temperature of the coldest ice simulated in this work).

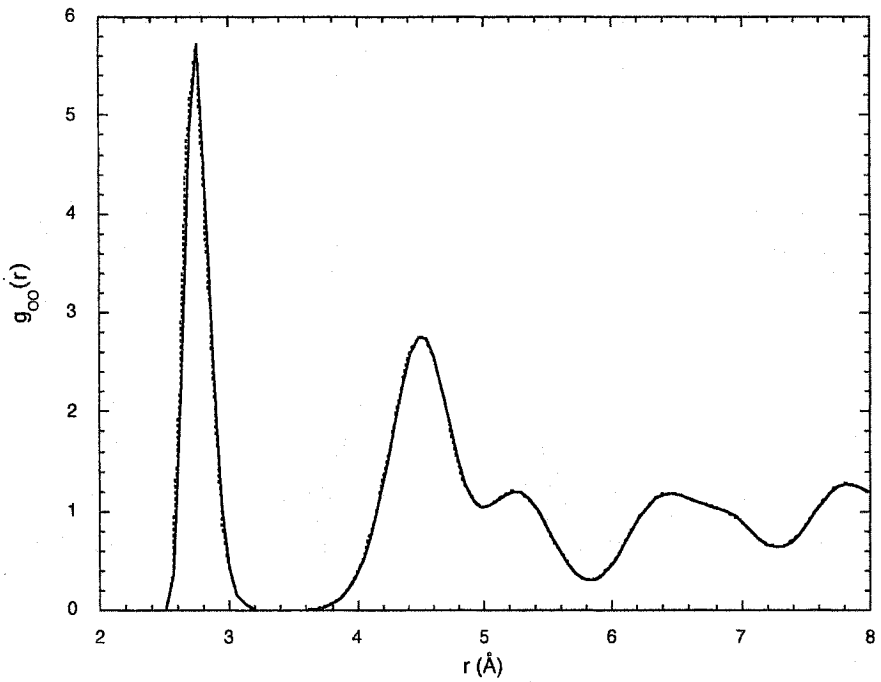

Figure 8.1. Convergence of the oxygen-oxygen radial distribution function for quantum H_2O ice Ih (at 160 K) with respect to the value of the discretization parameter P. The results represented by a dotted line and a solid line correspond to the values P=5 and 6, respectively.

Fig. 8.1 shows the oxygen-oxygen radial distribution function of quantum H_2O ice Ih obtained in quantum simulations using 5 and 6 beads. As can be clearly seen, the functions are essentially identical (and identical to the result for P=7, not shown). This observation is further confirmed with the oxygen-hydrogen radial distribution functions shown in Fig. 8.2. It is also apparent that the radial distribution functions of Fig. 8.1 and 8.2 are much more structured than the ones obtained in the liquid simulations, in

agreement with the expected ordered arrangement of the molecules in ice in relation to liquid water.

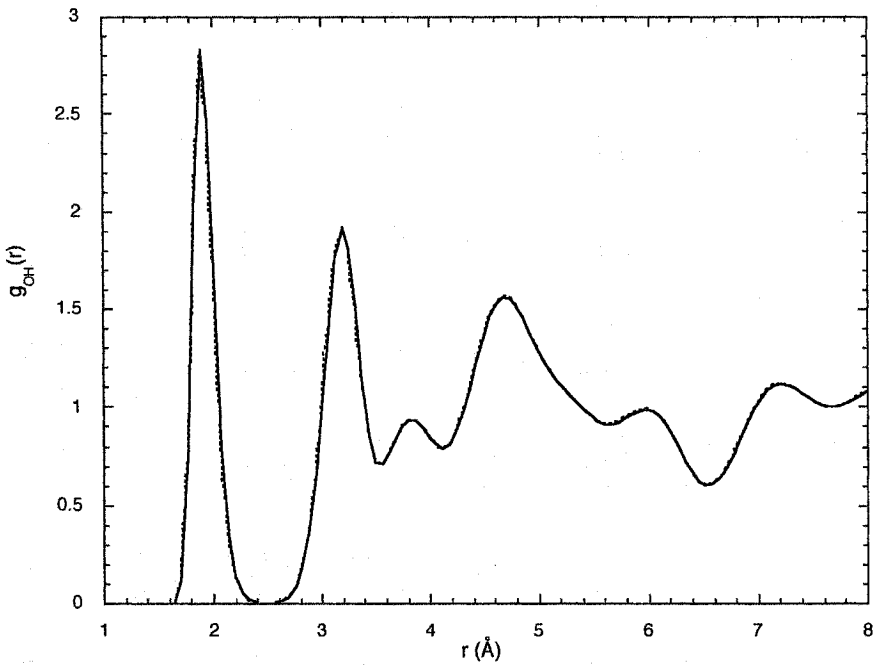

Figure 8.2. Convergence of the oxygen-hydrogen radial distribution function of quantum H_2O ice Ih (at 160 K) with respect to the value of the discretization parameter P. The results represented by a dotted line and a solid line correspond to the values P=5 and 6, respectively.

Fig 8.3 shows the linear velocity time correlation functions obtained in quantum simulations of ice Ih at 160 K with P=5 and P=6. It can be observed that the functions are identical within their statistical errors. Additional comparison with other properties confirmed that P=5 provided converged results. Consequently, all quantum simulations were carried out with 5 beads. This result is not as surprising as it may first appear since in Section 7.3 it has been already seen that the molecular uncertainty of ice at 235 K was significantly lower than those of liquid water between 238 K and 373 K. As will be seen later on in this Chapter, the molecular uncertainty of ice in the temperature range of interest always remains smaller than that of liquid water.

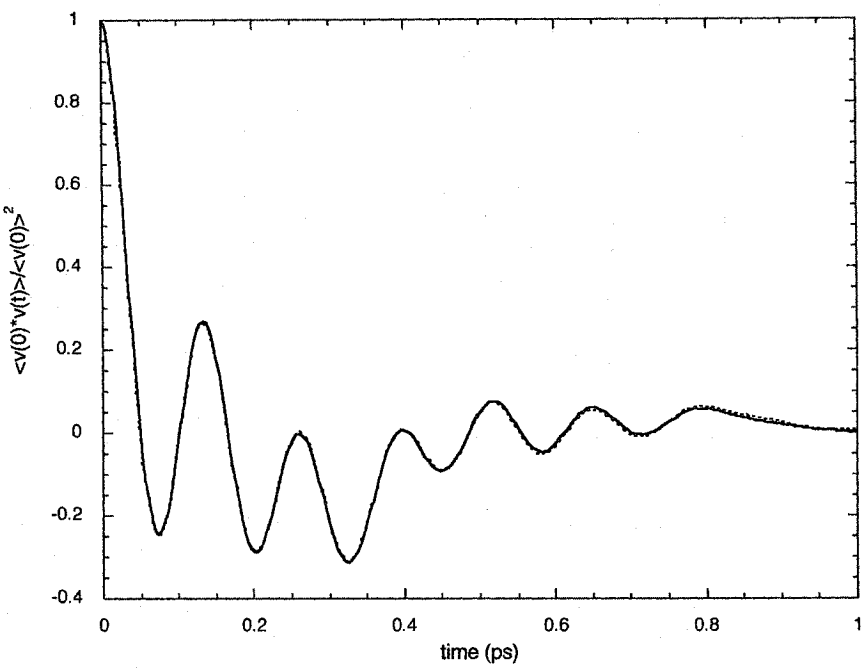

Figure 8.3. Convergence of the linear velocity time correlation function for quantum of H_2O ice Ih (at 160 K) with respect to the value of the discretization parameter P. The results represented by a dotted line and a solid line correspond to the values P=5 and 6, respectively.

8.2. QUANTUM EFFECTS AND MODEL COMPARISON

This section discusses the results obtained in classical and quantum simulations of ice Ih at 220 K on three rigid water models; TIP4P [61], SPC/E [67] and TIP4Pew [68] (the same models used in Chapter 7 to study liquid water). An analysis on the structural properties including radial and spatial distribution functions, energy and molecular uncertainty is presented first. This is followed by a discussion of the linear and angular velocity time correlation functions.

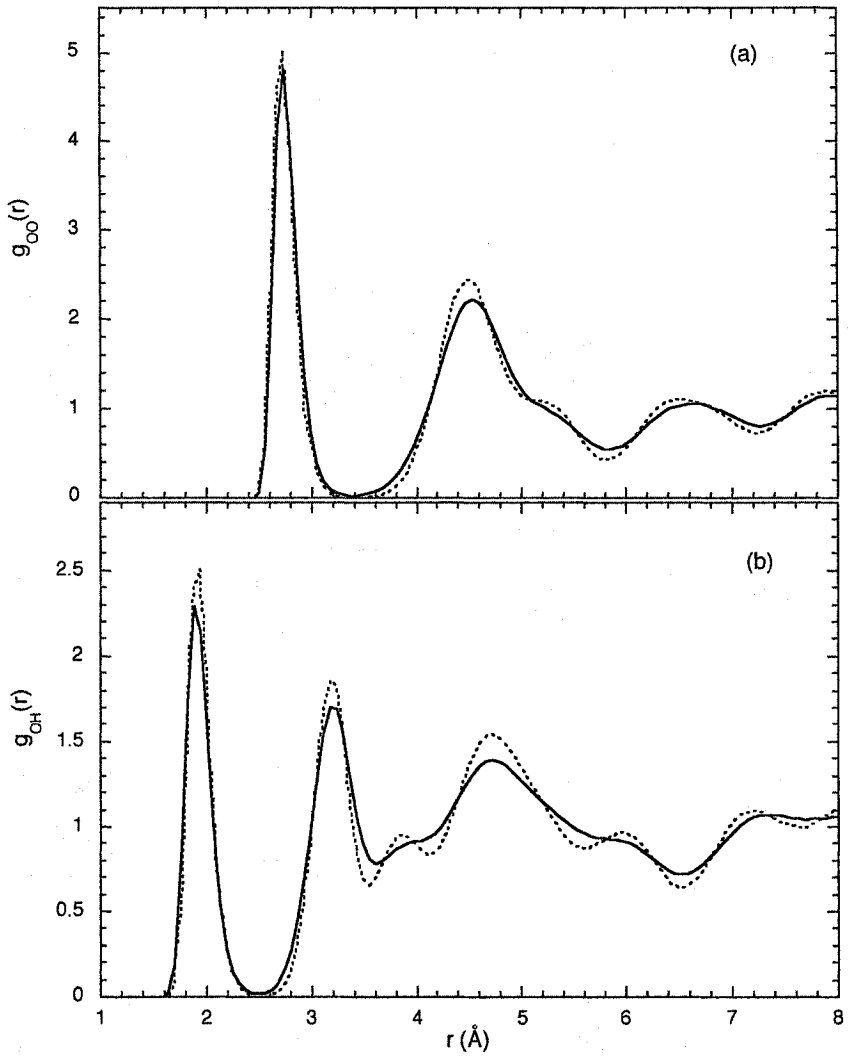

Figure 8.4. Oxygen-oxygen (a) and oxygen-hydrogen (b) radial distribution functions of classical and quantum TIP4P ice Ih at 220 K. The results represented by dotted and solid lines correspond to the classical and quantum simulations, respectively.

Fig 8.4 shows the oxygen-oxygen and oxygen-hydrogen radial distribution functions of classical and quantum simulations at 220 K with the TIP4P water model. The oxygen-oxygen radial distribution functions (classical and quantum) exhibit a maximum at 2.72 Å in very good agreement with the experimental oxygen-oxygen distance of 2.759±0.002 Å at 223 K [153]. Both classical and quantum simulations gave very similar values for these distances. As can be clearly seen in both functions, quantum

ice exhibits decreased maxima and slightly raised minima, and thereby is less structured than classical ice. It is also noted that, the first peak in the oxygen-oxygen and oxygen-hydrogen RDFs is noticeably diminished by quantization. The maximum at about 4.6 Å in the oxygen-oxygen RDF, as well as the minimum at about 3.5 Å in the oxygen-hydrogen RDF, are slightly shifted outward in the quantum result compared with the classical. Taking into account the scale difference in the plots of Fig. 8.4, one concludes that the overall effect of quantization in both functions is comparable. On the other hand, since the spatial correlation in a crystalline structure has a much longer range than in liquid phase, the differences between classical and quantum ices are still noticeable at distances of about 7 Å, in contrast to the much shorter ranged structural effects seen in liquid water.

Fig. 8.5 shows the results obtained in classical and quantum simulations of SPC/E ice Ih at 220 K. Interestingly, although the classical oxygen-oxygen RDF is very similar to the one obtained in the classical simulation of TIP4P ice (Fig. 8.4) the classical oxygen-hydrogen RDF indicates that there are notable differences between the classical TIP4P and SPC/E ices. Indeed, the peaks at about 3.9 Å and 6.0 Å, clearly noticeable in the classical TIP4P oxygen-oxygen RDF in Fig. 8.4, are much smaller in the classical SPC/E oxygen-oxygen RDF. The oxygen-oxygen and oxygen-hydrogen distances are still similar to the ones obtained with the TIP4P model and experimentally [49]. As in the TIP4P results, the softening of the structure when going from classical to quantum simulations is apparent. It is also apparent that the softening of the structure due to quantization extends over many angstroms. The results presented in Fig. 8.5 are

qualitatively similar to the ones obtained by Garret and co-workers [16] using PIMC simulations of Ice Ih at 240 with the SPC model (see Section 4.2.3).

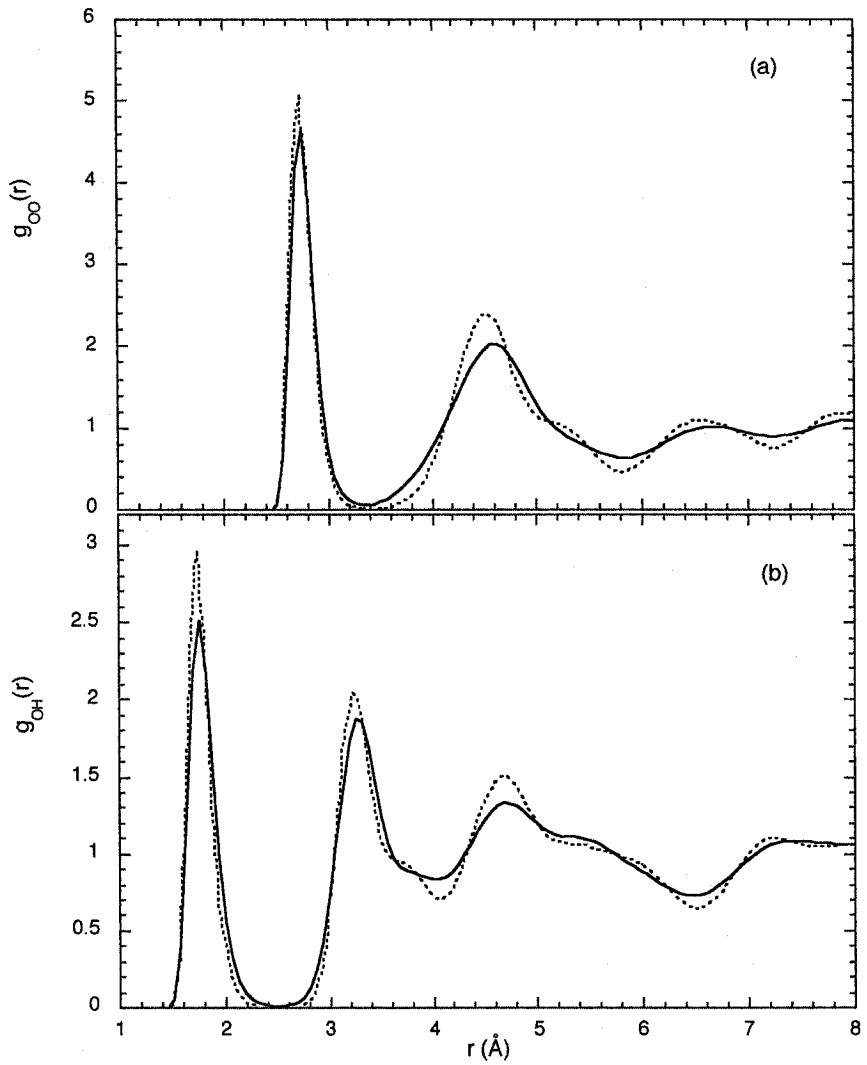

Figure 8.5. Oxygen-oxygen (a) and oxygen-hydrogen (b) radial distribution functions of classical and quantum SPC/E ice Ih at 220 K. The results represented by dotted and solid lines correspond to the classical and quantum simulations, respectively.

In Fig. 8.6, the radial distribution functions obtained in classical and quantum simulations of TIP4Pew ice at 220 K are presented. The results are very similar to those

obtained with the TIP4P water model shown in Fig 8.4. The effects of quantization are comparable to those described previously in Figs. 8.4 and 8.5.

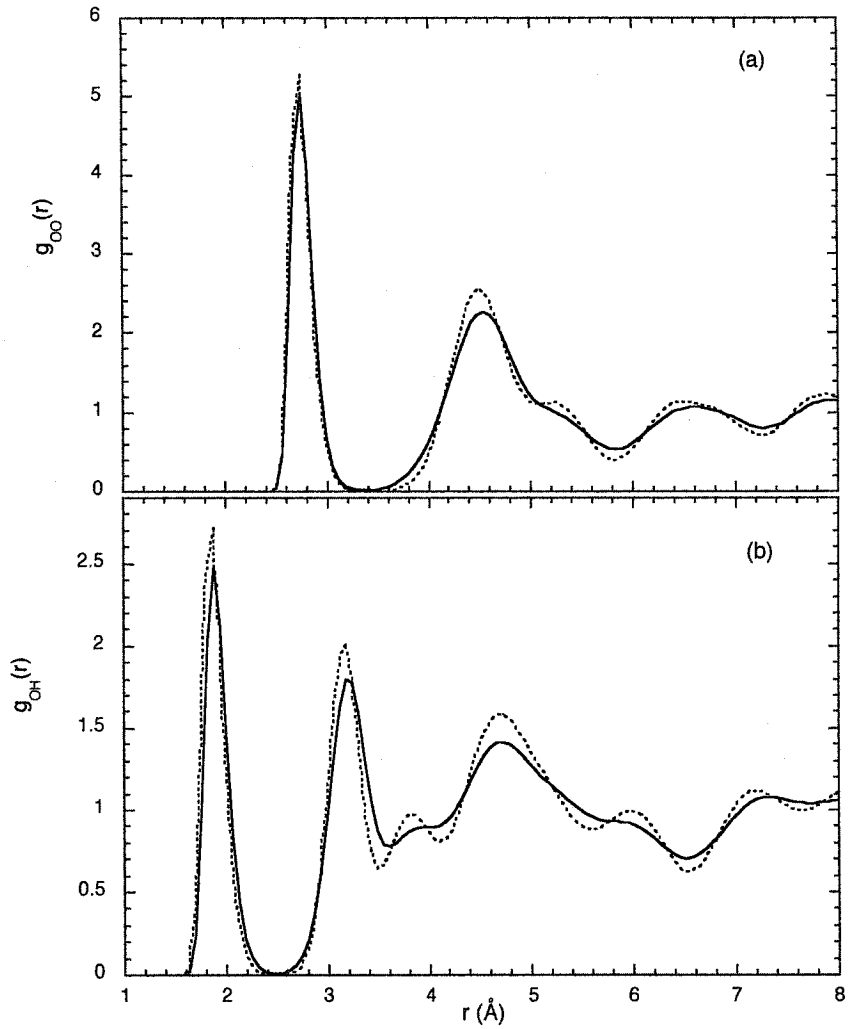

Figure 8.6. Oxygen-oxygen (a) and oxygen-hydrogen (b) radial distribution functions of classical and quantum TIP4Pew ice Ih at 220 K. The results represented by dotted and solid lines correspond to the classical and quantum simulations, respectively.

Fig. 8.7 shows the oxygen-oxygen spatial distribution functions of classical and quantum TIP4P ice Ih at 220K. The isosurfaces correspond to $g_{OO}(\mathbf{r}_{ij}) = 2.8$ and only include the first neighbour features. The structural manifestation of the quantum effects on the first neigbours is relatively small. We can see a slight shift outward of the H-

accepting feature. However, the most notable effect is on the region that joins both H-donating features where the quantum distribution "penetrates" slightly on the region with classical lower probability. This result indicates that the motion of the water molecule in the quantum lattice is slightly less restricted than in classical ice and is in agreement with the observation (made from Fig. 8.4) that the former is a less structured solid. The quantum effects here, however, are far less dramatic than in liquid water because molecular diffusion in ice is absent.

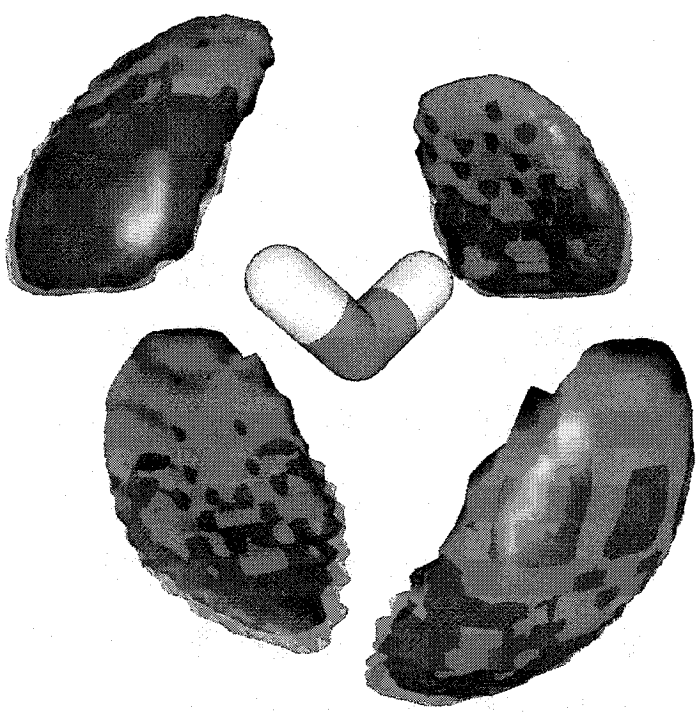

Figure 8.7. Oxygen-oxygen spatial distribution function of classical (red) and quantum (semi-transparent blue) TIP4P ice Ih at 220 K. The isosurfaces correspond to $g_{OO}(\mathbf{r}_{ij}) = 2.8$. In the figure only the first neighbour features ($\mathbf{r}_{ij}$<3.5 Å) are shown.

A quantitative comparison of the impact of quantization upon simulated ice at 220 K for all three models is presented in Table 8.1. The TIP4P water model exhibits the largest relative energy shift followed by the TIP4Pew and the SPC/E models. These results are in agreement with the observed trends in liquid water at 298 K (see Tables 7.1 and 7.4). The molecular uncertainty exhibits somewhat less model dependence than that found in liquid water simulations. It is important to note that the energy shifts and the molecular uncertainties observed for ice are consistently smaller than the corresponding values obtained in liquid phase (see Table 7.4). According to the results presented and discussed in Section 7.3, this is a consequence of the strong interactions between water molecules, which prevents the beads from "taking advantage" of the effective weakening of the harmonic (bead-bead) interaction (see Equation 6.13) implied in the lowering of temperature. It is noted that the relative shift in energy obtained from PIMC simulations of the SPC water potential at 220K by Garret and co-workers [16] is larger than the values calculated in this work.

Table 8.1. Intermolecular potential energies (in kJ/mol) and quantum molecular uncertainties (in degrees) obtained in the classical and quantum simulations of three water models at 220 K.

Model	Energy		Relative shift (%)	Quantum Uncertainty
	Classical	Quantum		
TIP4P	-50.84±0.02	-47.49±0.02	6.6	10.2
SPC/E	-55.28	-52.44	5.1	9.8
TIP4Pew	-58.48	-55.01	5.9	10.0
SPC [a]	-50.6	-46.0	9	-

(a) PIMC results from reference [16]

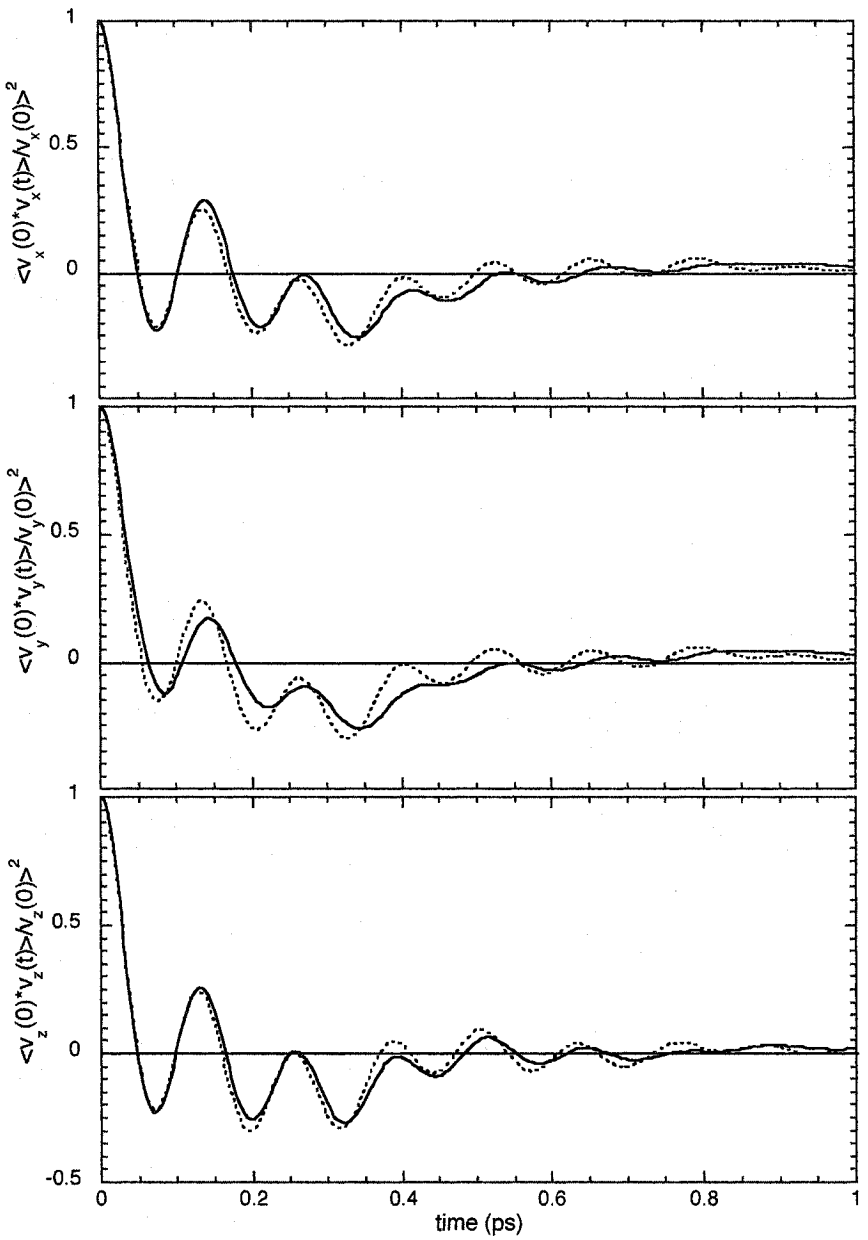

Figure 8.8. Components of the linear velocity time correlation functions for classical and quantum TIP4P ice Ih at 220 K. The results represented by the dotted and solid lines correspond to the classical and quantum simulations, respectively.

The present rigid-body-CMD methodology allows the calculation of (approximate) quantum time correlation functions. Fig. 8.8 shows the components of the velocity time correlation function obtained in classical and quantum simulations of TIP4P

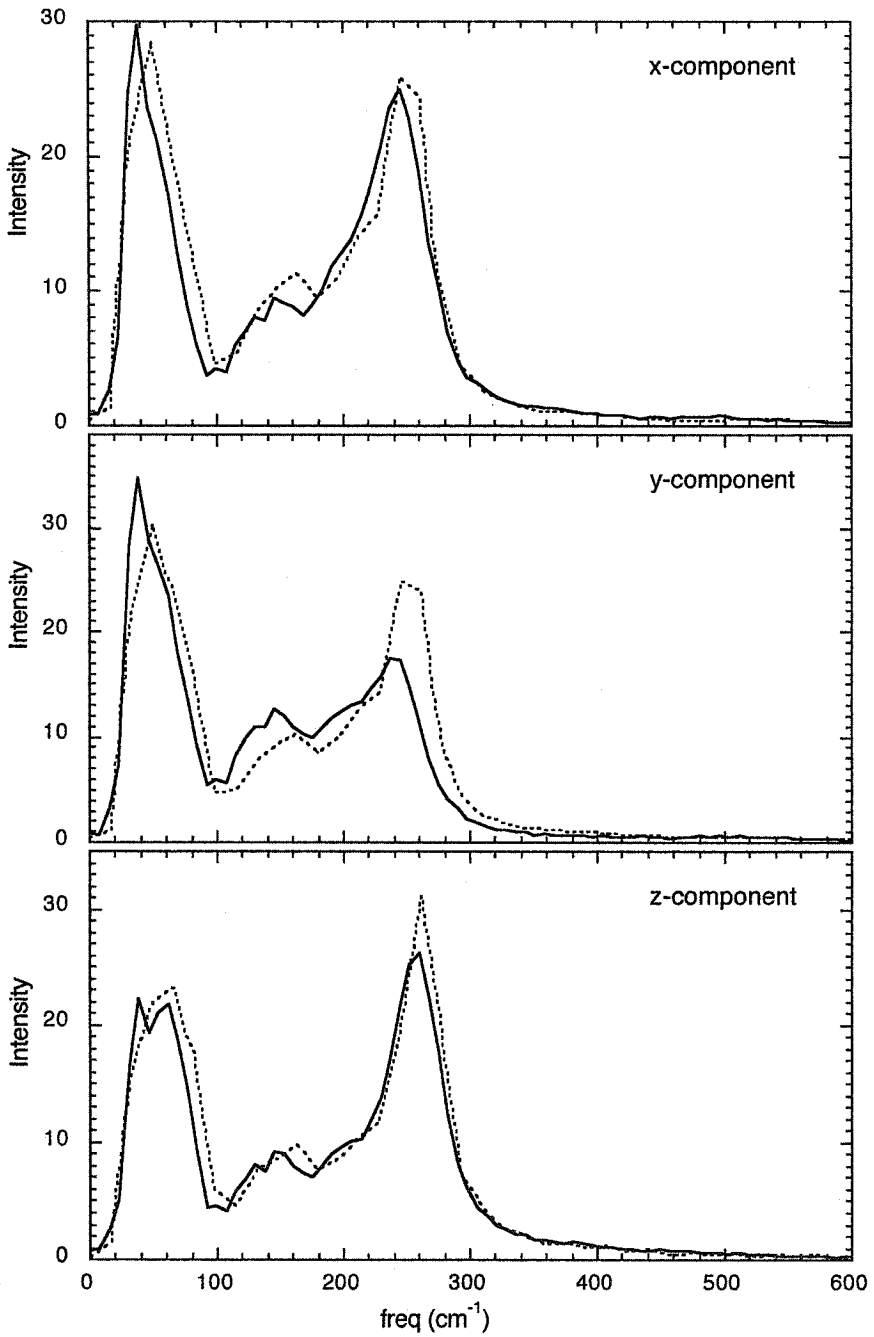

Figure 8.9. Fourier transform of the components of the linear velocity time correlation functions for classical and quantum TIP4P ice Ih at 220 K. The results represented by dotted and solid lines correspond to the classical and quantum simulations, respectively.

ice at 220 K. In the quantum functions, the maxima and minima are displaced slightly towards longer times with respect to the classical functions. This behaviour is particularly

noticeable in the y component. Quantum effects are better observed in the power spectrum of these functions plotted in Fig. 8.9. Since these power spectra are directly related to the translational motions of the centers-of-mass, the peaks shown in Fig. 8.9 have been previously identified experimentally by incoherent inelastic neutron scattering experiments [154] and have also been reported in classical molecular dynamics simulations of ice Ih [155,156]. The low frequency peak corresponds to the transverse acoustic phonons, the intermediate region to the longitudinal acoustic modes, and the high frequency peak to the optic modes [154,155]. The overall shape of the spectra agrees reasonable well with experiment [154]. The effect of quantization is manifested in a rather small, but consistent, shift to lower frequencies, and appears slightly more pronounced on the y component. Since the y axis is perpendicular to the molecular plane, this result is congruent with some of the observations made in Fig. 8.7 about a more pronounced quantum effect in the H-donating features of the local molecular structure. The shape of the classical and quantum spectra remains otherwise about the same.

The components of the angular velocity time correlation functions were also computed and are shown in Fig. 8.10. A dampening in the functions is observed as well as a displacement of the maxima and minima to longer times. The power spectrum of these functions, which contains information about the librational motion of the water molecule in the lattice, is given in Fig. 8.11. The broad bands observed are indicative of the complexity of this motion. The x component extends to higher frequencies in comparison with the other two components as a result of having the lowest inertia moment. These librational bands have also been determined experimentally [154] and

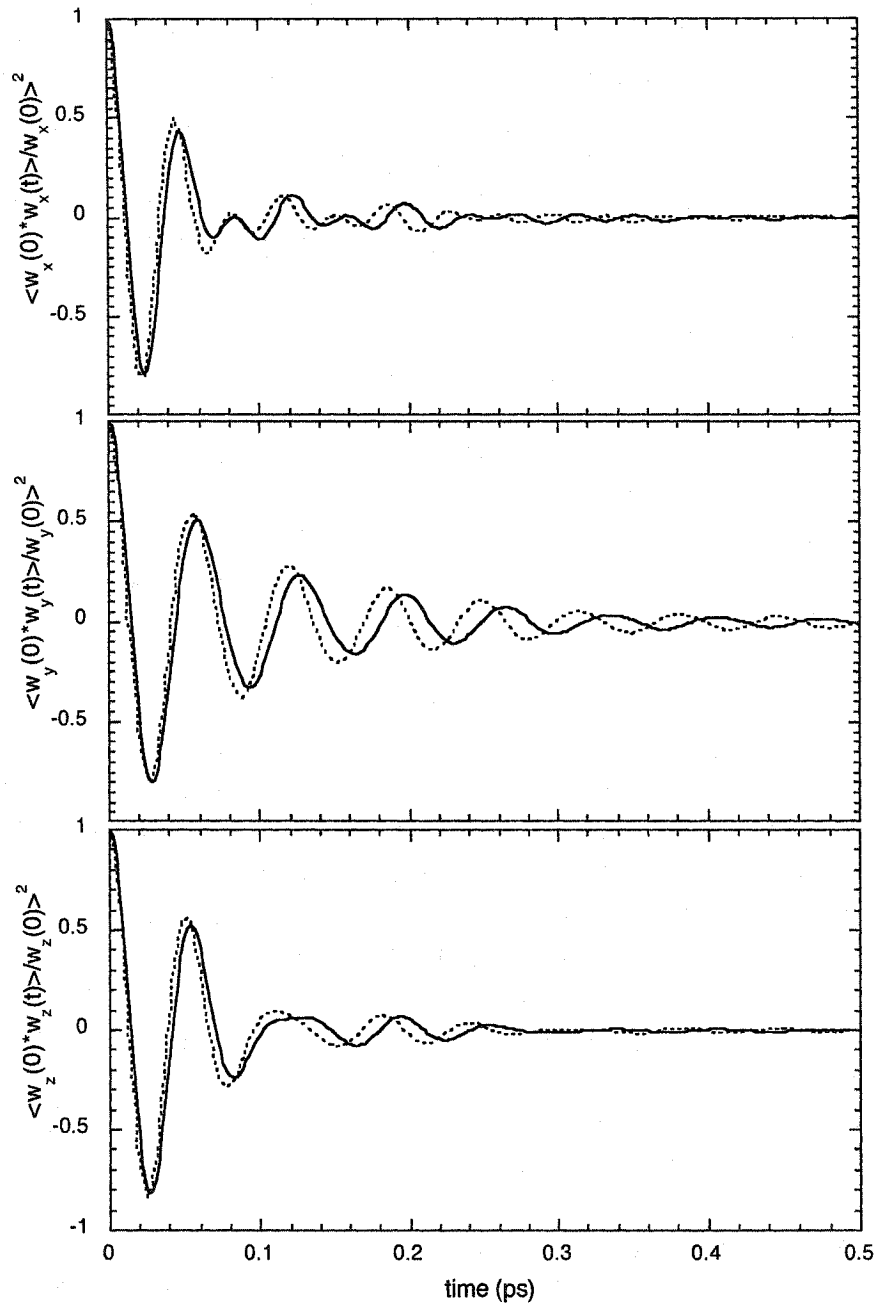

Figure 8.10. Components of the angular velocity time correlation functions for classical and quantum TIP4P ice Ih at 220 K. The results represented by dotted and solid lines correspond to the classical and quantum simulations, respectively.

reported in previous classical molecular dynamic simulations [155,156]. The translational bands can also be seen in Fig. 8.11 at lower frequencies with much lower intensity, which

indicates that there is some weak coupling between translational and rotational motions in ice.

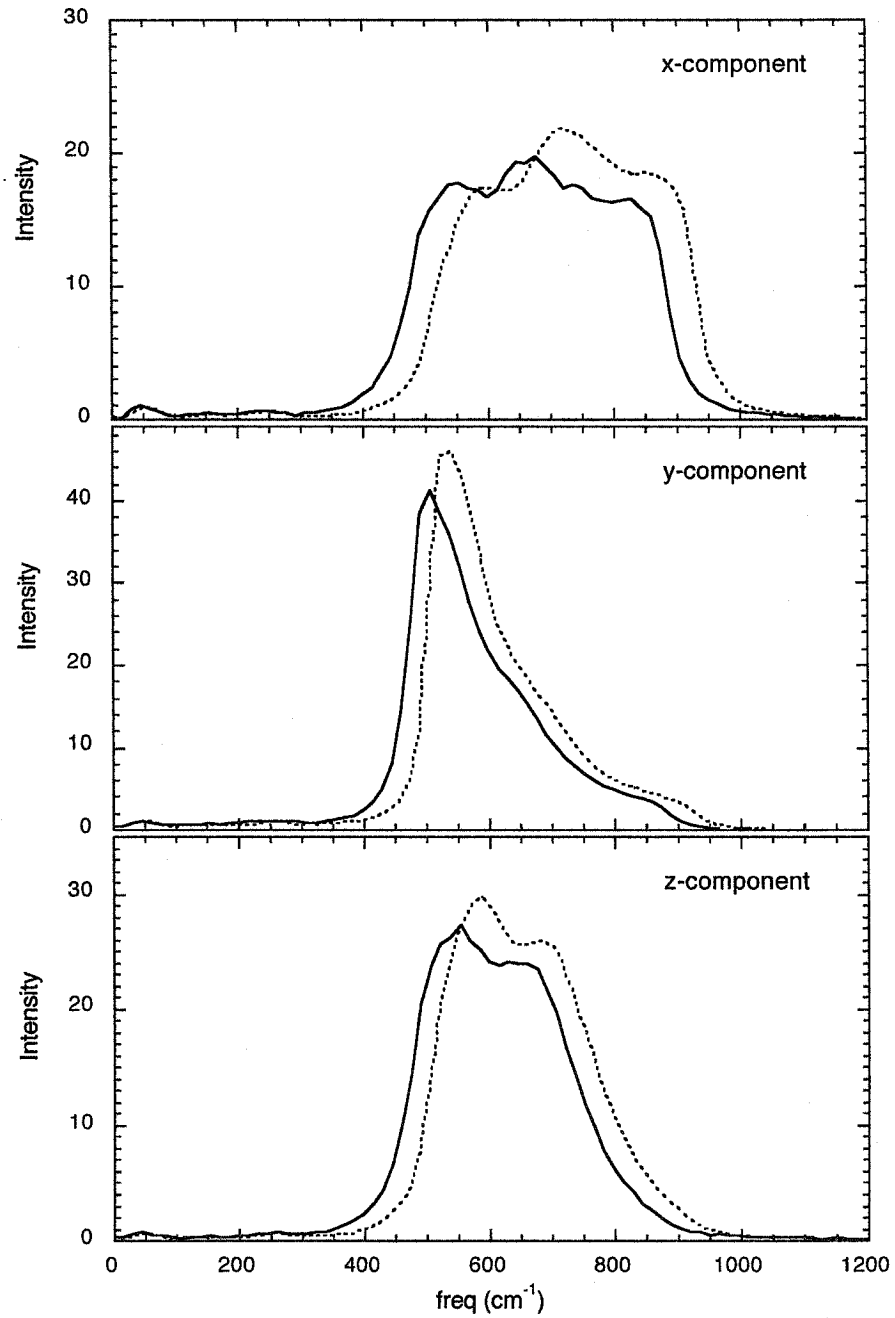

Figure 8.11. Fourier transform of the components of the angular velocity time correlation functions for classical and quantum TIP4P ice Ih at 220 K. The results represented by dotted and solid lines correspond to the classical and quantum simulations, respectively.

The effect of quantization, a 30-50 cm^{-1} shift to lower frequencies, is much more pronounced in these rotational functions than in the power spectra of the translational motion (see Fig. 8.8). This is, however, expected because the orientational coordinates are directly affected by quantization. The shift, on the other hand, seems to be comparable for all three components. To the best of the author's knowledge, these shifts have not been previously reported in the literature. They can only be calculated via path integral simulations (due to the fact that they are associated with the proton uncertainty), however equilibrium path integral calculations do not contain real time dynamical information. It is in these circumstances that the concept of the centroid becomes most useful.

The quantum effects on the lattice vibrations were also examined for the SPC/E and TIP4Pew models. The power spectra obtained for classical and quantum SPC/E ice at 220 K are presented in Figs. 8.12 and Fig 8.13. Fig. 8.12 displays the power spectra of the components of the linear velocity time correlation functions, whereas Fig. 8.13 shows the corresponding power spectra of the components of the angular velocity time correlation function. The results are again very similar to those obtained for the TIP4P model. There is a shift to lower frequencies that is much more pronounced in the librational band than the one experienced by the lower frequency modes. The results for the TIP4Pew model (not shown) are analogous to the ones presented above and are a further confirmation of the reported behaviour.

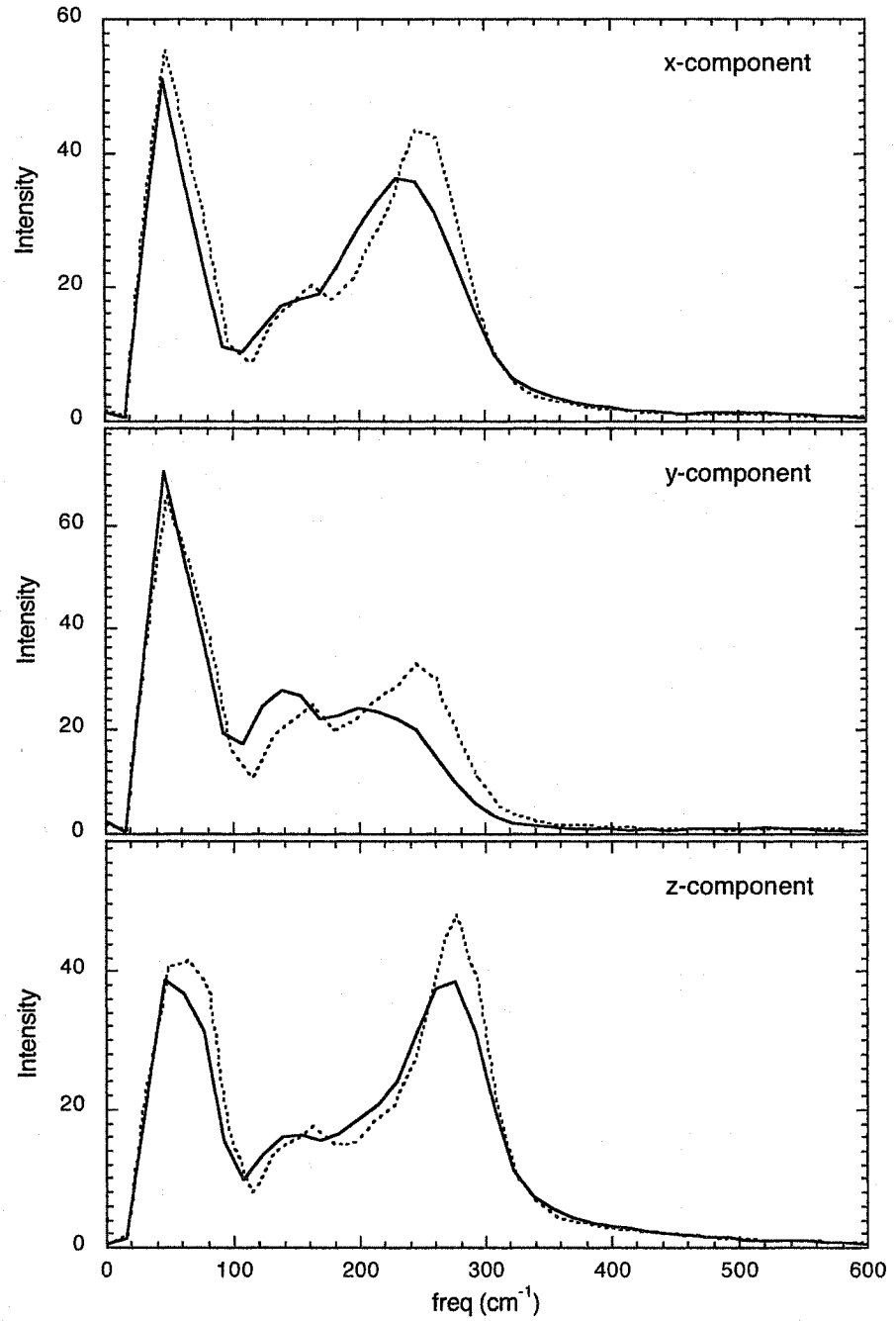

Figure 8.12. Fourier transform of the components of the linear velocity time correlation functions for classical and quantum SPC/E ice Ih at 220 K. The results represented by dotted and solid lines correspond to the classical and quantum simulations, respectively.

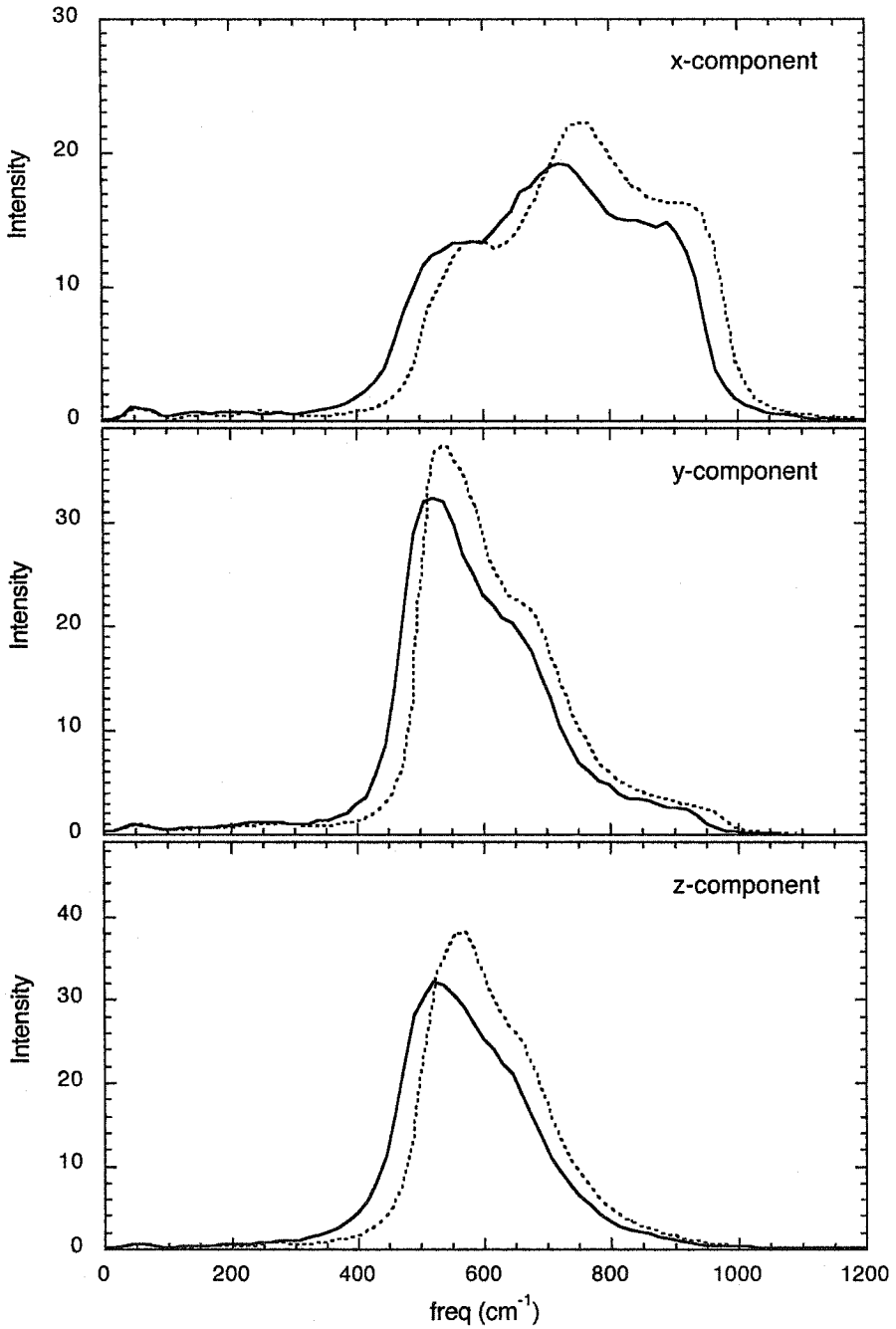

Figure 8.13. Fourier transform of the components of the angular velocity time correlation functions for classical and quantum SPC/E ice Ih at 220 K. The results represented by dotted and solid lines correspond to the classical and quantum simulations, respectively.

8.3. TEMPERATURE DEPENDENCE

It is interesting to analyze how temperature modifies the influence of quantization in ice. The general behaviour expected according to quantum statistical mechanics (and in particular in the path integral picture) was discussed in Section 7.3; as temperature increases the quantum effects become smaller. In this section, the results from quantum and classical simulations of ice Ih carried out with the TIP4P water model over a range of temperatures from 160 K to 235 K are presented.

The oxygen-oxygen radial distribution functions of ice Ih at 160 K and 235 K for classical and quantum liquid water are presented in Fig. 8.14. The maximum of the first peak, at about 2.8 Å, exhibits strong temperature dependence in the classical functions, as well as in the quantum results. The influence of quantization is apparent at both temperatures. While the changes in the first peak due to quantization are somewhat similar at both temperatures, the changes in the second peak, between 4 Å and 5 Å, are more pronounce at 235 K. Quantization, additionally, shifts these peaks slightly towards larger distances. It is important to note that, overall, the effect of the softening of the structure in this functions appears more pronounced at the higher temperature.

Fig. 8.14 shows the classical and quantum oxygen-hydrogen radial distribution functions of ice Ih at 160 and 235 K. Quantum effects, manifested as a softening of the functions and as a slight shift of the main features to larger distances, are apparent at both temperatures. Both effects are associated with a diminished attractive interaction in the

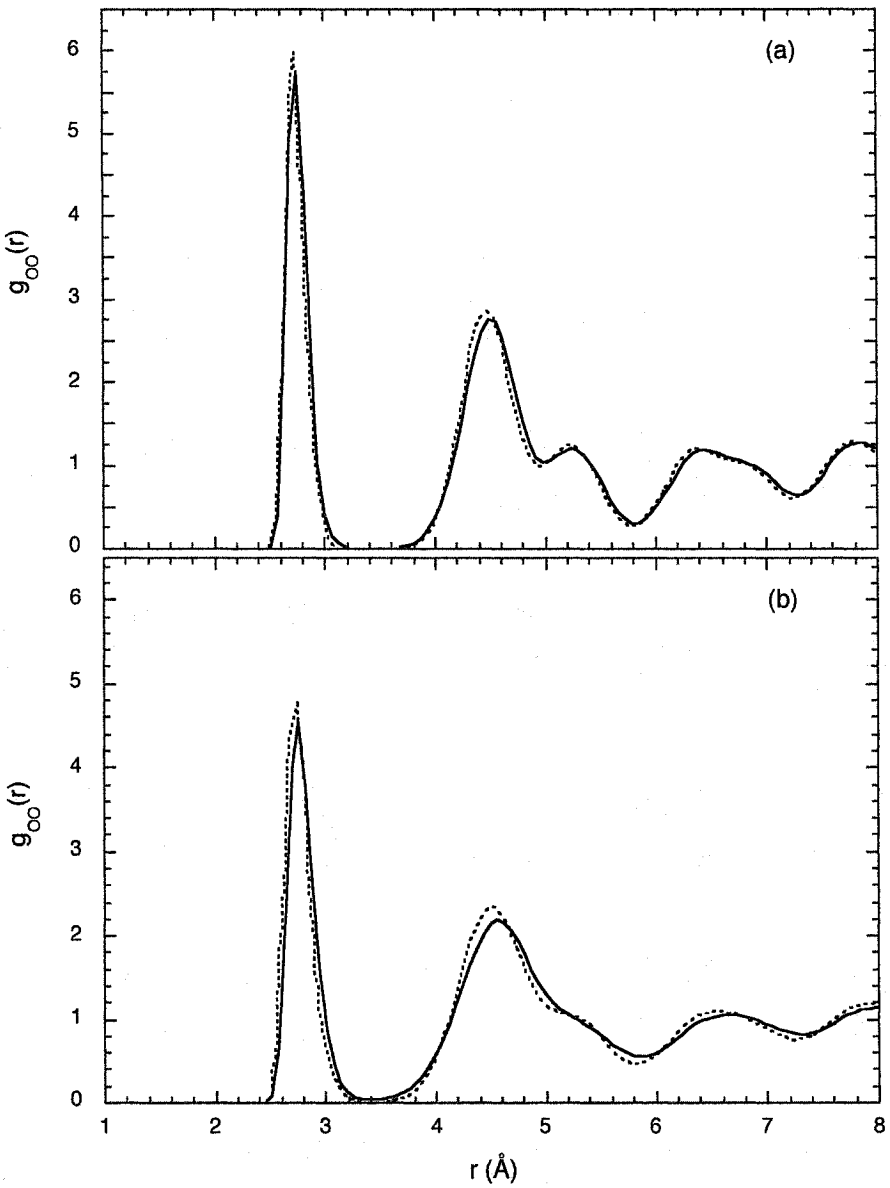

Figure 8.14. Oxygen-oxygen radial distribution functions of liquid TIP4P water at 160 K (a) and 235 K (b). The dotted and solid lines correspond to the classical and quantum, simulation results, respectively.

quantum system in comparison with the classical ice. The effect of "structure-softening" appears to impact specific structural features somewhat differently at different temperatures. For example, the third peak (between 3.4 and 4 Å), is more strongly affected by quantization at the lower temperature, however, this effect in the fourth peak

(at about 4.6 Å) is more pronounced at 235 K. Consequently, the effects of quantization on these functions were judged to be comparable.

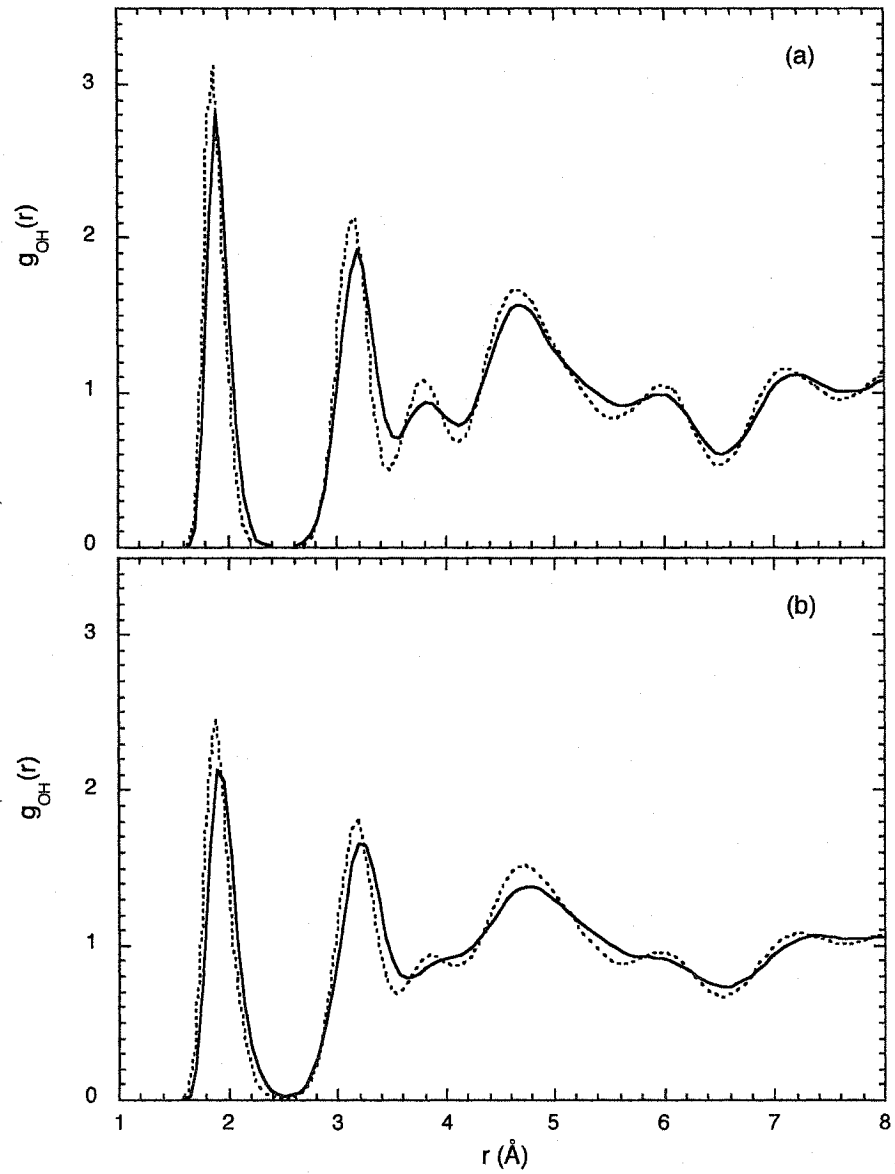

Figure 8.15. Oxygen-hydrogen radial distribution functions of liquid TIP4P water at 160 K (a) and 235 K (b). The dotted and solid lines correspond to the classical and quantum, simulation results, respectively.

The results obtained for the average intermolecular potential energies (in kJ/mol) in the classical and quantum simulations of TIP4P ice Ih are plotted as a function of

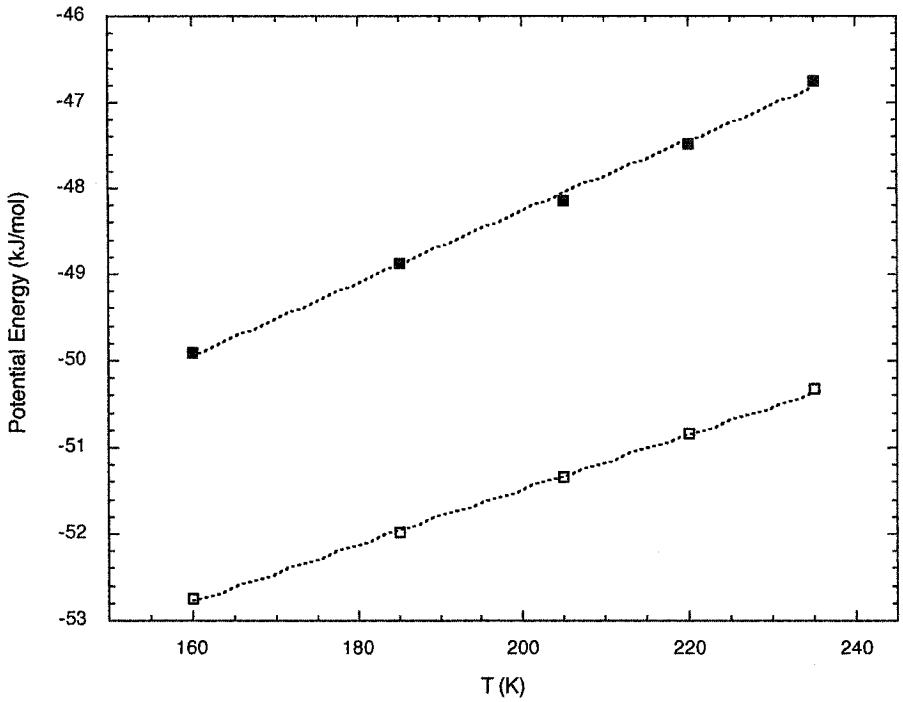

Figure 8.16. Intermolecular potential energy in kJ/mol as a function of temperature. The full squares are the results from the quantum simulations and the squares are the classical results.

temperature in Fig. 8.16. Clearly, the intermolecular potential energy is higher for the quantum simulations than for the corresponding classical ones for all the temperatures studied. It is important to point out that whereas the absolute shift in energies is smaller in ice than in water (see Fig. 7.17), described as an equivalent temperature shift it is larger in ice (85 K vs 60 K for liquid water). The (Quantum-Classical) potential energy difference for ice does not increase with the lowering of the temperature as in liquid water, but in fact decreases slightly as can be seen in Fig. 8.17. This is indicative of a higher heat capacity for the quantum crystal in comparison with classical ice. Fig. 8.17 indicates that, in the temperature range studied, the largest absolute quantum effects do not occur in the lowest temperature ices, but in fact at an intermediate region where the liquid and the solid phases meet. This result is in disagreement with Garret and co-

workers [16], where it was noted that the impact of quantum effects in the energy grows when temperature decreases. Moreover, at the temperatures where both phases coexist, the quantum effects in the energy are bigger in the liquid phase than in ice (also see Fig. 8.22).

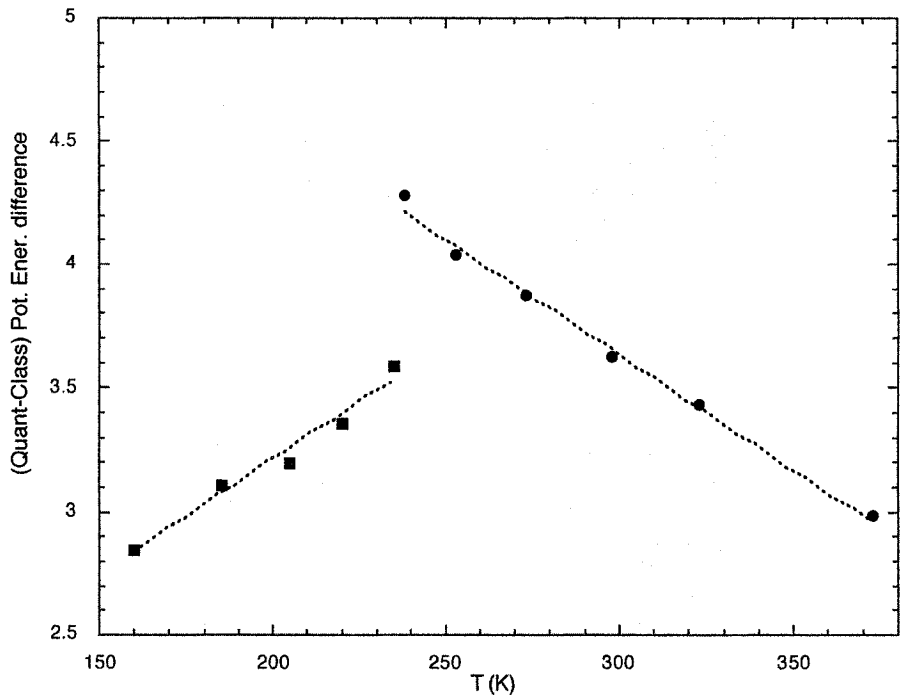

Figure 8.17. Quantum-minus-classical intermolecular potential energy difference (in kJ/mol) as a function of temperature. The full squares are the ice results and the circles are the liquid results (from Fig. 7.16).

It is reasonable to expect that the trends observed for the intermolecular potential energy with temperature are, at least qualitatively, related to the molecular uncertainty. In Fig. 8.18, the molecular uncertainty is plotted as a function of temperature, where this graph also includes the results obtained in quantum simulations of liquid water (see Section 7.3). Interestingly, the molecular uncertainty in ice decreases when the temperature is lowered; this is also consistent with the previous observation that the intermolecular potential energy difference decreases with temperature. According to the

discussion in Section 7.3, this behaviour of decreasing molecular uncertainty when temperature is lowered is a consequence of the strength of the confining potential determined by the local molecular environment.

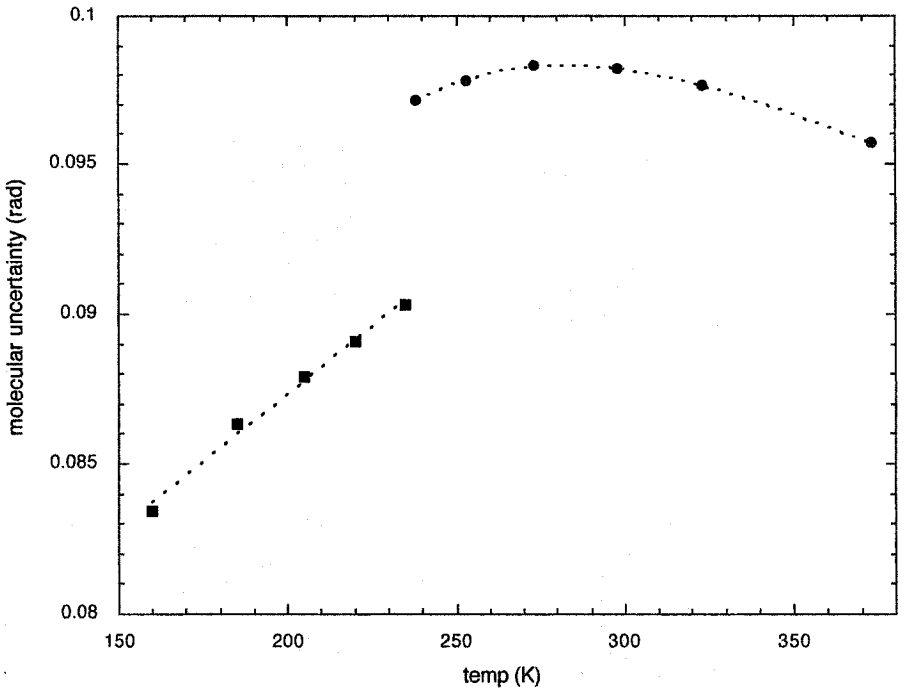

Figure 8.18. Estimated molecular uncertainty of the water molecule in quantum ice Ih as a function of temperature (squares). The graph includes the values for liquid water (dots) from Fig. 7.19.

The dynamical behaviour was also extracted from the present ice simulations and compared at different temperatures. The power spectra of the linear velocity time correlation function of classical and quantum ice at 160 and 235 K are shown in Fig. 8.19. It can be seen that the higher frequency band shifts slightly towards lower frequencies with increased temperatures. Quantization, on the other hand, also shifts the spectra towards lower frequencies, and its effect is more pronounced in the higher frequency bands than on the other features of the spectra at both temperatures. The power spectra of the angular velocity time correlation function of classical and quantum ice Ih at

160 K and 235 K, shown in Fig. 8.20, reveals a consistent shift of their principal (librational) band towards lower frequencies at both temperatures. The quantum effects on these functions appear very similar at both temperatures.

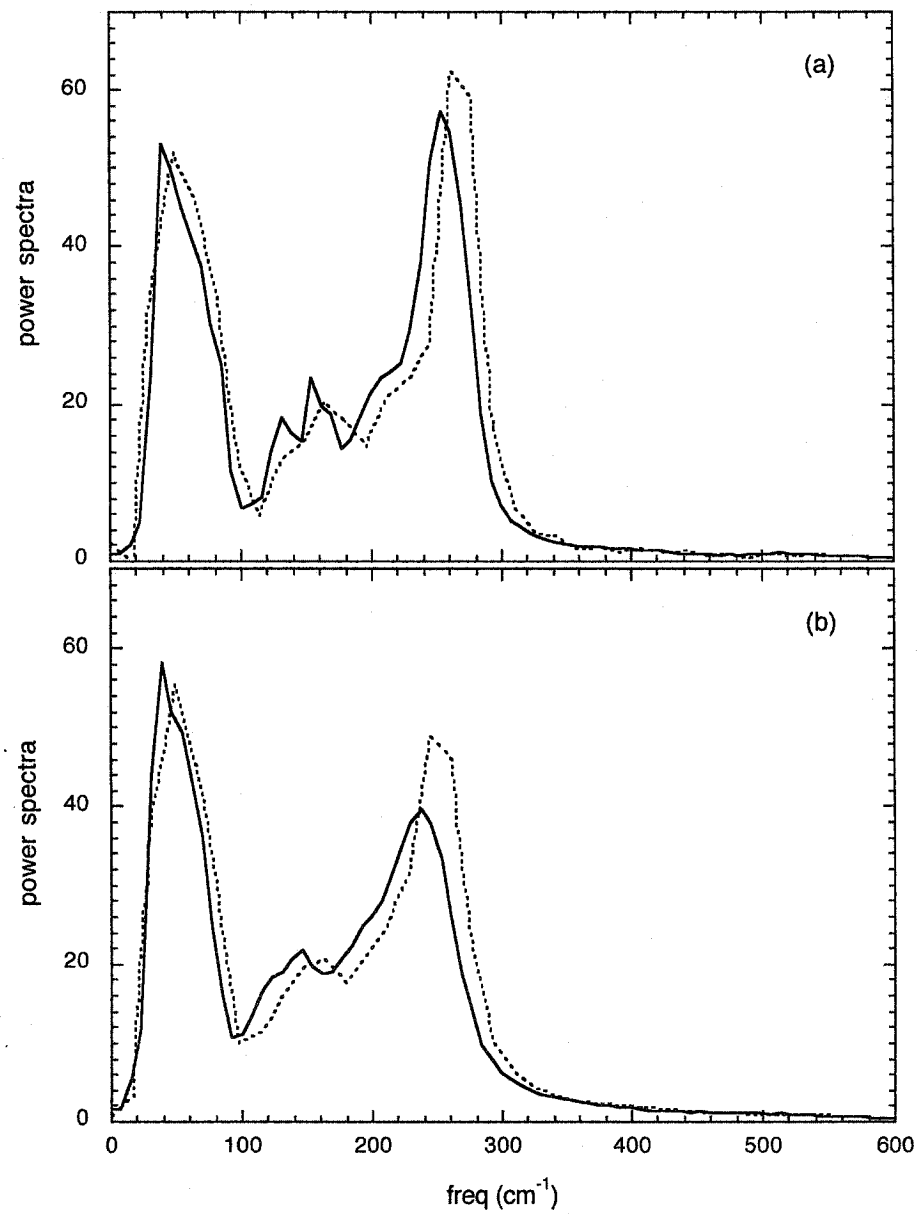

Figure 8.19. Fourier transform of the linear velocity time correlation function for classical and quantum TIP4P ice Ih at (a) 160 K and (b) 235 K. The results represented by dotted and solid lines correspond to the classical and quantum simulations, respectively.

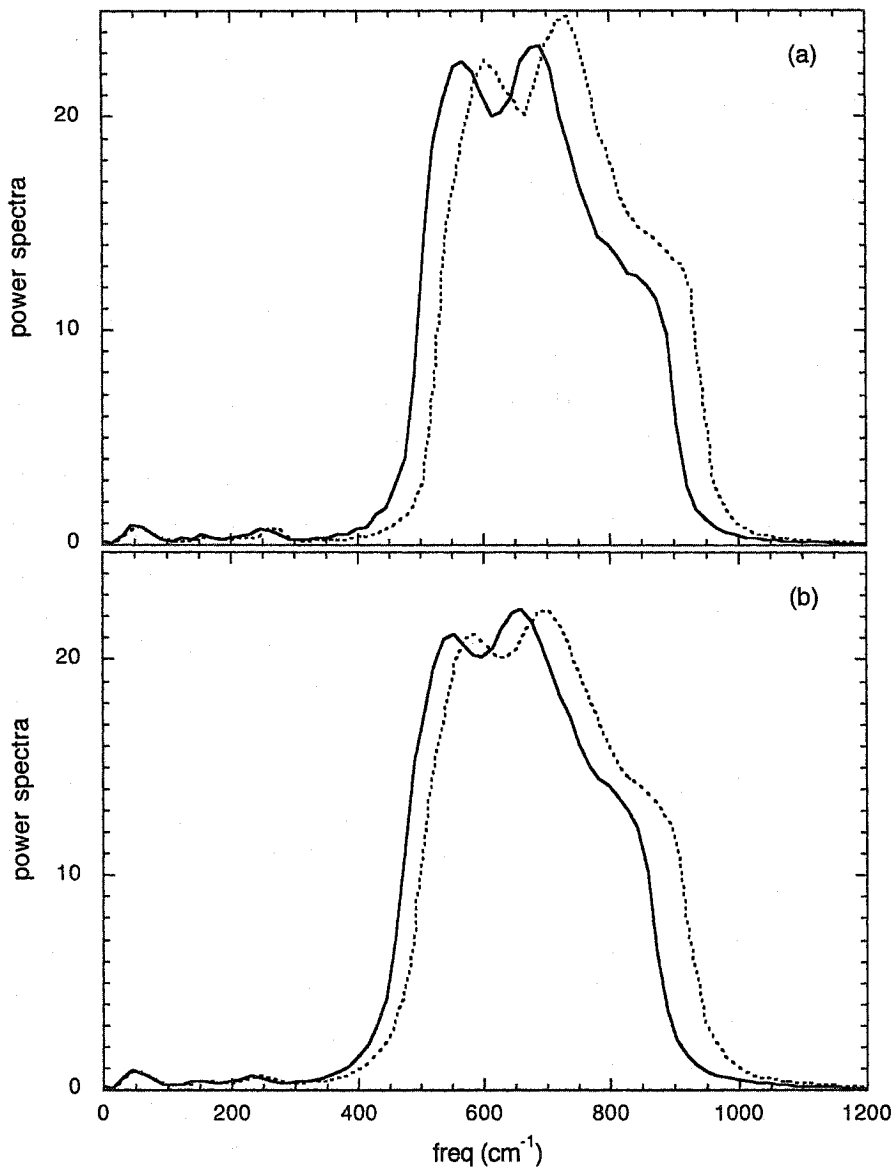

Figure 8.20. Fourier transform of the angular velocity time correlation function for classical and quantum TIP4P ice Ih at (a) 160 K and (b) 235 K. The results represented by dotted and solid lines correspond to the classical and quantum simulations, respectively.

8.4. CLASSICAL VS QUANTUM MELTING: PRELIMINARY RESULTS

In this final section, the results from "computer experiments" of ice melting are presented. The discussion is intended to be a preliminary evaluation of the differences between the mechanical phase transition that occurs when super-heated ice Ih melts following a classical or a quantum dynamics.

Both "experiments" (classical and quantum) were carried out starting with a well-equilibrated configuration of simulated ice Ih at 235 K. The temperature was then increased in 5 degrees increments, allowing for 2 ps of equilibration and 10 ps of averaging at each step. This procedure was repeated until a phase transition was detected. The point immediately before the identified phase transition, as well as those after it, were equilibrated for a total of 40 ps and then averaged over 10 ps. This equilibration period of 40 ps allows us to establish a well-defined mechanical phase transition temperature, T_{mph}, where the super-heated ice remains crystalline over the observation time at temperatures lower than T_{mph} and is observed to melt for temperatures at or above T_{mph}. The thermodynamic melting temperature, T_m, is the temperature at which the bulk liquid and solid phases are in equilibrium. Thus, for our "melting experiment" T_m would correspond to the melting temperature where the transition occurs after an infinite equilibration time. Therefore, these two temperatures must satisfy the relationship $T_{mph}>T_m$, which implies that any calculated value of T_{mph} will be strongly influenced by kinetic factors. An accurate determination of the thermodynamic melting temperature,

would only be possible from a much more extensive simulation study, for example, of heterogeneous systems [157,158].

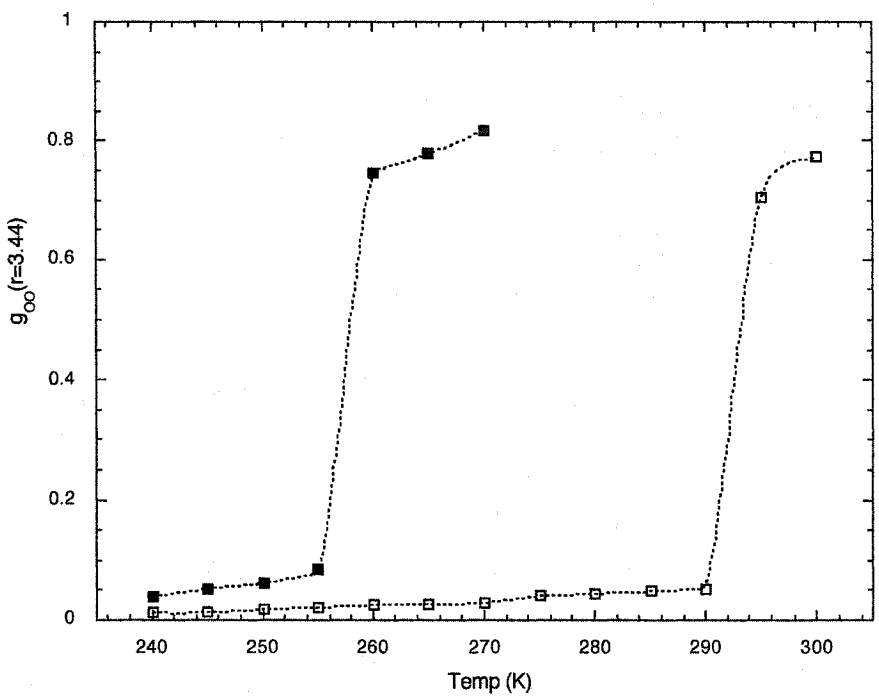

Figure 8.21. Dependence of the value of the oxygen-oxygen RDF at 3.44 Å as a function of temperature for the classical and quantum melting of ice Ih. The results represented by open squares and solid squares correspond to classical and quantum simulations, respectively.

Fig 8.21 shows the value of the oxygen-oxygen radial distribution function at 3.44Å obtained from appropriate series of classical and quantum simulations as a function of temperature. The existence of a near-zero value in this function for ice is very closely related to the essentially zero diffusion coefficient of the crystalline phase. In liquid water, however, the oxygen-oxygen RDF has a minimum slightly less than 1 at this distance. The radial distance 3.44 Å demarcates a reasonable limit between the first and the second coordination shells, a region that is crucially different in ice and liquid water. Indeed, the integral $4\pi\rho\int_0^{3.44} r^2 g_{OO}(r)dr$, which represents a coordination number, gives

the values 4 and about 4.5 for ice and liquid water, respectively. This extra-coordination in the liquid is due to the interstitial water [149] (see Section 7.4). The parameter $g_{OO}(r = 3.44)$ was used first by Garret and co-workers in a PIMC simulation of ice Ih melting [16].

According to Fig. 8.21, the mechanical phase transition occurs just above 290 K in the classical simulation and just above 255 K in the quantum "experiment". This difference of about 35 degrees should be an upper bound of the expected shift of the thermodynamic melting temperature. This result is in qualitative agreement with that reported by Garret and co-workers [16] on the SPC water model. They noted that quantum SPC ice Ih melts at 260 K and classical SPC ice Ih at a 20 degree higher temperature. Their mechanical phase transitions, however, were not as sharp as the ones in Fig. 8.21 and lead them to conclude that the use of classical simulations in water for temperatures of 300 K and above is justified. The results shown in this work however do not verify this conclusion.

The results of Fig. 8.21 are further confirmed by Fig. 8.22. The latter figure shows the intermolecular potential energy (in kJ/mol) obtained in the classical and quantum melting "experiments" as a function of temperature. The figure also includes well-converged values of the intermolecular potential energy obtained for classical and quantum ice, as well as classical and quantum liquid water. These latter values, which are the result of much longer simulations, serve to confirm the quality of the results obtained in the melting processes. Fig. 8.22 verifies that the intermolecular energy difference

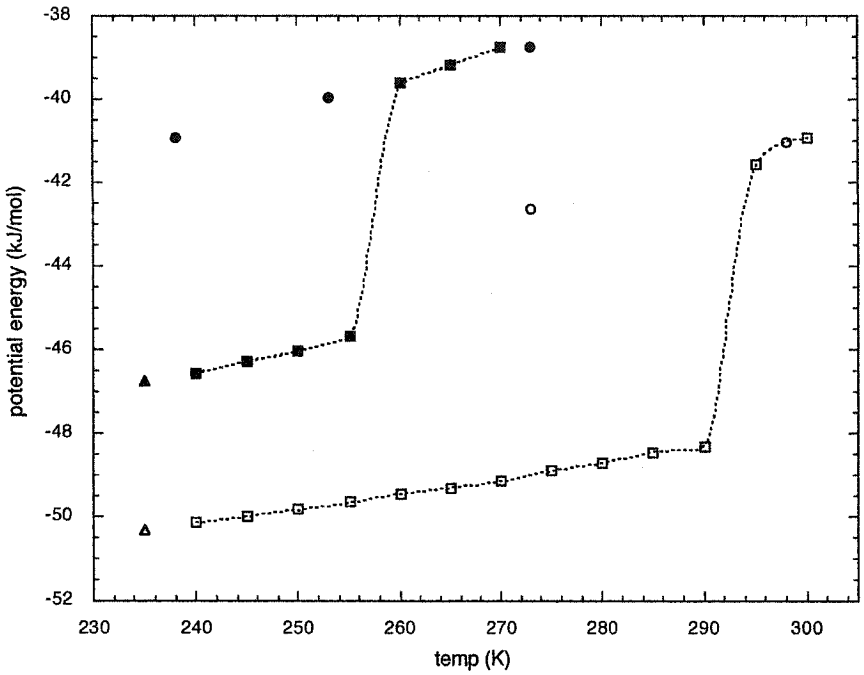

Figure 8.22. Average intermolecular potential energies (in kJ/mol) as a function of temperature for the classical (open squares) and quantum (solid squares) melting of ice Ih. The graph also includes well-converged values of classical (open triangles) and quantum (solid triangles) ice at 235 K and classical (open circles) and quantum (dots) liquid water.

between classical and quantum ice is smaller in ice than in liquid water. This observation is in agreement with the results presented in Section 8.3 but differs from the conclusions of Garret and co-workers [16] on classical and quantum melting of SPC ice Ih.

Finally, it would seem that this (thesis) work would not be complete without the inclusion of some illustrative examples of quantum and classical liquid water and ice configurations. Fig. 8.22 shows two instantaneous molecular configurations, taken from the classical melting runs at temperatures of 290 K and 295 K. Fig. 8.23, on the other hand, shows two instantaneous molecular configurations from the quantum melting experiment at 255 K and 260 K. Since the figures only represent an instantaneous coordinate "measurement", they do not necessarily reflect fully the inherent properties of

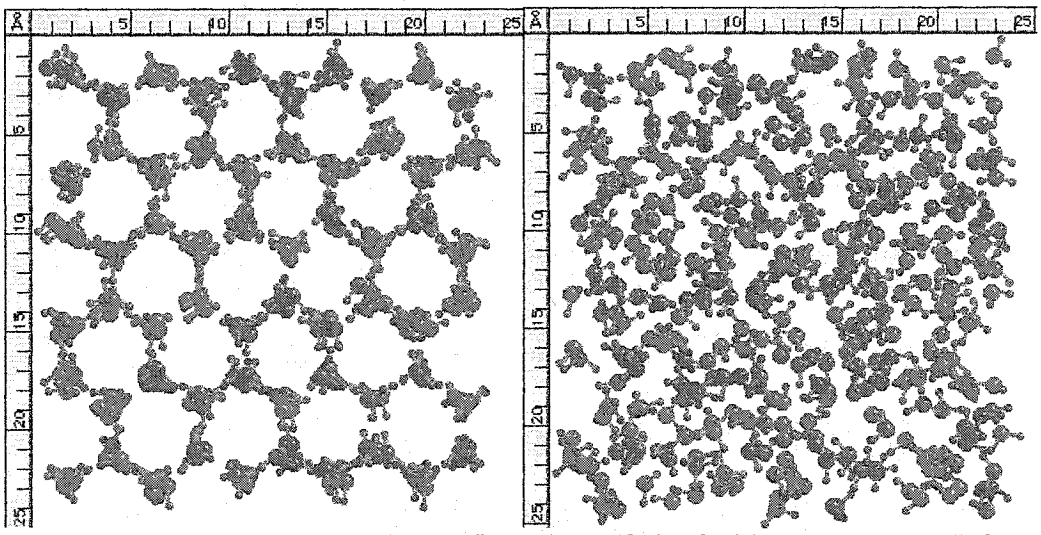

Figure 8.23. Instantaneous molecular configurations of classical ice Ih at 290 K (left) and the resulting liquid water at 295 K (right).

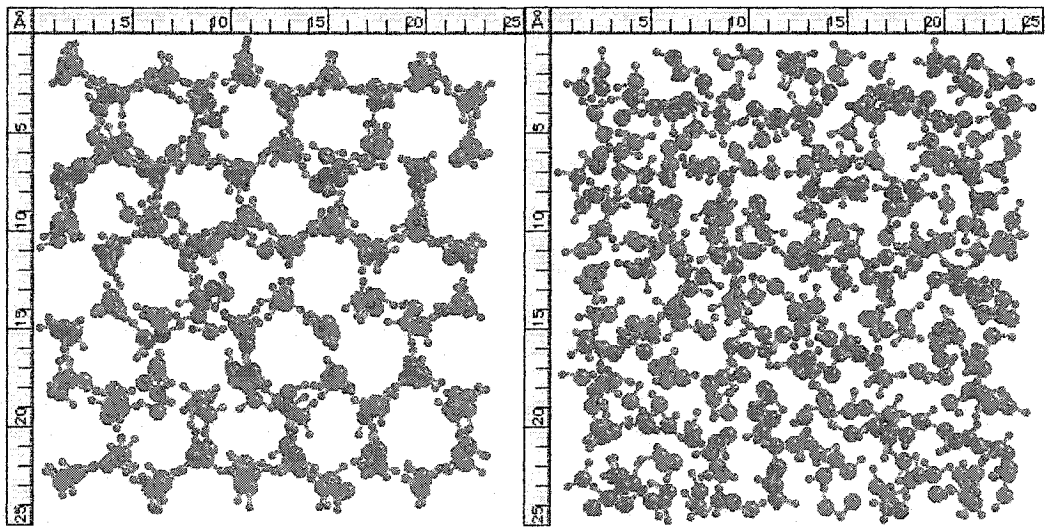

Figure 8.24. Instantaneous molecular configurations of quantum ice Ih at 255 K (left) and the resulting liquid water at 260 K (right).

the system from which they have been taken (something that can only be achieved otherwise with the appropriate statistical averaging). Nevertheless, the much colder quantum ice seems to exhibit slightly more disorder than the higher temperature classical ice, in agreement with expectations.

9. CONCLUSIONS

In this thesis, the development of a CMD methodology for systems of rigid bodies has been presented by introducing the new concept of an *orientational centroid* and by designing an algorithm that samples homogeneously the quantum mechanical orientational uncertainty. Due to the subtleties associated with the orientational space, this development is by no means a direct or straightforward extension of the standard CMD method. Since the only explicit requirement is the validity of a rigid molecular model, this method is expected to be advantageous for quantum simulations of simple molecular systems (such as H_2O, NH_3, CH_4, etc.) in condensed phase and near their classical limit. The requirement of rigidity provides a very significant increase in computational efficiency by taking advantage of the absence of vibrations and a lower value of the discretization parameter P. The *rigid body-CMD* method permits the calculation of equilibrium and dynamical bulk properties of the system; it should be applicable to the study of a number of processes (such as melting, crystallization, solvation, etc) where molecular vibrations might be considered of minor importance. It is worth noting that although the applications carried out in this thesis employed only empirical molecular models, this method could be implemented in conjunction with more complex models or even with the appropriate quantum mechanical electronic evaluation in an *ab initio path integral centroid molecular dynamics* simulation. Such an approach could significantly benefit from the enhanced efficiency arising from the approximation of rigidity as demonstrated in this thesis.

Naturally, the rigid body-CMD method has some limitations, a detailed analysis of which can be useful in order to identify the scenarios where the method can be used and the expected accuracy of its application. One of the most important assumptions is that the existence of an orientational centroid and the guarantee of its conservation imply that the quantum time correlation functions can be calculated according to the CMD prescription (see, for example, Equation 7.3). This assumption can be tested by doing a comparative study on simple systems with this and other methods (like for example, CMD). The implementation of the rigid body-CMD method as presented in Chapter 6 may also be improved. A suggestion along this line is to implement dynamical constraints on the rotational equations of motion (Equations 6.20 and 6.21) based on a time derivative of Equations 6.27-6.29 and the appropriate generalization for more than three beads. The dynamics generated by the resulting equations of motion should be superior to the dynamics of those implemented for this work (for example, it may precisely conserve energy).

This thesis presents and discusses the results obtained from an extensive application of the *rigid body-CMD* method on liquid water and ice Ih. Since this work reports the first study where rigid body-CMD has been applied to the simulation of a model liquid system in which the molecules have been treated as rigid bodies, considerable attention was paid to the parameterization and characterization of the methodology. Liquid water at room temperature was investigated using simple (rigid) water models, primarily the TIP4P potential. The systematic examination of the isotopic effects in the bulk properties of liquid water, reveals that this approach, has successfully

reproduced the results for the equilibrium and dynamical properties of light and heavy water as obtained from experiment and from previous path integral simulations. It is shown that the removal of the vibrational degrees of freedom, accompanied by the relatively low value of the discretization parameter (P=5) required for convergence, allow the present approach to be significantly (at least 20 times) faster than standard CMD. The technique, at the same time, recovers at a quantitative level essentially the full effect of quantization observed previously in quantum simulations with flexible models. This also implies that even within quantum dynamics, flexibility does not play a critical role in determining the bulk properties of liquid water. Furthermore, as a result of the considerably enhanced computational efficiency of the rigid-body CMD simulations, it was possible to generate significantly longer real-time trajectories with the accompanying reduction in the statistical errors in the properties of interest.

Explicit inclusion of the orientational degrees of freedom additionally allows a quantitative analysis of the rotational uncertainty of the H_2O and D_2O water molecules and its effect on the components of the angular velocity time correlation function. As expected, a notably larger impact of quantization was observed in H_2O than in D_2O. Its influence on rotational dynamics, particularly librational motion and dipole relaxation times, is consistent with a "softening" of the intermolecular interactions. The enhancement of the linear self-diffusion coefficient (by roughly 50%) at ambient conditions is an indirect effect of quantization and reflects the importance of rotational-translational coupling in the dynamics of liquid water. In addition, simulations with two other models further verified the results obtained for TIP4P liquid water. After all, the

quantum mechanical uncertainty of the protons is an inherent property of nature that manifests itself in liquid water, and its effects should be reproducible for any water-like molecular model (of reasonable quality). This study confirms that, whereas classical simulations are unable to, quantum dynamical calculations, can within a rigid-body approximation, reproduce the known isotope effects in water.

The simulations carried out at several temperatures allowed us to realize the increasing importance of quantum effects in the equilibrium and especially in the dynamical properties of water in the supercooled region. The curious behaviour of the molecular uncertainty of water with temperature and its relations to the local molecular environment was also uncovered. In addition, the phenomenon of "effective tunneling" in liquid water was characterized in an unambiguous manner, and its relationship to the mechanism of diffusion was revealed. The distinction between the impact of quantum effects and the increase in the temperature was also established.

The investigation of the quantum effects in ice Ih served to complement the liquid water study. It was found that although the impact of quantization in energy was equivalent to a temperature increase of about 80°C, the molecular uncertainty in ice Ih was smaller than the one found in liquid water. This later observation was consistently verified for three different models and (with TIP4P) at several temperatures. The shifts associated with the impact of quantization on the low frequency modes were also reported. In order to illustrate the simulation of a process where the *rigid body-CMD* method might be of use to provide important physical insights, the preliminary results of a comparative study of classical and quantum melting of ice Ih were also presented.

There are many other studies that can be performed. It would be interesting to study the dependence of the molecular uncertainty in liquid water at higher pressures where water behaves more like a "normal" liquid. It is also interesting to evaluate the isotopic effects in ice by studying D_2O, which would provide further possibilities of comparison with experiments. The investigation of other (higher pressure) phases of ice could also be of interest. The melting temperature of ice Ih could be calculated more accurately by studying the coexistence of liquid water and ice. Liquid water crystallization may also be an important (and technically achievable) process for which to apply the rigid body-CMD method.

One of the most important conclusions from this work, that should be relevant for the community interested in the simulation of liquid water and the development of water models, is that the quantum mechanical uncertainty of the protons in water have an important effect on the water properties. Therefore, a systematic improvement in the description of liquid water by the use of increasingly accurate model potentials in classical simulations or *ab initio* molecular dynamics approaches is, at the very least, limited. Any such technique makes an explicit assumption of proton localization which have been shown here to be non-negligible.

Finally, in the introductory chapter of this thesis an argument was made for the utility of computer simulations. Among other advantages, computer simulations allow us to create an artificial situation where the importance of the parameters of interest can be tested. This thesis has made extensive use of this concept by "turning on" and "turning off" an essential property of nature, *the quantum mechanical uncertainty*. This fictitious

procedure has permitted a direct analysis of the importance of quantum effects in water. It is my hope that this thesis has made some contribution in the understanding of liquid water and ice and that the rigid body-CMD method will continue being applied in some other relevant contexts.

APPENDIX. *QUATERNION PARAMETERS AND ROTATIONS*

Mathematical properties of quaternions

A quaternion, as the name suggests, may be regarded as a 4-tuple of real numbers, that is as an element of R^4 [127]. In this case one would write $\hat{q} \equiv (q_0, q_1, q_2, q_3)$ where q_0, q_1, q_2 and q_3 are simply real numbers or scalars. There is also an alternative way of representing a quaternion, by defining its *scalar part* to be some real number q_0 and its *vector part* by $\mathbf{q}$, which is an ordinary vector in R^3, $\mathbf{q} = \mathbf{i}q_1 + \mathbf{j}q_2 + \mathbf{k}q_3$, with **i**, **j**, and **k** as the standard orthonormal basis in R^3. Then, a quaternion $\hat{q}$ is the sum [127]

$$\hat{q} \equiv q_0 + \mathbf{i}q_1 + \mathbf{j}q_2 + \mathbf{k}q_3 . \qquad \textbf{(A-1)}$$

This quaternion will exhibit the following properties [127].

i) Equality

If $\hat{q} \equiv q_0 + \mathbf{i}q_1 + \mathbf{j}q_2 + \mathbf{k}q_3$ and $\hat{p} \equiv p_0 + \mathbf{i}p_1 + \mathbf{j}p_2 + \mathbf{k}p_3$, then $\hat{q} = \hat{p}$ if and only if

$$q_0 = p_0,\ q_1 = p_1,\ q_2 = p_2 \text{ and } q_3 = p_3. \qquad \textbf{(A-2)}$$

ii) Addition

$$\hat{q} + \hat{p} \equiv q_0 + p_0 + \mathbf{i}(q_1 + p_1) + \mathbf{j}(q_2 + p_2) + \mathbf{k}(q_3 + p_3). \qquad \textbf{(A-3)}$$

iii) Multiplication

$$c\hat{q} \equiv cq_0 + \mathbf{i}cq_1 + \mathbf{j}cq_2 + \mathbf{k}cq_3, \tag{A-4}$$

where c is a scalar.

$$\hat{p}\hat{q} = p_0\, q_0 \; -\mathbf{p}\cdot\mathbf{q} + p_0\,\mathbf{q} + q_0\,\mathbf{p} + \mathbf{p}\times\mathbf{q}, \tag{A-5}$$

where $\mathbf{p}\times\mathbf{q} = \begin{vmatrix} \mathbf{i} & \mathbf{j} & \mathbf{k} \\ p_1 & p_2 & p_3 \\ q_1 & q_2 & q_3 \end{vmatrix}$ and since this term is not commutative, neither is the quaternion product. The product of quaternions $\hat{p}\hat{q} = \hat{r}$ may be written using the algebra of matrices,

$$\begin{bmatrix} r_0 \\ r_1 \\ r_2 \\ r_3 \end{bmatrix} = \begin{bmatrix} p_0 & -p_1 & -p_2 & -p_3 \\ p_1 & p_0 & -p_3 & p_2 \\ p_2 & p_3 & p_0 & -p_1 \\ p_3 & -p_2 & p_1 & p_0 \end{bmatrix} \cdot \begin{bmatrix} q_0 \\ q_1 \\ q_2 \\ q_3 \end{bmatrix}. \tag{A-6}$$

It is important to notice that Equations A-5 and A-6 arise by the use of the relationship $\mathbf{i}^2 = \mathbf{j}^2 = \mathbf{k}^2 = \mathbf{ijk} = -1$, which implies that quaternions are a generalization of complex numbers [127].

iv) Complex conjugate

The complex conjugate is defined as

$$\hat{q}^* \equiv q_0 - \mathbf{i}q_1 - \mathbf{j}q_2 - \mathbf{k}q_3, \tag{A-7}$$

and using results above (Equations A-5 or A-6 and A-7) it is easily shown that $(\hat{p}\hat{q})^* = \hat{q}^*\,\hat{p}^*$.

v) Norm

The quaternion norm is given by

$$N(\hat{q}) = |\hat{q}| = \sqrt{\hat{q}^* \hat{q}} = \sqrt{q_0^2 + q_1^2 + q_2^2 + q_3^2}\,. \qquad \textbf{(A-8)}$$

It is clear that if a quaternion has norm 1 each of its components must have an absolute values less than or equal to 1. Such quaternions are called *unit* or *normalized.* It is easy to show [127] that the norm of a product is equal to product of the norms, $N^2(\hat{p}\hat{q}) = N^2(\hat{p})N^2(\hat{q})$. It then follows that the product of two *unit* quaternions is again a *unit* quaternion.

vi) Inverse

The quaternion inverse is defined as

$$[\hat{q}]^{-1} = \frac{\hat{q}^*}{N^2(\hat{q})}. \qquad \textbf{(A-9)}$$

It is obvious that if $\hat{q}$ is a unit quaternion then its inverse is equal its complex conjugate, $[\hat{q}]^{-1} = \hat{q}^*$.

Another useful way of writing a unit quaternion is [127]

$$\hat{q} = q_0 + \mathbf{q} = \cos\theta + \mathbf{u}\sin\theta, \qquad \textbf{(A-10)}$$

where $-\pi < \theta \leq \pi$ and $\mathbf{u} = \frac{\mathbf{q}}{|\mathbf{q}|} = \frac{\mathbf{q}}{\sin\theta}$. Within this form, there is an explicit reference to a vector and an angle, the parameters that one expect to find in a rotation operator; the similarity with the polar representation of a complex number is noteworthy.

Quaternion rotation operator and angular velocity

There is a one-to-one correspondence between vectors (say $\mathbf{v}$) in R^3 and quaternions with the form $\hat{v} = 0 + \mathbf{v}$ [127]. Such quaternions are called *pure quaterions*. In the equations below it will be assumed that the vector notation in a quaternion product is implicitly represented by its corresponding pure quaternion.

It can be proven that a vector $\mathbf{v}$ in R^3, written in a quaternion form $\hat{v} = 0 + \mathbf{v} \rightarrow \mathbf{v}$, suffers a rotation in this space when the following operator is applied [127]

$$\mathbf{w} = \hat{q}\mathbf{v}\hat{q}^* = R_q(\mathbf{v}), \qquad \textbf{(A-11)}$$

where $\hat{q}$ is a unit (non necessarily a pure) quaternion and $\hat{w} = 0 + \mathbf{w} \rightarrow \mathbf{w}$. With the aid of some simple vector algebra it is possible to derive such a result,

$$\hat{w} = \hat{q}\mathbf{v}\hat{q}^* = \hat{q}(\mathbf{v}\cdot\mathbf{q} + q_0\mathbf{v} - \mathbf{v}\times\mathbf{q})$$

$$= q_0(\mathbf{v}\cdot\mathbf{q}) - \mathbf{q}\cdot(q_0\mathbf{v} - \mathbf{v}\times\mathbf{q}) + q_0(q_0\mathbf{v} - \mathbf{v}\times\mathbf{q}) + (\mathbf{v}\cdot\mathbf{q})\mathbf{q} + \mathbf{q}\times(q_0\mathbf{v} - \mathbf{v}\times\mathbf{q}) \qquad \textbf{(A-12)}$$

where the rule for quaternions product (Equation A-5) has been applied. It is clear that,

$$q_0(\mathbf{v}\cdot\mathbf{q}) - \mathbf{q}\cdot(q_0\mathbf{v} - \mathbf{v}\times\mathbf{q}) = 0, \qquad \textbf{(A-13)}$$

which means that the quaternion $\hat{w}$ is just a vector. Now using

$$\hat{q} = \cos\left(\frac{\theta}{2}\right) + \mathbf{v}\sin\left(\frac{\theta}{2}\right), \tag{A-14}$$

where θ is related to the angle of rotation and $\mathbf{u}$ is the rotation axis, we may write

$$\mathbf{w} = q_0^2\mathbf{v} - 2q_0(\mathbf{v}\times\mathbf{q}) + (\mathbf{v}\cdot\mathbf{q})\mathbf{q} - \mathbf{q}\times\mathbf{v}\times\mathbf{q} =$$

$$= \left(\cos\frac{\theta}{2}\right)^2\mathbf{v} - 2\left(\cos\frac{\theta}{2}\right)\left(\sin\frac{\theta}{2}\right)(\mathbf{v}\times\mathbf{u}) + \left(\sin\frac{\theta}{2}\right)^2(\mathbf{v}\cdot\mathbf{u})\mathbf{u} - \left(\sin\frac{\theta}{2}\right)^2\mathbf{u}\times\mathbf{v}\times\mathbf{u}$$

$$= \left(\cos\frac{\theta}{2}\right)^2\mathbf{v} - (\sin\theta)(\mathbf{v}\times\mathbf{u}) + \left(\sin\frac{\theta}{2}\right)^2(\mathbf{v}\cdot\mathbf{u})\mathbf{u} - \left(\sin\frac{\theta}{2}\right)^2\mathbf{v} + \left(\sin\frac{\theta}{2}\right)^2(\mathbf{v}\cdot\mathbf{u})\mathbf{u}$$

$$= 2\left(\sin\frac{\theta}{2}\right)^2(\mathbf{v}\cdot\mathbf{u})\mathbf{u} - (\sin\theta)(\mathbf{v}\times\mathbf{u}) + (\cos\theta)\mathbf{v}$$

$$= (\mathbf{v}\cdot\mathbf{u})\mathbf{u} - (\sin\theta)(\mathbf{v}\times\mathbf{u}) + (\cos\theta)(\mathbf{v} - (\mathbf{v}\cdot\mathbf{u})\mathbf{u}). \tag{A-15}$$

Equation A-15 is the well known *rotation formula* [128] of a vector $\mathbf{v}$ around an axis $\mathbf{u}$ through an angle θ (note that the rotation angle is twice the angle that appear in the quaternion representation, Equation A-14).

It is now possible to find the time derivative of a quaternion [127]. Since any two rotations can be written as a resultant one (*Euler's theorem* [128]), then any two unitary quaternions may be related by some transition quaternion. Therefore, we may relate $\hat{q}(t)$ and $\hat{q}(t+\Delta t)$ by

$$\hat{q}(t+\Delta t) = \hat{q}(t)\,\Delta\hat{r}(t), \tag{A-16}$$

where $\Delta\hat{r}(t) = \cos\left(\frac{\Delta\alpha}{2}\right) + \mathbf{v}(t)\sin\left(\frac{\Delta\alpha}{2}\right)$ is the incremental transition quaternion. Its rotation angle is $\Delta\alpha$ about an axis defined by the unit vector $\mathbf{v}(t)$.

Consider an infinitesimal variation of the rotation angle,

$$\Delta\hat{r}(t) = \cos\left(\frac{\Delta\alpha}{2}\right) + \mathbf{v}(t)\sin\left(\frac{\Delta\alpha}{2}\right) = 1 + \mathbf{v}(t)\frac{\Delta\alpha}{2}. \tag{A-17}$$

Then,

$$\hat{q}(t+\Delta t) = \hat{q}(t)\left(1 + \mathbf{v}(t)\frac{\Delta\alpha}{2}\right),$$

and defining $\frac{d\hat{q}}{dt} = \lim_{\Delta t\to 0}\frac{\hat{q}(t+\Delta t) - \hat{q}(t)}{\Delta t}$, we obtain [127]

$$\frac{d\hat{q}}{dt} = \lim_{\Delta t\to 0}\frac{\hat{q}(t)\mathbf{v}(t)\Delta\alpha}{2\Delta t} = \frac{\hat{q}(t)\mathbf{w}(t)}{2}, \tag{A-18}$$

where $\mathbf{w}(t) = \frac{\mathbf{v}(t)\Delta\alpha}{\Delta t}$ is the angular velocity vector. In matrix form the derivative of a quaternion (Equation A-6) may be written as

$$\frac{d\hat{q}}{dt} = \frac{1}{2}\begin{bmatrix} q_0 & -q_1 & -q_2 & -q_3 \\ q_1 & q_0 & -q_3 & q_2 \\ q_2 & q_3 & q_0 & -q_1 \\ q_3 & -q_2 & q_1 & q_0 \end{bmatrix}\cdot\begin{bmatrix} 0 \\ w_1 \\ w_2 \\ w_3 \end{bmatrix}. \tag{A-19}$$

If one defines an initial quaternion, $\hat{q}$, as $\hat{q} \equiv q_0 + \mathbf{i}q_1 - \mathbf{j}q_2 + \mathbf{k}q_3$ the formula A-19 transforms into

$$\frac{d\hat{q}}{dt} = \begin{bmatrix} \dot{q}_0 \\ \dot{q}_1 \\ -\dot{q}_2 \\ \dot{q}_3 \end{bmatrix} = \frac{1}{2} \begin{bmatrix} q_0 & -q_1 & q_2 & -q_3 \\ q_1 & q_0 & -q_3 & -q_2 \\ -q_2 & q_3 & q_0 & -q_1 \\ q_3 & q_2 & q_1 & q_0 \end{bmatrix} \cdot \begin{bmatrix} 0 \\ w_1 \\ w_2 \\ w_3 \end{bmatrix}. \qquad \textbf{(A-20)}$$

Solving for the angular velocity one obtains

$$\begin{bmatrix} 0 \\ w_1 \\ w_2 \\ w_3 \end{bmatrix} = 2 \begin{bmatrix} q_0 & -q_1 & q_2 & -q_3 \\ q_1 & q_0 & -q_3 & -q_2 \\ -q_2 & q_3 & q_0 & -q_1 \\ q_3 & q_2 & q_1 & q_0 \end{bmatrix}^T \begin{bmatrix} \dot{q}_0 \\ \dot{q}_1 \\ -\dot{q}_2 \\ \dot{q}_3 \end{bmatrix}, \qquad \textbf{(A-21)}$$

which can be transformed into a more convenient form after some matrix manipulations,

$$\begin{bmatrix} w_1 \\ w_2 \\ w_3 \\ 0 \end{bmatrix} = 2 \begin{bmatrix} -q_3 & q_0 & q_2 & -q_1 \\ -q_0 & -q_3 & q_1 & q_2 \\ q_1 & -q_2 & q_0 & -q_3 \\ q_2 & q_1 & q_3 & q_0 \end{bmatrix} \cdot \begin{bmatrix} \dot{q}_2 \\ \dot{q}_1 \\ \dot{q}_3 \\ \dot{q}_0 \end{bmatrix}. \qquad \textbf{(A-22)}$$

Equation A-22, appearing as a natural consequence of the application of the mathematical properties of quaternions, was derived by Evans (see Equation 27 in reference [129]) in a different way; Evans uses the simplicity of the orientation metric as a guide to the associated simplicity of the equations of motion. The definition of $\hat{q} \equiv q_0 + \mathbf{i}q_1 - \mathbf{j}q_2 + \mathbf{k}q_3$, used by Evans and here, is conventional. It is important to note that the relationship

$$q_1\dot{q}_1 + q_2\dot{q}_2 + q_3\dot{q}_3 + q_4\dot{q}_4 = 0 \qquad \textbf{(A-23)}$$

has a clear physical interpretation, as the time derivative of the normalization property of unit quaternions (Equation A-8). This equation appears added as a dynamical constraint in Evans's derivation [129].

Evans found [129,130] quaternion parameters to be more efficient than the conventional Euler angles in the evaluation of the rotation matrix and their numerical stability. The reason behind this fact is simple; the principal angular velocity is related to the time derivatives of the Euler angles, ϕ-θ-ψ, as follow [128],

$$\begin{bmatrix} w_1 \\ w_2 \\ w_3 \end{bmatrix} = \begin{bmatrix} \sin\theta\sin\psi & \cos\psi & 0 \\ \sin\theta\cos\psi & -\sin\psi & 0 \\ \cos\theta & 0 & 1 \end{bmatrix} \cdot \begin{bmatrix} \dot{\phi} \\ \dot{\theta} \\ \dot{\psi} \end{bmatrix}. \qquad \textbf{(A-24)}$$

Then, for example, when $\theta = 0$ the orientation matrix is singular and its inverse does not exist. Thus, although the rotational equations of motion expressed in Euler angles are simple [128],

$$\begin{aligned} \dot{L}_1 &= T_1 + (I_2 - I_3)w_2w_3 \\ \dot{L}_2 &= T_2 + (I_3 - I_1)w_3w_1 \\ \dot{L}_3 &= T_3 + (I_1 - I_2)w_1w_2, \end{aligned} \qquad \textbf{(A-25)}$$

where $\dot{L}_i$ is the time derivative of the angular momentum, T_i is the torque and I_i is the principal inertia moment about axis i, respectively, the singularities associated with the use of Euler angles as generalized orientational variables are a severe drawback.

In contrast, Equation A-22 (the quaternion analog of Equation A-24), which can also be written as $\hat{w} = 2 \cdot \Xi \cdot \dot{\hat{q}}$, never fails because in order for Ξ to be singular it is necessary that $q_0^2 + q_1^2 + q_2^2 + q_3^2 = 0$ which severely violates the unitary character of the quaternion.

REFERENCES

1. D. A. McQuarrie, *Statistical Thermodynamics* (Harper & Row, New York, 1973).

2. D. Chandler, *Introduction to modern Statistical Mechanics*, (Oxford University Press, New York, 1986).

3. T. L. Hill, *An Introduction to Statistical Thermodynamics*, (Dover Publications, New York, 1986).

4. M. P. Allen and D. J. Tildesley, *Computer Simulation of Liquids* (Clarendon Press, Oxford, 1989).

5. J. P. Hansen and I. R. Macdonald, *Theory of simple liquids*, (Academic Press, London, 1986).

6. D. M. Heyes, *The liquid state. Applications of molecular simulations*, (John Wiley & Sons, Chichester, 1998).

7. R. P. Feynman and A. R. Hibbs, *Quantum Mechanics and Path Integrals* (McGraw-Hill, New York, 1965).

8. R. P. Feynman, *Statistical Mechanics: a set of lectures*, (Reading, Massachusetts, 1972).

9. J. Berne and D. Thirumalai, Ann. Rev. Phys. Chem. 37, 401-24 (1986).

10. D. Chandler in *Liquids, Freezing and Glass Transition* ed J. P. Hansen, D. Levesque and J. Zinn-Justin (Amsterdan: Norh-Holland, 1991).

11. M. Parrinello and A. Rahman, J. Chem. Phys. 80, 860 (1984).

12. R. A. Kuharski and P. J. Rossky, J. Chem. Phys. 82, 5164 (1985).

13. A. Wallqvist and B. J. Berne, Chem. Phys. Letter. 117, 214 (1985).

14. G. S. del Buono, P. J. Rossky amd J. Schnitker, J. Chem. Phys. 95, 3728 (1991).

15. H. A. Stern and B. J. Berne, J. Chem. Phys. 115, 7622 (2001).

16. H. Gai, G. K. Schenter and B. C. Garret, J. Chem. Phys. 104, 680 (1996).

17. G. Voth in *Advances in Chemical Physics, Volume XCIII*, edited by I. Prigogine and Stuart A. Rice (John Wiley & Sons, 1996).

18. G. A. Voth in *Theoretical Methods in Condensed Phase Chemistry*, ed by S. D Schwartz (2000).

19. J. Lobaugh and G. A. Voth, J. Chem. Phys. 106, 2400, (1997).

20. B. Guillot and Y. Guissani, J. Chem. Phys. 108, 10162 (1998).

21. *Water a comprehensive treatise*, Edited by F. Franks (Plenum Press, New York, 1972).

22. D. Eisenberg and W. Kauzman, *The structure and properties of water*, (Clarendon Press, Oxford, 1969).

23. F. Franks, *Water a matrix of life*, (Royal Society of Chemistry, Cambridge, 2000).

24. A. Ben-Naim, *Water and aqueous solutions. Introduction to a molecular theory*, (Plenum Press, New York, 1974).

25. A. Wallqvist and R. D. Mountain in *Reviews in Computational Chemistry*, Vol. 13, edited by K. B. Lipkowitz and D. B. Boyd (John Wiley & Sons, 1999);

26. B. Guillot, J. Mol. Liq. 101, 219 (2002).

27. M. Allesch, E. Schwegler, F. Gygi and Giulia Galli, *J. Chem. Phys.* 120, 5192 (2004).

28. P. A. Egelstaff, *An Introduction to the Liquid State*, 2nd ed. (Clarendon, Oxford, 1992).

29. A. H. Narten and H. A. Levy, J. Chem. Phys. 55, 2263 (1971).

30. A. Guinier, *X-ray Difraction in Crystals, Imperfect Crystals and Amorphous Bodies*, (Dover, New York, 1994).

31. J. M. Sorenson, G. Hura, R. M. Glaeser, T. Head-Gordon, J. Chem. Phys. 113, 9140 (2000).

32. J. M. Sorenson, G. Hura, R. M. Glaeser, T. Head-Gordon, J. Chem. Phys. 113, 9149 (2000).

33. A. K. Soper and R. N. Silver, Phys. Rev. Lett. 49, 471 (1982).

34. A. K. Soper, F. Bruni and M. A. Ricci, J. Chem. Phys. 106, 247 (1997).

35. A. K. Soper and A. Luzar, J. Chem. Phys. 97, 1320 (1992).

36. A. K. Soper, J. Chem. Phys. 101, 6888 (1994).

37. P. Postorino, M. A. Ricci, A. K. Soper, J. Chem. Phys. 101, 4123 (1994).

38. R. H. Tromp, J. Chem. Phys. 101, 6220 (1994).

39. N. Metropolis, A. W. Rosenbluth, M. N. Rosenbluth, A. H. Teller and E. Teller, J. Chem. Phys. 21, 1087 (1953).

40. B. J. Alder and T. E. Wainwright, J. Chem. Phys. 31, 459 (1959).

41. J. M. Halle, Molecular Dynamics Simulation: Elementary methods, (John Wiley & Sons, Inc, New York, 1992).

42. Wm. G. Hoover, *Computational Statistical Mechanics*, (Elsevier Science Publisher B. V., 1991).

43. D. J. Evans and G. P. Morris, *Statistical Mechanics of Nonequilibrium Liquids*, (Academic Press, London, 1990)

44. C. P. Dettman and G.P. Morris, Phys. Rev. E, 54, 2495 (1996).

45. S. Nosé, J. Chem. Phys. 81, 511 (1984).

46. W. G. Hoover, Phys. Rev. A 31, 1695 (1985).

47. G. J. Martyna and M. L. Klein, J. Chem. Phys. 97, 2635, 1992.

48. H. C. Andersen, J. Chem. Phys. 72, 2384 (1980).

49. V. F. Petrenko and R. W. Whitworth, *Physics of ice*, (Oxford University Press, New York, 1999).

50. S. A. Clough, Y. Beers, G. P. Klein and L. S. Rothman, J. Chem. Phys. 59, 2254 (1973).

51. W. S. Benedict, N. Gailar and E. K. Plyler, J. Chem. Phys. 24, 1139 (1956).

52. A. V. Gubskaya and P. G. Kusalik J. Chem. Phys., 117, 5290 (2002).

53. G. Tammann, Annalen der Physik, Series 4, 2, 1 (1900).

54. From http://www.lsbu.ac.uk/water/ by M. Chaplin 2004.

55. I. Kirshenbaum, *Physical properties and analysis of heavy water*, (McGraw Hill, New York, 1951).

56. W. M. Jones, JACS, 74, 6065, (1952).

57. M. Goldblatt, J. Phys. Chem. 68, 147 (1964).

58. L. Haar, J. S. Gallagher and G. S. Kell, NBS/NRC Steam Tables, Hemisphere, Washington, D. C., 1984.

59. G. Jancso and W. A. van Hook, Chem. Rev. 74, 689 (1974).

60. H. J. C. Berendsen, J. P. M. Postma, W. G. van Gunsteren and J. Hermans, in Intermolecular Forces, ed. B. Pullman (Reidel, Dordrecht, 1981).

61. W. L. Jorgensen, J. Chandrasekhar, J. D. Madura, R. W. Impey and M. L. Klein, J. Chem. Phys. 79, 926 (1983).

62. F. H. Stillinger and A. Rahman, J. Chem. Phys. 60, 1545 (1974);

63. T. Head-Gordon and F. H. Stillinger, J. Chem. Phys. 98, 3313 (1993).

64. J. R. Errington and A. Z. Panagiotopoulos, J. Phys. Chem. B 102 7470 (1998).

65. Y. S. Baydal, M. L. Saboungi, K. L. Price, S. D. Shastri, D. R. Haeffner and A. K. Soper, J. Chem. Phys. 112, 9206 (2000).

66. G. Hura, J. M. Sorenson, R. M. Glaeser and T. Head-Gordon, J. Chem. Phys. 113, 9140 (2000).

67. H. J. C. Berendsen, J. R. Grigera and T. P. Straatsma, J. Phys. Chem. 91, 6269 (1987).

68. H. W. Horn, W. C. Swope, J. W. Pitera, J. D. Madura, T. J. Dick, G. L. Hura, T. Head-Gordon, J. Chem. Phys. 120, 9665 (2004)

69. K. Toukan and A. Rahman, Phys. Rev. B 31, 2643 (1985).

70. H. L. Lemberg and F. H. Stillinger, J. Chem. Phys. 62, 1677 (1975); A. Rahman, F. H. Stillinger and F. Lemberg, J. Chem. Phys. 63, 5223 (1975); F. H. Stillinger and A. Rahman, J. Chem. Phys. 68, 666 (1978); M. D. Duh, D. N. Perera and A. D. J. Haymet, J. Chem. Phys. 102, 3736 (1995).

71. K. Ichikawa, Y. Kameda, T. Yamaguchi, H. Wakita and M. Misawa, Mol. Phys. 73, 79 (1991).

72. P. Alström, A. Wallqvist, S. Engström and B. Jönsson, Mol. Phys. 68, 563 (1989).

73. M. Sprik, J. Chem. Phys. 95, 2283 (1991).

74. P. Cieplak, P. Kollman and T. Lybrand, J. Chem. Phys. 92, 6755 (1990).

75. S. W. Rick, S. J. Stuart and B. J. Berne, J. Chem. Phys. 101, 6141 (1994).

76. H. Saint-Martin, C. Medinas-Lianos and I. Ortega-Blake, J. Chem. Phys. 93, 6448 (1990).

77. A. Wallqvist, P. Alström, G. Karlström, J. Phys. Chem. 94, 1649 (1990); A. Wallqvist, P. O. Astrand, J. Chem. Phys. 102, 6559 (1995).

78. I. M. Svishchev, P. G. Kusalik, J. Wang and R. J. Boyd, J. Chem. Phys. 105, 4742 (1996).

79. *Molecular Dynamics: From Classical to Quantum Methods*, edited by P. B. Balbuena and J. M. Seminario (Elsevier, Amsterdam, 1999).

80. A. Szabo and N. S. Ostlund, *Modern Quantum Chemistry. Introduction to advanced Molecular Structure Theory* (McGraw-Hill, New York, 1989)

81. R. Parr and W. Yang, *Density-Functional Theory of Atoms and Molecules* (Oxford University Press, New York 1989)

82. W. H. Press, B. P. Flannery, S. A. Teukolsky and W. T. Vetterling, *Numerical Recipes* (Cambridge University Press, Cambridge, 1986).

83. K Uehara, M. Ishitobi, T. Oda and Y. Iwatari, Mol. Simul. 18, 385 (1997).

84. R. Car and M. Parrinello, Phys. Rev. Lett. 55, 2471-74 (1985).

85. G. Pastore, E. Smargiassi and F. Buda, Phys. Rev. A 44, 6334 (1991).

86. C. Lee, D. Vanderbrilt, K. Laasonen, R. Car and M. Parrinello, Phys. Rev. B 47, 4863 (1993).

87. K. Laasonen, M. Sprik, M. Parrinello, R. Car, J. Chem. Phys. 99, 9080 (1993).

88. D. Vanderbilt, Phys. Rev. B: Condens. Matter 43, 1993-2006 (1991).

89. M. Sprik, J. Hutter and M. Parrinello, J. Chem. Phys. 105, 1142 (1996).

90. P. L. Silvestrelli and M. Parrinello, Phys. Rev. Lett. 82, 3308 (1999).

91. J. C. Grossman, E. Schwegler, E. W. Draeger, F. Gygi and G. Galli, J. Chem. Phys 120, 300 (2004).

92. J. A. Barker, J. Chem. Phys. 70, 2914 (1979).

93. E. L. Pollock and D. M. Ceperley, Phys. Rev. B 30, 2555 (1984).

94. M. Parrinello and A. Rahman, J. Chem. Phys. 80, 860 (1984).

95. M. Tukerman in *Quantum Simulations of Complex Many-Body Systems: From Theory to Algorithms*, Lecture Notes, J. Grotendorst, D. Marx, A. Muramatsu (Eds.), Jon von Neumann Institute for Computing, Jülich, NIC Series, 2002.

96. M. F. Trotter, Proc. Am. Math. Soc. 10, 545 (1959).

97. L. S. Schulman, *Techniques and Applications of Path Integration* (John Wiley & Sons, New York,1981).

98. W. Greiner, *Quantum Mechanics: An Introduction* (Springer-Verlag, Berlin, 1989).

99. M. E. Tuckerman, B. J. Berne, G. J. Martyna and M. L. Klein, J. Chem. Phys. 99, 2796 (1993).

100. G. J. Martyna, A. Hughes and M. E. Tuckerman, J. Chem. Phys. 110, 3275 (1999).

101. R. Egger and C. H. Mak in *Quantum Simulations of Complex Many-Body Systems: From Theory to Algorithms*, Lecture Notes, J. Grotendorst, D. Marx, A. Muramatsu (Eds.), Jon von Neumann Institute for Computing, Jülich, NIC Series, 2002.

102. J. R. Reimers and R. O. Watts, Chem. Phys. Letters 94, 222 (1982); J. R. Reimers and R. O. Watts, Mol. Phys. 52, 357 (1984).

103. L. M. Sese, Molecular Physics 81, 1297 (1993).

104. F. X. Prielmeier, E. W. Lang, R. J. Speedy and H. D. Ludemann, Ber Bunsenges. Phys. Chem. 92, 1111 (1988); K. Krrynicky, C. D. Green, And D. W. Sawyer, Faraday Discuss. Chem. Soc. 66, 199 (1980).

105. J. Cao and G. A. Voth, J. Chem. Phys. 99, 10070 (1993)

106. J. Cao and G. A. Voth, J. Chem. Phys. 100, 5093 (1994)

107. J. Cao and G. A. Voth, J. Chem. Phys. 100, 5106 (1994)

108. J. Cao and G. A. Voth, J. Chem. Phys. 100, 6157 (1994)

109. J. Cao and G. A. Voth, J. Chem. Phys. 100, 6168 (1994)

110. S. Jang and G. A. Voth, J. Chem. Phys. 111, 2357 (1999)

111. S. Jang and G. A. Voth, J. Chem. Phys. 111, 2371 (1999)

112. M. E. Tuckerman, D. Marx, M. L. Klein, M. Parrinello, J. Chem. Phys. 104, 5579 (1996).

113. D. Marx, M. Parrinello, J. Chem. Phys. 104, 4077 (1997).

114. B. Chen, I. Ivanov, M. L. Klein and M. Parrinello, Phys. Rev. Lett. 91, 215503-1 (2003).

115. F. D Rossini, J. W. Knowlton and H. L. Johnston, J. Res. Natl. Bur. Stand. 24, 369 (1940); L. Haar, J. S. Gallagher and G. S. Kell, *NBS/NRC Steam Tables* (Hemisphere Washington, 1984); P. G. Hill, R. D. C. Mac Millan and V. Lee, J. Chem. Ref. Data 11, 1 (1982).

116. R. Ramirez and T. López-Ciudad in *Quantum Simulations of Complex Many-Body Systems: From Theory to Algorithms*, Lecture Notes, J. Grotendorst, D. Marx, A. Muramatsu (Eds.), Jon von Neumann Institute for Computing, Jülich, NIC Series, 2002.

117. E. P. Wigner, Z. Phys. Chem. B, 203 (1932).

118. M. Hillery, R. F. O'connell, M. O. Scully and E. P. Wigner, Phys. Rep. 106, 121 (1984).

119. M. Pascolli, P. Bordone, R. Brunetti and C. Jacoboni, Phys. Rev. B 58, 3503 (1998).

120. A. Messiah, *Quantum Mechanics* (John Wiley, New York, 1961).

121. R. Kubo, M. Toda and N. Hashitsume, *Statistical Physics II* (Springer, Berlin, 1992).

122. N. Blinov and P. N. Roy, J. Chem. Phys. 115, 7822 (2001).

123. R. P. Feynman, Phys. Rev. 84, 108 (1951).

124. R. F. Snider, J. Math. Phys. 5, 1586 (1964).

125. D. Reichman, P. N. Roy, S. Jang and G. A. Voth, J. Chem. Phys. 113, 919 (2000).

126. D. J. Evans and S. Murad, Mol. Phys. 68, 1219 (1989)

127. J. B. Kuipers, *Quaterions and rotation sequences* (Princeton University Press, Princeton, 1999).

128. R. Goldstain, *Classical Mechanics* 2nd ed. (Addison-Wesley Publishing Company, 1980).

129. D. J. Evans, Mol. Phys. 34, 317 (1977).

130. D. J. Evans and S. Murad, Mol. Phys., 34, 327 (1977).

131. D. J. Evans and S. Murad, Mol. Phys. 69, 607 (1990).

132. L. Schulman, Phys. Rev. 176, 1558 (1968).

133. L. Hernández de la Peña and P. G. Kusalik, Mol. Phys. 102, 927 (2004).

134. S.R. Buss and J. P. Fillmore, ACM T Graphic 20, 95 (2001).

135. L. D. Kudriatsev, *Curso de Analisis Matematico* (Editorial Mir, Moscu, 1983).

136. A. V. Gubskaya and P. G. Kusalik J. Chem. Phys., 117, 5290 (2002).

137. M. Pavese, S. Jang and G. A. Voth, Pararell Computing 26 (2000) 1025-1041.

138. L. Hernández de la Peña and P. G. Kusalik, J. Chem. Phys. 121, 5992 (2004).

139. I. M. Svishchev and P. G. Kusalik, J. Phys. Chem., 98, 728 (1994).

140. I. M. Svishchev and P. G. Kusalik, J. Chem. Soc. Faraday Trans., 90, 1405 (1994).

141. M. Mizoguchi, Y. Hori and Y. Tominaga, J. Chem. Phys., 97, 1961 (1992).

142. M. Hermanns, *Parallel programming in Fortran 95 using Open-MP*, School of Aeronautical Engineering, Universidad Politecnica de Madrid, Spain (2002).

143. R. J. Speedy and C. A. Angell, J. Chem. Phys. 65, 851 (1976)

144. D. Rasmussen and A. P. Mackenzie, J. Chem. Phys. 59, 5003 (1973)

145. G. S. Kell CRC Handbook of Chemistry and Physics, 56th Edition, 1975-1976.

146. S. R. Billeter, P. M. King and W. F. van Gunsteren, J. Chem. Phys. 100, 6692 (1994).

147. P. L. Chau and A. J. Hardwick, Mol. Phys. 93, 511 (1998).

148. P. H. Poole, F. Sciortinio, U. Essmann and H. E. Stanley, Phys. Rev. E 48, 3799 (1993).

149. P. G. Kusalik and I. M. Svishchev, Science 265, 1219 (1994)

150. P. G. Kusalik, A. Laaksonen and I. M. Svishchev in Molecular Dynamics. From Classical to Quantum methods (Ed. By P. B. Balbuena and J. M. Seminario, Elsevier, Amsterdam, 1999)

151. A. K. Soper, Physica B 214, 448 (1995).

152. P. V. Hobbs, *Ice Physics* (Clarendon Press, Oxford, 1974).

153. H. J. Prask, S. F. Trevino, J. D. Gault and K. W. Logan, J. Chem. Phys. 56, 3217 (1972).

154. W. F. Kuhs and M. S. Lehmann, Water Science Reviews 2, 1 (1986).

155. J. S. Tse, M. L. Klein and I. R. MacDonald, J. Chem. Phys. 81, 6124 (1984).

156. C. J. Burnham and J. C. Li, J. Phys. Chem. B 101, 6192 (1997).

157. H. M. van Pinxteren and J. W. M. Frenkel, Surf. Sci. 275, 365 (1992); L. A. Baez and P. Clancy, Mol. Phys. 86, 385 (1995).

158. S. C. Gay, E. J. Smith and A. D. J. Haymet, J. Chem. Phys. 116, 8876 (2002).